frontiers | Research Topics

Diffusion-weighted MR imaging (DW-MRI) and diffusion-weighted MR spectroscopy (DW-MRS)

Edited by
Maryam Afzali, Lars Mueller, André Döring, Clemence Ligneul, Chloe Najac and Itamar Ronen

Published in
Frontiers in Neuroscience
Frontiers in Oncology
Frontiers in Neuroimaging

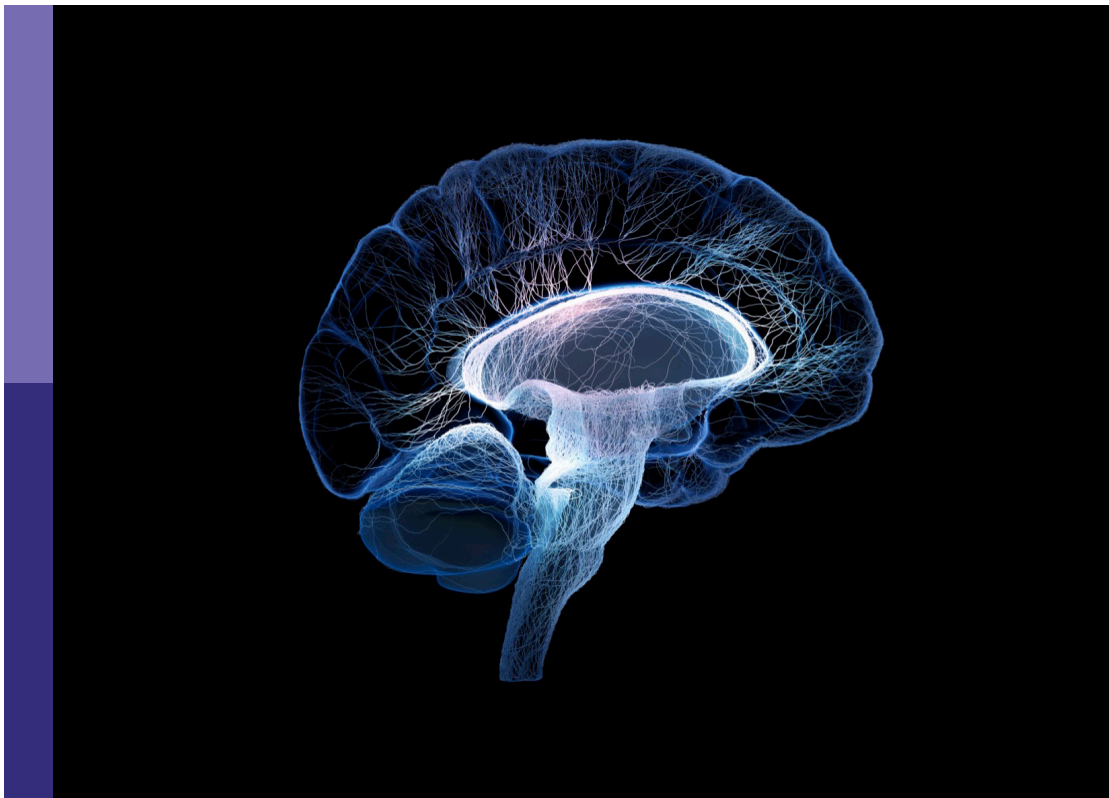

ISSN 1664-8714
ISBN 978-2-8325-5075-5
DOI 10.3389/978-2-8325-5075-5

About Frontiers

Frontiers is more than just an open access publisher of scholarly articles: it is a pioneering approach to the world of academia, radically improving the way scholarly research is managed. The grand vision of Frontiers is a world where all people have an equal opportunity to seek, share and generate knowledge. Frontiers provides immediate and permanent online open access to all its publications, but this alone is not enough to realize our grand goals.

Frontiers journal series

The Frontiers journal series is a multi-tier and interdisciplinary set of open-access, online journals, promising a paradigm shift from the current review, selection and dissemination processes in academic publishing. All Frontiers journals are driven by researchers for researchers; therefore, they constitute a service to the scholarly community. At the same time, the *Frontiers journal series* operates on a revolutionary invention, the tiered publishing system, initially addressing specific communities of scholars, and gradually climbing up to broader public understanding, thus serving the interests of the lay society, too.

Dedication to quality

Each Frontiers article is a landmark of the highest quality, thanks to genuinely collaborative interactions between authors and review editors, who include some of the world's best academicians. Research must be certified by peers before entering a stream of knowledge that may eventually reach the public - and shape society; therefore, Frontiers only applies the most rigorous and unbiased reviews. Frontiers revolutionizes research publishing by freely delivering the most outstanding research, evaluated with no bias from both the academic and social point of view. By applying the most advanced information technologies, Frontiers is catapulting scholarly publishing into a new generation.

What are Frontiers Research Topics?

Frontiers Research Topics are very popular trademarks of the *Frontiers journals series*: they are collections of at least ten articles, all centered on a particular subject. With their unique mix of varied contributions from Original Research to Review Articles, Frontiers Research Topics unify the most influential researchers, the latest key findings and historical advances in a hot research area.

Find out more on how to host your own Frontiers Research Topic or contribute to one as an author by contacting the Frontiers editorial office: frontiersin.org/about/contact

Diffusion-weighted MR imaging (DW-MRI) and diffusion-weighted MR spectroscopy (DW-MRS)

Topic editors

Maryam Afzali — University of Leeds, United Kingdom
Lars Mueller — University of Leeds, United Kingdom
André Döring — Center for Biomedical Imaging (CIBM), Switzerland
Clemence Ligneul — University of Oxford, United Kingdom
Chloe Najac — Leiden University Medical Center (LUMC), Netherlands
Itamar Ronen — Brighton and Sussex Medical School, United Kingdom

Citation

Afzali, M., Mueller, L., Döring, A., Ligneul, C., Najac, C., Ronen, I., eds. (2024). *Diffusion-weighted MR imaging (DW-MRI) and diffusion-weighted MR spectroscopy (DW-MRS)*. Lausanne: Frontiers Media SA.
doi: 10.3389/978-2-8325-5075-5

Table of contents

frontiers | Frontiers in Oncology

TYPE Original Research
PUBLISHED 28 April 2023
DOI 10.3389/fonc.2023.1139189

OPEN ACCESS

EDITED BY
Maryam Afzali,
University of Leeds, United Kingdom

REVIEWED BY
Mami Iima,
Kyoto University, Japan
Yan Lin,
Second Affiliated Hospital of Shantou University Medical College, China

*CORRESPONDENCE
Tao Ai
aitao007@hotmail.com

†These authors have contributed equally to this work

RECEIVED 06 January 2023
ACCEPTED 17 April 2023
PUBLISHED 28 April 2023

CITATION
Qin Y, Wu F, Hu Q, He L, Huo M, Tang C, Yi J, Zhang H, Yin T and Ai T (2023) Histogram analysis of multi-model high-resolution diffusion-weighted MRI in breast cancer: correlations with molecular prognostic factors and subtypes. *Front. Oncol.* 13:1139189. doi: 10.3389/fonc.2023.1139189

Histogram analysis of multi-model high-resolution diffusion-weighted MRI in breast cancer: correlations with molecular prognostic factors and subtypes

Yanjin Qin[1†], Feng Wu[2†], Qilan Hu[1], Litong He[1], Min Huo[3], Caili Tang[1], Jingru Yi[1], Huiting Zhang[4], Ting Yin[5] and Tao Ai[1*]

[1]Department of Radiology, Tongji Hospital, Tongji Medical College, Huazhong University of Science and Technology, Wuhan, China, [2]Department of Radiology, Xiangyang Central Hospital, Affiliated Hospital of Hubei University of Arts and Science, Xiangyang, China, [3]Department of Radiology, Xiantao First People's Hospital Affiliated to Yangtze University, Xiantao, China, [4]Magnetic Resonance (MR) Scientific Marketing, Siemens Healthineers Ltd., Wuhan, China, [5]Magnetic Resonance (MR) Collaborations, Siemens Healthineers Ltd., Chengdu, China

Objective: To investigate the correlations between quantitative diffusion parameters and prognostic factors and molecular subtypes of breast cancer, based on a single fast high-resolution diffusion-weighted imaging (DWI) sequence with mono-exponential (Mono), intravoxel incoherent motion (IVIM), diffusion kurtosis imaging (DKI) models.

Materials and Methods: A total of 143 patients with histopathologically verified breast cancer were included in this retrospective study. The multi-model DWI-derived parameters were quantitatively measured, including Mono-ADC, IVIM-*D*, IVIM-*D**, IVIM-*f*, DKI-Dapp, and DKI-Kapp. In addition, the morphologic characteristics of the lesions (shape, margin, and internal signal characteristics) were visually assessed on DWI images. Next, Kolmogorov–Smirnov test, Mann-Whitney *U* test, Spearman's rank correlation, logistic regression, receiver operating characteristic (ROC) curve, and Chi-squared test were utilized for statistical evaluations.

Results: The histogram metrics of Mono-ADC, IVIM-*D*, DKI-Dapp, and DKI-Kapp were significantly different between estrogen receptor (ER)-positive *vs*. ER-negative groups, progesterone receptor (PR)-positive *vs*. PR-negative groups, Luminal *vs*. non-Luminal subtypes, and human epidermal receptor factor-2 (HER2)-positive *vs*. non-HER2-positive subtypes. The histogram metrics of Mono-ADC, DKI-Dapp, and DKI-Kapp were also significantly different between triple-negative (TN) *vs*. non-TN subtypes. The ROC analysis revealed that the area under the curve considerably improved when the three diffusion models were combined compared with every single model, except for distinguishing lymph node metastasis (LNM) status. For the morphologic characteristics of the tumor, the margin showed substantial differences between ER-positive and ER-negative groups.

Conclusions: Quantitative multi-model analysis of DWI showed improved diagnostic performance for determining the prognostic factors and molecular subtypes of breast lesions. The morphologic characteristics obtained from high-resolution DWI can be identifying ER statuses of breast cancer.

KEYWORDS

diffusion weight imaging, diffusion kurtosis imaging, intravoxel incoherent motion, breast cancer, prognosis, molecular subtypes

Introduction

Diffusion-weighted imaging (DWI) has been proven to be a potential diagnostic tool for the evaluation of breast lesions (1). In clinical practice, single-shot echo planar imaging (ss-EPI) sequence is commonly utilized in breast DWI protocols due to fast acquisition time (2, 3). However, previous studies have seldom evaluated the morphologic analysis of lesions on ss-EPI images due to geometric distortion and poor spatial resolution (4, 5). Readout-segmented EPI (rs-EPI) can reduce distortions and maintain high resolution, but it was limited by long scan times (6). Recently, the simultaneous multislice (SMS) technique, which allows the exciting acquire multiple slices at once, has been introduced to reduce the scan time (7, 8). The SMS technique was combined with rs-EPI to generate images with less image distortion and higher spatial resolution for breast lesions in a clinically acceptable scanning duration (9, 10). The application of SMS rs-EPI makes it feasible to qualitatively assess the morphologic characteristics of breast lesions.

In addition to the qualitative analysis of SMS rs-EPI images, our study also focused on the quantitative analysis of multi-model DWI. Conventional DWI is based on a mono-exponential (Mono) model that was first proposed to reflect the random Brownian motion of water molecules diffusing into biological media by quantifying apparent diffusion coefficient (ADC) values (11). However, water diffusion in complex biological media may be influenced by the blood microcirculation in capillaries, leading to a non-Gaussian distribution (12, 13). To address this, advanced diffusion models, including intravoxel incoherent motion (IVIM) and diffusion kurtosis imaging (DKI), have been developed to reflect the diffusion behavior of water molecules in tumors more accurately (14). A few studies have investigated the correlations between IVIM- or DKI-derived parameters with several clinical prognostic factors and molecular subtypes. However, the conclusions have still not reached a consensus (15, 16). Furthermore, most studies have reported that more information can be parsed from histogram analysis, which can reflect the microstructures and heterogeneity of breast cancer (17–20).

Therefore, the aim of this study was to apply three diffusion models (Mono, IVIM, and DKI) to determine the parameters valuable for differentiating between prognostic factor statuses and molecular subtypes, as well as to assess the correlations of morphologic characteristics with prognostic factors and molecular subtypes.

Materials and methods

Patients

This retrospective study was approved by our institutional review board, and informed consent was obtained. From September 2020 to May 2021, 216 female patients who underwent breast MRI in our hospital and fulfilled the following criteria were selected: (1) the patients did not undergo chemotherapy, or any other interventions before they were examined by MRI; (2) the pathologic type of breast lesions was confirmed by surgery or biopsy; and (3) relevant pathologic data of patients were complete. The exclusion criteria included: 1) non-mass like enhancement lesions detected on dynamic contrast-enhanced (DCE)-MRI (n = 34); 2) the max diameter of mass lesions< 1cm (n = 16); 3) poor DWI image quality due to patient motion or susceptibility artifact (n = 23). Only the largest lesion was analyzed when multiple lesions were detected in the bilateral breast. Finally, 143 patients (mean age, 48.57 ± 12.01 years, range, 26 – 81 years) with 143 mass lesions (mean diameter, 2.48 ± 0.95 cm) were included in the study. More detailed characteristics of the 143 patients are summarized in Table 1.

MRI scans

Breast MRI was performed on a 3T MRI scanner (MAGNETOM Skyra, Siemens Healthcare, Erlangen, Germany) using a dedicated 16-channel phased-array bilateral breast surface coil. The breast MRI protocol included the following sequences: axial fat-saturated T2-weighted imaging, T1-weighted DCE-MRI with the time-resolved angiography (TWIST) with a volumetric interpolated breath-hold examination (VIBE) technique, and SMS rs-EPI sequence. Detailed imaging parameters are provided in Table 2.

Image analysis

The images were independently analyzed by two breast readers (with 3 and 5 years of experience, respectively) using an in-house-developed DKI tool software. Both readers were informed that the

TABLE 1 Study population and histopathological characteristics.

Characteristics		N (%)
Age at diagnosis	≤ 50	78 (54.5)
	> 50	65 (45.5)
Long diameter (cm)	> 2	91 (63.6)
	≤ 2	52 (36.4)
Side	Right	68 (47.6)
	Left	75 (52.4)
Menopausal status	Premenopausal	74 (51.7)
	Postmenopausal	69 (48.3)
Histological type	IDC	109 (76.2)
	ILC	11 (7.7)
	Papillary carcinoma	8 (5.6)
	DCIS	15 (10.5)
ER	Positive	80 (55.9)
	Negative	63 (44.1)
PR	Positive	76 (53.1)
	Negative	67 (46.9)
HER2	Positive	48 (33.6)
	Negative	95 (66.4)
Ki-67	Positive	79 (55.2)
	Negative	64 (44.8)
LNM	Positive	49 (34.3)
	Negative	94 (65.7)
Molecular subtypes		
Luminal A		45 (31.5)
Luminal B		41 (28.7)
HER2-positive		25 (17.5)
Triple-negative		32 (22.3)
Morphological features		
Shape	Round	24 (16.8)
	Oval	49 (34.3)
	Irregular	70 (48.9)
Margin	Smooth	76 (53.1)
	Spiculated	16 (11.2)
	Irregular	51 (35.7)
Signal	Homogenous	55 (38.4)
	Heterogenous	64 (44.8)
	Rim	24 (16.8)

DCIS, Ductal carcinoma in situ; IDC, Invasive ductal carcinoma; ILC, Invasive lobular carcinoma; ER, Estrogen receptor; PR, Progesterone receptor; HER2, Human epidermal growth factor receptor 2; LNM, Lymph nodes metastasis; TN, Triple-negative.

patients had breast cancer but were blinded to the detailed pathologic data. Two-dimensional (2D) region of interest (ROI) were manually delineated, which excluded the cystic or necrotic portions of the tumor, on high-*b*-value (*b*=1000 s/mm^2) SMS rs-EPI images, with the reference of the corresponding T2-weighted and DCE-MRI images. The ROI was then copied to other parametric maps [including ADC, pure diffusion (*D*), pseudo-diffusion coefficient (*D**), perfusion fraction (*f*), apparent diffusional kurtosis (Kapp), and apparent diffusion coefficient (Dapp) maps] using the DKI tool software. Finally, the histogram information of each ROI map was generated, including mean, median, percentile values (25th and 75th), kurtosis, and skewness. For example, the mean and 75th percentile metrics of Mono-ADC were presented as Mono-ADC$_{mean}$ and Mono-ADC$_{75th}$, respectively.

The corresponding mathematical expressions were as follows:

1. Mono-exponential model (16):

$$Sb/S0 = \exp\ (-bADC)$$

where S_b is the signal intensity on the DWI image at a certain *b* value (800 sec/mm^2) and S_0 is the signal intensity value in the voxels with *b* values of 0.

2.DKI model (21):

$$\ln[S(b)/S0] = -bD_{app} + \frac{1}{6}b^2D_{app}^2K_{app}$$

where S_b is he signal intensity on the DWI image according to all b-values (0, 50, 100, 200, 400, 800, 1000, and 2000 sec/mm^2). D_{app} represents the non-Gaussian diffusion coefficient and K_{app} represents the apparent kurtosis coefficient without unit.

3. IVIM model (22):

$$S_b/S_0 = (1-f)\exp(-bD) + fexp[-b(D*+D)]$$

where S_b is he signal intensity on the DWI image according to the b-value (0, 50, 100, 200, and 400 sec/mm^2). *D* is the true diffusion coefficient representing the simple movement of water molecules in the tissue (unit: mm^2/s), *D** is the pseudo-diffusion coefficient representing perfusion-related diffusion (unit: mm^2/s), and *f* is the fraction of fast diffusion representing the diffusion linked to microcirculation ($0 \le f \le 1$).

Morphologic analysis

Two experienced readers independently assessed several morphologic characteristics on SMS rs-EPI images with *b* = 1000 mm^2/s according to the Breast Imaging Reporting and Data System lexicon (BI-RADS edition 2013). Since enhancement is mostly used to evaluate breast lesions on DCE-MRI, two readers evaluated breast lesions on DWI images using internal signal characteristics, which were defined as lesions with homogeneous signal, heterogeneous signal, or only high-signal at the rim (23, 24). Each morphological characteristic was specifically evaluated as follows:

a. Lesion shape: 1 for round, 2 for oval, 3 for irregular.

TABLE 2 Sequence parameters for T2-weighted imaging, SMS rs-EPI, and DCE-MRI.

Parameters	T2WI	SMS rs-EPI	DCE-MRI
Repetition time (ms)	3700	2350	5.24
Echo time (ms)	101	72	2.46
Field of view (mm^2)	320 x 320	280 x 280	320 x 320
Matrix	224 x 320	122 x 188	182 x 320
Slice thickness (mm)	4	5	1.5
Pixel bandwidth (Hz/Px)	347	887	780
Parallel imaging	GRAPPA (x2)	GRAPPA (x2)	CAIPIRINHA (x4)
b-values (sec/mm^2)	/	0, 50, 100, 200, 400, 800, 1000, 2000	/
Readout segment	/	5	/
Multi-slice mode	/	Slice acceleration (x2)	/
Temporal resolution (sec/phase)	/	/	5.74
Acquisition time (min:sec)	2:06	4:39	5:57

SMS, Simultaneous multi-slice; DCE, Dynamic contrast-enhanced; GRAPPA, Generalized autocalibrating partially parallel acquisition; CAIPIRINHA, Controlled aliasing in parallel imaging results in higher acceleration.
/ indicates Non-applicable.

b. Lesion margin: 1 for smooth, 2 for spiculated, 3 for irregular.
c. Lesion internal signal characteristics: 1 for heterogeneous, 2 for homogeneous, 3 for rim.
d. The max diameter of lesion was measured on the largest tumor section.

Histopathologic assessment

Histopathologic results were obtained from the electronic medical records of each patient in our hospital. Estrogen receptor (ER) positivity and progesterone receptor (PR) positivity were defined as the presence of 1% or more positively stained nuclei in 10 high-power fields (25). Human epidermal growth factor receptor 2 (HER2) was considered positive if it was scored 3+ for immunohistochemically stained tissue, or gene amplification was observed with fluorescence *in situ* hybridization (FISH) (26). More than 20% of cancer nuclei were positively stained for Ki-67 (12). Lymph node metastasis (LNM) was confirmed by the clinician performing the histopathologic examination (13). According to the statuses of ER, PR, HER2, and Ki-67, the breast tumors were further classified as Luminal A, Luminal B, HER2-positive, and triple-negative (TN) (27).

Statistical analysis

All statistical analyses were performed using MedCalc software (version 15.0, Ostend, Belgium) and SPSS software (version 26.0, IL, USA). The inter-reader agreement for diffusion parameters and morphological characteristics was assessed by using the intraclass correlation coefficient (ICC): ICC ≤ 0.40, poor agreement; 0.40 - 0.59, fair agreement; 0.60 - 0.74, good agreement; 0.75 - 1.00, excellent agreement. The categorical variables were as follows: prognostic factors including ER, PR, HER2, Ki-67, and LNM (positive *vs.* negative) and molecular subtypes (Luminal type *vs.* non-Luminal type, TN type *vs.* non-TN type, and HER2-positive type *vs.* non-HER2-positive type). All data were tested first with the Kolmogorov–Smirnov test for normality analysis. The quantitative diffusion parameters and max diameter of lesions between different subgroups were compared using the Mann–Whitney *U* test. Spearman correlations were used to characterize the correlations of multi-model-derived histogram metrics with prognostic factors and molecular subtypes. With pathologic results as the gold standard, the receiver operating characteristic (ROC) curve analysis was used to assess the diagnostic efficacy of each parameter or each model, and the area under the ROC curve (AUC) was calculated. Then, the largest AUC of each parameter was selected to establish the IVIM model (*D*, *D**, and *f*), the DKI model (Kapp and Dapp), and the combined three diffusion models (Mono, IVIM, and DKI) using logistic regression. The AUC comparisons were performed using the DeLong test. The morphologic characteristics were compared using the Chi-squared test. For all tests, the significance was set at $p < 0.05/8 = 0.00625$ (control for multiple comparisons across five prognostic factors and three molecular subtypes).

Results

Inter-reader agreement

As shown in Table 3, there was an excellent agreement between two readers regarding the representative mean and median metrics of diffusion parameters (range of ICCs, 0.827 – 0.939) and morphological characteristics including the shape, margin, and internal signal (range of ICCs, 0.857 – 0.890).

10.3389/fonc.2023.1139189

TABLE 3 Interobserver agreement for diffusion parameters and morphological characteristics by two readers.

Parameters	Metrics	ICC	95% Confidence Interval
Mono-ADC	mean	0.893	0.854 – 0.922
	median	0.882	0.839 – 0.914
IVIM-*D*	mean	0.861	0.807 – 0.900
	median	0.827	0.759 – 0.875
IVIM-*D**	mean	0.939	0.915 – 0.956
	median	0.918	0.885 – 0.941
IVIM-*f*	mean	0.832	0.766 – 0.879
	median	0.871	0.820 – 0.907
DKI-Kapp	mean	0.889	0.849 – 0.919
	median	0.933	0.908 – 0.951
DKI-Dapp	mean	0.927	0.900 – 0.947
	median	0.918	0.888 – 0.940
Morphological characteristics			
Shape		0.857	0.807 – 0.895
Margin		0.867	0.819 – 0.902
Internal signal		0.890	0.851 – 0.920

ICC, intraclass correlation coefficient. D* is pseudo-diffusion coefficient.

Relationship of diffusion parameters with prognostic factors and molecular subtypes

The histogram metrics of various diffusion parameters among prognostic factors and molecular subtypes of breast cancer are displayed in Table 4. For Mono-ADC, IVIM-*D*, and DKI-Dapp, all histogram metrics (mean, median, 25th, and 75th percentile) were significantly lower while DKI-Kapp histogram metrics were significantly higher in ER-positive groups compared to those in ER-negative groups (all $p< 0.0625$), the same trend was found in PR-positive groups compared with the PR-negative groups (all $p< 0.0625$).

Luminal type *vs*. non-Luminal type revealed that considerable differences originated from histogram metrics (mean, median, 25th, and 75th percentile) of Mono-ADC, IVIM-*D*, DKI-Kapp, and DKI-Dapp (all $p< 0.0625$). Significantly higher histogram metrics (mean, median, 25th, and 75th percentile) of Mono-ADC and DKI-Dapp while lower histogram metrics (mean, median, 25th, and 75th percentile) of DKI-Kapp were found in the TN type than in the non-TN type (all p< 0.0625). Additionally, the Mono-ADC (mean, median, 25th, and 75th percentile), IVIM-*D*(mean, median, and 75th percentile), and DKI-Dapp (mean, median, 25th, and 75th percentile) values were significantly higher and the DKI-Kapp (mean, median, and 25th percentile) values were significantly lower in the HER2-positive type than in the non-HER2-positive type (all $p< 0.0625$). No statistically significant difference was observed in the negative and positive groups between HER2, Ki-67, and LNM (all $p > 0.00625$).

Considerable correlations were observed between ER and PR groups as well as Luminal, TN, and HER2-positive types. Diffusion parameters (Mono-ADC, IVIM-*D*, DKI-Dapp, and DKI-Kapp) largely involved the histogram metrics (mean, median, 25th, and 75th percentile). When including all parameters in three diffusion models, 74 correlations were remarkable (Figure 1).

Among single model parameters, $\text{Mono-ADC}_{\text{median}}$ and $\text{Mono-ADC}_{\text{mean}}$ generated the best AUC in the positive and negative groups between ER (AUC = 0.766, $p< 0.001$) and PR (AUC = 0.735, $p< 0.001$), respectively. Meanwhile, $\text{DKI-Kapp}_{\text{kurtosis}}$, $\text{IVIM-}D_{\text{skewness}}$, and $\text{DKI-Dapp}_{\text{skewness}}$ generated the best AUC in the positive and negative groups between HER2 (AUC = 0.632, $p = 0.010$), Ki-67 (AUC = 0.572, $p = 0.049$), and LNM (AUC = 0.603, $p = 0.044$), respectively. Regarding the differentiation of Luminal type *vs*. non-Luminal type, TN type *vs*. non-TN type, as well as HER2-positive type *vs*. non-HER2-positive type, the best AUC was derived from the $\text{Mono-ADC}_{\text{mean}}$ (AUC = 0.785, $p< 0.001$), $\text{Mono-ADC}_{25\text{th}}$ (AUC = 0.719, $p< 0.001$), and $\text{Mono-ADC}_{75\text{th}}$ (AUC = 0.738, $p< 0.001$), respectively (Table 5).

Among single models, the DKI model generated the best AUC in the HER2-positive and HER2-negative groups (AUC = 0.622, $p = 0.017$), Ki-67-negative and Ki-67-positive groups (AUC = 0.611, $p = 0.022$), and LNM-positive and LNM-negative groups (AUC = 0.617, $p = 0.022$). The Mono model generated the best AUC in the ER-positive and ER-negative groups (AUC = 0.766, $p< 0.001$), PR-positive and PR-negative groups (AUC = 0.735, $p< 0.001$), Luminal type *vs*. non-Luminal type (AUC = 0.785, $p< 0.001$), as well as TN type *vs*. non-TN type (AUC = 0.719, $p< 0.001$). Both Mono and DKI

10.3389/fonc.2023.1139189

TABLE 4 Comparisons of mono, IVIM and DKI histogram metrics between different groups with molecular prognostic factors and subtypes.

		ER		PR		HER2		Ki-67	
Parameters	Histogram metrics	Negative	Positive	Negative	Positive	Negative	Positive	Negative	Positive
Mono-ADC	25th	**0.869 ± 0.147**	**0.739 ± 0.118**	**0.853 ± 0.149**	**0.746 ± 0.125**	0.789 ± 0.148	0.809 ± 0.144	0.788 ± 0.135	0.803 ± 0.156
	Median	**0.963 ± 0.163**	**0.812 ± 0.122**	**0.948 ± 0.163**	**0.817 ± 0.130**	0.867 ± 0.160	0.902 ± 0.159	0.868 ± 0.144	0.888 ± 0.172
	Mean	**0.979 ± 0.163**	**0.827 ± 0.126**	**0.964 ± 0.165**	**0.832 ± 0.131**	0.880 ± 0.161	0.921 ± 0.160	0.881 ± 0.145	0.904 ± 0.174
	75th	**1.073 ± 0.192**	**0.906 ± 0.141**	**1.060 ± 0.192**	**0.909 ± 0.146**	0.960 ± 0.181	1.018 ± 0.187	0.964 ± 0.168	0.991 ± 0.198
	Kurtosis	3.739 ± 1.815	3.650 ± 1.859	3.615 ± 1.783	3.755 ± 1.887	3.903 ± 2.001	3.266 ± 1.370	3.597 ± 1.708	3.764 ± 1.937
	Skewness	0.612 ± 0.676	0.509 ± 0.717	0.615 ± 0.633	0.500 ± 0.752	0.582 ± 0.741	0.499 ± 0.610	0.453 ± 0.764	0.636 ± 0.634
IVIM-*D*	25th	**0.990 ± 0.234**	**0.857 ± 0.205**	**0.971 ± 0.231**	**0.867 ± 0.214**	0.914 ± 0.229	0.919 ± 0.228	0.909 ± 0.230	0.921 ± 0.227
	Median	**1.128 ± 0.226**	**0.994 ± 0.174**	**1.113 ± 0.226**	**1.000 ± 0.178**	1.044 ± 0.210	1.072 ± 0.207	1.041 ± 0.189	1.063 ± 0.224
	Mean	**1.147 ± 0.223**	**1.008 ± 0.168**	**1.131 ± 0.224**	**1.016 ± 0.172**	1.059 ± 0.205	1.091 ± 0.206	1.056 ± 0.181	1.080 ± 0.224
	75th	**1.280 ± 0.238**	**1.136 ± 0.185**	**1.266 ± 0.241**	**1.141 ± 0.184**	1.182 ± 0.214	1.235 ± 0.232	1.183 ± 0.190	1.213 ± 0.243
	Kurtosis	3.440 ± 1.553	3.349 ± 1.366	3.376 ± 1.519	3.401 ± 1.390	3.585 ± 1.613	3.002 ± 0.944	3.416 ± 1.583	3.367 ± 1.337
	Skewness	0.459 ± 0.628	0.390 ± 0.608	0.481 ± 0.597	0.366 ± 0.631	0.465 ± 0.650	0.331 ± 0.537	0.328 ± 0.682	0.495 ± 0.550
IVIM-*D**	25th	3.211 ± 4.432	2.775 ± 3.992	2.884 ± 3.961	3.040 ± 4.393	3.188 ± 4.477	2.530 ± 3.531	3.292 ± 4.543	2.704 ± 3.875
	Median	8.321 ± 5.900	7.307 ± 5.040	7.857 ± 5.536	7.663 ± 5.387	7.818 ± 5.462	7.627 ± 5.448	8.050 ± 5.501	7.513 ± 5.412
	Mean	10.022 ± 4.871	9.096 ± 4.040	9.533 ± 4.460	9.478 ± 4.439	9.583 ± 4.435	9.347 ± 4.472	9.741 ± 4.719	9.312 ± 4.208
	75th	14.621 ± 6.304	13.424 ± 5.334	14.180 ± 6.017	13.749 ± 5.617	14.020 ± 5.387	13.816 ± 6.576	13.963 ± 6.027	13.941 ± 5.632
	Kurtosis	5.959 ± 9.492	5.912 ± 4.516	5.874 ± 5.417	5.984 ± 4.538	5.868 ± 5.174	6.060 ± 4.527	5.445 ± 3.703	6.327 ± 5.762
	Skewness	1.282 ± 1.001	1.278 ± 0.907	1.256 ± 1.004	1.301 ± 0.898	1.236 ± 0.961	1.367 ± 0.921	6.327 ± 5.762	1.333 ± 1.029
IVIM-*f*	25th	0.027 ± 0.025	0.025 ± 0.023	0.026 ± 0.025	0.026 ± 0.025	0.027 ± 0.025	0.024 ± 0.021	0.026 ± 0.024	0.026 ± 0.023
	Median	0.052 ± 0.029	0.051 ± 0.031	0.052 ± 0.029	0.052 ± 0.032	0.052 ± 0.032	0.052 ± 0.027	0.055 ± 0.033	0.050 ± 0.029
	Mean	0.058 ± 0.028	0.057 ± 0.030	0.057 ± 0.028	0.058 ± 0.031	0.057 ± 0.031	0.059 ± 0.027	0.061 ± 0.032	0.055 ± 0.027
	75th	0.082 ± 0.041	0.081 ± 0.046	0.082 ± 0.040	0.082 ± 0.047	0.080 ± 0.046	0.084 ± 0.041	0.087 ± 0.049	0.077 ± 0.039
	Kurtosis	3.695 ± 2.332	3.597 ± 2.970	3.533 ± 2.255	3.735 ± 3.049	3.814 ± 3.168	3.296 ± 1.327	3.388 ± 1.720	3.845 ± 3.283

(Continued)

TABLE 4 Continued

		ER		PR		HER2		Ki-67	
Parameters	Histogram metrics	Negative	Positive	Negative	Positive	Negative	Positive	Negative	Positive
	Skewness	0.626 ± 0.709	0.624 ± 0.758	0.591 ± 0.702	0.654 ± 0.765	0.662 ± 0.786	0.551 ± 0.619	0.611 ± 0.643	0.635 ± 0.804
DKI-Kapp	25th	**0.796 ± 0.128**	**0.901 ± 0.158**	**0.811 ± 0.126**	**0.893 ± 0.167**	0.872 ± 0.159	0.820 ± 0.139	0.867 ± 0.142	0.844 ± 0.163
	Median	**0.883 ± 0.125**	**0.993 ± 0.165**	**0.895 ± 0.126**	**0.988 ± 0.171**	0.956 ±0.168	0.921 ± 0.136	0.966 ± 0.137	0.927 ± 0.173
	Mean	**0.878 ± 0.124**	**0.991 ± 0.148**	**0.890 ± 0.122**	**0.986 ± 0.155**	0.956 ± 0.151	0.911 ± 0.140	0.957 ± 0.144	0.928 ± 0.151
	75th	**0.963 ± 0.133**	**1.081 ± 0.160**	**0.973 ± 0.128**	**1.078 ± 0.169**	1.037 ± 0.164	1.013 ± 0.149	1.051 ± 0.154	1.011 ± 0.162
	Kurtosis	3.594 ± 2.031	3.653 ± 1.885	3.618 ± 2.153	3.635 ± 1.753	3.751 ± 1.909	3.381 ± 2.009	3.567 ± 1.765	3.675 ± 2.087
	Skewness	-0.124 ± 0.752	0.005 ± 0.812	-0.136 ± 0.742	0.023 ± 0.821	0.021 ± 0.804	-0.195 ± 0.738	-0.046 ± 0.813	-0.056 ± 0.769
DKI-Dapp	25th	**1.179 ± 0.209**	**1.003 ± 0.208**	**1.148 ± 0.211**	**1.014 ± 0.217**	1.072 ± 0.238	1.087 ± 0.194	1.079 ± 0.206	1.075 ± 0.239
	Median	**1.318 ± 0.227**	**1.124 ± 0.203**	**1.298 ± 0.227**	**1.131 ± 0.213**	1.195 ± 0.241	1.238 ± 0.219	1.205 ± 0.217	1.213 ± 0.249
	Mean	**1.335 ± 0.223**	**1.146 ± 0.205**	**1.316 ± 0.225**	**1.153 ± 0.211**	1.215 ± 0.241	1.259 ± 0.211	1.222 ± 0.217	1.236 ± 0.245
	75th	**1.481 ± 0.265**	**1.274 ± 0.220**	**1.467 ± 0.265**	**1.276 ± 0.224**	1.339 ± 0.262	1.417 ± 0.256	1.352 ± 0.245	1.377 ± 0.275
	Kurtosis	3.469 ± 1.641	3.311 ± 1.160	3.314 ± 1.575	3.439 ± 1.210	3.552 ± 1.528	3.041 ± 0.992	3.419 ± 1.243	3.349 ± 1.505
	Skewness	0.503 ± 0.671	0.471 ± 0.604	0.507 ± 0.602	0.466 ± 0.661	0.540 ± 0.657	0.377 ± 0.571	0.387 ± 0.673	0.562 ± 0.590
		LNM		Luminal		TN		HER2	
Parameters	Histogram metrics	Negative	Positive	Non-Luminal	Luminal	Non-TN	TN	Non-HER2-positive	HER2-positive
Mono-ADC	25th	0.805 ± 0.151	0.780 ± 0.137	**0.878 ± 0.142**	**0.742 ± 0.123**	**0.772 ± 0.139**	**0.878 ± 0.143**	**0.779 ± 0.142**	**0.877 ± 0.144**
	Median	0.885 ± 0.165	0.867 ± 0.150	**0.975 ± 0.159**	**0.815 ± 0.126**	**0.853 ± 0.150**	**0.967 ± 0.163**	**0.856 ± 0.152**	**0.984 ± 0.155**
	Mean	0.903 ± 0.167	0.877 ± 0.150	**0.991 ± 0.160**	**0.830 ± 0.128**	**0.869 ± 0.152**	**0.982 ± 0.165**	**0.871 ± 0.154**	**1.002 ± 0.155**
	75th	0.986 ± 0.192	0.966 ± 0.172	**1.087 ± 0.190**	**0.908 ± 0.143**	**0.953 ± 0.174**	**1.071 ± 0.196**	**0.952 ± 0.174**	**1.107 ± 0.184**
	Kurtosis	3.726 ± 1.954	4.084 ± 2.561	3.733 ± 1.897	3.660 ± 1.802	3.645 ± 1.780	3.842 ± 2.032	3.709 ± 1.860	3.593 ± 1.738
	Skewness	0.645 ± 0.635	0.380 ± 0.785	0.616 ± 0.667	0.513 ± 0.720	0.525 ± 0.704	0.657 ± 0.680	0.552 ± 0.709	0.564 ± 0.661
IVIM-*D*	25th	0.920 ± 0.249	0.907 ± 0.182	**0.996 ± 0.236**	**0.862 ± 0.206**	0.897 ± 0.210	0.981 ± 0.273	0.895 ± 0.231	1.016 ± 0.181
	Median	1.057 ± 0.225	1.046 ± 0.174	**1.138 ± 0.227**	**0.997 ± 0.175**	1.034 ± 0.195	1.120 ± 0.240	**1.030 ± 0.201**	**1.160 ± 0.212**
	Mean	1.073 ± 0.220	1.063 ± 0.177	**1.158 ± 0.224**	**1.011 ± 0.169**	1.049 ± 0.189	1.142 ± 0.242	**1.047 ± 0.199**	**1.178 ± 0.202**

(Continued)

TABLE 4 Continued

Parameters	Histogram metrics	ER		PR		HER2		Ki-67	
		Negative	Positive	Negative	Positive	Negative	Positive	Negative	Positive
	75th	1.201 ± 0.232	1.198 ± 0.199	**1.294 ± 0.239**	**1.137 ± 0.184**	1.178 ± 0.209	1.276 ± 0.248	**1.174 ± 0.211**	**1.319 ± 0.231**
	Kurtosis	3.437 ± 1.540	3.296 ± 1.259	3.368 ± 1.521	3.403 ± 1.405	3.323 ± 1.354	3.617 ± 1.737	3.461 ± 1.497	3.049 ± 1.145
	Skewness	0.429 ± 0.614	0.403 ± 0.625	0.470 ± 0.590	0.387 ± 0.633	0.394 ± 0.613	0.513 ± 0.628	0.421 ± 0.632	0.416 ± 0.547
IVIM-*D**	25th	3.278 ± 4.341	2.371 ± 3.831	3.033 ± 4.076	2.923 ± 4.275	2.779 ± 4.028	3.619 ± 4.689	3.112 ± 4.381	2.282 ± 3.055
	Median	8.010 ± 5.551	7.262 ± 5.238	8.117 ± 5.747	7.513 ± 5.246	7.642 ± 5.281	8.140 ± 6.029	7.683 ± 5.450	8.088 ± 5.488
	Mean	9.706 ± 4.516	9.116 ± 4.289	9.726 ± 4.687	9.356 ± 4.278	9.356 ± 4.298	10.015 ± 4.913	9.535 ± 4.447	9.357 ± 4.454
	75th	14.146 ± 5.909	13.578 ± 5.599	14.291 ± 6.284	13.736 ± 5.466	13.732 ± 5.710	14.712 ± 6.095	13.994 ± 5.634	13.752 ± 6.604
	Kurtosis	6.106 ± 5.296	5.600 ± 4.243	5.984 ± 5.763	5.899 ± 4.367	6.014 ± 4.668	5.648 ± 5.904	5.831 ± 4.806	6.412 ± 5.668
	Skewness	1.287 ± 0.998	1.267 ± 0.847	1.270 ± 1.049	1.287 ± 0.878	1.306 ± 0.933	1.191 ± 1.002	1.261 ± 0.910	1.371 ± 1.118
IVIM-*f*	25th	0.027 ± 0.023	0.023 ± 0.025	0.027 ± 0.025	0.025 ± 0.023	0.025 ± 0.023	0.029 ± 0.028	0.026 ± 0.024	0.024 ± 0.022
	Median	0.053 ± 0.030	0.049 ± 0.032	0.053 ± 0.030	0.051 ± 0.031	0.051 ± 0.030	0.055 ± 0.034	0.052 ± 0.032	0.050 ± 0.025
	Mean	0.059 ± 0.030	0.055 ± 0.029	0.059 ± 0.029	0.057 ± 0.030	0.056 ± 0.028	0.062 ± 0.035	0.058 ± 0.031	0.054 ± 0.019
	75th	0.083 ± 0.045	0.079 ± 0.042	0.084 ± 0.042	0.080 ± 0.045	0.080 ± 0.041	0.088 ± 0.052	0.082 ± .047	0.078 ± 0.024
	Kurtosis	3.719 ± 3.064	3.490 ± 1.825	3.597 ± 2.395	3.669 ± 2.896	3.570 ± 2.628	3.882 ± 2.965	3.727 ± 2.904	3.231 ± 1.335
	Skewness	0.618 ± 0.785	0.638 ± 0.632	0.591 ± 0.744	0.647 ± 0.731	0.607 ± 0.713	0.684 ± 0.814	0.657 ± 0.751	0.471 ± 0.641
DKI-Kapp	25th	0.846 ± 0.169	0.871 ± 0.119	**0.794 ± 0.124**	**0.895 ± 0.159**	**0.867 ± 0.164**	**0.813 ± 0.106**	**0.873 ± 0.151**	**0.769 ± 0.141**
	Median	0.936 ± 0.170	0.960 ± 0.133	**0.879 ± 0.125**	**0.988 ± 0.164**	**0.961 ± 0.164**	**0.887 ± 0.121**	**0.961 ± 0.159**	**0.867 ± 0.131**
	Mean	0.932 ± 0.156	0.957 ± 0.132	**0.873 ± 0.119**	**0.986 ± 0.149**	**0.957 ± 0.155**	**0.886 ± 0.105**	**0.959 ± 0.145**	**0.856 ± 0.136**
	75th	1.020 ± 0.167	1.047 ± 0.144	**0.956 ± 0.127**	**1.077 ± 0.161**	**1.049 ± 0.165**	**0.961 ± 0.117**	1.046 ± 0.158	0.950 ± 0.141
	Kurtosis	3.388 ± 1.489	4.084 ± 2.561	3.738 ± 2.298	3.553 ± 1.679	3.629 ± 1.951	3.619 ± 1.951	3.571 ± 1.749	3.891 ± 2.713
	Skewness	-0.068 ± 0.708	-0.020 ± 0.926	-0.151 ± 0.789	0.015 ± 0.782	-0.060 ± 0.801	-0.023 ± 0.744	0.001 ± 0.769	-0.315 ± 0.830
DKI-Dapp	25th	1.084 ± 0.235	1.062 ± 0.201	**1.185 ±0.197**	**1.005 ± 0.212**	**1.044 ± 0.217**	**1.192 ± 0.211**	**1.056 ± 0.227**	**1.176 ± 0.182**
	Median	1.214 ±0.243	1.201 ± 0.219	**1.335 ±0.218**	**1.126 ± 0.207**	**1.176 ± 0.225**	**1.326 ± 0.230**	**1.180 ± 0.230**	**1.345 ± 0.205**

(Continued)

TABLE 4 Continued

Parameters	Histogram metrics	ER		PR		HER2		Ki-67	
		Negative	Positive	Negative	Positive	Negative	Positive	Negative	Positive
	Mean	1.238 ± 0.242	1.214 ± 0.213	**1.352 ± 0.216**	**1.148 ± 0.206**	**1.196 ± 0.221**	**1.347 ± 0.234**	**1.202 ± 0.231**	**1.359 ± 0.195**
	75th	1.371 ± 0.270	1.354 ± 0.246	**1.503 ± 0.261**	**1.275 ±0.220**	**1.331 ± 0.249**	**1.483 ± 0.272**	**1.331 ± 0.252**	**1.527 ± 0.250**
	Kurtosis	3.458 ± 1.483	3.231 ± 1.189	3.414 ± 1.674	3.358 ± 1.174	3.290 ± 1.182	3.694 ± 1.937	3.449 ± 1.420	3.057 ± 1.026
	Skewness	0.563 ± 0.622	0.337 ± 0.631	0.500 ± 0.636	0.476 ± 0.633	0.444 ± 0.623	0.628 ± 0.654	0.517 ± 0.639	0.336 ± 0.585

The data for significance is shown in bold ($p < 0.0625$). ER, Estrogen receptor; PR, Progesterone receptor; HER2, Human epidermal growth factor receptor 2; LNM, Lymph nodes metastasis; TN, Triple-negative.

models generated the best AUC in the HER2-positive type *vs*. non-HER2-positive type (AUC = 0.738, $p< 0.001$) (Table 5).

Regarding the differentiation of positive and negative groups between ER, PR, HER2, and Ki-67, the AUC of the combination of Mono, IVIM, and DKI resulted in the best discriminatory power compared with either model alone. The comparisons of Luminal type versus non-Luminal type, TN type versus non-TN type, and HER2-positive type versus non-HER2-positive type revealed that AUC considerably improved when the combination of Mono, IVIM, and DKI was used compared with either model alone (Table 5).

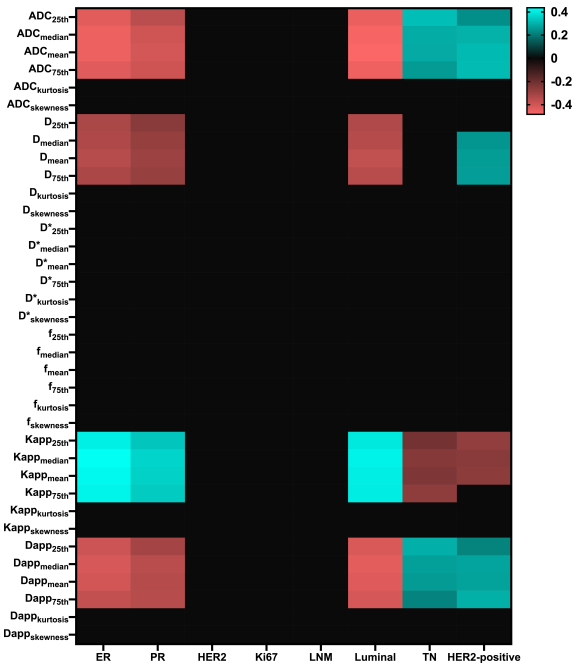

FIGURE 1
Matrix plot of the Pearson correlation coefficients between multi-model histogram parameters with molecular prognostic factors and subtypes. Colored entries indicate significant correlations ($p<0.0625$) with positive (blue) or negative (red). ER, Estrogen receptor; PR, Progesterone receptor; HER2, Human epidermal growth factor receptor 2; LNM, Lymph nodes metastasis; TN, Triple-negative.; D*, pseudo-diffusion coefficient.

Comparison of morphologic characteristics between the groups of molecular prognostic factors and subtypes

As summarized in Table 6, the results demonstrated that the margin of breast cancer had significant differences between the ER-positive and ER-negative groups ($p = 0.002$). No significant differences were observed in residual groups (all $p > 0.00625$). Two representative cases are shown in Figures 2; 3.

Discussion

In this study, we evaluated the correlation of Mono, IVIM, and DKI parameters with prognostic factors and molecular subtypes of breast cancer using histogram analysis. The Mono and DKI models yielded greater AUC to discriminate prognostic factors and molecular subtypes compared with the IVIM model. The AUC significantly improved when the combination of the three diffusion models was used compared with either model alone except for discriminating LNM-positive and negative. Additionally, the qualitative DWI analysis based on the morphologic characteristics could distinguish between ER-positive and -negative groups.

Previous studies have demonstrated the correlations of diffusion parameters derived from Mono, IVIM, and DKI models with breast cancer prognostic factors (18, 26, 28, 29). ER overexpression could inhibit angiogenesis to reduce perfusion contribution as well as increase cellularity to restrict water diffusion (11, 12, 29). Low perfusion contribution and high cellularity could both result in decreased histogram metrics of Mono-ADC, DKI-Dapp, and IVIM-*D* and increased histogram metrics of DKI-Kapp in the ER-positive group. The higher DKI-$Kapp_{mean}$ in ER-positive tumors was consistent with the result of Yang et al. (16). Due to similarities

10.3389/fonc.2023.1139189

TABLE 5 AUC of histogram metrics derived from mono, IVIM, and DKI models to predict molecular prognostic factors and subtypes.

	ADC	*D*	*D**	*f*	Kapp	Dapp	ADC	*D*	*D**	*f*	Kapp	Dapp
Metrics	ER-positive *vs*.ER-negative						PR-positive *vs*. PR-negative					
25th	0.752	0.687	0.513	0.523	0.737	**0.752**	0.705	0.648	0.511	0.508	0.692	0.679
Median	**0.766**	0.693	0.551	0.512	**0.753**	0.739	0.730	0.662	0.510	0.512	**0.707**	**0.704**
Mean	0.765	**0.702**	0.555	0.511	0.746	0.734	**0.735**	**0.671**	0.506	0.507	0.704	0.699
75th	0.750	0.689	**0.585**	**0.526**	0.742	0.717	0.728	0.665	0.534	0.531	0.698	0.701
Kurtosis	0.504	0.521	0.523	0.515	0.55	0.531	0.457	0.541	**0.559**	**0.533**	0.575	0.596
Skewness	0.518	0.537	0.535	0.514	0.538	0.507	0.516	0.549	0.556	0.527	0.558	0.514
Single model	0.766	0.706			0.755		0.735	0.671			0.719	
Three models	0.784						0.747					
Metrics	HER2-positive *vs*. HER2-negative						Ki-67-positive *vs*. Ki-67-negative					
25th	0.537	0.518	0.529	0.523	0.607	0.517	0.515	0.504	**0.539**	0.502	0.526	0.506
Median	0.565	0.541	0.500	0.540	0.581	0.557	0.518	0.508	0.524	0.557	**0.544**	0.505
Mean	0.584	0.552	0.503	0.559	0.581	0.566	0.524	0.516	0.522	**0.563**	0.535	0.509
75th	0.593	0.578	0.509	**0.575**	0.547	**0.602**	0.525	0.519	0.502	0.558	0.542	0.519
Kurtosis	**0.602**	**0.617**	0.527	0.504	**0.632**	0.593	0.514	0.503	0.501	0.539	0.527	0.538
Skewness	0.554	0.579	**0.545**	0.537	0.572	0.588	**0.569**	**0.572**	0.508	0.508	0.508	**0.560**
Single model	0.602	0.620			0.622		0.569	0.588			0.611	
Three models	0.659						0.630					
Metrics	LNM-positive *vs*. LNM-negative						Luminal *vs*. Non-Luminal					
25th	0.550	**0.540**	**0.563**	**0.577**	0.546	0.543	0.766	0.697	0.501	0.521	0.733	0.746
Median	0.534	0.514	0.541	0.568	0.544	0.521	0.781	0704	0.5234	0.526	**0.741**	**0.758**
Mean	0.546	0.507	0.543	0.548	0.554	0.535	**0.785**	**0.718**	0.528	0.527	0.738	0.752
75th	0.529	0.510	0.536	0.540	0.557	0.521	0.772	0.706	0.5151	**0.545**	0.737	0.741
Kurtosis	0.505	0.513	0.525	0.502	**0.559**	0.517	0.519	0.545	**0.556**	0.523	0.553	0.565
Skewness	**0.592**	0.501	0.514	0.514	0.525	**0.603**	0.503	0.529	0.561	0.529	0.562	0.532
Single model	0.592	0.580			0.617		0.785	0.722			0.773	
Three models	0.616						0.796					
Metrics	TN *vs*. Non-TN						HER2-positive *vs*. Non-HER2-positive					
25th	**0.719**	0.630	0.531	**0.541**	0.647	**0.704**	0.679	0.672	0.535	0.514	0.696	0.663
Median	0.701	0.625	0.525	0.513	0.673	0.684	0.726	0.689	**0.527**	0.526	0.696	0.707
Mean	0.697	**0.636**	0.532	0.529	0.662	0.678	0.737	0.698	0.508	0.511	**0.701**	0.705
75th	0.677	0.620	0.549	0.526	**0.685**	0.648	**0.738**	**0.699**	0.526	0.543	0.672	**0.723**
Kurtosis	0.508	0.531	0.573	0.514	0.513	0.503	0.541	0.512	0.505	0.522	0.572	0.612
Skewness	0.531	0.569	**0.577**	0.526	0.519	0.555	0.532	0.624	0.509	**0.579**	0.625	0.620
Single model	0.719	0.655			0.714		0.738	0.714			0.738	
Three models	0.736						0.747					

The best AUC of every diffusion parameter is shown in bold. ER, Estrogen receptor; PR, Progesterone receptor; HER2, Human epidermal growth factor receptor 2; LNM, Lymph nodes metastasis; TN, Triple-negative; D*, pseudo-diffusion coefficient.

10.3389/fonc.2023.1139189

TABLE 6 Magnetic resonance imaging morphological characteristics of molecular prognostic factors and subtypes.

		Max diameter		Shape				Margin				Internal signal			
groups			p-value	Round	Oval	Irregular	p-value	smooth	spiculated	irregular	p-value	homogeneous	heterogeneous	rim	p-value
ER	Positive	2.40 ± 0.96	0.269	11	37	32	0.092	52	13	15	0.002*	39	27	14	0.040
	Negative	2.59 ± 1.00		13	18	32		31	4	28		19	34	10	
PR	Positive	2.39 ± 0.90	0.209	11	34	31	0.253	49	9	18	0.187	21	34	12	0.097
	Negative	2.59 ± 1.01		13	21	33		34	8	25		9	11	14	
HER2	Positive	2.44 ± 0.90	0.788	10	16	22	0.544	27	6	15	0.953	20	19	9	0.840
	Negative	2.51 ± 0.99		14	39	42		56	11	28		38	42	15	
Ki-67	Positive	2.52 ± 0.94	0.409	17	30	32	0.214	51	7	21	0.186	30	34	15	0.668
	Negative	2.43 ± 0.97		7	25	32		32	10	22		28	27	9	
LNM	Positive	2.48 ± 0.95	0.992	6	18	25	0.443	26	6	17	0.652	20	21	8	0.994
	Negative	2.48 ± 0.96		12	39	35		57	11	26		38	40	16	
Luminal *vs.*		2.40 ± 0.93	0.230	12	16	29	0.106	55	13	18	0.010	42	30	14	0.034
Non-Luminal type		2.60 ± 0.10		5	16	10		28	4	25		16	31	10	
TN *vs.*		2.62 ± 0.99	0.301	6	10	16	0.636	16	3	13	0.332	8	19	5	0.074
Non-TN type		2.45 ± 0.95		18	45	48		67	14	30		50	42	19	
HER2-positive *vs.*		2.58 ± 1.03	0.680	6	6	13	0.230	12	1	12	0.069	8	12	5	0.626
Non-HER2-poitive type		2.46 ± 0.84		18	49	51		71	16	31		50	49	19	

*indicates that the correlation is significant at the level of 0.00625 (double-tailed). ER, Estrogen receptor; PR, Progesterone receptor; HER2, Human epidermal growth factor receptor 2; LNM, Lymph nodes metastasis; TN, Triple-negative.

in hormone receptor effects, PR-positive tumors also have same trend as ER-positive tumors. In our study, the histogram metrics of various diffusion parameters failed to reveal a remarkable difference between the statuses of HER2, Ki-67, and LNM. We speculated that this difference might be related to the inclusion of lesions, the selection of the *b* values, and the delineation of the ROI.

In terms of molecular subtypes, we analyzed them statistically in the form of binary classification. Previous studies demonstrated that IVIM-D_{75th} was lower in the Luminal type than in the HER2-positive type, and higher IVIM-*D* and lower IVIM-*D** in Luminal A type than in the other subtypes (25, 30). These results were not entirely consistent with our study. Due to the Luminal type being defined as ER and/or PR positive, histogram metrics of Mono-ADC, IVIM-*D*, DKI-Dapp, and DKI-Kapp can be used to distinguish Luminal type from non-Luminal type, as similar to distinguishing ER and PR status. You et al. revealed that DKI-Kapp $_{entropy}$ value could identify the HER2-positive type and non-HER2-positive type (20). Our study also showed DKI-Kapp histogram metrics, particularly mean, median, and 25th percentile, could differentiate HER2-positive type and non-HER2-positive type. Suo et al. have demonstrated higher Mono-ADC values in the TN subtype than in other subtypes (12); this tendency was also observed in our study with higher Mono-ADC, IVIM-D, and DKI-Dapp histogram metrics in the TN type than those in the non-TN type. The reason may be that the TN type shows a decrease in tumor cellularity with an associated increase in diffusion (31, 32). In summary, various diffusion parameters can quantify tissue cell density, perfusion contribution, and water motion *in vivo* and may serve as a potential biomarker for differentiating molecular subtypes.

Besides comparing individual parameters, the ROC of various models was also compared. The present study revealed that the AUC of the Mono or DKI model was higher than that of the IVIM model. That is, the Mono or DKI model was superior to the IVIM model in evaluating the correlations of prognostic factors and

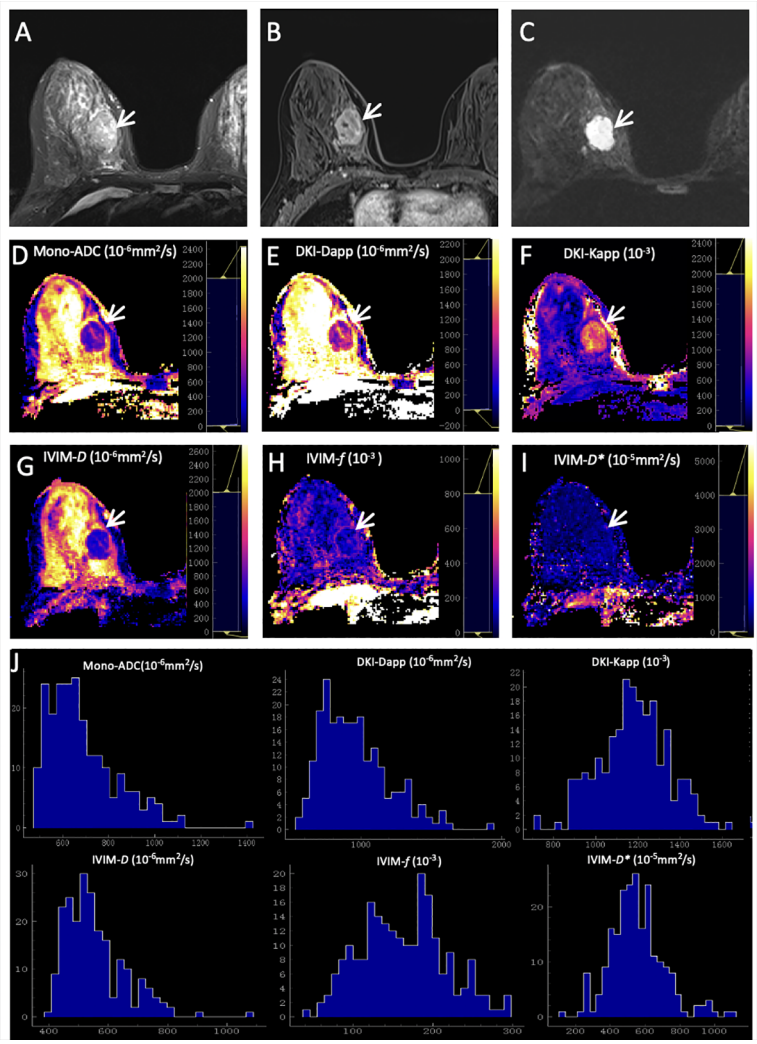

FIGURE 2
Representative images of a grade 2 invasive ductal carcinoma in the right breast of a 42-year-old woman. This tumor was with positive expression of estrogen receptor (95%) and progesterone receptor (20%), high Ki-67 (40%), and negative HER2 expression. **(A)** T2WI. **(B)** This mass is oval and with obvious enhancement (arrow) on axial DCE-MRI. **(C)** This mass shows oval shape, smooth margin, and homogeneous signal on DWI (b-value = 1000 mm^2/s) (arrow). ADC **(D)**, Dapp **(E)**, Kapp **(F)**, *D* **(G)**, *f* **(H)**, and *D** **(I)** maps and histograms of each map **(J)** are as shown.

molecular subtypes of breast cancers. Yang et al. demonstrated that the DKI model was not superior to the Mono model in reflecting the prognostic information of breast cancer (16). Cho et al. demonstrated that the AUC of the IVIM model was higher than that of the Mono model, whereas Feng reported that the AUC of the IVIM model was lower than that of the Mono model (15, 17). The contradictory results might have resulted from the distinct choices of multi-*b* values and poor repeatability of multi-models. Therefore, the diagnostic value of the three models with various ranges of multi-*b* values needs further exploration.

Kul et al. reported that the morphology evaluated on DWI provided 83%-84% accuracy in distinguishing between benign and malignant lesions (33). However, Kang et al. reported that the specificity of the high-signal rim in DWI was higher than that of the ADC_{mean} value (80.6% *vs.* 63.9%) (34). Related studies include one by Cho, who showed that ER-positive tumor tends to show a not-circumscribed margin in mammography compared to ER-negative tumors (35). Different from our present study, the characteristic of smooth margin was more frequently observed in ER-positive tumors. Another study by Yuan et al, reported that the rate of burr sign in ER-positive in DCE-MRI was higher than that in negative groups (36). The trend was also observed in our study but was not significant. Although this study was a preliminary work, the morphologic characteristics assessed using SMS rs-EPI might provide a noninvasive tool for assessing the biologic characteristics and heterogeneity of breast cancers.

The present study had several limitations. First, the patient population was relatively small, and hence a selection bias might exist. Second, 2D ROI was manually drawn on the slice with the largest tumor diameter. This method did not reflect the overall tumor heterogeneity. Third, all MRI data were obtained in a single

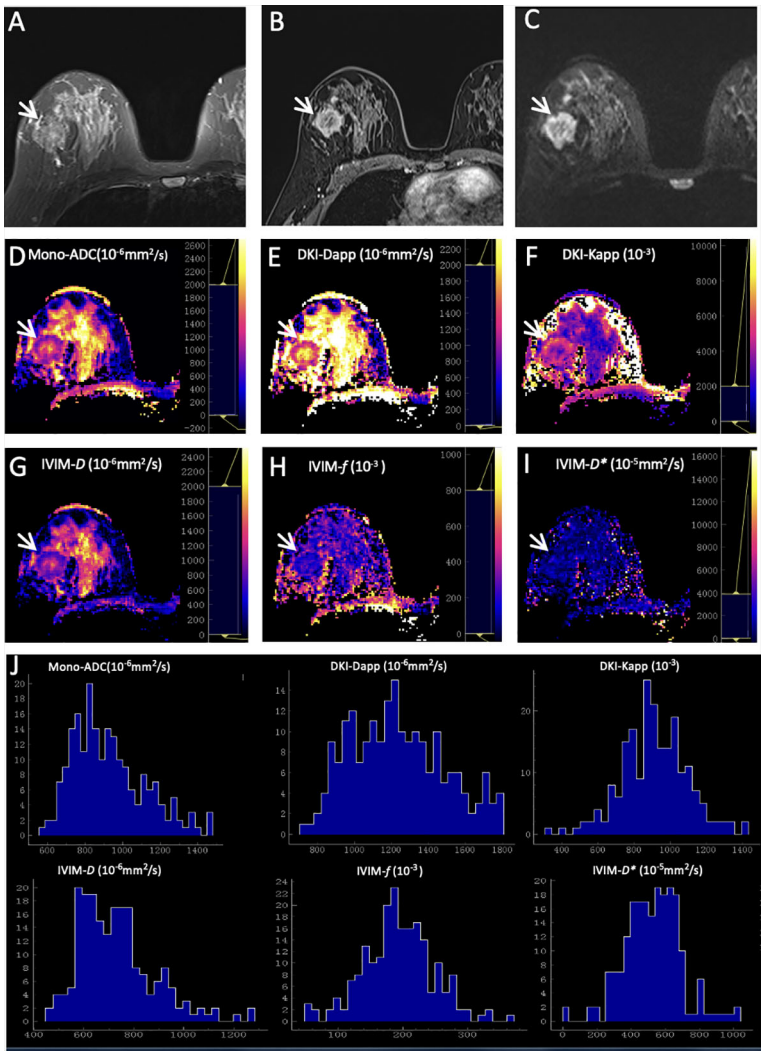

FIGURE 3
Representative images of a grade 3 invasive ductal carcinoma in the right breast of a 48-year-old woman. This tumor was with negative expression of estrogen receptor (0) and progesterone receptor (0), high Ki-67 (50%), and positive HER2 expression. **(A)** T2WI. **(B)** This mass is irregular and with obvious enhancement (arrow) on axial DCE-MRI. **(C)** This mass shows irregular shape, irregular margin, and heterogeneous signal on DWI (b-value = 1000 mm^2/s) (arrow). ADC **(D)**, Dapp **(E)**, Kapp **(F)**, *D* **(G)**, *f* **(H)**, and *D** **(I)** maps and histograms of each map **(J)** are as shown.

institution. Further studies are needed to verify the generalizability and reproducibility of our results.

In conclusion, the histogram metrics of multiparametric DWI and morphologic characteristics might be of use in providing prognostic information regarding breast cancer, thus potentially contributing to individualized treatment plans for patients with breast cancer.

Data availability statement

The datasets presented in this article are not readily available because the datasets generated or analyzed during the study are available from the corresponding author on reasonable request. Requests to access the datasets should be directed to YQ, yanjinqin125@163.com.

Author contributions

Conceptualization: YQ, FW, and TA. Data curation: YQ, CT, QH, LH. Formal analysis: YQ, QH, FW, and LH. Investigation: YQ, JY, and QH. Methodology: YQ, FW, CT, and MH. Project administration: TA. Software: TY and HZ. Supervision: TA. Visualization: YQ, FW, and MH. Writing - original draft: YQ and FW. Writing - review and editing: TA and TY. All authors contributed to the article and approved the submitted version.

Funding

This research was supported by the Keypoint Research and Development Program of Hubei Province (Grant Number: 2022BCE019).

Conflict of interest

Authors HZ and TY were employed by the company Siemens Healthineers Ltd.

The remaining authors declare that the research was conducted in the absence of any commercial or financial relationships that could be construed as a potential conflict of interest.

Publisher's note

References

1. Luo HB, Du MY, Liu YY, Wang M, Qing HM, Wen ZP, et al. Differentiation between luminal a and b molecular subtypes of breast cancer using pharmacokinetic quantitative parameters with histogram and texture features on preoperative dynamic contrast-enhanced magnetic resonance imaging. *Acad Radiol* (2020) 27(3):e35–44. doi: 10.1016/j.acra.2019.05.002

2. Weiss J, Martirosian P, Taron J, Othman AE, Kuestner T, Erb M, et al. Feasibility of accelerated simultaneous multislice diffusion-weighted MRI of the prostate. *J Magn Reson Imaging* (2017) 46(5):1507–15. doi: 10.1002/jmri.25665

3. Hu Y, Zhan C, Yang Z, Zhang X, Zhang H, Liu W, et al. Accelerating acquisition of readout-segmented echo planar imaging with a simultaneous multi-slice (SMS) technique for diagnosing breast lesions. *Eur Radiol* (2021) 31(5):2667–76. doi: 10.1007/s00330-020-07393-5

4. Tang C, Qin Y, Hu Q, Ai T. Diagnostic value of multi-model high-resolution diffusion-weighted MR imaging in breast lesions: based on simultaneous multi-slice readout-segmented echo-planar imaging. *Eur J Radiol* (2022) 154:110439. doi: 10.1016/j.ejrad.2022.110439

5. Filli L, Ghafoor S, Kenkel D, Liu W, Weiland E, Andreisek G, et al. Simultaneous multi-slice readout-segmented echo planar imaging for accelerated diffusion-weighted imaging of the breast. *Eur J Radiol* (2016) 85(1):274–8. doi: 10.1016/j.ejrad.2015.10.009

6. Jiang JS, Zhu LN, Wu Q, Sun Y, Liu W, Xu XQ, et al. Feasibility study of using simultaneous multi-slice RESOLVE diffusion weighted imaging to assess parotid gland tumors: comparison with conventional RESOLVE diffusion weighted imaging. *BMC Med Imaging* (2020) 20(1):93. doi: 10.1186/s12880-020-00492-1

7. McKay JA, Church AL, Rubin N, Emory TH, Hoven NF, Kuehn-Hajder JE, et al. A comparison of methods for high-Spatial-Resolution diffusion-weighted imaging in breast MRI. *Radiology* (2020) 297(2):304–12. doi: 10.1148/radiol.2020200221

8. Phi Van VD, Becker AS, Ciritsis A, Reiner CS, Boss A. Intravoxel incoherent motion analysis of abdominal organs: application of simultaneous multislice acquisition. *Invest Radiol* (2018) 53(3):179–85. doi: 10.1097/RLI.0000000000000426

9. Barth M, Breuer F, Koopmans PJ, Norris DG, Poser BA. Simultaneous multislice (SMS) imaging techniques. *Magn Reson Med* (2016) 75(1):63–81. doi: 10.1002/mrm.25897

10. Tavakoli A, Attenberger UI, Budjan J, Stemmer A, Nickel D, Kannengiesser S, et al. Improved liver diffusion-weighted imaging at 3 T using respiratory triggering in combination with simultaneous multislice acceleration. *Invest Radiol* (2019) 54 (12):744–51. doi: 10.1097/RLI.0000000000000594

11. Maric J, Boban J, Ivkovic-Kapicl T, Djilas D, Vucaj-Cirilovic V, Bogdanovic-Stojanovic D. Differentiation of breast lesions and distinguishing their histological subtypes using diffusion-weighted imaging and ADC values. *Front Oncol* (2020) 10:332. doi: 10.3389/fonc.2020.00332

12. Suo S, Zhang D, Cheng F, Cao M, Hua J, Lu J, et al. Added value of mean and entropy of apparent diffusion coefficient values for evaluating histologic phenotypes of invasive ductal breast cancer with MR imaging. *Eur Radiol* (2019) 29(3):1425–34. doi: 10.1007/s00330-018-5667-9

13. Huang Y, Lin Y, Hu W, Ma C, Lin W, Wang Z, et al. Diffusion kurtosis at 3.0T as an in vivo imaging marker for breast cancer characterization: correlation with prognostic factors. *J Magn Reson Imaging* (2019) 49(3):845–56. doi: 1002/jmri.26249

14. He M, Song Y, Li H, Lu J, Li Y, Duan S, et al. Histogram analysis comparison of monoexponential, advanced diffusion-weighted imaging, and dynamic contrast-enhanced MRI for differentiating borderline from malignant epithelial ovarian tumors. *J Magn Reson Imaging* (2020) 52(1):257–68. doi: 10.1002/jmri.27037

15. Cho GY, Moy L, Kim SG, Baete SH, Moccaldi M, Babb JS, et al. Evaluation of breast cancer using intravoxel incoherent motion (IVIM) histogram analysis: comparison with malignant status, histological subtype, and molecular prognostic factors. *Eur Radiol* (2016) 26(8):2547–58. doi: 10.1007/s00330-015-4087-3

16. Yang ZL, Li Y, Zhan CA, Hu YQ, Guo YH, Xia LM, et al. Evaluation of suspicious breast lesions with diffusion kurtosis MR imaging and connection with prognostic factors. *Eur J Radiol* (2021) 145:110014. doi: 10.1016/j.ejrad.2021.110014

17. Feng W, Gao Y, Lu XR, Xu YS, Guo ZZ, Lei JQ. Correlation between molecular prognostic factors and magnetic resonance imaging intravoxel incoherent motion histogram parameters in breast cancer. *Magn Reson Imaging* (2022) 85:262–70. doi: 10.1016/j.mri.2021.10.027

18. Kim EJ, Kim SH, Park GE, Kang BJ, Song BJ, Kim YJ, et al. Histogram analysis of apparent diffusion coefficient at 3.0t: correlation with prognostic factors and subtypes of invasive ductal carcinoma. *J Magn Reson Imaging* (2015) 42(6):1666–78. doi: 10.1002/jmri.24934

19. Choi Y, Kim SH, Youn IK, Kang BJ, Park WC, Lee A, et al. Rim sign and histogram analysis of apparent diffusion coefficient values on diffusion-weighted MRI in triple-negative breast cancer: comparison with ER-positive subtype. *PloS One* (2017) 12(5):e0177903. doi: 10.1371/journal.pone.0177903

20. You C, Li J, Zhi W, Chen Y, Yang W, Gu Y, et al. The volumetric-tumour histogram-based analysis of intravoxel incoherent motion and non-Gaussian diffusion MRI: association with prognostic factors in HER2-positive breast cancer. *J Transl Med* (2019) 17(1):182. doi: 10.1186/s12967-019-1911-6

21. Kang HS, Kim JY, Kim JJ, Kim S, Lee NK, Lee JW, et al. Diffusion kurtosis MR imaging of invasive breast cancer: correlations with prognostic factors and molecular subtypes. *J Magn Reson Imaging* (2022) 56(1):110–20. doi: 10.1002/jmri.27999

22. Le Bihan D. What can we see with IVIM MRI? *Neuroimage* (2019) 187:56–67. doi: 10.1016/j.neuroimage.2017.12.062

23. Kishimoto AO, Kataoka M, Iima M, Honda M, Miyake KK, Ohashi A, et al. The comparison of high-resolution diffusion weighted imaging (DWI) with high-resolution contrast-enhanced MRI in the evaluation of breast cancers. *Magn Reson Imaging* (2020) 71:161–9. doi: 10.1016/j.mri.2020.03.007

24. Barentsz MW, Taviani V, Chang JM, Ikeda DM, Miyake KK, Banerjee S, et al. Assessment of tumor morphology on diffusion-weighted (DWI) breast MRI: diagnostic value of reduced field of view DWI. *J Magn Reson Imaging* (2015) 42(6):1656–65. doi: 10.1002/jmri.24929

25. Lee YJ, Kim SH, Kang BJ, Kang YJ, Yoo H, Yoo J, et al. Intravoxel incoherent motion (IVIM)-derived parameters in diffusion-weighted MRI: associations with prognostic factors in invasive ductal carcinoma. *J Magn Reson Imaging* (2017) 45 (5):1394–406. doi: 10.1002/jmri.25514

26. Suo S, Cheng F, Cao M, Kang J, Wang M, Hua J, et al. Multiparametric diffusion-weighted imaging in breast lesions: association with pathologic diagnosis and prognostic factors. *J Magn Reson Imaging* (2017) 46(3):740–50. doi: 10.1002/jmri.25612

27. Boria F, Tagliati C, Baldassarre S, Ercolani P, Marconi E, Simonetti BF, et al. Morphological MR features and quantitative ADC evaluation in invasive breast cancer: correlation with prognostic factors. *Clin Imaging* (2018) 50:141–6. doi: 10.1016/j.clinimag.2018.02.011

28. Horvat JV, Iyer A, Morris EA, Apte A, Bernard-Davila B, Martinez DF, et al. Histogram analysis and visual heterogeneity of diffusion-weighted imaging with apparent diffusion coefficient mapping in the prediction of molecular subtypes of invasive breast cancers. *Contrast Media Mol Imaging* (2019) 2019:2972189. doi: 10.1155/2019/2972189

29. Horvat JV, Bernard-Davila B, Helbich TH, Zhang M, Morris EA, Thakur SB, et al. Diffusion-weighted imaging (DWI) with apparent diffusion coefficient (ADC) mapping as a quantitative imaging biomarker for prediction of immunohistochemical receptor status, proliferation rate, and molecular subtypes of breast cancer. *J Magn Reson Imaging* (2019) 50(3):836–46. doi: 10.1002/jmri.26697

30. Kawashima H, Miyati T, Ohno N, Ohno M, Inokuchi M, Ikeda H, et al. Differentiation between luminal-a and luminal-b breast cancer using intravoxel incoherent motion and dynamic contrast-enhanced magnetic resonance imaging. *Acad Radiol* (2017) 24(12):1575–81. doi: 10.1016/j.acra.2017.06.016

31. Li Q, Xiao Q, Yang M, Chai Q, Huang Y, Wu PY, et al. Histogram analysis of quantitative parameters from synthetic MRI: correlations with prognostic factors and molecular subtypes in invasive ductal breast cancer. *Eur J Radiol* (2021) 139:109697. doi: 10.1016/j.ejrad.2021.109697

32. Youk JH, Son EJ, Chung J, Kim JA, Kim EK. Triple-negative invasive breast cancer on dynamic contrast-enhanced and diffusion-weighted MR imaging: comparison with other breast cancer subtypes. *Eur Radiol* (2012) 22(8):1724–34. doi: 10.1007/s00330-012-2425-2

33. Kul S, Metin Y, Kul M, Metin N, Eyuboglu I, Ozdemir O, et al. Assessment of breast mass morphology with diffusion-weighted MRI: beyond apparent diffusion coefficient. *J Magn Reson Imaging* (2018) 48(6):1668–77. doi: 10.1002/jmri.26175

34. Kang BJ, Lipson JA, Planey KR, Zackrisson S, Ikeda DM, Kao J, et al. Rim sign in breast lesions on diffusion-weighted magnetic resonance imaging: diagnostic accuracy and clinical usefulness. *J Magn Reson Imaging* (2015) 41(3):616–23. doi: 10.1002/jmri.24617

35. Cho N. Imaging features of breast cancer molecular subtypes: state of the art. *J Pathol Transl Med* (2021) 55(1):16–25. doi: 10.4132/jptm.2020.09.03

36. Yuan C, Jin F, Guo X, Zhao S, Li W, Guo H, et al. Correlation analysis of breast cancer DWI combined with DCE-MRI imaging features with molecular subtypes and prognostic factors. *J Med Syst* (2019) 43(4):83. doi: 10.1007/s10916-019-1197-5

frontiers | Frontiers in Neuroscience

TYPE Original Research
PUBLISHED 10 May 2023
DOI 10.3389/fnins.2023.1106350

OPEN ACCESS

EDITED BY
Lars Mueller,
University of Leeds, United Kingdom

REVIEWED BY
Julio Ernesto Villalon-Reina,
University of Southern California, United States
Nguyen Minh Duc,
Pham Ngoc Thach University of Medicine, Vietnam

*CORRESPONDENCE
Santiago Aja-Fernández
✉ sanaja@tel.uva.es

RECEIVED 23 November 2022
ACCEPTED 30 March 2023
PUBLISHED 10 May 2023

CITATION
Martín-Martín C, Planchuelo-Gómez Á, Guerrero ÁL, García-Azorín D, Tristán-Vega A, de Luis-García R and Aja-Fernández S (2023) Viability of AMURA biomarkers from single-shell diffusion MRI in clinical studies.
Front. Neurosci. 17:1106350.
doi: 10.3389/fnins.2023.1106350

Viability of AMURA biomarkers from single-shell diffusion MRI in clinical studies

Carmen Martín-Martín[1], Álvaro Planchuelo-Gómez[1,2], Ángel L. Guerrero[3,4], David García-Azorín[3], Antonio Tristán-Vega[1], Rodrigo de Luis-García[1] and Santiago Aja-Fernández[1]*

[1]Laboratorio de Procesado de Imagen (LPI), Universidad de Valladolid, Valladolid, Spain, [2]Cardiff University Brain Research Imaging Centre (CUBRIC), School of Psychology, Cardiff University, Cardiff, United Kingdom, [3]Headache Unit, Department of Neurology, Hospital Clínico Universitario de Valladolid, Valladolid, Spain, [4]Department of Medicine, Universidad de Valladolid, Valladolid, Spain

Diffusion Tensor Imaging (DTI) is the most employed method to assess white matter properties using quantitative parameters derived from diffusion MRI, but it presents known limitations that restrict the evaluation of complex structures. The objective of this study was to validate the reliability and robustness of complementary diffusion measures extracted with a novel approach, Apparent Measures Using Reduced Acquisitions (AMURA), with a typical diffusion MRI acquisition from a clinical context in comparison with DTI with application to clinical studies. Fifty healthy controls, 51 episodic migraine and 56 chronic migraine patients underwent single-shell diffusion MRI. Four DTI-based and eight AMURA-based parameters were compared between groups with tract-based spatial statistics to establish reference results. On the other hand, following a region-based analysis, the measures were assessed for multiple subsamples with diverse reduced sample sizes and their stability was evaluated with the coefficient of quartile variation. To assess the discrimination power of the diffusion measures, we repeated the statistical comparisons with a region-based analysis employing reduced sample sizes with diverse subsets, decreasing 10 subjects per group for consecutive reductions, and using 5,001 different random subsamples. For each sample size, the stability of the diffusion descriptors was evaluated with the coefficient of quartile variation. AMURA measures showed a greater number of statistically significant differences in the reference comparisons between episodic migraine patients and controls compared to DTI. In contrast, a higher number of differences was found with DTI parameters compared to AMURA in the comparisons between both migraine groups. Regarding the assessments reducing the sample size, the AMURA parameters showed a more stable behavior than DTI, showing a lower decrease for each reduced sample size or a higher number of regions with significant differences. However, most AMURA parameters showed lower stability in relation to higher coefficient of quartile variation values than the DTI descriptors, although two AMURA measures showed similar values to DTI. For the synthetic signals, there were AMURA measures with similar quantification to DTI, while other showed similar behavior. These findings suggest that AMURA presents favorable characteristics to identify differences of specific microstructural properties between clinical groups in regions with complex fiber architecture and lower dependency on the sample size or assessing technique than DTI.

KEYWORDS

alternative metrics, AMURA, brain, diffusion magnetic resonance imaging, DTI, migraine

1. Introduction

Diffusion Magnetic Resonance Imaging (dMRI) is an imaging modality employed to assess diverse *in vivo* physiological and pathological conditions of the human body in clinical studies. It has been widely used in the study of the brain and neurological disorders (Rovaris et al., 2005; Goveas et al., 2015; Galbán et al., 2017; Mekkaoui et al., 2017). It allows the characterization of the diffusivity of water molecules within the tissue, providing information about the microscopic configuration and structural connectivity of the brain, especially inside the white matter (WM).

The most relevant feature of dMRI is its ability to measure directional variance, i.e., anisotropy, which, inside the brain, is related to structural connectivity between areas. The most common methodology to estimate the anisotropy is via the diffusion tensor (DT) (Basser et al., 1994; Westin et al., 2002).

In order to use it in clinical studies, the information provided by the DT must be translated into some scalar measures that describe different features of diffusion within every voxel. That way, metrics like fractional anisotropy (FA) were defined and widely employed to characterize damaged tissues in multiple neurological and psychiatric disorders (Kochunov et al., 2012; Bette et al., 2016; Mole et al., 2016; Herbert et al., 2018). However, from the early stages of DT imaging (DTI), it was clear that the Gaussian assumption oversimplifies the diffusion process.

In the past few decades, many techniques have been proposed to overcome the limitations of DTI, usually requiring the acquisition of larger amounts of diffusion data (Assemlal et al., 2011; Novikov et al., 2019). Most of these techniques rely on the estimation of more advanced diffusion descriptors, such as the Ensemble Average diffusion Propagator (EAP), which is the probability density function of the motion of the water molecules within a voxel (Wedeen et al., 2005; Özarslan et al., 2013; Tristán-Vega and Aja-Fernández, 2021).

A complete analysis of the EAP requires many diffusion-weighted images (DWI) with several (moderate to high) b-values in a multi-shell acquisition. The information provided by the EAP is usually adapted to scalar measures that describe different aspects of diffusion. The most frequently employed measures are the return-to-origin probabilities (RTOP), return-to-plane probabilities (RTPP), return-to-axis probabilities (RTAP) and the propagator anisotropy (PA) (Wu et al., 2008; Descoteaux et al., 2011; Hosseinbor et al., 2013; Özarslan et al., 2013; Ning et al., 2015).

The accurate estimation of these measures requires the calculation of the EAP, which commonly involves: (1) long acquisition times; (2) several shells with large b-values, which may be difficult to acquire in many commercial MRI scanners; and (3) heavy computational burdens with very long processing times. These three issues have hindered the general adoption of EAP-related metrics in the clinical routine, despite the growing interest in the exploration of their potential applicability (Avram et al., 2016; Brusini et al., 2016; Zucchelli et al., 2016; Boscolo Galazzo et al., 2018).

To overcome these limitations and facilitate the widespread use of advanced diffusion metrics in clinical studies, a new approach called Apparent Measures Using Reduced Acquisitions (AMURA) has been recently proposed (Aja-Fernández et al., 2020, 2021, 2022). The method allows the estimation of diffusion measures such as RTOP, RTAP, and PA, while reducing the number of necessary samples and the computational cost. AMURA can mimic the sensitivity of EAP-based measures to microstructural changes when only a small number of shells (even one) is available. To do so, AMURA assumes a prior model for the behavior of the radial q-space instead of trying to numerically describe it, yielding simplified expressions that can be computed easily even from single-shell acquisitions.

One additional advantage of AMURA is that it can be easily integrated into the processing pipeline of current existing single-shell dMRI protocols and databases to unveil anatomical details that may remain hidden in traditional DT-based studies. AMURA has proved its potential in some exploratory studies with clinical data focusing on Parkinson's disease and Mild Cognitive Impairment (Aja-Fernández et al., 2020, 2021), as well a recent clinical study on migraine (Planchuelo-Gómez et al., 2020c).

In this work, we aim to assess the viability of different diffusion descriptors extracted with AMURA for the study of a neurological disorder in DTI-type datasets. Note that, initially, AMURA was designed to work with b-values over 2,000 s/mm^2, since the effects measured with RTOP, RTPP, and RTAP were better showed at higher values of b. However, results in clinical data have shown its potential at lower b-values (Aja-Fernández et al., 2022). Thus, we will explore the viability of these technique to model DTI-type acquisitions, i.e., dMRI datasets acquired with those protocols usually employed for the estimation of DTI and its derived parameters, such as fractional anisotropy (FA) or mean diffusivity (MD). These acquisitions are commonly single-shell, and only include one non-zero b-value, usually in the order of $b = 1,000$ s/mm^2.

We have selected migraine as a case study. Migraine is an attractive pathology for the evaluation of the quality of alternative diffusion metrics, since the differences between patients and controls that have been found using dMRI in the literature are scarce and subtle (Planchuelo-Gómez et al., 2020b). In migraine, differences are usually hard to find in comparison with other disorders such as schizophrenia or Alzheimer's disease, and they require a large number of subjects per group and good quality data. Thus, migraine will allow us to check the capability of different techniques to detect subtle changes.

Migraine is a disabling primary disorder characterized by recurrent episodes of headache, which usually last 4-72 hours and present at least two of the following four characteristics: moderate to severe pain intensity, unilateral location, pulsating quality, and aggravation with physical activity (Third edition of the International Classification of Headache Disorders, ICHD-3). A common distinction when studying migraine is made between episodic migraine (EM), in which patients suffer from headache less than 15 days per month, and chronic migraine (CM), in which patients suffer from headache at least 15 days per month.

A recent study identified statistically significant differences in migraine using advanced diffusion measures calculated with AMURA (Planchuelo-Gómez et al., 2020c). This study identified higher RTOP values in CM patients compared to EM, and lower RTPP values in EM compared to HC.

Given the fact that AMURA-derived measures have shown promising results for the characterization of subtle WM changes

in migraine, the main objective of this study was the assessment of the reliability and the robustness of AMURA metrics acquired with a typical acquisition employed in a clinical context. Our purpose is to validate the viability of these metrics for clinical studies even when acquisition protocols are suboptimal for this methodology. Specifically, we will use migraine as a case study and DTI-type acquisitions, where only one shell is acquired at $b = 1,000$ s/mm^2.

2. Materials and methods

2.1. Advanced diffusion measures from single shell acquisitions: AMURA

AMURA was proposed in Aja-Fernández et al. (2020) as a methodology to calculate advanced diffusion metrics from reduced acquisitions compatible with commercial scanners and general clinical routine. It allows the estimation of different diffusion-related scalars using a lower number of samples with a single-shell acquisition scheme. AMURA considers that, if the amount of data is reduced, a restricted diffusion model consistent with single-shell acquisitions must be assumed: the (multi-modal) apparent diffusivity does not depend on the *b*-value, so that a mono-exponential behavior is observed for every spatial direction. According to Basser and Jones (2002), in the mammalian brain, the mono-exponential model is predominant for values of *b* up to 2,000 s/mm^2 and it can be extended to higher values (up to 3,000 s/mm^2) if appropriate multi-compartment models of diffusion are employed.

This methodology allows shorter MRI acquisitions and very fast calculation of scalars. Since the mono-exponential model only holds within a limited range around the measured *b*-value, the measures derived this way must be seen as *apparent* values at a given *b*-value, related to the original ones but dependent on the selected shell. The AMURA metrics used in this work are (Aja-Fernández et al., 2020, 2021, 2022):

1. Return-to-origin probability (RTOP), also known as probability of zero displacement, it is related to the probability density of water molecules that minimally diffuse within the diffusion time τ.
2. Return-to-plane probability (RTPP), which is a good indicator of restrictive barriers in the axial orientation.
3. Return-to-axis probability (RTAP), an indicator of restrictive barriers in the radial orientation.
4. Apparent Propagator Anisotropy (APA), an alternative anisotropy metric. It quantifies how much the propagator diverges from the closest isotropic one.
5. Diffusion Anisotropy (DiA), an alternative derivation of APA.
6. Generalized Moments, specifically we will consider the full moments of order 2 (q-space Mean Square Displacement, qMSD) and 1/2 ($\Upsilon^{1/2}$).

2.2. Dataset

2.2.1. Participants

The sample of this study was originally composed of 56 patients with CM, 54 patients with EM and 50 healthy controls (HC) that participated in previous studies (Planchuelo-Gómez et al., 2020a,b). Three patients with EM were discarded due to misregistration errors.

Inclusion criteria included diagnosis of EM or CM following the ICHD-3 (all the available versions), stable clinical situation, and first screening related to migraine just before the recruitment. Exclusion criteria were use of preventive treatments before the MRI acquisition, migraine onset in people older than 50 years, recently developed migraine (less than 1 year), frequent painful conditions, psychiatric and neurological disorders different to migraine, and pregnancy. Further details are available at Planchuelo-Gómez et al. (2020b).

The local Ethics Committee of Hospital Clínico Universitario de Valladolid approved the study (PI: 14-197). Additionally, all participants read and signed a written consent form prior to their participation.

The detailed demographic and clinical features of the three groups are shown in Table 1. No statistically significant differences in age or gender were found between the three groups. Patients with CM showed significantly higher duration of migraine, frequency of headache and migraine attacks and medication overuse, and a lower presence of aura.

2.2.2. MRI acquisition

For patients with migraine, the images were acquired at least 24h after the last migraine attack and before 2 weeks after the clinical visit to the headache unit. High resolution 3D T1-weighted followed by DWI were acquired using a Philips Achieva 3T MRI unit (Philips Healthcare, Best, The Netherlands) with a 32-channel head coil.

The acquisition of T1-weighted images was carried out using a Turbo Field Echo sequence with the following parameters: repetition time (TR) = 8.1 ms, echo time (TE) = 3.7 ms, flip angle = 8^o, 256 × 256 matrix size, spatial resolution of 1 × 1 × 1 mm^3 and 160 sagittal slices covering the whole brain.

The acquisition parameters for DWI were TR = 9,000 ms, TE = 86 ms, flip angle = 90^o, 61 diffusion gradient orientations, one baseline volume, *b*-value = 1,000 s/mm^2, 128 × 128 matrix size, spatial resolution of 2 × 2 × 2 mm^3 and 66 axial slices covering the whole brain.

All the images were acquired in the same session with a total acquisition time of 18 min.

2.3. Analysis of the data

2.3.1. dMRI preprocessing

Image preprocessing steps consisted of (1) denoising based on the Marchenko-Pastur Principal Component Analysis procedure (Veraart et al., 2016), (2) eddy currents and motion correction, and (3) correction for B1 field inhomogeneity. The MRtrix software (Tournier et al., 2019) was employed to carry out these steps, using the *dwidenoise*, *dwipreproc*, and *dwibiascorrect* tools (Zhang et al., 2001; Smith et al., 2004; Andersson and Sotiropoulos, 2016; Veraart et al., 2016). Further, a whole brain mask for each subject was obtained with the *dwi2mask* tool (Dhollander et al., 2016).

TABLE 1 Clinical and demographic characteristics of healthy controls (HC), episodic migraine (EM), and chronic migraine (CM).

	HC (n = 50)	EM (n = 51)	CM (n = 56)	Statistical test
Gender, male/female	11/39 (22/78%)	7/44 (14/86%)	6/50 (11/89%)	$\chi^2_{(2,N=157)} = 2.74$ $p = 0.25$ †
Age (years)	36.1 ± 13.2	36.6 ± 7.9	38.1 ± 8.7	$\chi^2_{(2)} = 2.79$, $p = 0.25$‡
Duration of migraine history (years)		13.1 ± 10.5	19.6 ± 10.4	U = 932.5, $p = 0.002$◇
Time from onset of chronic migraine (months)			24.5 ± 32.9	
Headache frequency (days/month)		3.6 ± 1.9	23.3 ± 6.3	U = 40.0, $p < 0.001$◇
Migraine frequency (days/month)		3.6 ± 1.9	13.9 ± 6.9	U = 99.5, $p < 0.001$◇
Medication overuse		0 (0%)	42 (75%)	$p < 0.001$*
Aura		9 (18%)	1 (2%)	$p = 0.006$*

†Chi-square test. ‡Kruskal-Wallis test. ◇Mann-Whitney U-test. *Fisher's exact test. Data are expressed as means ± SD.

2.3.2. Diffusion measures estimation

Two groups of diffusion measures were extracted. The former group is composed of three DTI classical metrics: FA, MD, axial diffusivity (AD), and radial diffusivity (RD). We considered only these measurements as they are the ones employed in most previous studies, particularly in the literature migraine, with no studies applying other measurements excluding the one carried out with this sample or the use of kurtosis (Ito et al., 2016).

These measures were estimated at each voxel using the *dtifit* tool from the FSL software (Jenkinson et al., 2012). FA measures the degree of anisotropy in the diffusion of water molecules inside each voxel, which reflects the degree of directionality of water diffusivity. MD is the average magnitude of water molecules diffusion. AD measures the water diffusion in the principal direction of WM fibers. RD describes the perpendicular diffusion of the principal direction (Pelletier et al., 2016).

The latter group includes the seven proposed q-space metrics calculated with AMURA: RTOP, RTAP, RTPP, APA, qMSD, DiA, and $\Upsilon^{1/2}$. The measures were calculated using dMRI-Lab[1] and MATLAB 2020a. AMURA measures rely on the expansion of spherical functions at a given shell in the basis of spherical harmonics (SH). Even SH orders up to six were fitted with a Laplace-Beltrami penalty $\lambda = 0.006$. A fixed value of $\tau = 70$ ms has been assumed for all the AMURA metrics. A visual comparison of the DTI and AMURA measures is shown in Figure 1.

2.4. Experiment with synthetic data

The main hypothesis of this work is that AMURA metrics are able to detect different diffusion properties than DTI in the white matter. In order to quantify this assumption, an illustrative synthetic experiment was carried out. We simulated a simple diffusion model that diverges from the diffusion tensor (DT). The simplest case is a 2-compartment model in which we considered that the main anisotropic diffusion was ruled by a zeppelin-shaped compartment (Alexander, 2008) and there was an isotropic compartment that stands for the free water fraction (Tristán-Vega et al., 2022):

$$S(b) = f \cdot Z_p(b, d_{||}, d_{\perp}) + (1 - f) \cdot \exp(-bD_0)$$

where $Z_p()$ is the zeppelin compartment, D_0 is the diffusivity of free water at body temperature (nearly $3.0 \cdot 10^{-6}$ μm^2/s), $d_{||}$ (μm^2/s) and $d_{\perp}$ (μm^2/s) are the parallel and perpendicular diffusivities that model the zeppelin and $(1 - f)$ is the free-water fraction.

For the experiment, different values of f were considered, ranging from 0.3 to 1. The value of $d_{||}$ was fixed and $d_{\perp}$ was changed as a function of f for two different cases

1. The FA obtained after estimating the DT from $S(b)$ is constant.
2. The MD obtained after estimating the DT from $S(b)$ is constant.

Sixty-one gradient directions and b = 1,000 s/mm^2 were considered. DTI and AMURA metrics were calculated from the synthetic signal.

In comparison with previous studies that assessed EAP-derived measures (Fick R. H. J. et al., 2016; Zucchelli et al., 2016), we employed a simpler model due to the different objective of our study. The previous studies were focused on a detailed characterization of the microstructure with the assessment of the sensitivity of the EAP measures under different conditions with a three-compartment model. The intracellular volume fraction and dispersion were additionally included compared to our experiment for the three-compartment model. In our study, the main objective was the assessment of AMURA measures compared to DTI in the context of clinical studies, i.e., comparison between clinical groups, with a reduced dMRI acquisition. Therefore, this synthetic experiment worked as a proof of concept to appreciate different properties of the AMURA and DTI measures, and not as a detailed analysis of the parameters in relation to microstructural features.

2.5. Statistical analysis

2.5.1. ROI analysis and TBSS

To test the capability of AMURA measures at b = 1,000 s/mm^2 to be used in clinical studies, two different statistical

1 Available at www.lpi.tel.uva.es/dmrilab.

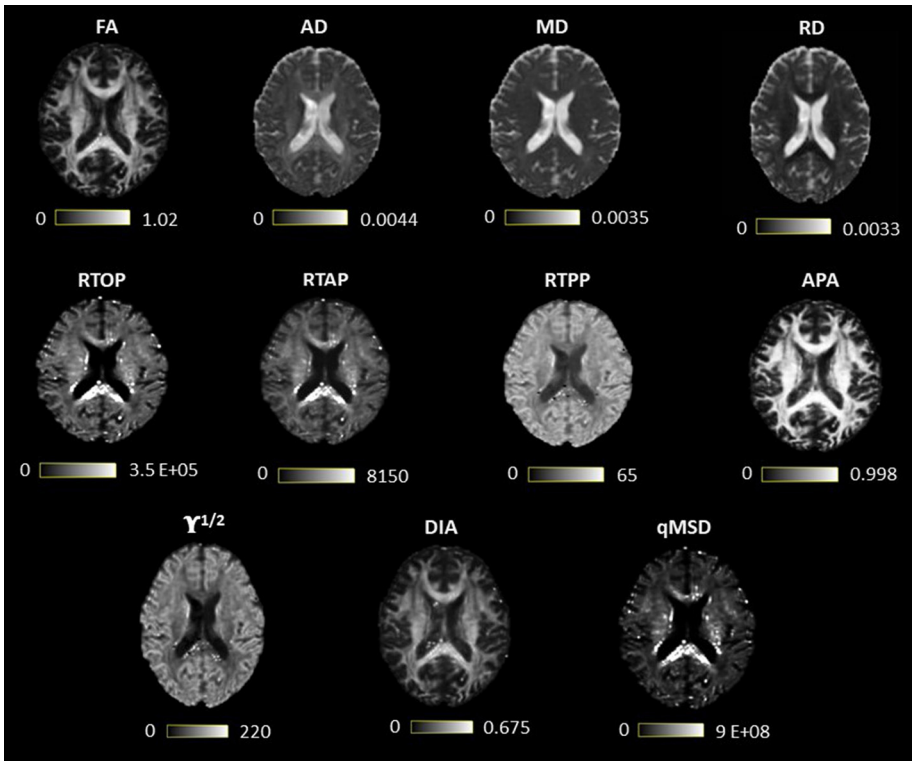

FIGURE 1
Visual comparison of diffusion tensor imaging (DTI) and measures from apparent measures using reduced acquisitions (AMURA). The first row contains the DTI measures, and the last two, the AMURA metrics.

analyses were considered: a region-oriented analysis and tract-based spatial statistics (TBSS) assessment. For both approaches, statistical differences between EM, CM, and HC were assessed with two-by-two comparisons. Forty-eight different regions of interest (ROIs) were identified using the Johns Hopkins University ICBM-DTI-81 White Matter Atlas (JHU WM) (Oishi et al., 2008). The first steps of the two assessing methods were common. The FA volumes were non-linearly registered to the Montreal Neurological Institute (MNI) space using the JHU WM template as reference. In the MNI space, the mean FA image for all the subjects was extracted and it was used to generate the white matter skeleton using a minimum FA value of 0.2. For each subject, the FA values were projected to the skeleton. For all the non-FA measures, the same registration used for the FA maps and projection to the skeleton obtained from the FA volumes were carried out.

For the ROI-based analysis, to obtain more robust measures, the average value of the metrics for each subject was obtained using voxels exclusively included in the white matter skeleton within the 2% and 98% percentiles of the corresponding skeleton values. Then we carried out a two-sampled-two-tailed, pooled variance *t*-test between each pair of groups (EM-HC, CM-HC, and EM-CM) for every measure and ROI.

The TBSS approach was conducted to mimic a clinical study following the basic procedure implemented in Planchuelo-Gómez et al. (2020c) and Planchuelo-Gómez et al. (2020b). In this assessment, the statistical comparisons were conducted using the *randomize* tool from FSL (Nichols and Holmes, 2002), which performs a permutation test. Specifically, 5,000 permutations and the threshold-free cluster enhancement (TFCE) procedure were employed (Smith and Nichols, 2009). Briefly, TFCE enhances zones of the voxelwise statistic maps that show spatial contiguity to obtain spatial clusters without using specific values to delimitate different spatial areas with similar values. We considered that an atlas-defined region presented statistically significant differences, after family-wise error correction and TFCE, when the voxels with differences contained a volume greater than 30 mm^3. Each ROI from the atlas could be part of one or more clusters defined by the TFCE procedure, i.e., TFCE was applied independently from the JHU WM atlas and the voxels for each region were extracted within the defined clusters by TFCE.

The threshold for statistical significance for all the statistical assessments was $p < 0.05$. It is worth noting that the purpose of the ROI-based analysis was not to carry out a complete and accurate clinical study, but to analyze the behavior of each measure separately. Thus, the results in this case were not corrected for multiple comparisons, causing some variations with the results reported in the literature. For the same reason, clinical covariates were not included in all the statistical comparisons.

Further, in relation to the ROI-based analysis, Cohen's D value was calculated over the different ROIs to quantify the effect size of the different DTI and AMURA scalars. In addition, the Cohen's *D*-value was obtained for the full WM to better describe what happened with each measure in the whole brain.

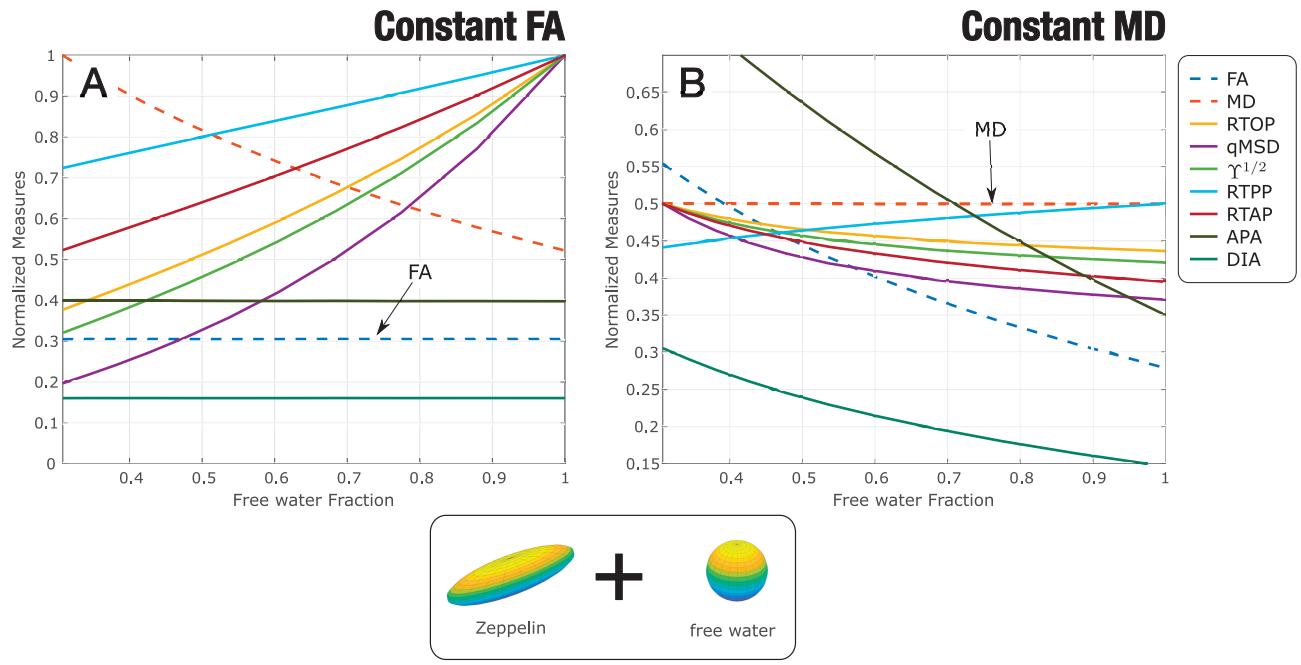

FIGURE 2
Experiment with synthetic data: a two-compartment model is considered, zeppelin + free water. The parameters of the zeppelin are modified so that the estimated diffusion tensor in every case shows: **(A)** constant FA; **(B)** constant MD. AMURA metrics have been calculated. Measures are normalized for better visualization.

2.5.2. Resampling of diffusion measures

To better understand the discrimination power of each measure, we analyzed their statistical significance in relation to the number of subjects in each group, i.e., the sample size. To that end, a resampling experiment was carried out. The number of subjects of each group (EM, CM, and HC) was progressively decreased from the original number to 10 subjects in each group, reducing five subjects for each iteration. For each iteration, 5,001 different subsamples were randomly obtained following a bootstrapping procedure. For each subsample, the ROI-based approach described in Section 2.5.1, i.e., the uncorrected t-tests of the diffusion descriptors from each JHU WM atlas ROI within the WM skeleton, was repeated. Specifically, for the tests with statistically significant differences in the reference comparisons with the whole sample, two-by-two comparisons between HC, EM, and CM groups were carried out. For each ROI, diffusion metric and specific configuration, a ROI was considered to have significant differences if at least the two-by-two comparison in 2,501 out of the 5,001 subsamples showed $p < 0.05$, value established as threshold for statistical significance, as in the whole sample. No kind of statistical correction was used for this experiment considering that our purpose was to study the behavior of the different metrics with the sample size.

2.5.3. Analysis of stability

The coefficient of quartile variation (CQV) was used to measure the stability across groups. The CQV is a measure of homogeneity (Altunkaynak and Gamgam, 2019) and it was used to assess the inter-subject variability, considering the diverse sample sizes from the analysis described in the previous section. The CQV is one of the most robust statistical measures as it depends on the quartiles, being less sensitive to outliers. Its use is as follows:

$$\mathrm{CQV} = \frac{Q_3 - Q_1}{Q_3 + Q_1} \cdot 100 \tag{1}$$

where Q_1 and Q_3 are the first and third quartile, respectively.

The CQV is calculated for each group and ROI, considering as figure of merit the median value of all the CQV of the different 5001 subsamples used in this experiment. The 95% confidence interval (95% CI) was set taking the 2.5 and 97.5 percentiles of the whole CQV values for each group of values. This 95% CI was compared between the diverse measures and regions for each sample size.

3. Results

3.1. Experiment with synthetic data

Results for the experiment with synthetic data are gathered in Figure 2: constant FA (Figure 2A) and constant MD (Figure 2B). All measures have been normalized for better visualization and comparison. When FA is set to constant, in this simple scenario, anisotropy-related metrics (PA and DiA) behave similarly. The other AMURA metrics detect the underlying change and grow with f, presenting qMSD, $\Upsilon^{1/2}$ and RTOP similar but higher slopes of opposite sense compared to MD, which decreases with f, begin the change of the RTAP almost identical to the one shown by the MD. On the other hand, when MD is set to constant, Figure 2B, all the AMURA measures are able to detect the changes in the signal, and the DiA presented a similar steep rate compared to the

FA, and higher steep rate values were appreciated in the case of APA. This example illustrates that, although interpretation of some AMURA measures can be similar to DTI measures, they are not really quantifying the diffusion signal in the same way. The variety of AMURA measures allows not only to detect similar patterns compared to DTI, but also to find complementary results.

3.2. ROI based statistical analysis

Eleven different measures were considered for the analysis: four DT-based measures (FA, AD, MD, RD) and seven AMURA-based (RTOP, RTAP, RTPP, qMSD, $\Upsilon^{1/2}$, APA, and DiA). Table 2 shows a p-value scheme for the 48 ROIs considered for each of the measures. Those ROIs that exhibit differences with statistical significance above 95% ($p < 0.05$) are highlighted in green and above 99% ($p < 0.01$) in amber. The size of the effect (Cohen's D) is shown for those ROIs with significant differences (in bold face those values in which $D > 0.5$).

Note that those metrics based on the DT showed a limited amount of differences with only three ROIs with statistically significant differences above 99% for EM vs. CM, two for CM vs. EM and two for CM vs. HC. In the EM vs. HC comparisons, the highest differences between AMURA and DTI metrics, with a greater number of statistically significant results for AMURA, were found: even in those cases in which the DT found differences, like the pontine crossing tract (PCT), the equivalent AMURA metrics showed a smaller p-value and higher effect sizes. RTOP, qMSD, and DiA were the metrics providing a higher number of statistically significant differences with the higher significance (see amber ROIs) and the greater effect size.

Regarding the other two sets of comparisons (CM-EM and CM-HC), AMURA metrics showed no clear higher number of differences compared to DTI metrics. In fact, AD and MD were able to detect more differences in the comparisons between CM and EM, coherently with previous studies (Planchuelo-Gómez et al., 2020b). This case suggests the complementary nature of DTI and AMURA. As shown in the preliminary example, both methods are quantifying different microstructure effects. Thus, AMURA seems more sensitive to changes between EM and controls, while DTI seems more sensitive to changes between the two types of migraine.

It is important to note that in all three comparisons, RD did not find any significant differences in any ROI, which is consistent with the findings reported in Planchuelo-Gómez et al. (2020b). Therefore, to streamline the presentation of data in the figures and tables that follow, RD will be omitted in the following experiments.

To better understand the behavior of both sets of measures, let us deeply analyze three specific regions. We selected the PCT, right inferior cerebellar peduncle (ICP-R) and the right external capsule (EC-R) for being the ones with the highest number of differences and the greatest effect sizes in Table 2. For each ROI, a box plot of the three groups is shown for each measure in Figure 3A. The boxes mark the median and 25 and 75 percentiles of the values of the different measures over the skeleton of the FA for all the subjects in each group. For better visualization, the median of each group is marked in red. The box plots are repeated in Figure 3B merging EM and CM in a single group that includes all migraine patients.

In the PCT, regarding DTI, the statistical analysis found differences between EM and HC for MD and AD, and between CM and HC for AD, but no differences were found between both migraine groups. In Figure 3A, we can see that, actually, MD showed a higher median value of EM and CM when compared with HC. These differences were kept in Figure 3B when considering the joint migraine group. On the other hand, AMURA showed significant differences between EM-HC and CM-EM. Only RTPP (a metric related to AD) and $\Upsilon^{1/2}$ Regarding the other two sets of comparisons (CM-EM and CM-HC), AMURA metrics showed no clear higher number of differences compared to DTI metrics. In fact, AD and MD were able to detect more differences in the comparisons between CM and EM. This would mean that AMURA better discriminates EM in this ROI. According to Figure 3A, that is precisely what is happening. See, for instance, RTOP and qMSD. In both cases, there is almost no difference between HC and CM, while EM shows smaller median and a reduced variance. On the other hand, RTPP behaves more similarly to AD: both migraine groups were similar but differ from the control-group.

For the ICP-R, according to Table 2, MD and AD differences were found for the EM-HC case, AMURA found differences for EM-HC and CM-HC and no differences were found for CM-EM. If we check Figure 3A we can see that both migraine groups presented similar values in this ROI. Statistically significant differences were found between CM and HC, presenting the RTOP, qMSD, and RTAP lower values in CM.

A similar effect can be observed in the EC-R, where no differences were found for DTI parameters, but for AMURA in the comparisons between HC and the two migraine groups. If we see Figure 3A, we can observe that AMURA metrics (RTOP and qMSD, for instance) discriminated CM and HC better than MD and AD. While in the MD and AD cases there is a reduction in the variance of the CM group, the change in the median is smaller, compared to CM and EM. If we pay attention to Figure 3B, we can see migraine and HC showed similar AD and MD values, while differences could be appreciated with RTOP, qMSD, and RTAP.

3.3. Effect size

In Table 2, the values of the Cohen's D were shown for those ROIs with significant differences. Figure 4 shows the absolute value of Cohen's D for eight selected ROIs (those with the largest number of differences) and for the three group comparisons.

The comparison between EM and HC, the AMURA metrics showed the largest effect sizes as measured by larger Cohen's D-values. Specifically, qMSD, RTOP, and DiA were consistently getting values over 0.5 (the threshold for medium effect) and, in some cases, near 0.8. In the right external capsule (EC-R), for instance, most AMURA metrics showed a moderate-large effect size while DTI metrics did not get to 0.5. Even in those regions where DTI values showed statistical differences and a moderate effect (PCT, ML-R), AMURA outperformed them. There is only one case, the MD in the ICP-R, where a DTI metric showed a moderate effect size. However, if we check Table 2, we can see that the effect size for MD is 0.75, but this value was slightly lower than the value for the qMSD (0.75 vs. 0.76).

TABLE 2 Results of the ROI-based statistical analysis and Cohen's D: EM vs. HC, CM vs. EM, and CM vs. HC.

	EPISODIC vs CONTROLS										
	FA	AD	MD	RD	RTOP	RTAP	RTPP	qMSD	APA	$\Upsilon^{\frac{1}{2}}$	DIA
MCP					0.44		0.32	**0.53**			
PCT		**0.59**	**0.55**		**0.77**	**0.65**	**0.61**	**0.68**	0.48	**0.74**	
GCC								0.47			
BCC								0.46			
SCC	**0.50**				**0.50**			**0.52**		0.39	**0.58**
Fx											0.32
CST-R	**0.50**				0.40			**0.53**	**0.64**		**0.68**
CST-L	0.39				0.38			0.43	0.48		**0.56**
ML-R	**0.62**				**0.62**			**0.71**	**0.66**		**0.64**
ML-L	0.52				**0.68**	**0.51**		**0.69**	**0.52**		**0.76**
ICP-R		0.48	**0.75**		**0.68**	**0.64**	**0.55**	**0.76**		**0.71**	**0.51**
ICP-L		0.41	**0.51**		0.49			**0.55**			
SCP-R								0.48			
SCP-L								0.44			
CP-R					0.43			**0.59**			**0.59**
CP-L											
ALIC-R					0.41			0.45	**0.59**		**0.51**
ALIC-L					0.44	0.45		0.43	0.42		0.45
PLIC-R					0.49			**0.51**	**0.51**		
PLIC-L			0.43		**0.56**	0.45		**0.56**	0.46		
RPIC-R											
RPIC-L					0.49			**0.52**			
ACR-R					0.49	**0.50**		**0.56**			
ACR-L											
SCR-R								0.48			
SCR-L											
PCR-R											
PCR-L											
PTR-R											
PTR-L											
SS-R					0.45			**0.52**			
SS-L											
EC-R					**0.72**	**0.72**		**0.83**	**0.76**		**0.74**
EC-L			0.47		**0.60**	**0.55**	0.46	**0.57**	**0.53**	0.49	
CG-R					0.47			**0.54**			
CG-L					0.47			0.46			
CH-R							0.22			0.32	
CH-L											
F/ST-R					**0.68**	**0.55**		**0.73**			**0.51**
F/ST-L											
SLF-R											
SLF-L		0.49					**0.51**			**0.51**	
SFOF-R	0.42								**0.59**		**0.51**
SFOF-L									0.48		0.44
UF-R	**0.53**	0.42				**0.50**			**0.66**		**0.64**
UF-L									0.47		
T-R											
T-L											

	CHRONIC VS EPISODIC										
	FA	AD	MD	RD	RTOP	RTAP	RTPP	qMSD	APA	$\Upsilon^{\frac{1}{2}}$	DIA
MCP		**0.65**					0.48			**0.56**	
PCT					**0.56**	**0.52**		**0.59**	**0.59**		**0.57**
GCC											
BCC											
SCC									0.49		
Fx											
CST-R											
CST-L			0.45								
ML-R											
ML-L											
ICP-R											
ICP-L											
SCP-R											
SCP-L											
CP-R											
CP-L			0.46								
ALIC-R			0.44						**0.55**		0.39
ALIC-L	0.44		0.49		0.45	0.46		0.45	**0.64**		**0.54**
PLIC-R		0.45	0.47								
PLIC-L		0.40	0.45								
RPIC-R											
RPIC-L											
ACR-R											
ACR-L											
SCR-R							0.40			0.41	
SCR-L											
PCR-R											
PCR-L											
PTR-R											
PTR-L											
SS-R		**0.55**									
SS-L											
EC-R											
EC-L			0.46					**0.57**		**0.56**	
CG-R											
CG-L											
CH-R											
CH-L											
F/ST-R								0.42			
F/ST-L									**0.59**		0.49
SLF-R											
SLF-L		0.48					0.46			0.45	
SFOF-R	0.40								**0.67**		0.49
SFOF-L	**0.50**				0.42			0.47	**0.63**		**0.57**
UF-R											**0.50**
UF-L											
T-R			0.31								
T-L					0.38	0.42					

	CHRONIC vs. CONTROLS										
	FA	AD	MD	RD	RTOP	RTAP	RTPP	qMSD	APA	$\Upsilon^{\frac{1}{2}}$	DIA
MCP											
PCT		0.47					0.39			0.34	
GCC											
BCC											
SCC											
Fx	0.44	0.47	0.48								0.44
CST-R	0.35								0.48		0.38
CST-L		0.43									0.24
ML-R	**0.63**				0.29	0.31		0.47	**0.57**		**0.59**
ML-L	**0.52**				0.34			0.41	**0.52**		0.50
ICP-R					**0.65**	0.48	**0.51**	**0.61**		**0.56**	0.39
ICP-L											
SCP-R											
SCP-L											
CP-R											
CP-L											
ALIC-R											
ALIC-L											
PLIC-R									0.34		
PLIC-L											
RPIC-R					0.48	0.39		0.47			
RPIC-L								0.40			
ACR-R											
ACR-L											
SCR-R											
SCR-L											
PCR-R											
PCR-L											
PTR-R											
PTR-L											
SS-R											
SS-L											
EC-R					0.39	0.42		0.41	**0.59**		**0.54**
EC-L											
CG-R											
CG-L											
CH-R											
CH-L											
F/ST-R											
F/ST-L											
SLF-R											
SLF-L											
SFOF-R											
SFOF-L											
UF-R											
UF-L											
T-R		0.16	0.37								
T-L							0.27			0.32	

Two-sample t-tests for DTI and AMURA measures and each of the ROIs defined by thee JHU WM atlas. The p-values represent the probability that a certain measure has identical means for both groups. ROIs exhibiting differences with statistical significance above 95% ($p < 0.05$) are marked in green and above 99% ($p < 0.01$) in amber. The Cohen's D of those ROIs showing statistical differences is included.

Regarding the comparison between CM and EM (Figure 4B), most measures showed low effect sizes, both for DTI and AMURA. The middle cerebral peduncle (MCP) for the AD and the right sagittal stratum (SSR) showed Cohen's D-values over 0.5 for the AD, while AMURA only achieved medium effects in the pontine crossing tract (PCT).

Finally, in the comparison between CM and HC (Figure 4C), the right external capsule (EC-R), the right medial lemniscus (ML-R) and the left medial lemniscus (ML-L), the APA and the DiA reached absolute values of Cohen's D higher than 0.5, showing at the same time significant differences. FA also showed moderate effect in ML-R and ML-L, while RTOP, qMSD, and $\Upsilon^{1/2}$ showed values over 0.5 in the right inferior cerebellar peduncle (ICP-R).

It is also interesting to analyze the behavior of each measure over the whole WM. Figure 5 shows the absolute Cohen's D in the whole WM for each measure. The biggest effect sizes were obtained for the comparison between EM vs. HC for AMURA. Coherently, this comparison also produced the highest number of ROIs with significant differences. The qMSD or the RTOP measures reached absolute Cohen's D-values close to 0.6, and, respectively, 27 and 22 ROIs with significant differences for the ROI analysis, 43 and 41 in TBSS. On the other hand, the comparison between CM and HC presented the lowest Cohen's D-values, none of them reaching 0.5. Regarding the comparison between CM and EM, the AD, MD were the measures with greatest Cohen's D-values, over 0.5.

3.4. Change of the sample size

Figure 6 shows the effects of changing the sample size for different DTI and AMURA-based measures for the three comparisons considered. We have selected 8 out of 11 metrics for better visualization of the graphics. Among the DTI measures, results with MD showed a relatively high number of ROIs with statistically significant differences using bigger samples sizes,

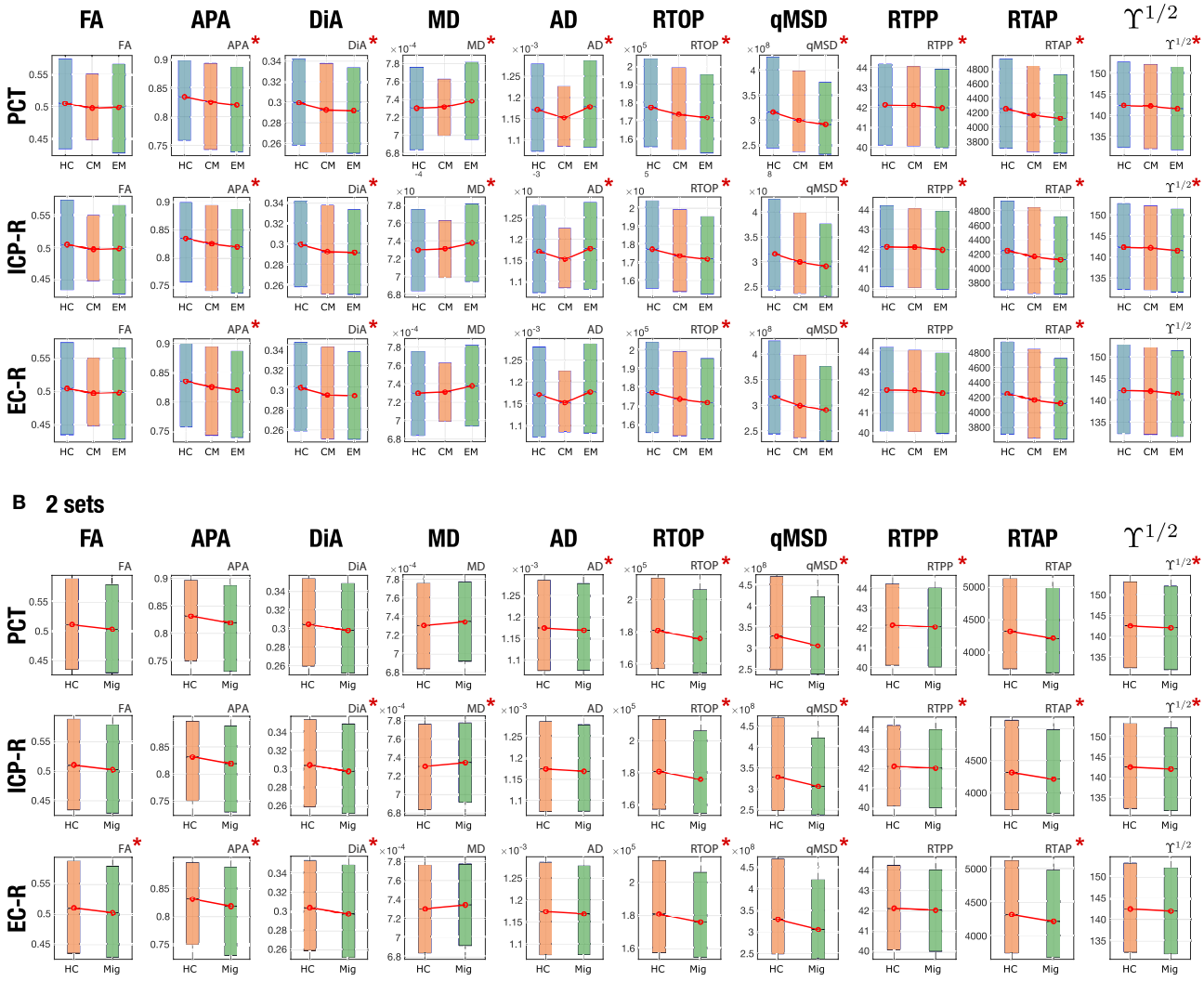

FIGURE 3
Boxplots of the distribution of different measures for EM, CM, and HC for three specific regions: PCT, ICP-R, and EC-R. The star marks those regions with statistically significant differences in the ROI analysis. **(A)** 3 sets (HC, CM, EM). **(B)** 2 sets (HC and migraine).

especially for the EM-CM comparison, as can be seen in Figure 6C. However, even in that case, the number of significant ROIs drastically decreased for a group sample size of 40. In addition, few ROIs with statistically significant differences were found for the rest of DTI measures and for the other two group comparisons, in any sample size, which made the assessment of the relationship between DTI measures and sample size unfeasible.

Results showed a stable behavior of AMURA measures in relation to the sample size, which can be understood as a linear dependence between the group sample size and the number of statistically significant ROIs. In Figure 6A, this behavior can be better understood and interpreted in measures such as qMSD, which was the most robust one in the comparison between EM and HC. Furthermore, RTOP, qMSD, and DiA also showed a robust behavior in the CM vs HC comparison. Notice that AMURA measures reached the lack of statistical significance ROIs for a group sample size of 10. However, when reducing the sample size to half ($N = 25$), most AMURA metrics still were able to find differences between groups, while only a few differences remained for the DTI case.

In order to better understand this effect, we now analyze the behavior of the measures in selected ROIS. We have chosen, according to results in Table 2, those 13 regions in which DTI measures showed differences with the original sample size for EM vs. HC (see Figure 7A). For those 13 ROIs, in 7 of them FA showed significant differences for $N = 50$, 5 for MD and 5 for AD (see ROIs marked in amber). Then, we look at the results for those specific ROIs for a reduced sample size of $N = 25$. Note that, in that case, when the number of subjects is reduced to half, the FA was only able to detect one ROI (out of 7), MD only one (out of 5), and AD none (ROIs marked in red). When we look to the AMURA metrics, we see that they were able to still keep most of those differences even for a reduced sample size

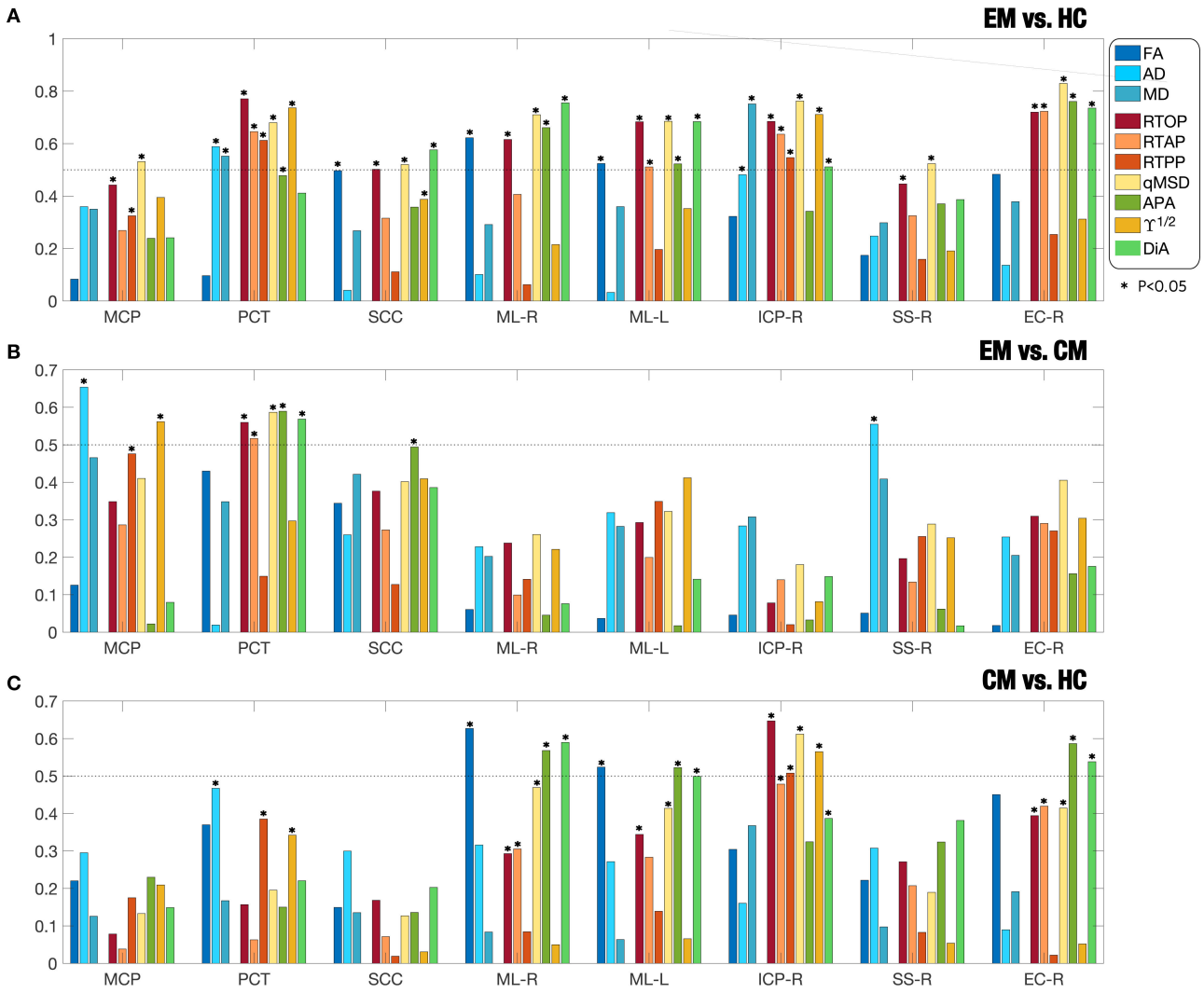

FIGURE 4
Absolute value of effect sizes (absolute Cohen's d) for associations between **(A)** EM and HC; **(B)** EM and CM; **(C)** CM and HC. Different DTI and AMURA metrics are considered for eight selected ROIs (MCP, PCT, SCC, ML-R, ML-L, ICP-R, SS-R, EC-R) according to the JHU WM Atlas. The star marks those regions with statistically significant differences in the ROI analysis.

(see ROIs marked in green): DiA and APA, anisotropy measures similar to the FA, were able to, respectively find 4 and 7 out of the original 7 FA ROIs. RTAP, and $\Upsilon^{1/2}$ succeed in finding 2 of the 5 MD ROIs, while RTOP finds 3 and qMSD 4 of them. In addition, with RTPP, 2 out of the 5 AD ROIs were identified for the reduced sample size. All in all, for this comparison, AMURA outperformed DTI in keeping the differences even for a smaller sample size.

As an illustration, in Figure 7B, the 13 considered ROIS are depicted. For each ROI, the metrics that showed significant differences for a sample size of $N = 25$ are displayed.

3.5. TBSS (original sample)

As we have previously stated, the ROI analysis carried out in the previous sections could be an illustrative example of the performance of the different metrics and it gives a valuable insight on the relation among them. However, since no statistical correction was considered, the results could not be acceptable for clinical studies. Thus, in order to mimic an actual clinical study, we have now repeated the analysis using TBSS for the three comparisons.

Using the DTI measures (FA, MD, AD, and RD), statistically significant differences between CM and EM patients were observed for two parameters. Patients with CM showed lower AD and MD values than EM in 40 and 38 out of 48 regions from the JHU-WM Atlas, respectively. No statistically significant differences were found using DTI measures between EM and HC or between CM and HC.

For the AMURA metrics, the comparison between patients with EM and HC showed the highest number of parameters with statistically significant differences. Significant lower RTOP, RTAP, qMSD, APA, DiA, and $\Upsilon^{1/2}$ values in EM compared to HC were found in 41, 39, 43, 27, 29, and 9 ROIs out of 48, respectively. Concerning the comparison between both groups of patients,

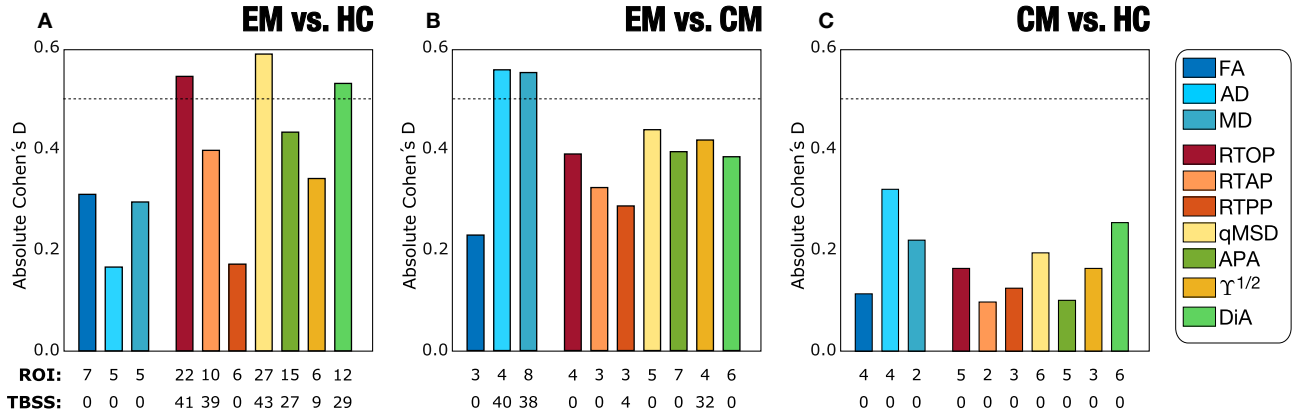

FIGURE 5
Absolute value of Cohen's *D*-values for the three group comparisons in the Full WM: **(A)** Episodic Migraine (EM) vs. Healthy Controls (HC); **(B)** EM vs. Chronic Migraine (CM); **(C)** CM vs. HC. DTI and AMURA measures are depicted. For each measure, the total number of ROIs that presented statistically significant differences obtained with the ROI and TBSS statistical approaches are also noted.

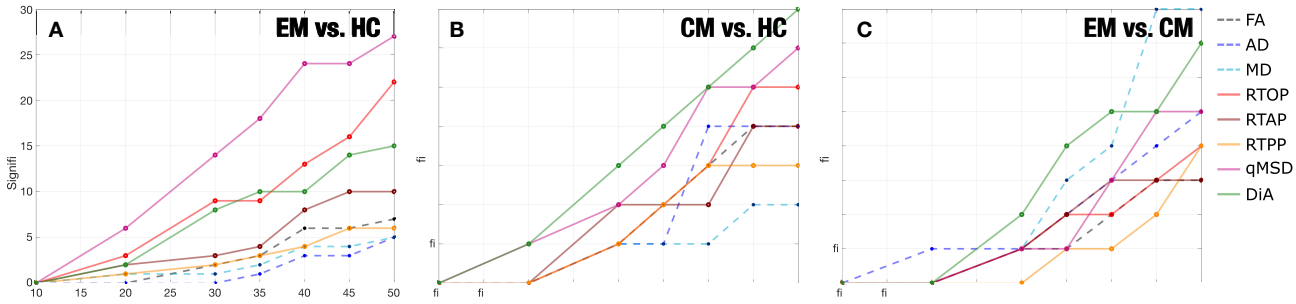

FIGURE 6
Number of ROIs with statistically significant differences by the resampling of diffusion measures reducing the number of subjects per group (sample size). **(A)** Episodic Migraine (EM) vs. Healthy Controls (HC). **(B)** Chronic Migraine (CM) vs. HC. **(C)** CM vs. EM. No statistical correction was considered. For each case the median of 5,001 permutations considered.

higher values in CM compared to EM were identified for the RTPP and $\Upsilon^{1/2}$ in 4 and 32 regions, respectively.

Figure 8 shows the TBSS results including all the ROIs that presented statistically significant differences together with the FA skeleton. On the one hand, for EM vs. HC and CM vs. HC comparisons, all the AMURA measures which showed significant differences are merged and depicted in the figure, that is, RTOP, RTAP, APA, qMSD, $\Upsilon^{1/2}$ and only DiA for EM vs. HC. On the other hand, DTI and AMURA measures can be distinguished in the last CM vs. EM comparison. For DTI, the merged measures depicted are AD and MD, while for AMURA are RTPP and $\Upsilon^{1/2}$. As it can be seen, AMURA measures showed differences in group comparisons where the DTI ones did not, as shown in the green circles. A summary with the previous TBSS results regarding the number of ROIs and the group comparisons can be found in Figure 9.

3.6. Analysis of stability

Figure 10 depicts the average values of CQV for all the DTI and AMURA-based diffusion measures. The measures with the highest stability (lowest CQV) were the RTPP and the APA, with an approximate average CQV of 2% considering all the regions. Other measures with relatively high stability were the three DTI measures (FA, MD, and AD), $\Upsilon^{1/2}$ and DIA, with CQV average values between 2% and 5%. The remaining DTI and AMURA descriptors (RD, RTAP, and RTOP), presented a moderate-high stability, with CQV average values between 5% and 10%. The descriptor with the lowest stability was the qMSD, with CQV average values between 15% and 20%.

Regarding the comparisons between the three groups of interest, after reducing the group sample size to 45 subjects, the assessment of the CQV 95% CI showed that the HC presented a general higher variability than patients with EM and CM. The parameters with a higher number of regions with statistically significant differences between HC and migraine patients according to the 95% CI were the three AMURA measures (RTOP, RTPP, and RTAP) and the MD, with 14–22 regions presenting differences. Additionally, in the comparison between HC and CM, the CQV of APA or $\Upsilon^{1/2}$ were significantly higher in HC than CM in 13 regions. The number of regions with CQV differences between CM and EM was lower compared to the comparison between HC and the patient groups. FA and MD were the descriptors with a higher number of regions (nine) that showed higher variance in EM compared to

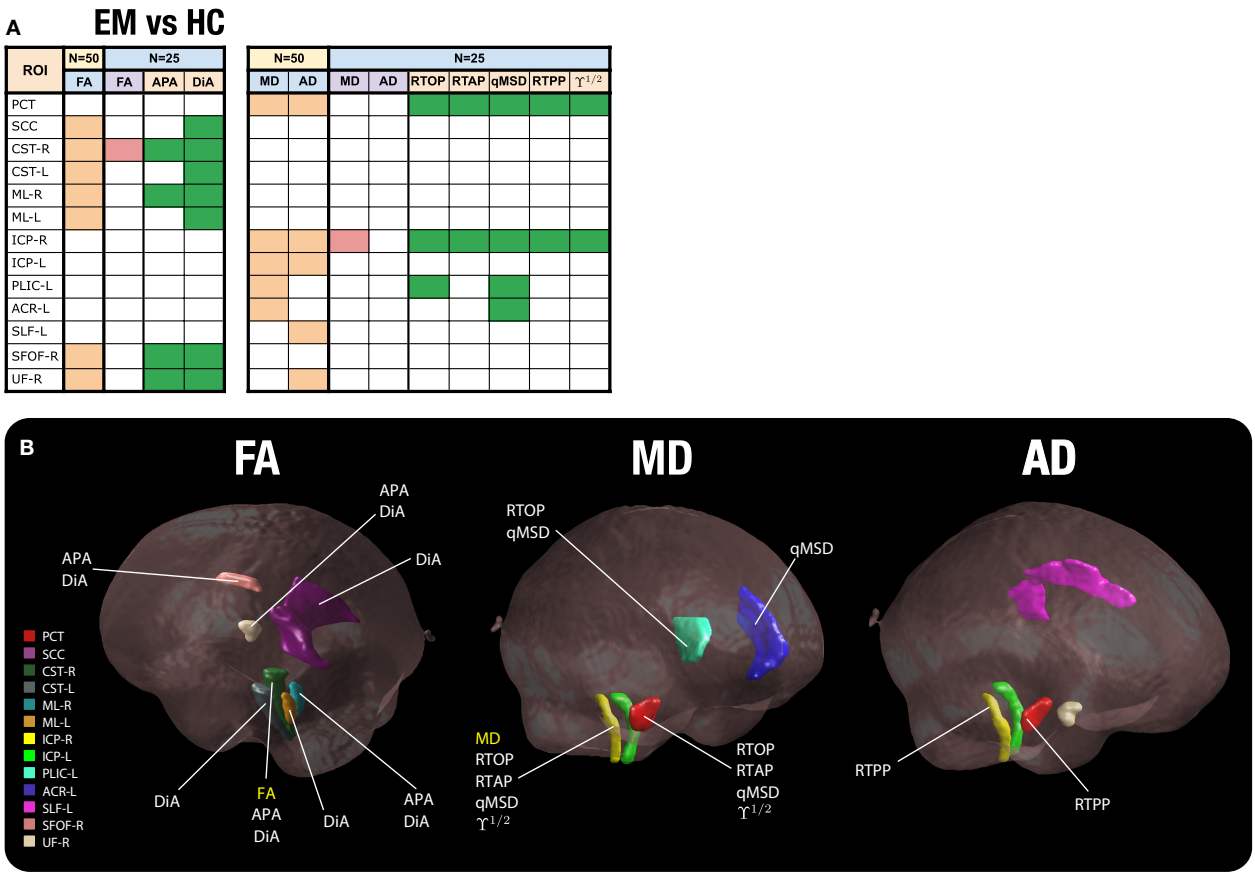

FIGURE 7
Significant ROIs found for a reduced sample size ($N = 25$). **(A)** Table of ROIs found at $N = 25$ compared to the original sample size (EM vs. HC). In amber, the ROIS with differences for DTI at the original sample size; in red, those ROIS with differences for DTI for a reduced sample size ($N = 25$); in green, those ROIS with differences for AMURA for a reduced sample size ($N = 25$). **(B)** The 13 ROIs detected by DTI at the original sample size are shown in the white matter. For each ROI, we have added the label of those metrics that show significant differences for a sample size of $N = 25$.

CM, and MD was also the parameter with more regions (eight) with significantly higher variance in CM.

4. Discussion and conclusions

In this study, we assessed the viability of advanced diffusion descriptors obtained with a novel approach, AMURA, in comparison with traditional DTI parameters. To this end, their capability to discriminate difference between clinical groups of interest was compared, together with the stability of these results for reduced sample sizes. Using synthetic and real data with a single-shell and low b-value, we observed that AMURA is sensitive to changes of parameters associated with the dMRI signal, showing a higher capability of discrimination between clinical groups, even for decreased sample sizes. Specifically, with AMURA we detected a larger number of ROIs with statistically significant differences between groups, or results complementary to those identified with DTI, presenting higher effect size but lower stability than DTI metrics.

Advanced diffusion descriptors such as RTOP, RTAP and APA have shown to be useful for the analysis of the WM of the brain (Aja-Fernández et al., 2020; Planchuelo-Gómez et al., 2020b,c). However, their conventional calculation requires acquisition protocols including several *b*-values, a high number of diffusion gradient directions and very long processing times. This makes them unfeasible for their use in clinical practice or in many commercial MRI scanners. Besides, the use of these metrics in retrospective studies is usually impossible since the acquisition protocols do not allow for it.

AMURA was proposed to allow the estimation of apparent versions of these advanced diffusion measures from reduced acquisitions (Aja-Fernández et al., 2020, 2021, 2022). It provides a fast and straightforward method to compute them from a single shell and very short processing times. Metrics calculated with AMURA have shown a high correlation with measures calculated using a multishell approach, such as MAP-MRI (Özarslan et al., 2013), MAPL (Fick R. H. et al., 2016), or MiSFIT (Tristán-Vega and Aja-Fernández, 2021), for high *b*-values (at least 2,000 s/mm^2). For lower values, these measures show a weaker correlation since the underlying features measured are better visible at higher *b*-values (Aja-Fernández et al., 2020, 2022). However, we hypothesized that AMURA metrics can still provide useful information at lower *b*-values, complementary to that obtained from DTI-based measures. This paper focuses precisely on that hypothesis and tries to elucidate whether AMURA-based measures

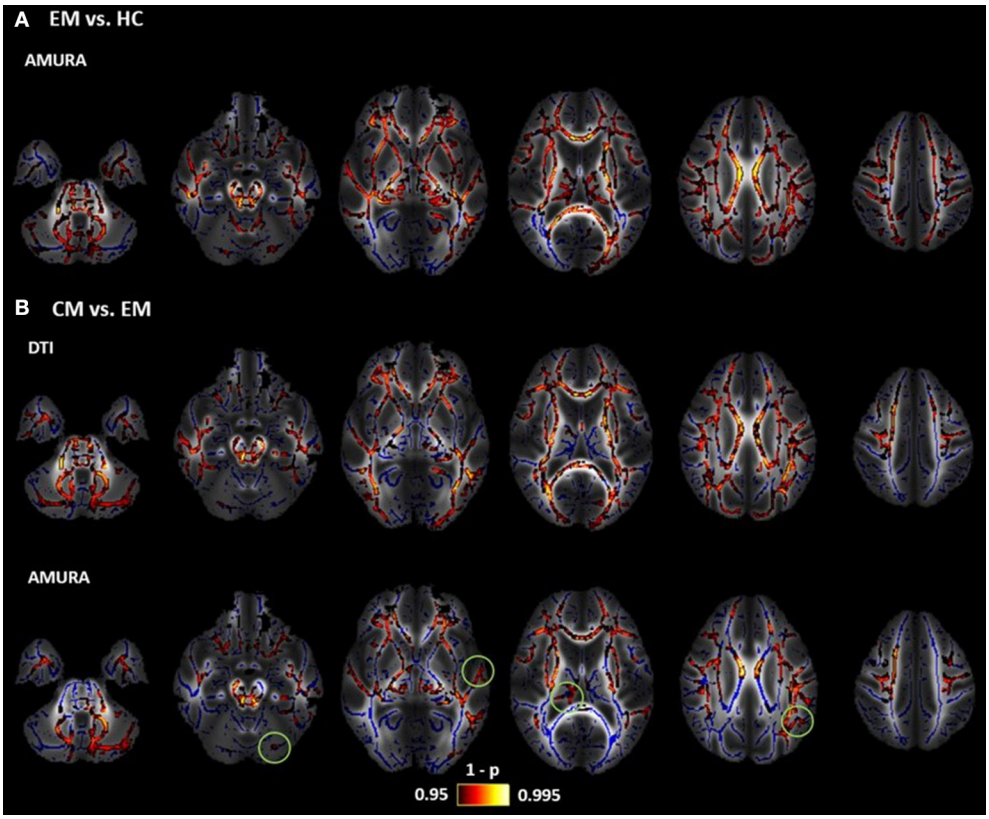

FIGURE 8
Results of TBSS analysis: statistically significant clusters of voxels distinguishing between DTI and AMURA approaches. Mean FA image at the background, FA skeleton colored in blue and significant ROIs colored in red-yellow. **(A)** Episodic Migraine (EM) vs. Healthy Controls (HC): merged AMURA measures (RTOP, RTAP, APA, qMSD, $\Upsilon^{1/2}$, and DiA). **(B)** CM vs. EM: merged DTI (AD and MD) and AMURA (RTPP and $\Upsilon^{1/2}$) measures. DTI measures do not detect any significant ROI either in EM vs. HC nor CM vs. HC. Green circles showed the areas where AMURA measures showed differences in group comparisons where the DTI ones did not.

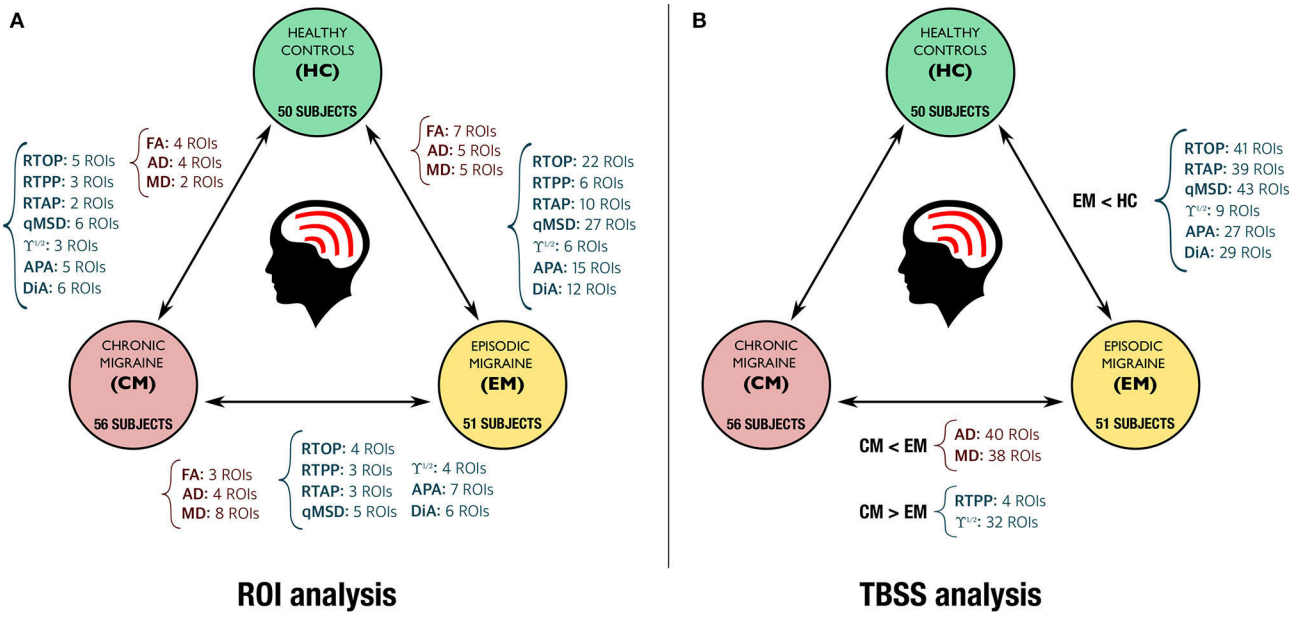

FIGURE 9
Summary of the statistically significant differences found with DTI (in red) and AMURA measures (in dark blue) for the comparison of the three groups. **(A)** ROI based analysis (no statistical correction). **(B)** TBSS analysis (with family-wise error correction).

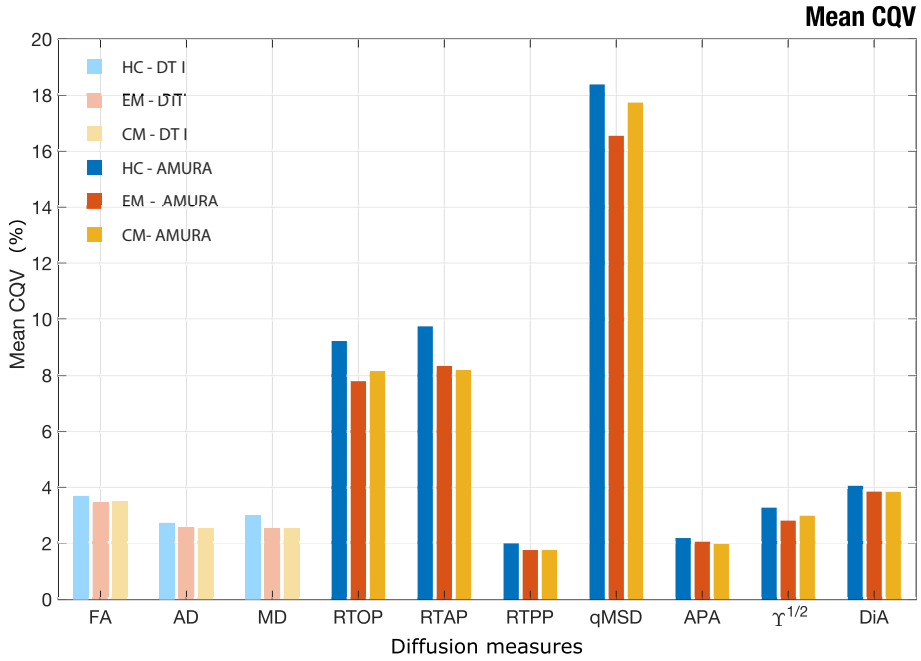

FIGURE 10
Mean CQV for each group of study considering the 48 ROIs of JHU-WM atlas. Healthy Controls (HC), Episodic Migraine (EM), and Chronic Migraine (CM). DTI and AMURA measures are shown. The measures with the higher stability have lower CQV.

obtained from standard DTI-type acquisitions are useful in group studies.

To that end, we have resorted to migraine as our target pathology, because of several reasons. First, diffusion MRI studies in the literature show that differences between patients and HC, or between different groups of patients (EM vs. CM) are subtle, as studies using small sample sizes have often reported no differences and even contradictory findings have been published (Chong and Schwedt, 2015; Messina et al., 2015; Neeb et al., 2015; Gomez-Beldarrain et al., 2016; Shibata et al., 2018; Coppola et al., 2020; Planchuelo-Gómez et al., 2020a).

To study the viability of AMURA-based measures, two different statistical analysis were carried out, including a ROI-based analysis and conventional TBSS, together with the assessment of the behavior of the diverse measures from reduces sample sizes and of the stability. We show that AMURA measures obtained from DTI-type acquisitions were able to successfully find statistically significant differences between the three groups under study (HC, EM, and CM), including differences that were not detected using DTI-based measures. Although AMURA showed additional differences between groups in a preliminary previous study (Planchuelo-Gómez et al., 2020c), the magnitude of the additional differences, particularly those between EM and HC, was unexpected.

With a single-shell and low *b*-value acquisition, AMURA shows itself as a method complementary to DTI, as reflected by the results from the TBSS analysis (Figure 9B). On the one hand, DTI-based AD and MD showed a good performance for the comparison between EM and CM, with a great number of ROIs with statistically significant differences, while AMURA-based measures detected equivalent but a lower number of differences. On the other hand, in the comparison between EM and HC, differences were only found using AMURA-based measures, and in a relatively large number of ROIs. The reason of these differences may be that both techniques represent changes associated with diverse pathophysiological mechanisms, as shown in the example with synthetic data, where only AMURA was able to identify changes of the free water fraction. Further studies on disorders with better characterized pathophysiology than migraine must be carried out to understand the different sensitivity to varied biological processes of DTI and AMURA.

Regarding the behavior of the DTI and AMURA measures in the synthetic experiment for diverse free water fractions, some AMURA parameters showed higher sensitivity to the free water changes. For constant FA, qMSD, $\Upsilon^{1/2}$, and RTOP presented higher changes for small changes of the free water fraction than the MD, while DiA and APA remained constant. For constant MD, DiA and FA showed similar changes and the APA showed higher changes than the FA, without constant values of any AMURA parameter. These results suggest that AMURA can better determine differences caused by changes of free water fraction in comparison with DTI, as some parameters presented higher sensitivity. Therefore, the consequence would be that AMURA measures may be able to find subtler differences between clinical groups compared to DTI, in line with previously reported results in migraine (Planchuelo-Gómez et al., 2020c).

The complementary nature of DTI- and AMURA-based measures is confirmed by the ROI-based analysis (Table 2 and Figure 9A). In the comparison between CM and EM, for instance, the MD was the metric that detected a higher number of regions

with statistically significant differences, but there were some ROIs with differences exclusively identified by one or more AMURA-based measures (e.g., the PCT). In the same way, there were ROIs with differences exclusively found with the MD or AD (e.g., the SS-R), and ROIs with differences identified by both DTI- and AMURA-based measures (e.g., the EC-L).

If we focus on those regions selected in Figure 3 (PCT, ICP-R, and EC-R) we can better understand what is happening with the behavior of the distribution of the different metrics inside the selected ROIs. First, let us focus on the anisotropy measures, FA, APA, and DiA. According to Table 2, there are no differences between groups for the FA for any of the three ROIs. On the other hand, APA and DiA reflected differences for EM vs. HC (for the three ROIs), for EM vs. CM (in the PCT) and CM vs. HC (both in EC-R). These results are confirmed by the boxplots in Figure 3, where AMURA-anisotropy measures were able to better separate the three groups. It is of interest to note that when migraine is considered as a single set, results are more similar for the three metrics, confirming that anisotropy differences between controls are migraine were really present. Regarding the other metrics, AD and MD were able to find significant differences in most cases for the three ROIs, according to Figure 3. However, AMURA metrics always find the same differences but with a greater size effect. As an example of this, we can focus on the PCT for EM vs. HC, where we can see that all the metrics succeed in finding differences but with different effect sizes.

All in all, from the results in Table 2 and Figure 3, we can see that the behavior of AMURA and DTI is similar, although MD and AD showed a lower variance for the CM group. The separation between the groups follows very similar trends within the three ROIs considered. However, AMURA manages to better find these existing differences, and with a larger effect size.

The sensitivity of AMURA-based measures was analyzed by further comparing the effect size found in the different comparisons between groups. A classical method to determine the magnitude of the differences between groups is Cohen's D, which considers the variability of the sample in relation to the average value. As illustrated in Figures 4, 5, DTI-based and AMURA-based measures showed comparable effect sizes for the EM-CM and CM-HC comparisons. In the first case, DTI-based AD and MD reached medium effect sizes (0.5; for the whole WM), while Cohen's D for FA barely exceeded small effect size threshold (0.2). For this last comparison, Cohen's D for AMURA-based measures varied between the small and the medium effect thresholds. For the comparison between CM and EM, however, Cohen's *D*-values were notably lower for all measures, barely reaching 0.3 for DTI-based AD. Finally, regarding the comparison between EM and HC, while DTI-based FA and MD reached Cohen's *D*-values around 0.3, AMURA-based RTOP, qMSD, and DIA reached values over 0.5. These differences in effect sizes among different measures and different group comparisons offer a good explanation for the results shown in Table 2 and Figure 9.

Whereas it may be tempting to think about EM and CM as different degrees of the same pathological process, recent results (Coppola et al., 2020; Planchuelo-Gómez et al., 2020a) support the hypothesis of EM and CM being different entities at the microstructural level, each accompanied by different changes in the WM. Following this hypothesis, DTI-based measures seem well-fitted to detect WM changes in CM, while AMURA-based methods perform remarkably well for the changes that occur in EM. Although the interpretation of changes in DTI or AMURA-based measures is not straightforward, results suggest that WM changes in EM with respect to HC (specifically, lower RTOP and RTAP) might be related to changes in the transverse diffusivity, while changes in CM with respect to EM (such as higher RTPP and lower AD) might be more related to changes in the diffusivity in the axonal or main direction. As previously stated, the complementary use of DTI and AMURA may be useful to detect changes of different nature using data obtained with a low *b*-value and single-shell acquisition. The specific pathophysiological mechanisms related to changes of diverse essence in AMURA must be assessed in future studies.

Considering the difficulty to obtain large sample sizes in group studies, it is important to assess the behavior of the diverse diffusion measures when the number of subjects per group is reduced. As depicted in Figure 6, both DTI-based and AMURA-based measures shared the expected trend, meaning that the number of ROIs with statistically significant differences decreases as the sample size is reduced. However, as shown in the experiment in Figure 7, when the number of samples is reduced to half, DTI metrics were no longer able to detect the differences between groups in most ROIs, whereas AMURA could. From the 13 ROIs considered in the experiment, DTI lost 11 of them when reducing the sample size, while AMURA only lost 2 of them. This effect favors the usage of AMURA metrics in studies with a small sample size.

The assessment of the stability provides another interesting perspective for the evaluation and comparison between different diffusion measures. The diffusion measures that showed higher stability (lower CQV) were AMURA-based APA and RTPP, and the DTI-based measures, while AMURA-based qMSD seems to present low stability. This high variability was expected, since qMSD is a quadratic measure, so it must show a greater range of variability. Interestingly, it presented a relatively high number of regions with statistically significant differences in the comparisons of both migraine groups against controls for diverse sample sizes despite their low stability. Therefore, the results of this study suggest that qMSD is able to characterize specific microstructural properties that are particularly difficult to find with other parameters. Moreover, as it has been suggested previously in this section, differences between both groups of patients with migraine and controls may be qualitatively distinct compared to the differences between CM and EM. Furthermore, qMSD is especially sensitive to short diffusion time scales (Ning et al., 2015).

It is important to note that the AMURA-based measures employed in this paper must be considered as apparent values at a given *b*-value, and their interpretation in terms of the microstructure properties may be different from that of the original EAP-based diffusion measures. Although the relationship between AMURA-based measures and their original counterparts deserves further study, in this paper we deliberately chose not to pursue this comparison to focus on the viability of AMURA-based measures to complement DTI in scenarios where EAP-based measures cannot be obtained.

This study presents limitations that must be pointed out. First, the pathophysiological interpretation of the different trends of the AMURA-based measures is not totally clear, so a description of the microstructural properties according to the values of each measure cannot be provided. As mentioned previously, the apparent nature of AMURA-based measures and their complex relationship with the original EAP-based measures prevent the direct adoption of interpretations from those EAP-based measures. Microstructural studies like those conducted for DTI-based measures (Alexander et al., 2007; Winklewski et al., 2018) are needed to fully understand the results obtained with AMURA.

Furthermore, the results obtained in this study cannot be directly translated to other pathologies affecting the WM of the brain. Even though AMURA can be expected to be a useful information to detect differences in group studies targeting other diseases, further research is needed to confirm that.

In conclusion, this study showed that the new AMURA-based measures can be easily integrated in group studies using single-shell dMRI acquisition protocols, and they can reveal WM changes that may remain hidden with traditional DT-based measures. The wide variety of AMURA, a fast and relatively simple approach, provides measures that allow to extract values that are able to find differences between groups for restricted sample sizes and dMRI acquisition protocols.

Data availability statement

The datasets used for this study belong to Hospital Clínico Universitario (Valladolid) and cannot be made public. Researchers may request access to them by contacting the corresponding author. Requests to access these datasets should be directed to sanaja@tel.uva.es.

Ethics statement

The studies involving human participants were reviewed and approved by Comité Ético, Hospital Clínico Universitario de Valladolid. The patients/participants provided their written informed consent to participate in this study.

Author contributions

CM-M: validation, formal analysis, investigation, writing—original draft, and writing—review and editing. ÁP-G: methodology, validation, formal analysis, investigation, data curation, writing—original draft, and writing—review and editing. ÁG and DG-A: methodology and validation. AT-V: methodology, validation, formal analysis, supervision, project administration, and funding acquisition. RL-G: methodology, validation, formal analysis, investigation, writing—original draft, supervision, project administration, and funding acquisition. SA-F: conceptualization, methodology, software, validation, formal analysis, investigation, writing—original draft, writing—review and editing, supervision, project administration, and funding acquisition. All authors contributed to the article and approved the submitted version.

Funding

This work was supported by Ministerio de Ciencia e Innovación PID2021-124407NB-I00 and TED2021-130758B-I00, funded by MCIN/AEI/10.13039/501100011033 and the European Union NextGenerationEU/PRTR, being MCIN: Ministerio de Ciencia e Innovación; AEI: Agencia Estatal de Investigación (with doi: 10.13039/501100011033); and PRTR: Plan de Recuperación, Transformación y Resiliencia. CM-M was funded by the Junta de Castilla y León and Fondo Social Europeo Plus (FSE+). ÁP-G was funded by the European Union - NextGenerationEU.

Conflict of interest

The authors declare that the research was conducted in the absence of any commercial or financial relationships that could be construed as a potential conflict of interest.

Publisher's note

Supplementary material

The Supplementary Material for this article can be found online at: https://www.frontiersin.org/articles/10.3389/fnins.2023.1106350/full#supplementary-material

References

Aja-Fernández, S., de Luis-García, R., Afzali, M., Molendowska, M., Pieciak, T., and Tristán-Vega, A. (2020). Micro-structure diffusion scalar measures from reduced MRI acquisitions. *PLoS ONE* 15:e0229526. doi: 10.1371/journal.pone.0229526

Aja-Fernández, S., Pieciak, T., Martín-Martín, C., Planchuelo-Gómez, Á., de Luis-García, R., and Tristán-Vega, A. (2022). Moment-based representation of the diffusion inside the brain from reduced DMRI acquisitions: Generalized AMURA. *Med. Image Anal.* 77:102356. doi: 10.1016/j.media.2022.102356

Aja-Fernández, S., Tristán-Vega, A., and Jones, D. K. (2021). Apparent propagator anisotropy from single-shell diffusion MRI acquisitions. *Magn. Reson. Med.* 85, 2869–2881. doi: 10.1002/mrm.28620

Alexander, A. L., Lee, J. E., Lazar, M., and Field, A. S. (2007). Diffusion tensor imaging of the brain. *Neurotherapeutics* 4, 316–329. doi: 10.1016/j.nurt.2007.05.011

Alexander, D. C. (2008). A general framework for experiment design in diffusion MRI and its application in measuring direct tissue-microstructure features. *Magn. Reson. Med*. 60, 439–448. doi: 10.1002/mrm.21646

Altunkaynak, B., and Gamgam, H. (2019). Bootstrap confidence intervals for the coefficient of quartile variation. *Commun. Stat. Simul. Comput*. 48, 2138–2146. doi: 10.1080/03610918.2018.1435800

Andersson, J. L., and Sotiropoulos, S. N. (2016). An integrated approach to correction for off-resonance effects and subject movement in diffusion MR imaging. *Neuroimage* 125, 1063–1078. doi: 10.1016/j.neuroimage.2015.10.019

Assemlal, H.-E., Tschumperlé, D., Brun, L., and Siddiqi, K. (2011). Recent advances in diffusion MRI modeling: angular and radial reconstruction. *Med. Image Anal*. 15, 369–396. doi: 10.1016/j.media.2011.02.002

Avram, A. V., Sarlls, J. E., Barnett, A. S., Özarslan, E., Thomas, C., Irfanoglu, M. O., et al. (2016). Clinical feasibility of using mean apparent propagator (MAP) MRI to characterize brain tissue microstructure. *NeuroImage* 127, 422–434. doi: 10.1016/j.neuroimage.2015.11.027

Basser, P. J., and Jones, D. K. (2002). Diffusion-tensor MRI: theory, experimental design and data analysis-a technical review. *NMR Biomed*. 15, 456–467. doi: 10.1002/nbm.783

Basser, P. J., Mattiello, J., and LeBihan, D. (1994). MR diffusion tensor spectroscopy and imaging. *Biophys. J*. 66, 259–267. doi: 10.1016/S0006-3495(94)80775-1

Bette, S., Huber, T., Wiestler, B., Boeckh-Behrens, T., Gempt, J., Ringel, F., et al. (2016). Analysis of fractional anisotropy facilitates differentiation of glioblastoma and brain metastases in a clinical setting. *Eur. J. Radiol*. 85, 2182–2187. doi: 10.1016/j.ejrad.2016.10.002

Boscolo Galazzo, I., Brusini, L., Obertino, S., Zucchelli, M., Granziera, C., and Menegaz, G. (2018). On the viability of diffusion MRI-based microstructural biomarkers in ischemic stroke. *Front. Neurosci*. 12:92. doi: 10.3389/fnins.2018.00092

Brusini, L., Obertino, S., Galazzo, I. B., Zucchelli, M., Krueger, G., Granziera, C., et al. (2016). Ensemble average propagator-based detection of microstructural alterations after stroke. *Int. J. Comput. Assist. Radiol. Surg*. 11, 1585–1597. doi: 10.1007/s11548-016-1442-z

Chong, C. D., and Schwedt, T. J. (2015). Migraine affects white-matter tract integrity: a diffusion-tensor imaging study. *Cephalalgia* 35, 1162–1171. doi: 10.1177/0333102415573513

Coppola, G., Di Renzo, A., Tinelli, E., Petolicchio, B., Di Lorenzo, C., Parisi, V., et al. (2020). Patients with chronic migraine without history of medication overuse are characterized by a peculiar white matter fiber bundle profile. *J. Headache Pain* 21, 1–8. doi: 10.1186/s10194-020-01159-6

Descoteaux, M., Deriche, R., Le Bihan, D., Mangin, J.-F., and Poupon, C. (2011). Multiple q-shell diffusion propagator imaging. *Med. Image Anal*. 15, 603–621. doi: 10.1016/j.media.2010.07.001

Dhollander, T., Raffelt, D., and Connelly, A. (2016). "Unsupervised 3-tissue response function estimation from single-shell or multi-shell diffusion MR data without a co-registered T1 image," in *ISMRM Workshop on Breaking the Barriers of Diffusion MRI, Vol. 5* (Lisbon).

Fick, R. H., Wassermann, D., Caruyer, E., and Deriche, R. (2016). MAPL: tissue microstructure estimation using Laplacian-regularized MAP-MRI and its application to HCP data. *NeuroImage* 134, 365–385. doi: 10.1016/j.neuroimage.2016.03.046

Fick, R. H. J., Pizzolato, M., Wassermann, D., Zucchelli, M., Menegaz, G., and Deriche, R. (2016). "A sensitivity analysis of q-space indices with respect to changes in axonal diameter, dispersion and tissue composition," in *2016 IEEE 13th International Symposium on Biomedical Imaging (ISBI)*, 1241–1244. doi: 10.1109/ISBI.2016.7493491

Galbán, C., Hoff, B., Chenevert, T., and Ross, B. (2017). Diffusion MRI in early cancer therapeutic response assessment. *NMR Biomed*. 30:e3458. doi: 10.1002/nbm.3458

Gomez-Beldarrain, M., Oroz, I., Zapirain, B. G., Ruanova, B. F., Fernandez, Y. G., Cabrera, A., et al. (2016). Right fronto-insular white matter tracts link cognitive reserve and pain in migraine patients. *J. Headache Pain* 17, 1–12. doi: 10.1186/s10194-016-0593-1

Goveas, J., O'Dwyer, L., Mascalchi, M., Cosottini, M., Diciotti, S., De Santis, S., et al. (2015). Diffusion-MRI in neurodegenerative disorders. *Magn. Reson. Imag*. 33, 853–876. doi: 10.1016/j.mri.2015.04.006

Herbert, E., Engel-Hills, P., Hattingh, C., Fouche, J.-P., Kidd, M., Lochner, C., et al. (2018). Fractional anisotropy of white matter, disability and blood iron parameters in multiple sclerosis. *Metab. Brain Dis*. 33, 545–557. doi: 10.1007/s11011-017-0171-5

Hosseinbor, A. P., Chung, M. K., Wu, Y.-C., and Alexander, A. L. (2013). Bessel Fourier orientation reconstruction (BFOR): an analytical diffusion propagator reconstruction for hybrid diffusion imaging and computation of q-space indices. *NeuroImage* 64, 650–670. doi: 10.1016/j.neuroimage.2012.08.072

Ito, K., Kudo, M., and Sasaki, M. (2016). Detection of changes in the periaqueductal gray matter of patients with episodic migraine using quantitative diffusion kurtosis imaging: preliminary findings. *Neuroradiology* 58, 115–120. doi: 10.1007/s00234-015-1603-8

Jenkinson, M., Beckmann, C. F., Behrens, T. E., Woolrich, M. W., and Smith, S. M. (2012). FSL. *Neuroimage* 62, 782–790. doi: 10.1016/j.neuroimage.2011.09.015

Kochunov, P., Williamson, D., Lancaster, J., Fox, P., Cornell, J., Blangero, J., et al. (2012). Fractional anisotropy of water diffusion in cerebral white matter across the lifespan. *Neurobiol. Aging* 33, 9–20. doi: 10.1016/j.neurobiolaging.2010.01.014

Mekkaoui, C., Reese, T. G., Jackowski, M. P., Bhat, H., and Sosnovik, D. E. (2017). Diffusion MRI in the heart. *NMR Biomed*. 30:e3426. doi: 10.1002/nbm.3426

Messina, R., Rocca, M. A., Colombo, B., Pagani, E., Falini, A., Comi, G., et al. (2015). White matter microstructure abnormalities in pediatric migraine patients. *Cephalalgia* 35, 1278–1286. doi: 10.1177/0333102415578428

Mole, J. P., Subramanian, L., Bracht, T., Morris, H., Metzler-Baddeley, C., and Linden, D. E. (2016). Increased fractional anisotropy in the motor tracts of Parkinson's disease suggests compensatory neuroplasticity or selective neurodegeneration. *Eur. Radiol*. 26, 3327–3335. doi: 10.1007/s00330-015-4178-1

Neeb, L., Bastian, K., Villringer, K., Gits, H. C., Israel, H., Reuter, U., et al. (2015). No microstructural white matter alterations in chronic and episodic migraineurs: a case-control diffusion tensor magnetic resonance imaging study. *Headache* 55, 241–251. doi: 10.1111/head.12496

Nichols, T., and Holmes, A. P. (2002). Nonparametric permutation tests for functional neuroimaging: a primer with examples. *Hum. Brain Mapp*. 15, 1–25. doi: 10.1002/hbm.1058

Ning, L., Westin, C.-F., and Rathi, Y. (2015). Estimating diffusion propagator and its moments using directional radial basis functions. *IEEE Trans. Med. Imag*. 34, 2058–2078. doi: 10.1109/TMI.2015.2418674

Novikov, D. S., Fieremans, E., Jespersen, S. N., and Kiselev, V. G. (2019). Quantifying brain microstructure with diffusion MRI: theory and parameter estimation. *NMR Biomed*. 32:e3998. doi: 10.1002/nbm.3998

Oishi, K., Zilles, K., Amunts, K., Faria, A., Jiang, H., Li, X., et al. (2008). Human brain white matter atlas: identification and assignment of common anatomical structures in superficial white matter. *Neuroimage* 43, 447–457. doi: 10.1016/j.neuroimage.2008.07.009

Özarslan, E., Koay, C. G., Shepherd, T. M., Komlosh, M. E., İrfanoğlu, M. O., Pierpaoli, C., et al. (2013). Mean apparent propagator (MAP) MRI: a novel diffusion imaging method for mapping tissue microstructure. *NeuroImage* 78, 16–32. doi: 10.1016/j.neuroimage.2013.04.016

Pelletier, A., Periot, O., Dilharreguy, B., Hiba, B., Bordessoules, M., Chanraud, S., et al. (2016). Age-related modifications of diffusion tensor imaging parameters and white matter hyperintensities as inter-dependent processes. *Front. Aging Neurosci*. 7:255. doi: 10.3389/fnagi.2015.00255

Planchuelo-Gómez, Á., García-Azorín, D., Guerrero, Á. L., Aja-Fernández, S., Rodríguez, M., and de Luis-García, R. (2020a). Structural connectivity alterations in chronic and episodic migraine: a diffusion magnetic resonance imaging connectomics study. *Cephalalgia* 40, 367–383. doi: 10.1177/0333102419885392

Planchuelo-Gómez, Á., García-Azorín, D., Guerrero, Á. L., Aja-Fernández, S., Rodríguez, M., and de Luis-García, R. (2020b). White matter changes in chronic and episodic migraine: a diffusion tensor imaging study. *J. Headache Pain* 21, 1–15. doi: 10.1186/s10194-019-1071-3

Planchuelo-Gómez, Á., García-Azorín, D., Guerrero, Á. L., de Luis-García, R., Rodríguez, M., and Aja-Fernández, S. (2020c). Alternative microstructural measures to complement diffusion tensor imaging in migraine studies with standard MRI acquisition. *Brain Sci*. 10:711. doi: 10.3390/brainsci10100711

Rovaris, M., Gass, A., Bammer, R., Hickman, S. J., Ciccarelli, O., Miller, D. H., et al. (2005). Diffusion MRI in multiple sclerosis. *Neurology* 65, 1526–1532. doi: 10.1212/01.wnl.0000184471.83948.e0

Shibata, Y., Ishiyama, S., and Matsushita, A. (2018). White matter diffusion abnormalities in migraine and medication overuse headache: a 1.5-t tract-based spatial statistics study. *Clin. Neurol. Neurosurg*. 174, 167–173. doi: 10.1016/j.clineuro.2018.09.022

Smith, S. M., Jenkinson, M., Woolrich, M. W., Beckmann, C. F., Behrens, T. E., Johansen-Berg, H., et al. (2004). Advances in functional and structural MR image analysis and implementation as FSL. *Neuroimage* 23, S208–S219. doi: 10.1016/j.neuroimage.2004.07.051

Smith, S. M., and Nichols, T. E. (2009). Threshold-free cluster enhancement: addressing problems of smoothing, threshold dependence and localisation in cluster inference. *Neuroimage* 44, 83–98. doi: 10.1016/j.neuroimage.2008.03.061

Tournier, J.-D., Smith, R., Raffelt, D., Tabbara, R., Dhollander, T., Pietsch, M., et al. (2019). MRtrix3: A fast, flexible and open software framework for medical image processing and visualisation. *Neuroimage* 202:116137. doi: 10.1016/j.neuroimage.2019.116137

Tristán-Vega, A., and Aja-Fernández, S. (2021). Efficient and accurate EAP imaging from multi-shell dMRI with micro-structure adaptive convolution

kernels and dual Fourier integral transforms (MiSFIT). *NeuroImage* 227:117616. doi: 10.1016/j.neuroimage.2020.117616

Tristán-Vega, A., París, G., de Luis-García, R., and Aja-Fernández, S. (2022). Accurate free-water estimation in white matter from fast diffusion MRI acquisitions using the spherical means technique. *Magn. Reson. Med*. 87, 1028–1035. doi: 10.1002/mrm.28997

Veraart, J., Novikov, D. S., Christiaens, D., Ades-Aron, B., Sijbers, J., and Fieremans, E. (2016). Denoising of diffusion MRI using random matrix theory. *Neuroimage* 142, 394–406. doi: 10.1016/j.neuroimage.2016.08.016

Wedeen, V. J., Hagmann, P., Tseng, W.-Y. I., Reese, T. G., and Weisskoff, R. M. (2005). Mapping complex tissue architecture with diffusion spectrum magnetic resonance imaging. *Magn. Reson. Med*. 54, 1377–1386. doi: 10.1002/mrm.20642

Westin, C.-F., Maier, S. E., Mamata, H., Nabavi, A., Jolesz, F. A., and Kikinis, R. (2002). Processing and visualization for diffusion tensor MRI. *Med. Image Anal*. 6, 93–108. doi: 10.1016/S1361-8415(02)00053-1

Winklewski, P. J., Sabisz, A., Naumczyk, P., Jodzio, K., Szurowska, E., and Szarmach, A. (2018). Understanding the physiopathology behind axial and radial diffusivity changes-what do we know? *Front. Neurol*. 9:92. doi: 10.3389/fneur.2018.00092

Wu, Y.-C., Field, A. S., and Alexander, A. L. (2008). Computation of diffusion function measures in q-space using magnetic resonance hybrid diffusion imaging. *IEEE Trans. Med. Imaging* 27, 858–865. doi: 10.1109/TMI.2008.922696

Zhang, Y., Brady, M., and Smith, S. (2001). Segmentation of brain MR images through a hidden Markov random field model and the expectation-maximization algorithm. *IEEE Trans. Med. Imaging* 20, 45–57. doi: 10.1109/42.906424

Zucchelli, M., Brusini, L., Méndez, C. A., Daducci, A., Granziera, C., and Menegaz, G. (2016). What lies beneath? Diffusion EAP-based study of brain tissue microstructure. *Med. Image Anal*. 32, 145–156. doi: 10.1016/j.media.2016.03.008

frontiers | Frontiers in Neuroscience

TYPE Erratum
PUBLISHED 09 June 2023
DOI 10.3389/fnins.2023.1228337

OPEN ACCESS

APPROVED BY
Frontiers Editorial Office,
Frontiers Media SA, Switzerland

*CORRESPONDENCE
Frontiers Production Office
production.office@frontiersin.org

RECEIVED 24 May 2023
ACCEPTED 24 May 2023
PUBLISHED 09 June 2023

CITATION
Frontiers Production Office (2023) Erratum: Viability of AMURA biomarkers from single-shell diffusion MRI in clinical studies.
Front. Neurosci. 17:1228337.
doi: 10.3389/fnins.2023.1228337

Erratum: Viability of AMURA biomarkers from single-shell diffusion MRI in clinical studies

Frontiers Production Office*

Frontiers Media SA, Lausanne, Switzerland

KEYWORDS

alternative metrics, AMURA, brain, diffusion magnetic resonance imaging, DTI, migraine

An Erratum on
Viability of AMURA biomarkers from single-shell diffusion MRI in clinical studies

by Martín-Martín, C., Planchuelo-Gómez, Á., Guerrero, Á. L., García-Azorín, D., Tristán-Vega, A., de Luis-García, R., and Aja-Fernández, S. (2023) *Front. Neurosci.* 17:1106350. doi: 10.3389/fnins.2023.1106350

Due to a production error, there was a mistake in Figure 4 and Figure 9 as published. Figure 4 had a formatting issue and part of Figure 9B was missing. The corrected Figure 4 and Figure 9 appear below.

The publisher apologizes for this mistake. The original article has been updated.

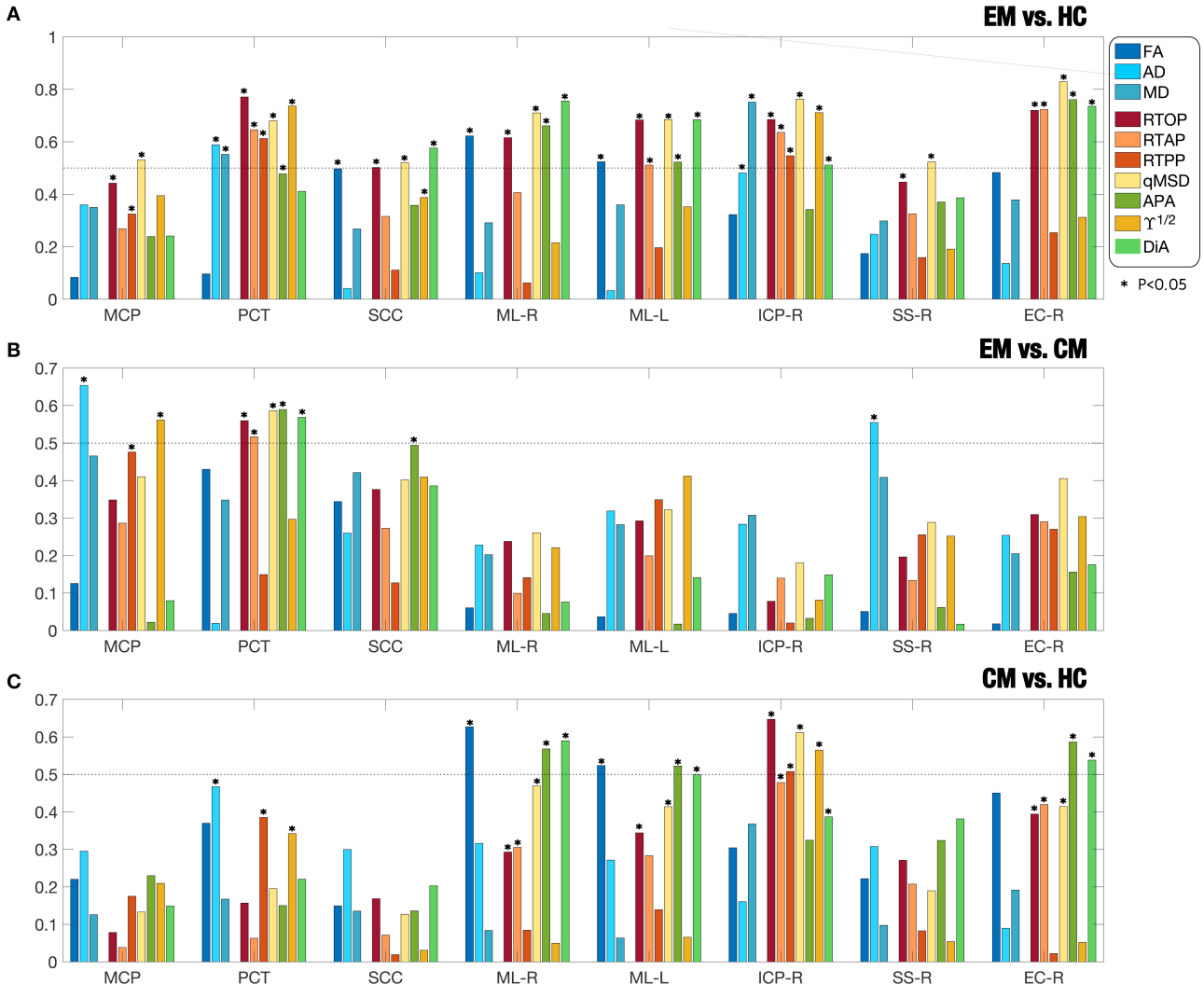
A
EM vs. HC
FA
AD
MD
RTOP
RTAP
RTPP
qMSD
APA
$\Upsilon^{1/2}$
DiA
* P<0.05
MCP
PCT
SCC
ML-R
ML-L
ICP-R
SS-R
EC-R
B
EM vs. CM
C
CM vs. HC

FIGURE 4

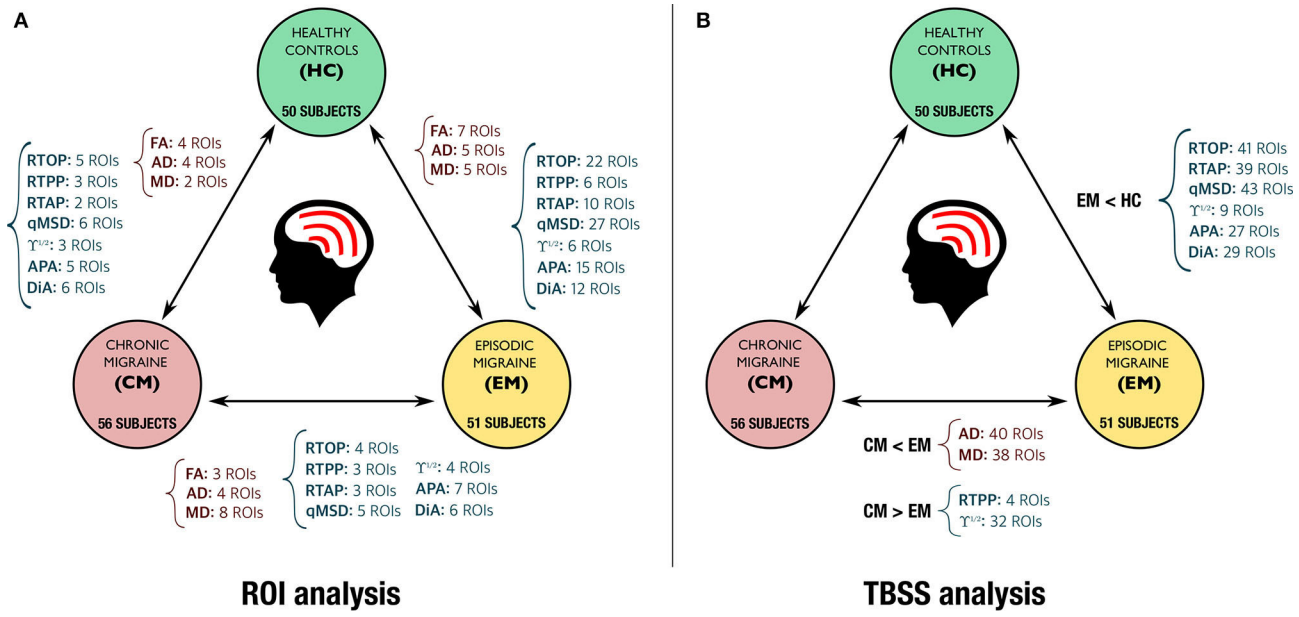
A
HEALTHY CONTROLS (HC) 50 SUBJECTS
CHRONIC MIGRAINE (CM) 56 SUBJECTS
EPISODIC MIGRAINE (EM) 51 SUBJECTS
RTOP: 5 ROIs
RTPP: 3 ROIs
RTAP: 2 ROIs
qMSD: 6 ROIs
ϒ1/2: 3 ROIs
APA: 5 ROIs
DiA: 6 ROIs
FA: 4 ROIs
AD: 4 ROIs
MD: 2 ROIs
FA: 7 ROIs
AD: 5 ROIs
MD: 5 ROIs
RTOP: 22 ROIs
RTPP: 6 ROIs
RTAP: 10 ROIs
qMSD: 27 ROIs
ϒ1/2: 6 ROIs
APA: 15 ROIs
DiA: 12 ROIs
FA: 3 ROIs
AD: 4 ROIs
MD: 8 ROIs
RTOP: 4 ROIs
RTPP: 3 ROIs
RTAP: 3 ROIs
qMSD: 5 ROIs
ϒ1/2: 4 ROIs
APA: 7 ROIs
DiA: 6 ROIs
ROI analysis
B
HEALTHY CONTROLS (HC) 50 SUBJECTS
CHRONIC MIGRAINE (CM) 56 SUBJECTS
EPISODIC MIGRAINE (EM) 51 SUBJECTS
EM < HC
RTOP: 41 ROIs
RTAP: 39 ROIs
qMSD: 43 ROIs
ϒ1/2: 9 ROIs
APA: 27 ROIs
DiA: 29 ROIs
CM < EM
AD: 40 ROIs
MD: 38 ROIs
CM > EM
RTPP: 4 ROIs
ϒ1/2: 32 ROIs
TBSS analysis

FIGURE 9

frontiers | Frontiers in Neuroscience

TYPE Methods
PUBLISHED 11 August 2023
DOI 10.3389/fnins.2023.1209521

OPEN ACCESS

EDITED BY
Itamar Ronen,
Brighton and Sussex Medical School,
United Kingdom

REVIEWED BY
Yogesh Rathi,
Harvard Medical School, United States
Yuliya S. Nikolova,
University of Toronto, Canada
Diana Valdes Cabrera, University of Toronto,
Canada in collaboration with reviewer YN

*CORRESPONDENCE
Erick J. Canales-Rodríguez
✉ erick.canalesrodriguez@epfl.ch

†These authors share last authorship

RECEIVED 20 April 2023
ACCEPTED 24 July 2023
PUBLISHED 11 August 2023

CITATION
Barakovic M, Pizzolato M, Tax CMW, Rudrapatna U, Magon S, Dyrby TB, Granziera C, Thiran J-P, Jones DK and Canales-Rodríguez EJ (2023) Estimating axon radius using diffusion-relaxation MRI: calibrating a surface-based relaxation model with histology.
Front. Neurosci. 17:1209521.
doi: 10.3389/fnins.2023.1209521

Estimating axon radius using diffusion-relaxation MRI: calibrating a surface-based relaxation model with histology

Muhamed Barakovic[1,2,3,4,5], Marco Pizzolato[6], Chantal M. W. Tax[3,7], Umesh Rudrapatna[3], Stefano Magon[5], Tim B. Dyrby[6,8], Cristina Granziera[1,2,9], Jean-Philippe Thiran[4,10,11], Derek K. Jones[3†] and Erick J. Canales-Rodríguez[4*†]

[1]Translational Imaging in Neurology (ThINk) Basel, Department of Biomedical Engineering, University Hospital Basel and University of Basel, Basel, Switzerland, [2]Department of Neurology, University Hospital Basel, Basel, Switzerland, [3]Cardiff University Brain Research Imaging Centre, Cardiff University, Cardiff, Wales, United Kingdom, [4]Signal Processing Laboratory 5 (LTS5), Ecole Polytechnique Fédérale de Lausanne (EPFL), Lausanne, Switzerland, [5]Roche Pharma Research and Early Development, Neuroscience and Rare Diseases, Roche Innovation Center, Basel, Switzerland, [6]Department of Applied Mathematics and Computer Science, Technical University of Denmark, Kongens Lyngby, Denmark, [7]Image Sciences Institute, University Medical Center Utrecht, Utrecht, Netherlands, [8]Danish Research Centre for Magnetic Resonance (DRCMR), Centre for Functional and Diagnostic Imaging and Research, Copenhagen University Hospital Amager and Hvidovre, Copenhagen, Denmark, [9]Research Center for Clinical Neuroimmunology and Neuroscience Basel (RC2NB), University Hospital Basel and University of Basel, Basel, Switzerland, [10]Radiology Department, Centre Hospitalier Universitaire Vaudois and University of Lausanne, Lausanne, Switzerland, [11]Centre d'Imagerie Biomédicale (CIBM), EPFL, Lausanne, Switzerland

Axon radius is a potential biomarker for brain diseases and a crucial tissue microstructure parameter that determines the speed of action potentials. Diffusion MRI (dMRI) allows non-invasive estimation of axon radius, but accurately estimating the radius of axons in the human brain is challenging. Most axons in the brain have a radius below one micrometer, which falls below the sensitivity limit of dMRI signals even when using the most advanced human MRI scanners. Therefore, new MRI methods that are sensitive to small axon radii are needed. In this proof-of-concept investigation, we examine whether a surface-based axonal relaxation process could mediate a relationship between intra-axonal T_2 and T_1 times and inner axon radius, as measured using postmortem histology. A unique *in vivo* human diffusion-T_1-T_2 relaxation dataset was acquired on a 3T MRI scanner with ultra-strong diffusion gradients, using a strong diffusion-weighting (i.e., b = 6,000 s/mm^2) and multiple inversion and echo times. A second reduced diffusion-T_2 dataset was collected at various echo times to evaluate the model further. The intra-axonal relaxation times were estimated by fitting a diffusion-relaxation model to the orientation-averaged spherical mean signals. Our analysis revealed that the proposed surface-based relaxation model effectively explains the relationship between the estimated relaxation times and the histological axon radius measured in various corpus callosum regions. Using these histological values, we developed a novel calibration approach to predict axon radius in other areas of the corpus callosum. Notably, the predicted radii and those determined from histological measurements were in close agreement.

KEYWORDS

brain, axon radius, diffusion MRI, T_2 relaxation, T_1 relaxation, histology

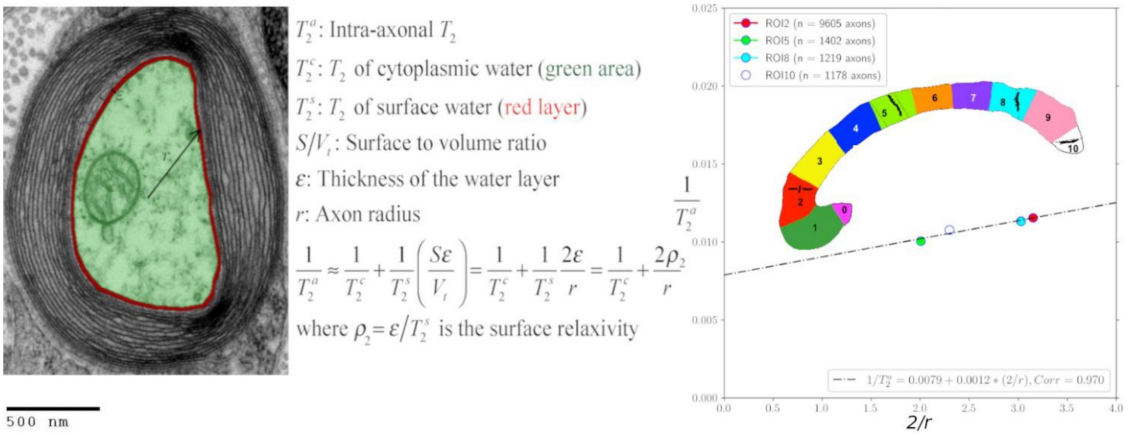

GRAPHICAL ABSTRACT
Surface-based relaxation model to predict axon radius.

Highlights

- Diffusion-relaxation MRI data were acquired using a high *b*-value acquisition.
- A diffusion-relaxation model to estimate the intra-axonal T_2 and T_1 was proposed.
- The histological inner axon radius modulated the estimated relaxation times.
- A surface-based relaxation model predicted the axon radius in the corpus callosum.
- The predicted axon radii agreed with the mean effective histological radius.

1. Introduction

The speed of action potentials along axons is partly determined by their radii (Goldstein and Rall, 1974). Axon radius explains the biggest variance in conduction speed, as demonstrated by previous studies (Hursh, 1939), with larger axons conducting faster than those with smaller radii (Waxman and Bennett, 1972; Costa et al., 2018; Drakesmith et al., 2019). Therefore, accurately measuring axon radii *in vivo* is essential for better understanding the neural mechanisms underlying brain function and their impact on diseases.

The diffusion Magnetic Resonance Imaging (dMRI) signal is sensitive to axon radii if strong diffusion encoding gradients (i.e., up to 300 mT/m in Connectom scanners (Jones et al., 2018) and 1,500 mT/m in animal preclinical scanners) are used (Assaf et al., 2004, 2008; Assaf and Basser, 2005; Alexander, 2008; Dyrby et al., 2013; Duval et al., 2015; De Santis et al., 2016; Veraart et al., 2020; Barakovic et al., 2021a). However, the main limitation of this approach is that the dMRI signals from axons with radii smaller than ~1–2 μm are practically indistinguishable from each other, even when the most advanced human Connectom scanners with ultra-strong (300 mT/m) gradients are employed in the data acquisition (Nilsson et al., 2017). Today, the challenge is that the peak of the axon radius distribution per voxel is below one micrometer in most brain regions, as observed in histology. Hence, most axon radii are below the lower bound for detection (Edgar and Griffiths, 2014; Dyrby et al., 2018). For an overview of the different strategies that have been employed to measure axon radius with dMRI, the reader is referred to Assaf and Basser (2005), Assaf et al. (2008, 2013), Alexander et al. (2010, 2019) Dyrby et al. (2013, 2018), Novikov et al. (2019), Fan et al. (2020), Jelescu et al. (2020), Veraart et al. (2020), Barakovic et al. (2021a), Pizzolato et al. (2023).

Theoretical reasons explain the lower sensitivity of dMRI to the inner radius of smaller axons. The commonly employed model [i.e., Gaussian phase approximation in the long-pulse limit (van Gelderen et al., 1994)] predicts an intra-axonal dMRI signal attenuation that depends on the fourth power of the radius r. Moreover, since the measured intra-axonal signal per voxel is the sum of all the individual intra-axonal signals weighted by each axon's contribution to the signal (scaling by an extra-factor r^2), larger axons contribute more than smaller axons to the measured signal. After considering these two factors together, an approximate expression for the mean "effective" dMRI-based radius r_{eff} per voxel can be derived, which depends on the higher-order moments of the unknown axon radius distribution. The resulting analytical expression $r_{eff} \approx \left(\langle r^6 \rangle / \langle r^2 \rangle\right)^{\frac{1}{4}}$ (where $\langle\rangle$ denotes the average over the distribution) demonstrates that the estimate is heavily weighted by the right-hand tail of the axon radius distribution (Burcaw et al., 2015; Veraart et al., 2020). Consequently, the estimated mean axon radius is mainly affected by the bigger axons from the fractions of axons larger than the lower bound. This explains why estimations may appear overestimated compared to histology (Alexander et al., 2010; Dyrby et al., 2018).

Finding another source of MRI contrast sensitive to the size of axons smaller than the diffusion resolution limit is essential. Various studies in porous media have demonstrated that the interaction between the water molecules and the confining pore surface reduces the observed transverse T_2 relaxation time (Brownstein and Tarr, 1977). This surface-based relaxation mechanism allows pore size to be estimated (Hurlimann et al., 1994; Slijkerman and Hofman, 1998; Sørland et al., 2007; Mohnke and Hughes, 2014; Müller-Petke et al., 2015). Notably, a similar T_2 relaxation model to predict the size of cells was proposed

previously (Brownstein and Tarr, 1979), and the idea of applying it to estimate the axon radius was suggested by Kaden and Alexander (2013). However, there is a lack of validation studies to demonstrate whether the inner axon radius modulates the intra-axonal relaxation times. This might be explained by the fact that approaches to estimating the intra-axonal relaxation times have only been developed recently (Veraart et al., 2018; McKinnon and Jensen, 2019; Barakovic et al., 2021b; Tax et al., 2021; Pizzolato et al., 2022). Furthermore, to our knowledge, no dataset is available that offers the combined histological information and relaxometry MRI data from the same sample, which are necessary for the estimation and comparison of these parameters.

The dMRI signals arising from the intra-axonal space can be isolated if a sufficiently high b-value is employed (i.e., $b > 4{,}000$ s/mm^2 for *in vivo* data), which significantly attenuates the signal from spins experiencing large displacements (Jensen et al., 2016; McKinnon and Jensen, 2019). As the confining axonal geometry restricts the self-diffusion motion of spins inside axons (assuming a slow exchange between the intra- and extra-axonal spaces), the strongly diffusion-weighted MRI signal should come from the intra-axonal spins. Thus, it is possible to fit a diffusion-relaxation model of intra-axonal relaxation to strongly diffusion-weighted MRI data collected at multiple diffusion gradient directions and different echo times. This approach, combined with taking the spherical mean (orientational average), was employed previously to estimate the mean intra-axonal T_2 time per voxel (McKinnon and Jensen, 2019) and bundle (Barakovic et al., 2021b), unconfounded by fiber orientation effects.

This proof of concept study investigates whether the intra-axonal T_2 and T_1 relaxation times are related to the inner axon radius and whether they can be employed to predict the mean effective radius. To do this, (1) we implemented two acquisition protocols and measured diffusion-T_1-T_2 and diffusion-T_2 weighted MRI data from three healthy volunteers, one of them scanned using both sequences; (2) we employed a diffusion-relaxation model to enable the estimation of both intra-axonal T_2 and T_1 relaxation times by using the spherical mean signals from the acquired data; (3) we fitted the estimated relaxation times to a surface-based relaxation model that depends on the histological axon radius; (4) using histology from some brain regions we calibrated the surface-based relaxation model to enable predicting axon radius in other brain regions, and (5) we compared the MRI-based estimated axonal radii with those obtained from two postmortem histological human brain datasets in several regions in the midsagittal Corpus Callosum (CC) cross-section. Additional details are provided at the end of the next section.

2. Theory

2.1. Surface-based relaxation model

Inspired by the standard surface-based relaxation model used in porous media (Zimmerman and Brittin, 1957; Brownstein and Tarr, 1979), we propose the following model described in **Figure 1** and Eqs. (1)–(2). We assume that in the intra-axonal space, there are two distinct water pools in fast exchange (Zimmerman and Brittin, 1957): the surface water immediately adjacent to the axonal membrane, e.g., see Le Bihan (2007), and the cytoplasmic water (i.e., axoplasm). The T_2 and T_1 relaxation times of the surface water are shorter because this water layer is in a more ordered state (both spatially and orientationally) than pure water (Halle, 1999; Finney et al., 2004) and the cytoplasmic water, due to the strong water-tissue interactions (Levy and Onuchic, 2004; Zhang et al., 2007). Moreover, the relaxation times of the cytoplasmic water are expected to be smaller than those of pure water and Cerebrospinal fluid because the water molecules in this pool could interact with cytoskeletal elements and a higher number of macromolecules (Beaulieu, 2002). The fast exchange assumption is reasonable if we consider that water molecules, on average, travel distances much larger than the axon radius for typical diffusion and echo times, as employed in this study.

According to the general model provided by Zimmerman and Brittin (1957), the inverse of the observed intra-axonal T_2 can be modeled by the linear combination of the inverse relaxation times of the surface water and the cytoplasmic water pools, weighted by their volume fractions. Although the volume of the surface water layer is much smaller than the total intra-axonal volume, its T_2 time (T_2^s) is much shorter than that of the cytoplasmic water (T_2^c). It thus could have a non-negligible impact on the observed intra-axonal (T_2^a) time. These assumptions are summarized in the following model:

$$\begin{aligned}\frac{1}{T_2^a} &= \frac{V - S\varepsilon}{V}\frac{1}{T_2^c} + \frac{S\varepsilon}{V}\frac{1}{T_2^s} \\ &\approx \frac{1}{T_2^c} + \frac{2\varepsilon}{r}\frac{1}{T_2^s} \\ &= \frac{1}{T_2^c} + \frac{2\rho_2}{r},\end{aligned} \tag{1}$$

where $\rho_2 = \varepsilon / T_2^s$ is the T_2 surface relaxivity; S is the surface area of the axonal membrane; V is the intra-axonal volume; ε is the thickness of the water layer. Note that when assuming a cylindrical axonal geometry, as commonly done in dMRI, the surface-to-volume ratio depends on the inner axon radius, $S/V = 2/r$. An equivalent expression was obtained for the intra-axonal T_1 time.

$$\frac{1}{T_1^a} \approx \frac{1}{T_1^c} + \frac{2\rho_1}{r}, \tag{2}$$

Where $\rho_1 = \varepsilon / T_1^s$ is the longitudinal surface relaxivity.

2.2. Axon radius estimation from intra-axonal relaxation times

By inverting Eqs. (1) or (2) it is possible to predict the inner axon radius from the estimated intra-axonal T_2^a and T_1^a relaxation times, respectively.

$$\begin{aligned} r &\approx \frac{2\rho_2}{\frac{1}{T_2^a} - \frac{1}{T_2^c}}, \\ r &\approx \frac{2\rho_1}{\frac{1}{T_1^a} - \frac{1}{T_1^c}}. \end{aligned} \tag{3}$$

However, this approach requires knowing T_2^c and ρ_2 or T_1^c and ρ_1 in advance. As these parameters are unknown and cannot be

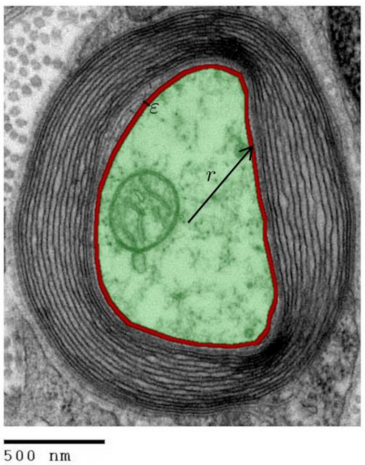

FIGURE 1
Transmission electron micrograph of a myelinated axon (adapted) illustrating the employed relaxation model for the intra-axonal space, composed of two pools (arbitrarily colored in green and red for illustrative purposes) in fast exchange (Zimmerman and Brittin, 1957). This model is equivalent to the Brownstein and Tarr (1977) model in the fast diffusion limit. The structured water (Le Bihan, 2007) adjacent to the inner axon surface (red) has a shorter T_2 than the cytoplasmic water (green). As the cytoplasmic water (i.e., axoplasm) interacts with large proteins, organelles, and cytoskeletal elements (LoPachin et al., 1991; Beaulieu, 2002), its T_2 is shorter than pure water. An equivalent model was assumed for the T_1 relaxation. [This transmission electron micrograph was deposited into the public domain by the Electron Microscopy Facility at Trinity College]. This is a file from the Wikimedia Commons, a collection of freely usable media files, under the terms of the GNU Free Documentation License, Version 1.2 or any later version published by the Free Software Foundation (Source: https://en.wikipedia.org/wiki/File:Myelinated_neuron.jpg). This file is licensed under the Creative Commons Attribution-Share Alike 3.0 Unported license (CC BY-SA 3.0). Any copy and remix of the original file must be distributed under the same or compatible license as the original.

estimated for each brain voxel without additional data, here we propose a histologically-informed calibration approach to calculate them.

The calibration is based on assuming that any dependence of T_2^c or T_1^c on the axon radius, owing to potential changes in the intra-axonal structure with the axon size (e.g., density of proteins, organelles, and cytoskeletal elements), is weak and can be neglected. That is, the dependence of T_2^a and T_1^a on the axon radius is dominated by the surface-to-volume ratio terms in Eqs. (1) and (2). Therefore, we assume that T_2^c, ρ_2, T_1^c and ρ_1 are constant across axons with different sizes. Nevertheless, we noted that the calibration process is equally helpful in predicting axon radius when T_2^c or T_1^c linearly varies with the radius. In that case, the linear models [Eqs. (1) and (2)] can be rewritten in terms of two alternative parameters. For more details, see the discussion subsection "Is the cytoplasmic T_2 constant?"

In this study, we collected *in vivo* diffusion-T_1-T_2 MRI data in a human brain to estimate T_2^a and T_1^a. We employed a reduced diffusion-T_2 relaxation sequence to validate our model further by scanning the same subject and two additional healthy volunteers, which allowed us to estimate T_2^a. Subsequently, we used histological information from four regions of interest (ROIs) located in the CC of a postmortem human brain to measure the mean histological axon radii. The mean intra-axonal relaxation times and histological axonal radii estimated in the four ROIs were combined to estimate T_2^c and ρ_2, and T_1^c and ρ_1 via linear regression (i.e., calibration step) from Eqs. (1) and (2). Then, using the calibrated parameters, we predicted axon radius in another eleven CC ROIs for each scanned subject via Eq. (3). Finally, we employed a second histological dataset containing data from nine postmortem human brains to further validate our results. All the details are provided in the "Methods" section.

3. Methods

3.1. Intra-axonal diffusion-relaxation models

As in McKinnon and Jensen (2019), we assume that for b = 6,000 s/mm^2 the *in vivo* dMRI signal comes from the intra-axonal space. Thus, the diffusion-T_1-T_2 relaxation model for the measured signal M for a given b, diffusion gradient unit vector $\hat{g}$, echo time (TE), repetition time (TR), and inversion time (TI) is

$$M(b,\hat{g},TE,TI) = kPDf_aM_a(b,\hat{g})\exp\left(-\frac{TE}{T_2^a}\right)\left|1-2\exp\left(-\frac{TI}{T_1^a}\right)+\exp\left(-\frac{TR}{T_1^a}\right)\right|+\eta, \quad (4)$$

where k is a scalar that depends on the MRI machine, pulse sequence, image-reconstruction algorithm, digital converter, etc.; PD is the proton density; f_a is the intra-axonal water volume fraction; $M_a(b,\hat{g})$ denotes the orientation-dependent diffusion-weighted signal from the intra-axonal compartment; η is the experimental noise, assumed to be additive; $|x|$ denotes the absolute value of x; T_2^a and T_1^a are the intra-axonal relaxation times.

Following the approach of Edén (2003), Lasič et al. (2014), Kaden et al. (2016a,b), Eq. (4) can be simplified by computing the orientation-averaged spherical mean signal $\bar{M}$ as:

$$\bar{M}(b,TE,TI) \approx K\exp\left(-\frac{TE}{T_2^a}\right)\left|1-2\exp\left(-\frac{TI}{T_1^a}\right)+\exp\left(-\frac{TR}{T_1^a}\right)\right|, \quad (5)$$

where T_2^a and T_1^a are the parameters to be estimated, along with the constant K (per voxel) that is proportional to the intra-axonal water volume fraction (i.e., $K = kPDf_a\bar{M}_a(b, \hat{g})$); it also depends on the intra-axonal diffusivities via $\bar{M}_a$.

It is important to note that in Eqs. (4)-(5), the T_1 relaxation terms follow the standard relaxation model (Bydder et al., 1998), which assumes an ideal inversion pulse (Pykett et al., 1983; Barral et al., 2010). Other acquisition sequences may require different models. For a comprehensive review of alternative relaxometry sequences and models, please refer to Stikov et al. (2015).

The diffusion-relaxation model in Eq. (5) is a more general version of the model proposed by McKinnon and Jensen (2019) for an inversion recovery sequence incorporating T_1 relaxation. The diffusion-T_2 model for dMRI data collected at multiple *TE*s (McKinnon and Jensen, 2019) without considering T_1 effects is,

$$\bar{M}(b, TE, TI) \approx K \exp\left(-\frac{TE}{T_2^a}\right). \quad (6)$$

3.2. MRI data acquisition and preprocessing

Human brain MRI data were acquired from three healthy volunteers, and one of them was scanned twice on a Siemens Connectom 3T system with 300 mT/m diffusion gradients (Cardiff University Brain Research Centre, Wales, UK). The ethics committee approved the study, and the participant provided written informed consent.

Two diffusion-relaxation protocols were implemented. A longer diffusion-T_1-T_2-weighted imaging sequence was designed to obtain independent estimates of the axon radius from the first subject's intra-axonal T_1 and T_2 times (male, 28 years old). A reduced diffusion-T_2 protocol was employed to scan three subjects (age-range = 28–39 years, mean-age = 32.3 ± 4.8 years, males), including the first subject that was also scanned with the longer sequence. Accordingly, for the second sequence, the axon radii were estimated from the intra-axonal T_2 times.

The diffusion-T_1-T_2 relaxation sequence comprised four images with b = 0 s/mm^2 and 48 diffusion directions at b = 6,000 s/mm^2 (diffusion gradient, 275 mT/m; diffusion times Δ/δ = 22/8 ms) for each of the following nine (*TE*, *TI*) combinations (in ms): (80, 200), (110, 200), (110, 331), (150, 200), (80, 906), (110, 906), (110, 1,500), (150, 906), (150, 1,500). The *TI*s were chosen empirically from relatively small to large values to obtain maps with different visual contrasts without nullifying the WM signal. The lowest *TE* was set to minimize the contribution of the myelin water (Mackay et al., 1994) to the measured signal, and the largest *TE* was chosen as a trade-off between image contrast and noise. For each (*TE*, *TI*) pair, one additional image with b = 0 s/mm^2 and opposite phase encoding direction was acquired to correct susceptibility distortions (Andersson et al., 2003; Andersson and Sotiropoulos, 2016). **Figure 2** shows the nine pairs of *TE*s and *TI*s. The *TR* was 5,000 ms, and the voxel size was 2.5 × 2.5 × 3.5 mm^3. Ten slices were acquired with matrix size and field of view of 88 × 88 and 220 × 220 mm^2, respectively. The acceleration factor was 2, and the total acquisition time was 42 min.

The diffusion-T_2 protocol employed a dMRI sequence that was repeated by changing the *TE*, using the following four values *TE*s = (73, 93, 118, and 150) ms with *TR* = 4,100 ms. The other sequence parameters (i.e., acceleration factor, diffusion times, b-value, diffusion directions, number of b0s images, diffusion gradient strength, matrix size, and field of view) were equal to those employed in the previous diffusion-T_1-T_2 sequence. The number of slices was 46, and the voxel size was 2.5 × 2.5 × 2.5 mm^3. The acquisition time per *TE* was 5 min, and the total scan time was 20 min.

Additionally, a structural T_1–weighted (T1w) image was collected for each subject using a 3D MPRAGE sequence with the following parameters: *TR* = 2,300 ms, *TE* = 2 ms, *TI* = 857 ms, voxel size = 1 mm isotropic, and flip angle = 9°, for the purposes of spatial normalization.

The nine diffusion-T_1-T_2 4D volumes with different *TE*s and *TI*s, and the four diffusion-T_2 4D volumes with different *TE*s were preprocessed separately in the following order: (1) noise level estimation and removal using the MP-PCA method (Veraart et al., 2016) by using the matrix centering and patch-based aggregation options (Manjon et al., 2013), as implemented in dipy (Garyfallidis et al., 2014)[1]; (2) attenuation of the Rician-noise dependent bias in the signal by implementing the postprocessing correction scheme proposed by Gudbjartsson and Patz (1995) and (3) motion, geometric distortions, and eddy current corrections using the "topup" and "eddy" tools included in FSL (Andersson et al., 2003; Andersson and Sotiropoulos, 2016).

3.3. Estimation of the intra-axonal relaxation times

Diffusion-T_1-T_2 model: after computing the spherical mean signal for each pair of the preprocessed diffusion-T_1-T_2 datasets with different *TE*s and *TI*s (see **Figure 2**), the intra-axonal relaxation times were estimated by fitting the diffusion-relaxation model in Eq. (5) using the "L-BFGS-B" method for bound constrained minimization included in the Scipy python library (Virtanen et al., 2020),[2] with the following bounds: $0 \leq K < \infty$, $40 \leq T_2^a(ms) \leq 2000$, and $300 \leq T_1^a(ms) \leq 5000$. The bounds for the intra-axonal relaxation times were chosen to be higher and lower than those expected for the myelin water and Cerebrospinal fluid (Mackay et al., 1994; Labadie et al., 2014), respectively.

Diffusion-T_2 model: the estimation was performed by fitting the diffusion-relaxation model in Eq. (6) to the spherical mean signals estimated from the diffusion-T_2 data, using the L-BFGS-B method (Virtanen et al., 2020) with the following bounds: $0 \leq K < \infty$, $40 \leq T_2^a(ms) \leq 2000$.

3.4. Histological samples

Two histological datasets were employed. The first one contains two histological samples measured on the same subject. The first sample, which we call "Histology1," was measured and reported by Caminiti et al. (2009). For completeness, we provide a summary of the histological procedures. Axon radii were measured in four regions of interest (i.e., ROI2, ROI5,

1 https://dipy.org/

2 https://docs.scipy.org

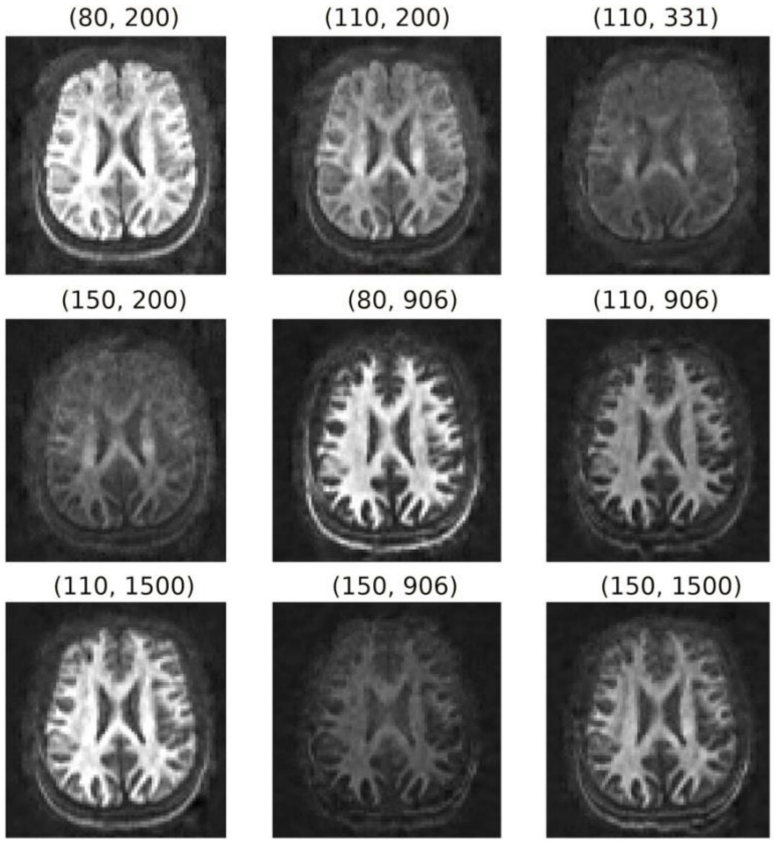

FIGURE 2
Orientation-averaged spherical mean signals for each pair of *TE* and *TI* (TE, TI) in ms. These images were used to fit the diffusion-relaxation model in Eq. (5).

ROI8, and ROI10) in the midsagittal CC cross-section of a postmortem human brain (female, 63 years old). These ROIs include axons connecting the prefrontal, motor, parietal and visual cortices, respectively. All analyses were performed with Neurolucida 7 software (MBF Biosciences) and a digital camera-mounted Olympus BX51 microscope. Three sagittal blocks of the CC were removed from the brain. The sample was immersion-fixed in 4% (w/vol) paraformaldehyde in phosphate-buffered saline solution within 27–30 h of death, cryoprotected, cut frozen, and stained for myelin. Axons were sampled within 112 × 87 μm^2 frames divided into 25-μm squares. The axonal profiles were chosen for measurement if they presented a dark complete or nearly complete myelin ring with a clear center. Longitudinally cut axons were excluded, and the radius of slightly obliquely cut axons (which appeared as ellipses) was approximated to its smallest radius. Since fixation artifacts were frequent, the sampling was restricted to profiles that could be followed through the thickness of the whole section. Limitations of the optical microscopy prevented measurement of axons radius smaller than ~0.17 μm. A different number of axons were measured per ROI, ranging from 1,178 (ROI10) to 9,605 (ROI2) axons. No correction for shrinkage effects was applied to the measured radii because accurate shrinkage estimates were unavailable. For more technical details, see Caminiti et al. (2009). The second sample, which we call "Histology2," was measured by the same team (Prof. Giorgio Innocenti) using the same material and following the same sampling procedure. The main difference was that this time, eleven ROIs (i.e., ROI0-ROI10) encompassing the whole midsagittal CC cross-section were analyzed, and the number of measured axons per ROI was smaller: from 153 (ROI5) to 720 (ROI1) axons. It is important to note that the spatial locations of ROI2, ROI5, ROI8, and ROI10 are the same in both histological samples. However, the sampling procedure employed in the Histology2 sample was repeated without including the axons measured in the Histology1 sample. The anatomical location of the ROIs in both histological samples and the number of measured axons per ROI are displayed in **Figure 3**.

The second histological dataset, which we call "Histology3," was reported by Wegiel et al. (2018). This electron microscopic study of the CC included nine control subjects (age-range = 4–52 years old; mean-age = 26.3 ± 15.8 years; postmortem-interval = 15 ± 6.6 h; six males and three females) with well-preserved CC ultrastructure. Each brain was fixed in 10% buffered formalin for at least 3 months, washed for 24 h in water to remove fixer, dehydrated, embedded in celloidin, and cut into 200-μm-thick sections. Samples were oriented to cut axons perpendicularly to the long axon axis and stained with a 2% solution of p-phenylenediamine. Each section was stained with uranyl acetate and photographed at a magnification of 15,000x using a Hitachi H7500 transmission electron microscope with an Advanced Microscopy Technique (AMT) Image Capture Engine (Danvers, MA). Axons from five different segments (i.e., I, II, III, IV, and V) of the midsagittal CC cross-sections of the nine control

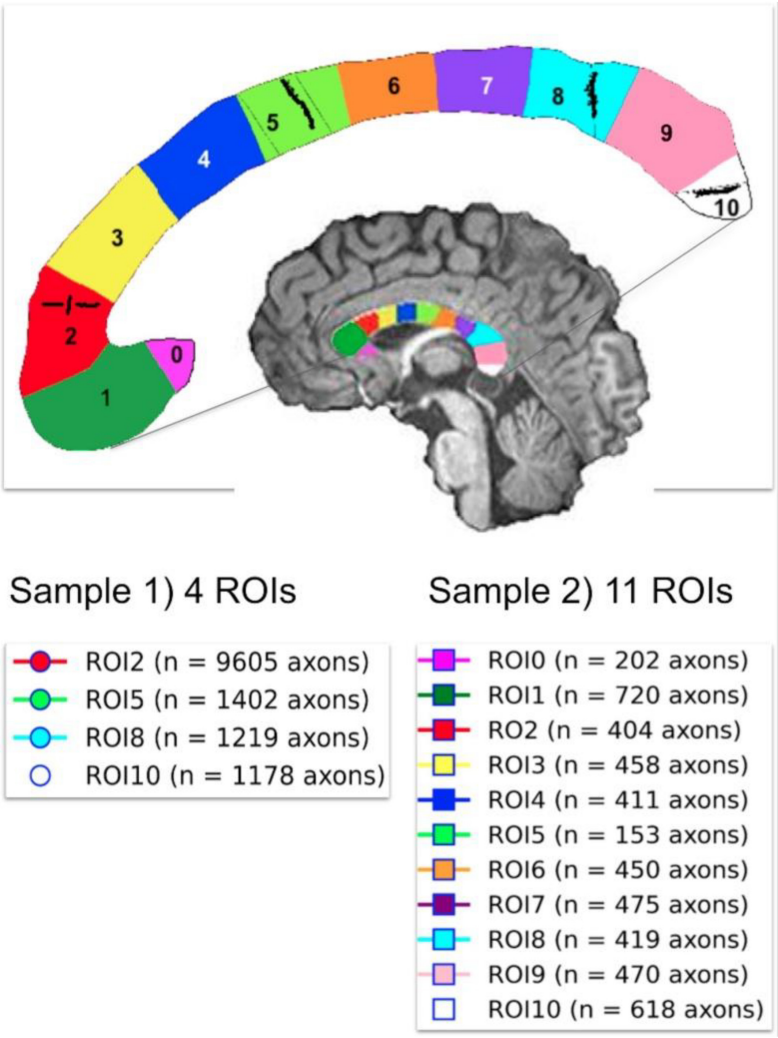

FIGURE 3
Anatomical location of the two independent histological samples of the first histological dataset (Histology1 and Histology2) taken from eleven regions of interest (ROIs) in the Corpus Callosum. The number of studied axons per sample and ROI are reported for each case. The second sample (Histology2) consisted of axons not included in the first sample (Histology1).

subjects were measured. The study was limited to myelinated axons, which were better preserved than non-myelinated axons. For each case, 12 electron micrographs were used, and background correction was applied to reduce the risk of distortions during image analysis. Axons were manually delineated, and the Image J software was employed to obtain the axon radius (Feret's radius, μm) and area (μm^2). No correction for shrinkage effects to the measured radii was reported. The total number of axons measured in the nine control subjects was 15,085 (1,676 per subject, and 335 per segment, on average). For additional details, see Wegiel et al. (2018).

We note that the CC segments employed in both histological datasets (i.e., Histology1-Histology2 and Histology3) are related. Segment I (Histology3) approximately corresponds to the union of ROI0, ROI1, and ROI2 (Histology1-Histology2); segment II is located around ROI3 and ROI4; the union of segments III and IV is similar to the union of ROI5, ROI6, and RO7; and segment V covers ROI8, ROI9 and ROI10. These relationships were used to compare the histological estimates from both studies and the MRI-based radius estimates.

3.5. Estimation of the mean histological effective radius

For each ROI of each sample, we estimated the mean histological axon radius. However, as the mean axon radius estimated from MRI generally differs from the mean histological radius (Burcaw et al., 2015; Veraart et al., 2020), we derived an approximate expression for the mean effective radius for our diffusion-relaxation models, finding that $r_{eff} \approx \langle r^2 \rangle / \langle r \rangle$, which differs from the previous result reported in Burcaw et al. (2015), Veraart et al. (2020) (The complete derivation is reported in the Appendix section). This key result shows that the mean effective radius derived from our model is not heavily weighted by the tail of the axon radius distribution as that in Burcaw et al. (2015),

Veraart et al. (2020). Consequently, we used this expression to estimate the mean effective histological axon radius for each CC ROI in both samples (see **Figure 3**), which was compared with the MRI-predicted mean radius.

In order to estimate the effective radius, knowing both the mean histological axon radius and the mean squared radius is required. For the Histology1 and Hostology2 samples, these values were calculated from the whole radius distribution per ROI. We don't have access to the radius distributions of the Histology3 sample. Fortunately, in that study, the mean histological radius and the mean axon area were reported (Wegiel et al., 2018). We used the mean axon area to estimate the mean squared radius assuming a circular geometry.

3.6. Spatial registration

The histologist that measured the axons in the Histology2 sample drew the locations of the eleven histological ROIs on the structural T1w image of the subject scanned using the diffusion-T_1-T_2 sequence, which we used to create a cluster mask. Therefore, we used that T1w image as a reference to spatially register the estimated parameter maps for all the subjects (i.e., intra-axonal relaxation times and K maps). The same affine registration matrix and non-linear deformation field were applied to each subject's estimated parameter map. These registration parameters were determined by non-linearly registering the estimated K map (whose visual appearance is similar to a T1w image, e.g., see **Figure 4** in the results section) to the reference T1w image. The registration was carried out using the state-of-the-art (Klein et al., 2009) Symmetric Normalization (SyN) method (Avants et al., 2008) implemented in the ANTs software (*ANTsPy*).[3] Before the registration, we corrected the K map and T1w image for spatial intensity variations due to B1-Radiofrequency field inhomogeneities using FSL (Smith et al., 2004). All the registered images were visually inspected to verify the accuracy of the normalization procedure. All the subsequent analyses employed the registered maps. Furthermore, the ROIs were eroded to remove peripheral voxels that do not correspond to the corpus callosum and are affected by partial volume effects with surrounding tissue and CSF.

The number of voxels included in each ROI ranges from 170 (ROI0) to 604 (ROI1) in the cluster mask defined in the reference T1w image. The equivalent number of voxels in the native space of the diffusion-T_1-T_2 MRI data with a lower spatial resolution (obtained after applying the resulting non-linear inverse registration to the cluster mask) ranges from 10 (ROI10) to 20 (ROI1).

3.7. Calibration step to predict axon radii

The first sample of the first histological dataset (Histology1) was employed to estimate the unknown parameters of the surface-based relaxation models in Eqs. (1)-(2). These equations were fitted independently using the mean intra-axonal T_2 and T_1 times and the mean effective histological radii estimated in the same four ROIs of the Histology1 sample. The fitting allowed us to determine the cytoplasmic T_2^c and T_1^c times and the surface relaxivity coefficients ρ_2 and ρ_1, which best explain the data in these regions. This was done by fitting the linear equation $y = mx + n$, where $y = 1/T_2^c$ and $x = 2/r$ for values from the four CC ROIs. Note that these parameters can be estimated as $\rho_2 = m$ and $T_2^c = 1/n$. A similar independent linear model was used to fit the T_1 data for estimating ρ_1 and T_1^c .

Subsequently, we predicted the mean effective axon radii, using Eq. (3), in the eleven CC ROIs of the second sample of the first dataset (Histology2) and the CC segments defined in the second histological dataset (Histology3). The forecasted and histological axon radii were compared using a linear regression model. The linear relationship among the parameters was quantified and tested by the slope and intercept of the fitted regression line and the Pearson correlation coefficient. It is important to mention that when there are two variables, such as in our study, the p-value of the slope of the regression line and the p-value of the correlation coefficient are identical. Therefore, to avoid redundancy, we have reported only the p-values of the slopes in our findings. In the Results section, we present the raw p-values without applying the correction for multiple comparisons. However, in the Discussion section, we mention the analyses that have survived the Bonferroni correction.

4. Results

4.1. diffusion-T_1-T_2 and Histology1-Histology2 data

Figure 4 shows the T_2^a, T_1^a, and K maps estimated from the *in vivo* diffusion-T_1-T_2 MRI data for different brain slices. The estimated relaxation times are within the expected range for white matter. The values in the whole medial part of the CC were distributed in the following ranges: $70 < T_2^a(ms) < 130$, $650 < T_1^a(ms) < 760$.

The results of the calibration step are depicted in **Figure 5**. It shows the regression line fitting the inverse of the mean intra-axonal T_2 per ROI to the inverse of the mean histological radius in the four ROIs of the Histology1 sample (for more details, see **Figure 1**), employing the surface-based relaxation model in Eq. (1), as described in the subsection "Calibration step to predict axon radii." The correlation coefficient between both variables was 0.97, and the p-value of the slope (i.e., for a hypothesis test whose null hypothesis is that the slope is zero) was $p = 0.03$. We found the calibrated parameters $T_2^c \approx 126.97$ ms and $\rho_2 \approx 1.16$nm/ms from the estimated coefficients.

In **Figure 6**, we compare the effective histological radii in the eleven ROIs of the Histology2 sample and those predicted using the intra-axonal T_2 times estimated from the *in vivo* diffusion-T_1-T_2 MRI data [Eq. (3)]. The intercept and slope of the regression line were 0.026 μm and 1.055, respectively; the correlation coefficient was 0.676, and the p-value for the slope and the correlation was $p = 0.022$. To further investigate the data, we analyzed a subset of seven ROIs, excluding the four ROIs in the same locations as those in the Histology1 sample. We obtained a slightly higher intercept

3 https://github.com/ANTsX/ANTsPy

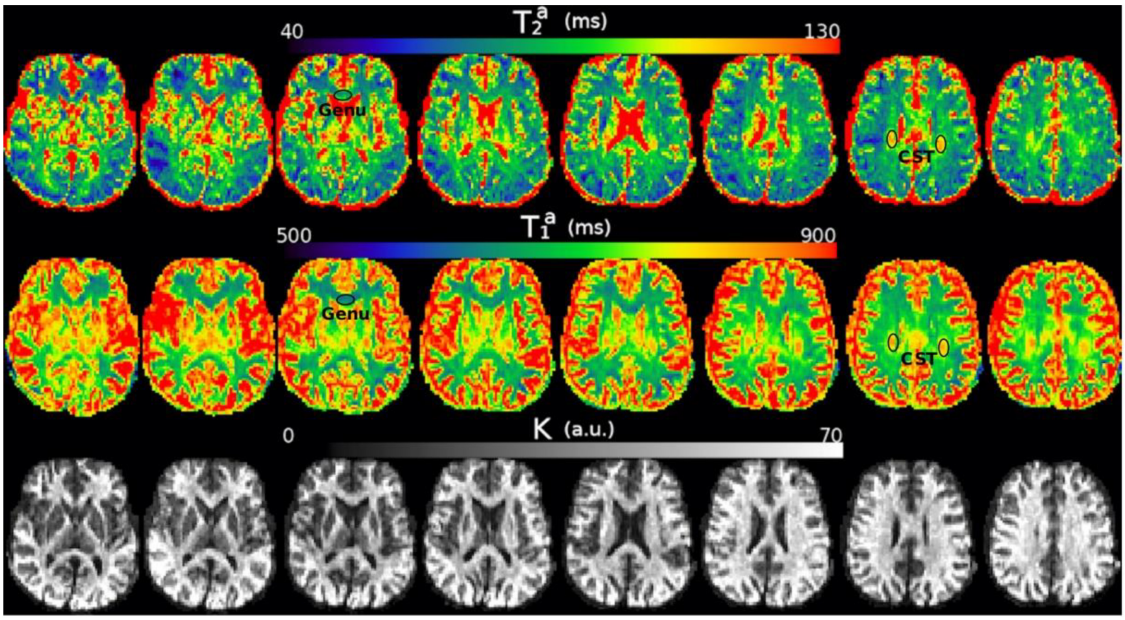

FIGURE 4
Axial slices of the T_2^a, T_1^a, and K maps estimated from the *in vivo* diffusion-T_1-T_2 relaxation MRI data in native space (i.e., before registering the images to the reference T1w image). Note that the intra-axonal relaxation times are only meaningful in the white matter because the assumptions underlying the estimation method are invalid in gray matter or CSF. The values of K (in arbitrary units) are higher in the white matter because this parameter is proportional to the intra-axonal volume. We highlight two regions with different intra-axonal relaxation times: the genu of the Corpus Callosum and the corticospinal tract (CST).

of 0.12 μm and a smaller slope of 0.89 compared to the analysis conducted with eleven ROIs. The resulting correlation coefficient decreased to 0.557, and the *p*-value for the slope was not significant, $p = 0.19$.

Figures 7, 8 show results from similar experiments using the intra-axonal T_1. Figure 7 depicts the linear fitting of the inverse of the mean intra-axonal T_1 per ROI estimated from *in vivo* diffusion-T_1-T_2 MRI data to the inverse of the mean effective radius corresponding to the Histology1 sample [Eq. (2)]. The correlation coefficient between both variables was 0.755 lower than that previously found for the intra-axonal T_2 in Figure 5, and the *p*-value of the slope and the correlation did not reach statistical significance, $p = 0.25$. From the estimated coefficients, we found the calibrated parameters to be $T_1^c \approx 870$ ms and $\rho_1 \approx 0.087$ nm/ms.

The linear relationship between the effective mean axon radius estimated in the Histology2 sample and the radius predicted by using the intra-axonal T_1 times [Eq. (3)] is shown in Figure 8. The intercept and slope of the regression line were 0.064 μm and 1.002, respectively. The correlation coefficient was 0.628, and the slope was significant, $p = 0.039$. When analyzing the subset of seven ROIs, excluding the four ROIs from the Histology1 sample, we obtained a new slope of 0.962 ($p = 0.16$), which was not statistically significant. The intercept was 0.065 μm, and the correlation coefficient was 0.598.

Table 1 reports the mean histological effective axon radius per ROI and the predicted values from the intra-axonal T_2 and T_1 times, respectively. The predicted axon radius from both intra-axonal T_2 and T_1 times were very similar to each other. A linear fitting between both estimates revealed a slope close to one (0.947) and an intercept close to zero (0.041 μm). The slope was significantly non-zero ($p = 4e{-}5$), and the correlation coefficient was 0.927.

4.2. Diffusion-T_2 and Histology1-Histology2-Histology3 data

We complement the results presented in the previous section by reporting the predicted radii for the subjects scanned with the diffusion-T_2 MRI sequence and by including the Histology3 dataset. Notably, the parameters T_2^c and ρ_2 were not recalibrated for these subjects; instead, we used the values estimated in the previous section.

The estimated intra-axonal T_2 values in the whole medial part of the CC for the three subjects were distributed in the following ranges 80–130 ms, 90–125 ms, and 85–115 ms, respectively.

In Figure 9, the predicted mean effective radius, derived from the intra-axonal T_2 times of the three subjects, is presented for all the CC ROIs. The figure also depicts the mean histological effective radius for the three histological samples (Histology1, Histology2, and Histology3).

To assess the validity of the calibrated parameters, which were estimated from the subject scanned with the diffusion-T_1-T_2 sequence, for the subjects scanned with the diffusion-T_2 sequence, we repeated the calibration process using the mean intra-axonal T_2 times estimated for the three subjects and the Histology1 sample as a reference, as before. The recalibrated parameters were remarkably similar to those obtained previously: $T_2^c \approx 127.17$ ms and $\rho_2 \approx 1.13$nm/ms.

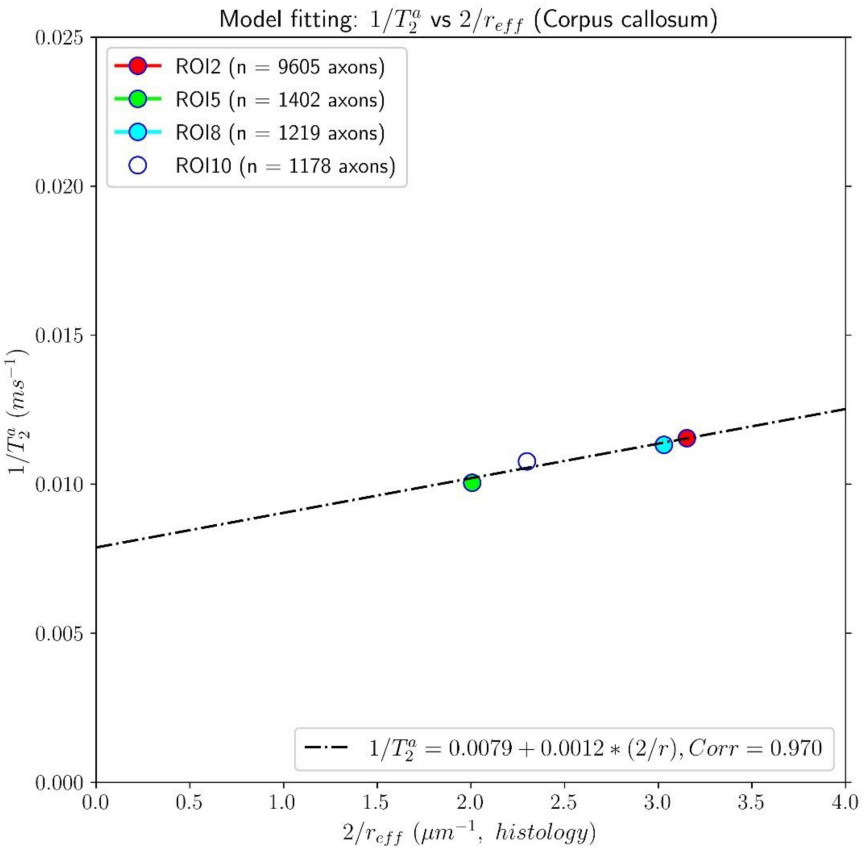

FIGURE 5
Linear fitting of the inverse of the intra-axonal T_2 times (*y*-axis) estimated from the *in vivo* diffusion-T_1-T_2 MRI data to the inverse of the inner axon radius (*x*-axis) measured from the first histological sample (Histology1) of the first histological dataset. The scatter plot depicts the mean values computed for all the voxels inside four corpus callosum (CC) regions of interest, corresponding to ROI2, ROI5, ROI8, and ROI10 in the Histology1 sample. The number of axons sampled for each CC ROI is displayed in the legend. The intercept and slope of the regression line were 0.0079 ms^{-1} and 0.00116, respectively. The slope of the regression line was significantly different from zero (p = 0.030).

We compared the T_2-based predicted radii for the subject that underwent two scans, using both diffusion-relaxation MRI sequences, which values are reported in **Figure 9** and **Table 1** (as Subject 3). The linear fitting between both estimates produced a statistically significant regression line with a slope close to one (0.993, $p < 0.001$) and an intercept close to zero (−0.029 μm). The correlation coefficient between both estimates was 0.884.

Finally, we employed the calibrated model to predict the axon radius across the whole WM. Axial and sagittal slices of the voxel-wise T_2-based inner axon radius estimated for all the subjects are shown in **Figure 10**. The maps are approximately symmetrical, the spatial variability of the estimated radius is apparent in both slices, and all subjects show a similar pattern of small and big axons in the same anatomical regions.

5. Discussion

This proof-of-concept study shows that (1) the intra-axonal T_2 and T_1 relaxation times are highly modulated by the axon radius (see **Figures 5**, **7**), as measured from histological data (see **Figure 3**), (2) a simple surface-based relaxation model can explain this dependence (see **Figure 1**), and (3) the intra-axonal relaxation times may also be sensitive to the smallest axons. Indeed, we did not observe a clear overestimation bias in the estimated axon radius (see **Figures 6**, **8**, **9**) in comparison to the histological values, as reported in previous dMRI studies (Assaf et al., 2008; Alexander et al., 2010; Dyrby et al., 2013; Horowitz et al., 2015) where only the largest radii might have been detected. This result suggests that our new approach may also be sensitive to differences in axon radius below the "diffusion resolution limit" of ∼1–2 μm. One possible explanation for this finding is that the intra-axonal T_2 times are not influenced by the strength of the diffusion gradients, as opposed to the intra-axonal radial diffusivities used to estimate axon radii in dMRI. Moreover, we found that the effective mean radius estimated by our approach, i.e., $r_{eff} \approx \langle r^2 \rangle / \langle r \rangle$, produces much smaller radii than those from diffusion models heavily weighted by the tail of the axon radius distribution, i.e., $r_{eff} \approx \left(\langle r^6 \rangle / \langle r^2 \rangle \right)^{\frac{1}{4}}$ (Burcaw et al., 2015; Veraart et al., 2020). This important result suggests that, from a modeling point of view, the employed diffusion-relaxation model may be more valuable than previous pure dMRI models for estimating axonal radii. The predicted mean effective radius obtained from the intra-axonal T_2 and T_1 times fell within a narrow range of 0.52–1.13 μm and 0.51–1.12 μm, respectively, which closely matched the range of histological axon radii (0.57–0.95 μm). The smallest predicted effective radii were observed in

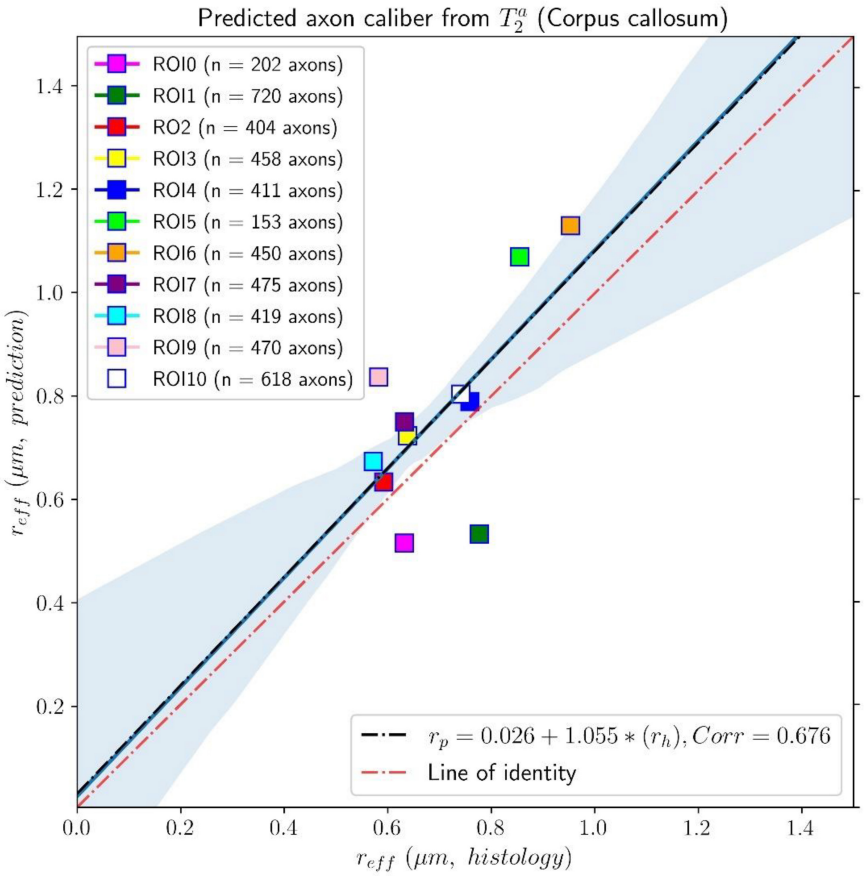

FIGURE 6
Linear fitting of the effective histological radius estimated from the second histological sample (Histology2) of the first histological dataset to the predicted radius from the intra-axonal T_2 times, calculated from the *in vivo* diffusion-T_1-T_2 MRI data. The scatter plot depicts the mean values computed for all the voxels inside the eleven corpus callosum (CC) regions, corresponding to ROI0-ROI10. The number of axons sampled for each CC ROI is displayed in the legend. The slope of the regression line was significantly different from zero (p = 0.022).

ROI1, ROI0, and ROI2, while the largest radii were found in ROI6 and ROI5, followed by ROI4, ROI9 and ROI10 (refer to **Table 1**). Nevertheless, we cannot rule out the possibility that the calibration step, informed by the histological values, may have reduced any potential overestimation effect.

Inspecting the estimated T_2^a and T_1^a relaxation maps (see **Figure 4**), we notice that both relaxation times tend to be smaller in the genu and splenium of the CC than in the corticospinal tract (connecting the motor cortex to the spinal cord). Although these values could be affected by fiber orientation effects with respect to the B0 field (see the subsection "Orientation dependence on relaxation times" in the Appendix), the corticospinal tract is characterized by axons with larger inner radius (Aboitiz et al., 1992; Innocenti et al., 2014; Barakovic et al., 2021a). This observation agrees with multi-echo T_2 relaxometry studies showing that the intra- and extra-axonal T_2 times (and the myelin content) in the corticospinal tract are larger than in the CC, e.g., see Yu et al. (2020), Canales-Rodríguez et al. (2021a,b,c). A consistent trend was observed in the T_2-based predicted axon radii for all three subjects, as shown in **Figure 10**. The voxel-wise maps in **Figure 10** and the ROI-based estimates in **Figure 9** agree with previous estimates derived from dMRI data acquired using much higher b-values (Veraart et al., 2021).

In agreement with our results, a previous multi-echo T_2 relaxometry study found a positive correlation between axon radius and T_2 (including both the intra- and extra-axonal compartments) in six samples of an excised and fixed rat spinal cord (Dula et al., 2010). Moreover, two previous experimental studies investigated the microstructural correlates of T_1 in white matter (Hofer et al., 2015; Harkins et al., 2016). In line with our findings, a significant correlation between $1/T_1$ and axon radius was reported by Harkins et al. (2016) in white matter tracts of a rat spinal cord. Similarly, the analysis performed by Hofer et al. (2015) found a tendency for the lowest T_1 in the genu of the human CC (composed of densely packed smaller axons) and the highest T_1 in the somatomotor region (dominated by fibers with large radii). In those studies, however, the estimated relaxation times characterize the relaxation process in the intra- and extra-axonal compartments combined. In contrast, we report a more specific relationship by analyzing the intra-axonal relaxation times associated with the inner axon radius.

A multi-gradient-echo MRI model was proposed to estimate axon density based on the susceptibility-driven non-monotonic time-dependent MRI signal decay (Nunes et al., 2017). They employed a simple (phenomenological) general-linear model to predict the average axonal diameters using four modeled

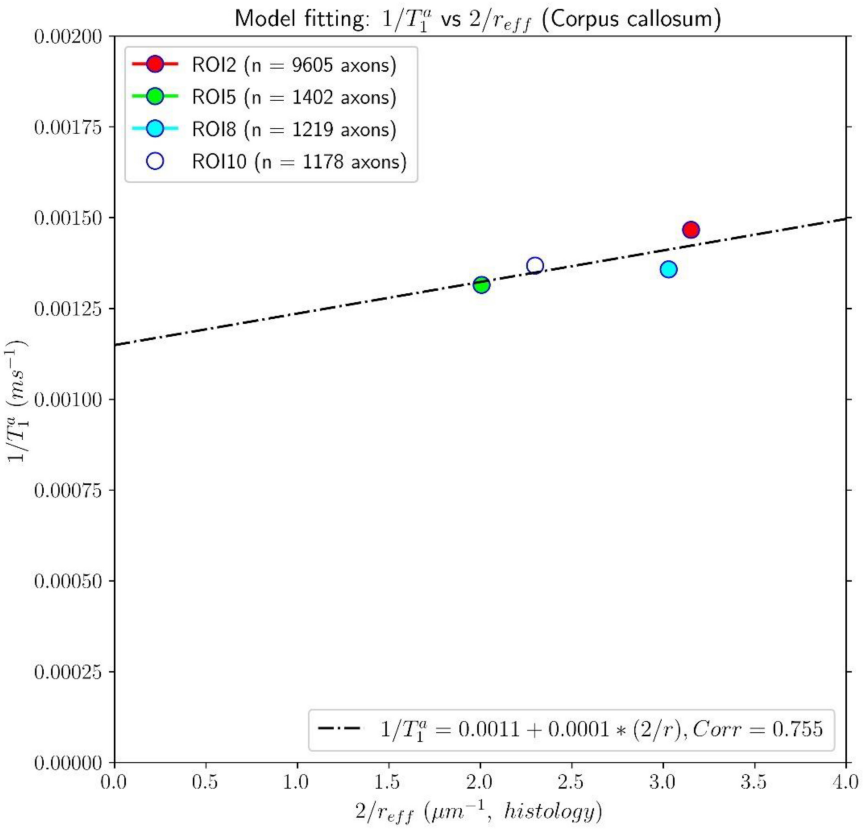

FIGURE 7
Linear fitting of the inverse of the intra-axonal T_1 times (*y*-axis) estimated from the *in vivo* diffusion-T_1-T_2 MRI data to the inverse of the inner axon radius (*x*-axis), measured from the first histological sample (Histology1) of the first histological dataset. The scatter plot depicts the mean values computed for all the voxels inside four corpus callosum (CC) regions, corresponding to ROI2, ROI5, ROI8, and ROI10. The number of axons sampled for each CC ROI is displayed in the legend. The intercept and slope of the regression line were 0.0011 and 0.000087. The *p*-value for the slope was not statistically significant ($p = 0.23$).

parameters, including the T_2 relaxation times of the intra- and extra-axonal compartments.

5.1. Impact on previous and future studies

Our study has important implications for previous and future dMRI studies of white matter microstructure. Previous studies, such as those by Assaf et al. (2008), Alexander et al. (2010), Zhang et al. (2011), Dyrby et al. (2013), Xu et al. (2014), Daducci et al. (2015), Horowitz et al. (2015), Huang et al. (2015), Benjamini et al. (2016), Drobnjak et al. (2016), Sepehrband et al. (2016b), Romascano et al. (2020), Harkins et al. (2021), Herrera et al. (2022), estimated axon radius without considering any T_2 dependence, assuming the same T_2 for all axons and intra- and extra-axonal water compartments. This simplification may affect the estimation of the intra-axonal diffusivities from which the axon radii are derived. Alternatively, this issue could be attenuated by using sufficiently high *b*-values, as shown in studies by Veraart et al. (2020), Pizzolato et al. (2022), which helps eliminate the contribution from the extra-axonal signal. However, this may be insufficient in voxels with a broad distribution of intra-axonal T_2 times. These multi-compartment models should be extended to include T_2 dependence, as discussed in studies by Veraart et al. (2018), Lampinen et al. (2019), Tax et al. (2021). Recently, (Ning et al., 2022) demonstrated that more accurate estimates of neurite size could be obtained by investigating the coupling between relaxation rate and diffusivity using multi-TE diffusion-relaxation MRI data. For further discussion on this issue, please refer to the Appendix subsection "Is the intra-axonal relaxation process mono-exponential and time-independent?"

5.2. Underlying assumptions and confounding factors

The proposed diffusion-relaxation model specifically applies to WM regions composed of myelinated axons, where the exchange of water molecules and other macromolecules and elements (such as iron/ferritin) between the intra- and extra-axonal spaces is negligible. In the human brain's CC, for example, more than 95% of axons in most regions are myelinated (Aboitiz et al., 1992). While the non-myelinated portions of the axon (i.e., nodes of Ranvier) contain a high density of voltage-gated ion channels that facilitate ion passage across the axonal membrane, including

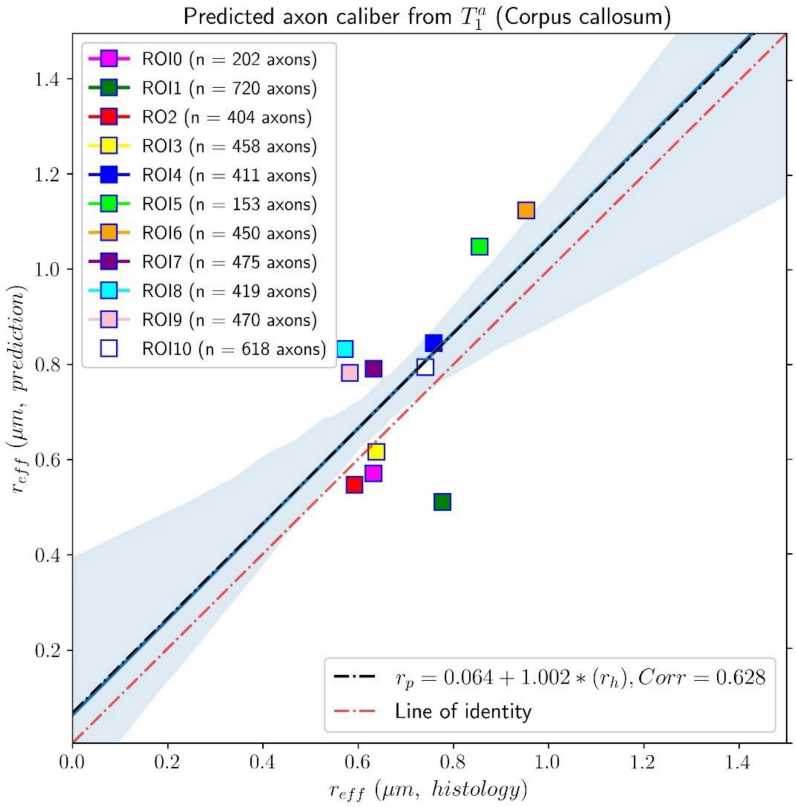

FIGURE 8
Linear fitting of the effective histological radius determined in the second histological sample (Histology2) of the first histological dataset to the predicted radius from the intra-axonal T_1 times estimated from the *in vivo* diffusion-T_1-T_2 MRI data. The scatter plot depicts the mean values computed for all the voxels inside the eleven corpus callosum (CC) regions, corresponding to ROI0-ROI10 in the Histology2 sample. The number of axons sampled for each CC ROI is displayed in the legend. The slope of the regression line was significantly different from zero (p = 0.039).

K + and Na + , which is associated with a concomitant water flux (Badaut et al., 2002), the myelinated portions of the axon (i.e., internodes) are not exposed to the extracellular environment.

TABLE 1 Mean effective radius (in μm) for each region of interest (ROI) in the corpus callosum.

ROI	Histology	T_2^a	T_1^a
ROI0	0.632	0.515	0.571
ROI1	0.777	0.533	0.511
ROI2	0.592	0.634	0.547
ROI3	0.638	0.723	0.616
ROI4	0.759	0.789	0.844
ROI5	0.855	1.069	1.047
ROI6	0.953	1.129	1.123
ROI7	0.633	0.750	0.791
ROI8	0.572	0.673	0.832
ROI9	0.583	0.836	0.782
ROI10	0.741	0.803	0.794

The anatomical location of each ROI is shown in Figure 3. The second row lists the radii corresponding to the Histology2 sample. The third and four rows report the predicted axon radii from the intra-axonal T_2 and T_1 times, respectively, estimated from the *in vivo* diffusion-T_1-T_2 MRI data.

Although the axonal membrane in the nodes of Ranvier is semipermeable to small diffusing molecules, such as water, the internodes' length is significantly greater [~100 times the outer axon diameter (Hursh, 1939; Rushton, 1951)] than the nodes of Ranvier [~1 μm (Arancibia-Cárcamo et al., 2017)]. As a result, most multi-compartment T_2 (Lancaster et al., 2003; Deoni et al., 2013) and "standard" dMRI models [see (Novikov et al., 2019) for a review] assume that the measured MRI signal is not significantly affected by the inter-compartmental molecular exchange in WM regions composed of myelinated axons.

Therefore, it is important to note that our model is unsuitable for GM or WM regions affected by demyelination processes, such as in Multiple Sclerosis, or any pathological condition with an increase in intra-axonal iron. These conditions can significantly reduce intra-axonal relaxation times and the estimated radii, rendering our model invalid. However, it is worth noting that we use long TEs in our model. If the intra-axonal T_2 time of a given axon is significantly reduced (e.g., below 20–40 ms) due to external factors, the contribution of this axon to the overall voxel-wise measured signal will be greatly diminished.

However, it is interesting that our calibration approach could also be extended to cases where water exchange between intra- and extra-axonal spaces is non-negligible, provided the exchange is similar across axons with different radii. In such cases, the effect of the exchange on the observed intra-axonal relaxation times can

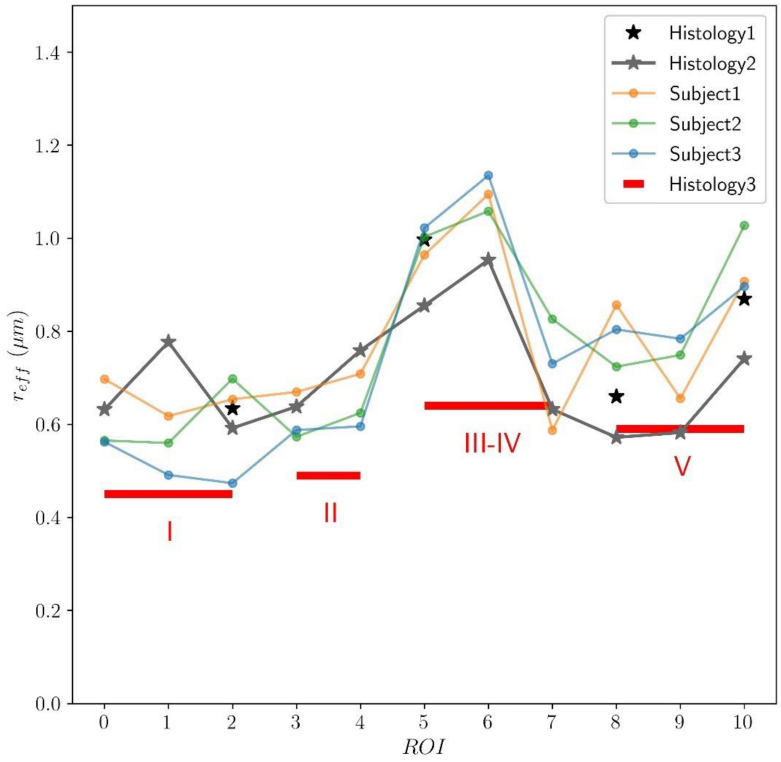

FIGURE 9
Predicted axon radius from intra-axonal T_2 times estimated from the *in vivo* diffusion-T_2 MRI data for the eleven ROIs (ROI0-ROI10) of the Histology2 sample. Additionally, as a reference, the mean effective histological radius calculated from the three histological samples (Histology1, Histology2, and Histology3) is also reported. Although the number and location of the ROIs used in the Histology3 sample differ from those employed in the Histology1-Histology2 samples, they can be regrouped to cover similar anatomical areas (see subsection "Histological samples" for more details). The histological and T_2-based radii follow the expected "low-high-low" trend in axon radii. The axon radii from the Histology1-Histology2 samples are consistently higher (about 25%) than those in the Histology3 sample.

be modeled by a global scaling of the cytoplasmic relaxation time, which is accounted for during calibration.

A more suitable approach for modeling systems that are coupled by means of a relaxation exchange process could be based on the Bloch-McConnell equations (McConnell, 1958), which generalize the relaxation model employed in this study [Eqs. (5) and (6)]. However, fitting such a model requires estimating additional parameters, including membrane permeability and extra-axonal relaxation times, which may be prone to numerical degeneracies. Additionally, the MRI acquisition time required for fitting the Bloch-McConnell model (using both high and low *b*-values) is longer than that required for our proposed model.

A study on human postmortem brains revealed that T_2^* is more sensitive than T_2 to changes in WM iron concentration (Langkammer et al., 2010). While it is established that the macromolecular and iron content is altered in certain pathologies (Stüber et al., 2014), more research is required to understand how these abnormalities affect the intra-axonal space and how they can impact the intra-axonal relaxation times.

We assume that signals measured at very high *b*-values are primarily attributable to the intra-axonal space, given that the signals from free-water and extra-axonal compartments decay more rapidly with the *b*-value (Veraart et al., 2020). To further suppress signals from tissue compartments with very short T_2s, such as myelin water (Mackay et al., 1994) and other confined water molecules, we also used long TEs. Hence, the resulting signals are expected to come from intra-axonal water molecules. However, there are other 1D-stick-like structures in the WM, such as the radiating processes of astrocytes, which can have large diameters that might contaminate the resulting signals (Veraart et al., 2020, 2021), as well as cell nuclei, vacuoles, and other restricted compartments (Andersson et al., 2020). Therefore, further studies are necessary to understand the potential effects of these compartments on the measured T_2 and predicted radii.

5.3. Acquisition sequences

The diffusion-T_1-T_2 sequence was implemented to investigate the impact of axon radius on the intra-axonal T_1 and T_2 times independently. Our results demonstrate that both relaxation times are sensitive to changes in axon radius, with T_2 exhibiting a slightly higher sensitivity. Consequently, we can obtain two separate estimates of axon radius using the relaxation times calculated from this sequence (see **Table 1**). However, this is not our recommended acquisition protocol due to the long acquisition time required. Alternatively, a more practical approach for estimating axon radius is to use the diffusion-T_2 sequence. A faster version of this sequence could be implemented by utilizing only two TEs, although the

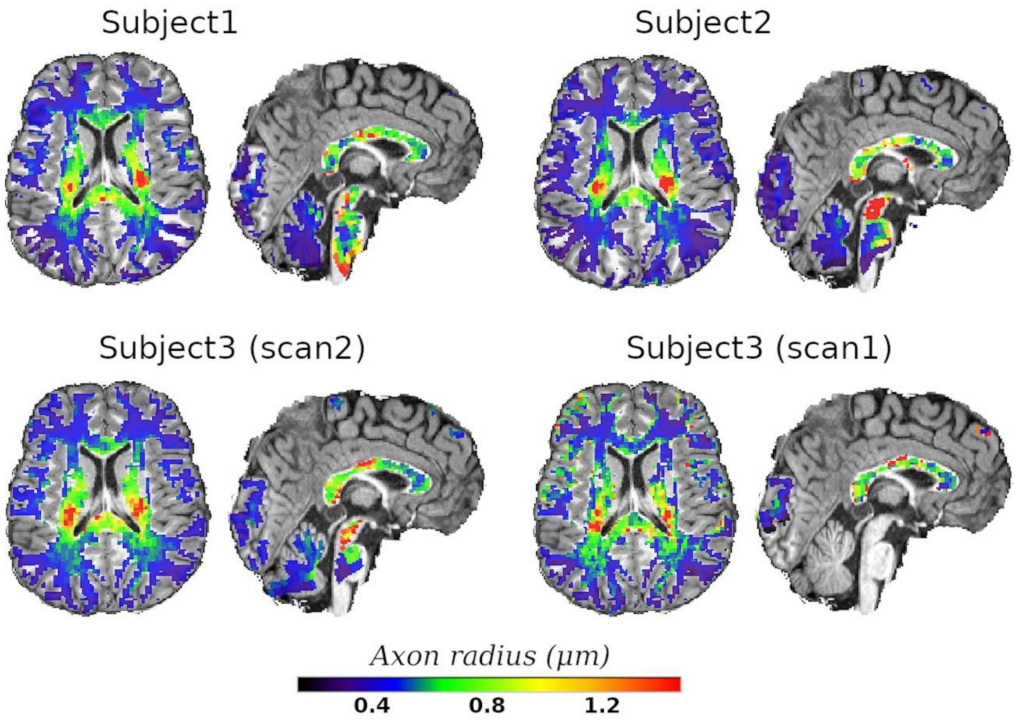

FIGURE 10
Axial and sagittal slices of the T_2-based inner axon radius for the three scanned subjects. Subject3 underwent two scans, with scan2 (46 slices) and scan1 (10 slices) representing the *in vivo* diffusion-T2 and diffusion-T1-T2 MRI data, respectively. All maps were normalized to the reference T1w image, where the histological CC ROIs were defined, and the predicted radii were plotted over the reference image. A white matter mask was used to suppress voxels in gray matter or cerebrospinal fluid.

resulting estimates may be more affected by underlying noise. This possibility shall be investigated in future studies.

When implementing these sequences, it is important to identify the optimal *b*-value to attenuate the extra-axonal signal. Based on *in vivo* human brain data and numerical experiments using analytical equations, the general rule of thumb is that a *b*-value in the range of 4,000–6,000 s/mm^2 is sufficient (Jensen et al., 2016; McKinnon and Jensen, 2019). In our study, we used the highest *b*-value within this range. However, it is worth noting that determining the optimal *b*-value involves a trade-off influenced by the SNR, which is affected by other sequence parameters, including the TE and voxel size. Our data were acquired using the Connectom 3T scanner at CUBRIC, which has been previously used to collect data with *b*-values up to 30,000 s/mm^2 (Veraart et al., 2020, 2021). Ultra-high *b*-values with very strong diffusion gradients are necessary for pure dMRI models to improve sensitivity to smaller axon radii (Nilsson et al., 2017). However, our sequences do not require *b*-values larger than 6,000 s/mm^2 because all the necessary information is derived from the relaxation times, which depend on the TEs/TIs.

5.4. Main limitations and future studies

While our study provides valuable insights into the relationship between axon radii and MRI relaxation times, it is important to acknowledge some limitations. First, the *in vivo* diffusion-relaxation MRI data and postmortem histological samples were obtained from different subjects of different ages and genders. Although some studies suggest that there are no sex differences in the fibers composition of the corpus callosum (Aboitiz et al., 1992), others have found age-related changes in axon size (Aboitiz et al., 1996), which may affect the comparison between the postmortem and *in vivo* measurements. Therefore, the estimated relaxation times of the cytoplasmic water and surface relaxivities must be considered as approximated guide values.

Second, the histological analysis of the second and third histological samples (Histology2 and Histology3, covering eleven and five CC sectors, respectively) are based on a reduced number of axons compared to the first (Histology1) sample. This may introduce sampling biases that could affect the accuracy of the histological radius estimates. An extended discussion is provided in the Appendix subsection "Histological tissue shrinkage and sampling issues." As such, a perfect agreement between the effective histological radius and the predicted MRI-based radius was not expected.

Third, the analysis was confined to the mid-sagittal plane of the CC. Therefore, the estimated mean cytoplasmic relaxation times and surface relaxivities are specific to this region. It is possible that different values may be obtained if other white matter tracts were included in the analysis. However, the extension of the analysis to other regions would require modeling the orientation susceptibility effects, which is beyond the scope of this proof-of-concept study. For more details, refer to the Appendix subsection "Orientation dependence on relaxation times."

Fourth, our study had a relatively small number of data points available for computing correlations, with only four ROIs to implement the calibration. This limited sample size restricts the statistical power and precision of the estimated correlations, leading to increased uncertainty and decreased reliability of the findings. While it is generally recommended to account for multiple comparisons to reduce the risk of false-positive findings, we opted not to implement such correction. Given the exploratory nature of our study, we prioritized sensitivity over stringent control of false positives. Consequently, our findings should be interpreted cautiously, requiring further validation in independent studies. However, for completeness, we report that if we correct our results for multiple comparisons using the Bonferroni method, only two analyses survive the correction: the correlation of the radii estimated using the T_2 and T_1 relaxation times reported in **Table 1** and the T_2-based predicted radii for the subject who underwent two scans, using the two diffusion-relaxation MRI sequences employed in this study.

Fifth, the proposed model is not suitable for GM or WM regions affected by demyelination processes or any pathological condition increasing intra-axonal iron. These conditions can significantly reduce intra-axonal relaxation times and the estimated radii, rendering the model invalid. A more detailed discussion of these underlying assumptions and confounding factors can be found in the previous subsection, "Underlying assumptions and confounding factors," in the Discussion section.

Sixth, the estimation of intra-axonal T_2 from the spherical mean of the strongly diffusion-weighted signal may be subject to bias due to the presence of isotropically-restricted compartments, including cell nuclei and vacuoles (Andersson et al., 2020). However, this issue can be mitigated by utilizing the spherical variance instead (Pizzolato et al., 2022). For more detailed information, please refer to the Appendix subsection "The effect of spherical cells: spherical mean vs. spherical variance."

Seventh, although the spherical mean signal is not affected by the presence of fiber crossings and orientation dispersion (Lindblom et al., 1977; Callaghan et al., 1979; Kaden et al., 2016a), it is influenced by the orientation susceptibility effect. In other words, the measured signal still depends on the angle between the B0 magnetic field and the fiber orientation. In our study, the regions of interest were located in the medial part of the CC, where the angle between the B0 vector field and the nerve fibers remains relatively constant. More details on this topic can be found in the Appendix subsection "Orientation dependence on relaxation times."

To better assess the generalizability of our approach, further validation studies are necessary. In particular, we plan to test our method using biomimetic phantoms with known ground truth (Hubbard et al., 2015; McHugh et al., 2018; Huang et al., 2021; Zhou et al., 2021) and *ex vivo* data from the same brains and multiple white matter regions. Such datasets would allow us to investigate whether the cytoplasmic relaxation times are truly independent of axon radius (see the Appendix subsection "Is the cytoplasmic T2 constant?"). This could be achieved by repeating the calibration process using different subsets of ROIs and comparing the resulting estimates. However, obtaining sufficient histological ROIs and measured axons per ROI will be crucial to minimize sampling bias and get robust results not affected by noise. Additionally, including data from the same brains (e.g., from non-human studies) will enable us to guarantee that we are studying the same axonal bundles.

An interesting future direction would be to utilize bundle-specific intra-axonal T_2 values (Barakovic et al., 2021b) to estimate bundle-specific inner axon radius, which could potentially resolve multiple axonal radii per voxel. This approach may potentially predict axon radius beyond the current dMRI resolution limit using clinical scanners. However, one limitation of translating the diffusion-relaxation MRI sequence to clinical scanners is the decreased signal-to-noise ratio resulting from using high b-values and long TEs. One potential solution to mitigate this could be to reduce the b-value to 4,000–5,000 s/mm^2 and use numerical simulations to determine the optimal range of TEs, based on the intra-axonal relaxation times reported in this study and the expected noise range.

Despite these limitations, our study provides a promising approach for estimating axon radii and understanding their relationship with MRI relaxation times. Future studies could address these limitations and expand the analysis to other brain regions to further validate the technique.

6. Code and data availability statement

The datasets used in this study and the Python code can be made available upon request from the corresponding authors, subject to the following terms and conditions. The mean effective histological radii of the Histology1, Histology2, and Histology3 samples are reported in **Figure 9** and **Table 1**, respectively. We can also share any other derived metric from the Histology1-Histology2 samples. Additional results for the Histology2 and Histology3 samples are available in Caminiti et al. (2009) and Wegiel et al. (2018), respectively. The MRI data will be available upon signing a data-sharing agreement with Cardiff University. Finally, we can provide the Python scripts used in this study upon request.

7. Appendix: effective axon radius

We derive the mean effective radius that can be estimated from the intra-axonal T_2 and T_1 relaxation times. For simplicity, we will separately analyses the components of the measured signals that exclusively depend on T_2 and T_1.

7.1. Axon radius estimated from T_2^a

The signal arising from the intra-axonal compartments is the sum of signals from the spins inside all axons. The measured T_2-weighted signal for a given echo time TE is

$$M(TE) = k \sum_{i=1}^{P} N_i \exp\left(-\frac{TE}{T_2^i}\right), \tag{7}$$

where P is the total number of axons, N_i is the number of spins inside the i^{th} axon with transverse relaxation time T_2^i, and k is a constant that depends on the sequence/scanner.

Assuming that the proton density (PD) does not depend on the axon radius, then

$$PD = \frac{N_i}{\pi r_i^2 h} = \frac{\sum_{i=1}^{P} N_i}{\sum_{i=1}^{P} \pi r_i^2 h} = \frac{N_t}{\sum_{i=1}^{P} \pi r_i^2 h}. \quad (8)$$

where $\pi r_i^2 h$ is the volume occupied by the i^{th} axon, h is the axon length, and N_t is the total number of spins in the intra-axonal space.

From Eq. (8) we obtain the following simplified relationship:

$$N_i = N_t \frac{r_i^2}{\sum_{i=1}^{P} r_i^2}, \quad (9)$$

By plugging Eq. (9) into Eq. (7) we get.

$$M(TE) = kN_t \sum_{i=1}^{P} \left(\frac{r_i^2}{\sum_{i=1}^{P} r_i^2} \right) \exp\left(-\frac{TE}{T_2^i} \right). \quad (10)$$

We estimate a single intra-axonal T_2 per voxel, which is equivalent to assuming that all the T_2s in Eq. (10) are equal to T_2^a (i.e., and hence that all axons in the voxel have the same radius $\bar{r}$); in that case, Eq. (10) becomes.

$$M(TE) \approx kN_t \sum_{i=1}^{P} \left(\frac{1}{P} \right) \exp\left(-\frac{TE}{T_2^a} \right) = kN_t \exp\left(-\frac{TE}{T_2^a} \right). \quad (11)$$

To understand how the distribution of axon radii in Eq. (10) affects the apparent T_2^a in Eq. (11), we use the following approximation.

$$kN_t \exp\left(-\frac{TE}{T_2^a} \right) \approx kN_t \sum_{i=1}^{P} \left(\frac{r_i^2}{\sum_{i=1}^{P} r_i^2} \right) \exp\left(-\frac{TE}{T_2^i} \right). \quad (12)$$

After plugging the surface-based relaxation model in Eq. (1) and removing common terms on both sides of the previous equation, we get

$$\exp\left(-\frac{2TE\rho_2}{\bar{r}} \right) \approx \sum_{i=1}^{P} \left(\frac{r_i^2}{\sum_{i=1}^{P} r_i^2} \right) \exp\left(-\frac{2TE\rho_2}{r_i} \right), \quad (13)$$

where we cancelled the contribution from the cytoplasmic T_2^c, which appears on both sides of the equation.

The exponential terms $2TE\rho_2/r_i$ are small (according to our data and results < 0.5), so we can expand the exponentials in Taylor series using a first-order approximation as

$$\begin{aligned} 1 - \frac{2TE\rho_2}{\bar{r}} &\approx \sum_{i=1}^{P} \left(\frac{r_i^2}{\sum_{i=1}^{P} r_i^2} \right) \left(1 - \frac{2TE\rho_2}{r_i} \right) \quad (14) \\ &= \sum_{i=1}^{P} \left(\frac{r_i^2}{\sum_{i=1}^{P} r_i^2} \right) - \sum_{i=1}^{P} \left(\frac{r_i 2TE\rho_2}{\sum_{i=1}^{P} r_i^2} \right) \\ &= 1 - 2TE\rho_2 \sum_{i=1}^{P} \left(\frac{r_i}{\sum_{i=1}^{P} r_i^2} \right) \end{aligned}$$

Therefore,

$$\begin{aligned} \frac{1}{\bar{r}} &\approx \sum_{i=1}^{P} \left(\frac{r_i}{\sum_{i=1}^{P} r_i^2} \right), \\ \bar{r} &\approx \frac{\sum_{i=1}^{P} r_i^2}{\sum_{i=1}^{P} r_i} = \frac{\langle r^2 \rangle}{\langle r \rangle}, \end{aligned} \quad (15)$$

This is the expression that we used to correct the histological radii, which is the mean effective radius estimated from this relaxation model.

7.2. Axon radius estimated from T_1^a

Following a similar approach, the measured T_1-weighted signal for a given TI is

$$\begin{aligned} M(TI) &= k \sum_{i=1}^{P} N_i \left| 1 - 2\exp\left(-\frac{TI}{T_1^i} \right) \right| \quad (16) \\ &= kN_t \sum_{i=1}^{P} \left(\frac{r_i}{\sum_{i=1}^{P} r_i^2} \right) \left| 1 - 2\exp\left(-\frac{TI}{T_1^i} \right) \right|. \end{aligned}$$

Note that we neglected the TR dependence because, in practice, this experimental parameter is much higher than the intra-axonal T_1, and its contribution is minor.

As we estimate a single apparent intra-axonal T_1 per voxel, our model is equivalent to assuming that all the T_1s are equal to T_1^a (i.e., all axons in the voxel have the same radius $\bar{r}$); thus, Eq. (16) becomes.

$$M(TI) = kN_t \left| 1 - 2\exp\left(-\frac{TI}{\bar{T}_1} \right) \right|. \quad (17)$$

To investigate how the distribution of axon radii in Eq. (16) affects the apparent T_1^a in Eq. (17), we use the approximation

$$kN_t \left| 1 - 2\exp\left(-\frac{TI}{\bar{T}_1} \right) \right| \approx kN_t \sum_{i=1}^{P} \left(\frac{r_i^2}{\sum_{i=1}^{P} r_i^2} \right) \left| 1 - 2\exp\left(-\frac{TI}{T_1^i} \right) \right|. \quad (18)$$

After plugging the surface-based relaxation model in Eq. (2) and removing common terms on both sides of Eq. (18) we obtain.

$$\exp\left(-\frac{2TI\rho_1}{\bar{r}} \right) \approx \sum_{i=1}^{P} \left(\frac{r_i^2}{\sum_{i=1}^{P} r_i^2} \right) \exp\left(-\frac{2TI\rho_1}{r_i} \right), \quad (19)$$

Note that Eq. (19) is similar to Eq. (13). Hence, we can get the same relationship given by Eq. (15) after using the first-order Taylor series approximation, which is justified by the small values of the exponential terms $2TI\rho_1/r_i$ (according to our MRI acquisition parameters and results < 0.3).

7.3. Histological tissue shrinkage and sampling issues

The histological datasets were inspected to investigate the trend in axon radii. As expected, the data followed the "low-high-low" pattern in axon radii, as shown in Figure 9. However, the mean effective histological radii differed between the samples. The axon radii from the Histology1-Histology2 samples were about 25% higher than those in the Histology3 sample. These differences could be due to genuine anatomical variations between the postmortem brains or related to the histological procedures and corresponding tissue shrinkage factors. The T_2-based predicted radii in all subjects

followed a similar "low-high-low" pattern closer to the values measured in the Histology1 sample, as this was the calibration sample.

In this study, the histological samples were not corrected for tissue shrinkage, which can affect the accuracy of the estimated axon radii. Consequently, the *in vivo* axons may be thicker than the reported histological values (Barazany et al., 2009; Horowitz et al., 2015). The extent of tissue shrinkage can vary widely depending on the used histological preparation techniques, with reported shrinkage factors ranging from 1 to 65% (Lamantia and Rakic, 1990; Aboitiz et al., 1992; Houzel et al., 1994; Riise and Pakkenberg, 2011). It is also unclear if shrinkage affects all brain axons equally, as previous research has shown varying shrinkage levels in different cellular compartments (Hursh, 1939). However, there is currently limited knowledge about the effects of shrinkage on CC axons in the human brain (Innocenti et al., 2019). Please refer to Dyrby et al. (2018) for further information on tissue shrinkage issues.

Sampling biases can impact histological radii measurements. One issue is that only a small amount of tissue is typically sampled, so the microstructure properties of these regions may not accurately represent properties in other regions within the ROIs (Assaf et al., 2008). Another issue is that larger axons can influence the mean effective radius more than the mean radius of the distribution. Since larger axons are less common, accurately detecting their proportions in a sample requires measuring a larger number of axons. We observed this effect in the Histology1 and Histology2 samples, where the effective radii in the four ROIs used in Histology1 (which had denser spatial sampling) were consistently higher than those in the same ROIs measured in the Histology2 sample (see **Figure 9**).

For these reasons, the presented histological results should not be considered the definitive "ground truth." Future studies should aim to identify optimal histological procedures, such as those suggested by Sepehrband et al. (2016b), and also explore the use of neural network approaches for automatic measurement of tens of thousands of axons per ROI to reduce sampling biases (Mordhorst et al., 2022). It is also worth noting that because the proposed calibration approach uses histological data as a reference, the predicted radii are relative to the specific histological sample employed.

7.4. The effect of spherical cells: spherical mean vs. spherical variance

A recent study showed that isotropically-restricted compartments might bias the intra-axonal T_2 estimated from the spherical mean of the strongly diffusion-weighted signal (Pizzolato et al., 2022). Thus, our estimates could be partially affected by cell nuclei, vacuoles, and other types of structures in the white matter (Andersson et al., 2020). As a remedy for that problem, it was proposed to use the spherical variance (Pizzolato et al., 2022) as a "filter" since the spherical variance of an ordered axon bundle would be high, but in an isotropic component would be close to zero. Although the results obtained in that study are promising, the spherical variance is more sensitive to noise than the spherical mean. Moreover, a larger number of diffusion gradient directions than that used in our study is necessary to employ this novel technique [48 vs. > 96 in Pizzolato et al. (2022)]. In future studies, we plan to acquire dMRI data using a higher angular resolution to compare both techniques' outputs and filter out any contribution from spherical cells.

7.5. Is the cytoplasmic T2 constant?

The cytoplasmic T_2 may be influenced by the intra-axonal microstructure, such as the number of organelles and the density of cytoskeletal elements such as neurofilaments, microtubules, and actin, as well as the chemical composition, including the type and density of macromolecules and water content.

Numerous morphometric studies have provided evidence of a linear correlation between neurofilament and microtubule numbers and axonal cross-sectional area (Friede and Samorajski, 1970; Hoffman et al., 1987). These studies suggest that myelinated axons contain more neurofilaments than microtubules and that the axon radius adjusts to maintain a constant density of neurofilaments. It was demonstrated that this relationship is regulated by the relative degree of phosphorylation of the mid-sized and heavy neurofilaments (Rao et al., 1998). Furthermore, the myelin-associated glycoprotein is implicated in the signaling cascade controlling neurofilament phosphorylation (Lunn et al., 2002) and axon radius. As neurofilaments are the more abundant cytoskeletal elements and their density is nearly constant in myelinated axons with different radii, we do not anticipate a relationship between cytoplasmic T_2 and axon radius mediated by neurofilament density in the axonal cytoskeleton.

However, a previous study using electron probe x-ray microanalysis (LoPachin et al., 1991) measured the concentrations of biologically relevant elements (such as Na, P, S, Ca, CI, K, and Mg, in mmol/kg dry or wet weight) and water content in the axoplasm of rat optic nerve myelinated axons. The study found that dry and wet weight concentrations of Na, P, S, and Ca were not dependent on the axonal radius. In contrast, the axoplasmic concentration of K, CI, and Mg was related to axon radius. Furthermore, the water content in medium and large axons was similar (between 91 and 92%) but slightly reduced in small axons (89%). These findings suggest that the chemical composition of the axoplasm depends on the axon radius (LoPachin et al., 1991). Therefore, until the effect of K, CI, and Mg on intra-axonal relaxation times is clarified, the surface-based relaxation model employed [i.e., Eqs. (1) and (2)] should be regarded as a first-order approximation.

Despite this limitation, our findings (refer to **Figures 5**, **7**) suggest a linear relationship between the inverse of intra-axonal relaxation times and axon radius, consistent with predictions made by the surface-based relaxation model we employed. Our empirical results demonstrate that the calibration step enables us to estimate the mean axon radius in various regions of the midsagittal CC (refer to **Figures 6**, **8**, **9**). As we did not observe any significant non-linear relationships between intra-axonal relaxation times and axon radii (within the range of measured radii in the midsagittal CC), we conclude that any non-linear dependence is weak and can be disregarded. Hence, either the cytoplasmic relaxation times remain constant, as assumed in this study, or they vary linearly with axon radius. In the following, we present some examples where the

calibrated model could predict the axon radius accurately, even if the cytoplasmic relaxation times depend on the axon radius.

Let us consider two distinct scenarios: In the first case, the cytoplasmic T_2 increases with the radius (similar to the observed trend for intra-axonal T_2 time), while in the second case, it decreases. The former corresponds to the model

$$\frac{1}{T_2^c(r)} = \frac{1}{T_2^{const}} + \frac{k}{r}, \tag{20}$$

where T_2^{const} is a constant term common to all axons and k is a constant quantifying how fast the cytoplasmic T_2 changes with r. By plugging this equation into our relaxation model [Eq. (1)], we get a similar model with redefined parameters

$$\frac{1}{T_2^a} = \frac{1}{T_2^{const}} + \frac{\gamma}{r}, \tag{21}$$

where $\gamma = 2\rho_2 + k$. Althout the new parameters T_2^{const} and γ cannot be interpreted as the cytoplasmic T_2 and surface relaxivity, they can be estimated by employing our calibration approach. Therefore, the resulting model would be equally valid for predicting axon radius.

The second case corresponds to a model that predicts a decrease in $T_2^c(r)$ for larger axons.

$$\frac{1}{T_2^c(r)} = \frac{1}{T_2^{const}} + kr. \tag{22}$$

After plugging Eq. (22) into Eq. (1) and regrouping terms, the relaxation model becomes.

$$\frac{1}{T_2^a} = \frac{1}{T_2^{const}} + \frac{(kr^2 + 2\rho_2)}{r}. \tag{23}$$

In our experiments, we observed a net reduction of T_2^a with r. Hence, the surface relaxivity term must dominate the relaxation over k, i.e., $2\rho_2/r > kr$ for the range of measured radii. The modified parameters to be calibrated in this model are T_2^{const} and $\gamma = 2\rho_2 + kr^2$. In this case, our model only provides a good approximation if the previous inequality becomes $2\rho_2/r >> kr$.

It is important to note that the models presented in this section [Eqs. (20)–(23)] are hypothetical and were discussed to illustrate the flexibility and limitations of the calibration approach in cases where the underlying assumptions are not met. Similar results can be obtained by using the intra-axonal T_1 time or assuming a surface relaxivity that depends on the radius.

7.6. Orientation dependence on relaxation times

By computing the spherical mean of the diffusion signal, the resulting orientation-averaged signal is independent of the fiber orientation distribution and thus is not affected by the presence of fiber crossings and varying levels of fiber orientation dispersion (Lindblom et al., 1977; Callaghan et al., 1979; Kaden et al., 2016a). However, the spherical mean does not eliminate the dependence on the orientation susceptibility effects, i.e., the measured signal still depends on the angle between the B0 magnetic field and the fiber orientation. Some previous studies have reported this orientation dependence for both the T_2^* and T_2 (Oh et al., 2013; Aggarwal et al., 2016; Gil et al., 2016) and T_1 (Knight and Kauppinen, 2016; Knight et al., 2017, 2018; Schyboll et al., 2018, 2020). Notably, while (McKinnon and Jensen, 2019) reported a significant intra-axonal T_2 orientation effect, a recent study found that extra-axonal T_2 is more affected by this phenomenon than intra-axonal T_2 (Tax et al., 2021). Given these inconsistent findings, further research is needed to determine whether the orientation-dependent T_2 effect is significant enough to be considered in this model.

In our study, the regions of interest were located in the medial part of the CC, where the angle between the B0 vector field and the nerve fibers remains relatively constant. Therefore, our findings are not likely affected by B0-orientation-related bias. However, the orientation effect should be modeled in brain regions with different fiber orientations, as it may affect the estimation. Despite this potential limitation, in **Figure 10**, we present T_2-based radius images across the entire white matter, showing the spatial variability of estimated radii across different regions, especially in the sagittal slices depicting the midsagittal CC cross-sections. The estimates from all subjects demonstrate a similar concordant pattern, as well as the maps of the same subject (Subject3) obtained from the two diffusion-relaxation MRI sequences, although some differences are noticeable due to the different voxel sizes used in both acquisitions.

7.7. Is the intra-axonal relaxation process mono-exponential and time-independent?

A recent theoretical formulation by Kiselev and Novikov (2018) demonstrated how the interplay between diffusion and spin dephasing in a heterogeneous environment could produce a non-mono-exponential time-dependent transverse relaxation signal. While this effect may be significant for short TEs, our relatively long TEs (i.e., > 73 ms) and diffusion times (Δ = 22 ms, δ = 8 ms) used in this study (compared to the small intra-axonal space where the restricted diffusion process takes place) indicate that a mono-exponential signal relaxation is expected for the spins inside each axon.

In our study, we estimated a single intra-axonal relaxation time per voxel. However, if axon radii are distributed with non-negligible variance, a more complete formulation must consider distributions of relaxation times. Estimating a non-parametric distribution of relaxation times is problematic from a practical point of view because a large number of TEs/TIs would be required. Nevertheless, an approach similar to that introduced in AxCaliber (Assaf et al., 2008) could be adopted by assuming a parametric form for such distributions, as shown in Sepehrband et al. (2016a). Future studies should investigate this generalization further.

Data availability statement

The raw data supporting the conclusions of this article will be made available by the authors, without undue reservation.

Ethics statement

The studies involving human participants were reviewed and approved by the Cardiff University Brain Research Centre, Wales, UK. The patients/participants provided their written informed consent to participate in this study.

Author contributions

MB and DJ: acquisition of data and design, analysis and interpretation, drafting of the manuscript, and critical revision. MP, SM, TD, CG, and J-PT: interpretation of data, drafting of the manuscript, and critical revision. CT and UR: acquisition of data, interpretation of data, drafting of the manuscript, and critical revision. EC-R: study conception and design, analysis and interpretation, drafting of the manuscript, and critical revision. All authors contributed to the article and approved the submitted version.

Funding

EC-R was supported by the Swiss National Science Foundation (SNSF), Ambizione grant PZ00P2_185814. DJ was supported by a Wellcome Trust Investigator Award (096646/Z/11/Z) and a Wellcome Trust Strategic Award (104943/Z/14/Z). TD has received funding from the European Research Council (ERC) under the European Union's Horizon Europe Research and Innovation Programme (grant agreement no.101044180). CT was supported by the Wellcome Trust (215944/Z/19/Z) and the Dutch Research Council (NWO, 17331). For the purpose of open access, the author has applied a CC-BY public copyright license to any author accepted manuscript version arising from this submission. The presented study is a tribute to Professor Giorgio Innocenti (1946–2021).

Conflict of interest

MB was an employee of Hays plc and a consultant for F. Hoffmann-La Roche Ltd. SM was an employee and shareholder of F. Hoffmann-La Roche Ltd.

The remaining authors declare that the research was conducted in the absence of any commercial or financial relationships that could be construed as a potential conflict of interest.

Publisher's note

References

Aboitiz, F., Rodríguez, E., Olivares, R., and Zaidel, E. (1996). Age-related changes in fibre composition of the human corpus callosum: Sex differences. *Neuroreport* 7, 1761–1764. doi: 10.1097/00001756-199607290-00013

Aboitiz, F., Scheibel, A. B., Fisher, R. S., and Zaidel, E. (1992). Fiber composition of the human corpus callosum. *Brain Res.* 598, 143–153. doi: 10.1016/0006-8993(92)90178-C

Aggarwal, M., Kageyama, Y., Li, X., and Van Zijl, P. C. (2016). B0-orientation dependent magnetic susceptibility-induced white matter contrast in the human brainstem at 11.7T. *Magn. Reson. Med.* 75, 2455–2463. doi: 10.1002/MRM.26208

Alexander, D. C. (2008). A general framework for experiment design in diffusion MRI and its application in measuring direct tissue-microstructure features. *Magn Reson Med* 60, 439–448. doi: 10.1002/mrm.21646

Alexander, D. C., Dyrby, T. B., Nilsson, M., and Zhang, H. (2019). Imaging brain microstructure with diffusion MRI: Practicality and applications. *NMR Biomed.* 32:e3841. doi: 10.1002/NBM.3841

Alexander, D. C., Hubbard, P. L., Hall, M. G., Moore, E. A., Ptito, M., Parker, G. J., et al. (2010). Orientationally invariant indices of axon diameter and density from diffusion MRI. *Neuroimage* 52, 1374–1389.

Andersson, J. L. R., and Sotiropoulos, S. N. (2016). An integrated approach to correction for off-resonance effects and subject movement in diffusion MR imaging. *Neuroimage* 125, 1063–1078. doi: 10.1016/j.neuroimage.2015.10.019

Andersson, J. L. R., Skare, S., and Ashburner, J. (2003). How to correct susceptibility distortions in spin-echo echo-planar images: Application to diffusion tensor imaging. *Neuroimage* 20, 870–888. doi: 10.1016/S1053-8119(03)00336-7

Andersson, M., Kjer, H. M., Rafael-Patino, J., Pacureanu, A., Pakkenberg, B., Thiran, J. P., et al. (2020). Axon morphology is modulated by the local environment and impacts the noninvasive investigation of its structure–function relationship. *Proc. Natl. Acad. Sci. U. S. A.* 117, 33649–33659.

Arancibia-Cárcamo, I. L., Ford, M. C., Cossell, L., Ishida, K., Tohyama, K., and Attwell, D. (2017). Node of ranvier length as a potential regulator of myelinated axon conduction speed. *eLife* 6:23329. doi: 10.7554/ELIFE.23329

Assaf, Y., Alexander, D. C., Jones, D. K., Bizzi, A., Behrens, T. E., Clark, C. A., et al. (2013). The CONNECT project: Combining macro- and micro-structure. *Neuroimage* 80, 273–282.

Assaf, Y., and Basser, P. J. (2005). Composite hindered and restricted model of diffusion (CHARMED) MR imaging of the human brain. *Neuroimage* 27, 48–58. doi: 10.1016/j.neuroimage.2005.03.042

Assaf, Y., Blumenfeld-Katzir, T., Yovel, Y., and Basser, P. J. (2008). AxCaliber: A method for measuring axon diameter distribution from diffusion MRI. *Magn. Reson. Med.* 59, 1347–1354. doi: 10.1002/mrm.21577

Assaf, Y., Freidlin, R. Z., Rohde, G. K., and Basser, P. J. (2004). New modeling and experimental framework to characterize hindered and restricted water diffusion in brain white matter. *Magn. Reson. Med.* 52, 965–978. doi: 10.1002/mrm.20274

Avants, B. B., Epstein, C. L., Grossman, M., and Gee, J. C. (2008). Symmetric diffeomorphic image registration with cross-correlation: Evaluating automated labeling of elderly and neurodegenerative brain. *Med. Image Anal.* 12, 26–41.

Badaut, J., Lasbennes, F., Magistretti, P. J., and Regli, L. (2002). Aquaporins in brain: Distribution, physiology, and pathophysiology. *J. Cereb. Blood Flow Metab.* 22, 367–378.

Barakovic, M., Girard, G., Schiavi, S., Romascano, D., Descoteaux, M., Granziera, C., et al. (2021a). Bundle-Specific Axon Diameter Index as a New Contrast to Differentiate White Matter Tracts. *Front. Neurosci.* 15:646034. doi: 10.3389/FNINS.2021.646034

Barakovic, M., Tax, C. M. W., Rudrapatna, U., Chamberland, M., Rafael-Patino, J., Granziera, C., et al. (2021b). Resolving bundle-specific intra-axonal T2 values within a voxel using diffusion-relaxation tract-based estimation. *Neuroimage* 227:117617. doi: 10.1016/j.neuroimage.2020.117617

Barazany, D., Basser, P. J., and Assaf, Y. (2009). In vivo measurement of axon diameter distribution in the corpus callosum of rat brain. *Brain* 132, 1210–1220. doi: 10.1093/BRAIN/AWP042

Barral, J. K., Gudmundson, E., Stikov, N., Etezadi-Amoli, M., Stoica, P., and Nishimura, D. G. (2010). A robust methodology for in vivo T1 mapping. *Magn. Reson. Med.* 64, 1057–1067. doi: 10.1002/MRM.22497

Beaulieu, C. (2002). The basis of anisotropic water diffusion in the nervous system – a technical review. *NMR Biomed.* 15, 435–455. doi: 10.1002/nbm.782

Benjamini, D., Komlosh, M. E., Holtzclaw, L. A., Nevo, U., and Basser, P. J. (2016). White matter microstructure from nonparametric axon diameter distribution mapping. *Neuroimage* 135, 333–344. doi: 10.1016/j.neuroimage.2016.04.052

Brownstein, K. R., and Tarr, C. E. (1977). Spin-lattice relaxation in a system governed by diffusion. *J. Magn. Reson.* 26, 17–24. doi: 10.1016/0022-2364(77)90230-X

Brownstein, K. R., and Tarr, C. E. (1979). Importance of classical diffusion in NMR studies of water in biological cells. *Phys. Rev. A* 19, 2446–2453. doi: 10.1103/PhysRevA.19.2446

Burcaw, L. M., Fieremans, E., and Novikov, D. S. (2015). Mesoscopic structure of neuronal tracts from time-dependent diffusion. *Neuroimage* 114, 18–37. doi: 10.1016/j.neuroimage.2015.03.061

Bydder, G. M., Hajnal, J. V., and Young, I. R. (1998). MRI: Use of the inversion recovery pulse sequence. *Clin. Radiol.* 53, 159–176. doi: 10.1016/S0009-9260(98)80096-2

Callaghan, P. T., Jolley, K. W., and Lelievre, J. (1979). Diffusion of water in the endosperm tissue of wheat grains as studied by pulsed field gradient nuclear magnetic resonance. *Biophys. J.* 28, 133–141. doi: 10.1016/S0006-3495(79)85164-4

Caminiti, R., Ghaziri, H., Galuske, R., Hof, P. R., and Innocenti, G. M. (2009). Evolution amplified processing with temporally dispersed slow neuronal connectivity in primates. *Proc. Natl. Acad. Sci. U. S. A.* 106:19551. doi: 10.1073/PNAS.0907655106

Canales-Rodríguez, E. J., Alonso-Lana, S., Verdolini, N., Sarró, S., Feria, I., Montoro, I., et al. (2021a). Age- and gender-related differences in brain tissue microstructure revealed by multi-component T2 relaxometry. *Neurobiol. Aging* 106, 68–79. doi: 10.1016/J.NEUROBIOLAGING.2021.06.002

Canales-Rodríguez, E. J., Pizzolato, M., Piredda, G. F. G. F., Hilbert, T., Kunz, N., Pot, C., et al. (2021b). Comparison of non-parametric T2 relaxometry methods for myelin water quantification. *Med. Image Anal.* 69:101959. doi: 10.1016/j.media.2021.101959

Canales-Rodríguez, E. J., Pizzolato, M., Yu, T., Piredda, G. F., Hilbert, T., Radua, J., et al. (2021c). Revisiting the T2 spectrum imaging inverse problem: Bayesian regularized non-negative least squares. *Neuroimage* 244:118582. doi: 10.1016/j.neuroimage.2021.118582

Costa, A. R., Pinto-Costa, R., Sousa, S. C., and Sousa, M. M. (2018). The regulation of axon diameter: From axonal circumferential contractility to activity-dependent axon swelling. *Front. Mol. Neurosci.* 11:319. doi: 10.3389/FNMOL.2018.00319

Daducci, A., Canales-Rodríguez, E. J., Zhang, H., Dyrby, T. B., Alexander, D. C., and Thiran, J.-P. P. (2015). Accelerated microstructure imaging via convex optimization (AMICO) from diffusion MRI data. *Neuroimage* 105, 32–44. doi: 10.1016/j.neuroimage.2014.10.026

De Santis, S., Jones, D. K., and Roebroeck, A. (2016). Including diffusion time dependence in the extra-axonal space improves in vivo estimates of axonal diameter and density in human white matter. *Neuroimage* 130, 91–103. doi: 10.1016/j.neuroimage.2016.01.047

Deoni, S. C. L. L., Matthews, L., and Kolind, S. H. (2013). One component? Two components? Three? The effect of including a nonexchanging "free" water component in multicomponent driven equilibrium single pulse observation of T1 and T2. *Magn. Reson. Med.* 70, 147–154. doi: 10.1002/mrm.24429

Drakesmith, M., Harms, R., Rudrapatna, S. U., Parker, G. D., Evans, C. J., and Jones, D. K. (2019). Estimating axon conduction velocity *in vivo* from microstructural MRI. *Neuroimage* 203:116186. doi: 10.1016/J.NEUROIMAGE.2019.116186

Drobnjak, I., Zhang, H., Ianuş, A., Kaden, E., and Alexander, D. C. (2016). PGSE, OGSE, and sensitivity to axon diameter in diffusion MRI: Insight from a simulation study. *Magn. Reson. Med.* 75, 688–700. doi: 10.1002/mrm.25631

Dula, A. N., Gochberg, D. F., Valentine, H. L., Valentine, W. M., and Does, M. D. (2010). Multiexponential T2, magnetization transfer, and quantitative histology in white matter tracts of rat spinal cord. *Magn. Reson. Med.* 63, 902–909. doi: 10.1002/MRM.22267

Duval, T., McNab, J. A., Setsompop, K., Witzel, T., Schneider, T., Huang, S. Y., et al. (2015). *In vivo* mapping of human spinal cord microstructure at 300 mT/m. *Neuroimage* 118, 494–507. doi: 10.1016/J.NEUROIMAGE.2015.06.038

Dyrby, T. B., Innocenti, G. M., Bech, M., and Lundell, H. (2018). Validation strategies for the interpretation of microstructure imaging using diffusion MRI. *Neuroimage* 182, 62–79.

Dyrby, T. B., Søgaard, L. V., Hall, M. G., Ptito, M., and Alexander, D. C. (2013). Contrast and stability of the axon diameter index from microstructure imaging with diffusion MRI. *Magn. Reson. Med.* 70, 711–721. doi: 10.1002/mrm.24501

Edén, M. (2003). Computer simulations in solid-state NMR. III. Powder averaging. *Concepts Magn. Reson. Part A* 18, 24–55. doi: 10.1002/CMR.A.10065

Edgar, J. M., and Griffiths, I. R. (2014). *White matter structure: A microscopist's view*. Cambridge, MA: Academic Press.

Fan, Q., Nummenmaa, A., Witzel, T., Ohringer, N., Tian, Q., Setsompop, K., et al. (2020). Axon diameter index estimation independent of fiber orientation distribution using high-gradient diffusion MRI. *Neuroimage* 222:117197. doi: 10.1016/J.NEUROIMAGE.2020.117197

Finney, J. L., Rand, R. P., Franks, F., Pettersson, L., Bowron, D. T., Engberts, J. B. F. N., et al. (2004). Water? What's so special about it? *Philos. Trans. R. Soc. B Biol. Sci.* 359:1145. doi: 10.1098/RSTB.2004.1495

Friede, R. L., and Samorajski, T. (1970). Axon caliber related to neurofilaments and microtubules in sciatic nerve fibers of rats and mice. *Anat. Rec.* 167, 379–387. doi: 10.1002/AR.1091670402

Garyfallidis, E., Brett, M., Amirbekian, B., Rokem, A., van der Walt, S., Descoteaux, M., et al. (2014). Dipy, a library for the analysis of diffusion MRI data. *Front. Neuroinform.* 8:8. doi: 10.3389/fninf.2014.00008

Gil, R., Khabipova, D., Zwiers, M., Hilbert, T., Kober, T., and Marques, J. P. (2016). An in vivo study of the orientation-dependent and independent components of transverse relaxation rates in white matter. *NMR Biomed.* 29, 1780–1790.

Goldstein, S. S., and Rall, W. (1974). Changes of action potential shape and velocity for changing core conductor geometry. *Biophys. J.* 14, 731–757. doi: 10.1016/S0006-3495(74)85947-3

Gudbjartsson, H., and Patz, S. (1995). The Rician distribution of noisy MRI data. *Magn Reson Med* 34, 910–914.

Halle, B. (1999). "Water in biological systems: The NMR picture," in *Hydration processes in biology: theoretical and experimental approaches*, ed. M.-C. Bellissent-Funel (Clifton, VA: IOS Press), 233–249.

Harkins, K. D., Beaulieu, C., Xu, J., Gore, J. C., and Does, M. D. (2021). A simple estimate of axon size with diffusion MRI. *Neuroimage* 227:117619. doi: 10.1016/j.neuroimage.2020.117619

Harkins, K. D., Xu, J., Dula, A. N., Li, K., Valentine, W. M., Gochberg, D. F., et al. (2016). The microstructural correlates of T1 in white matter. *Magn. Reson. Med.* 75, 1341–1345. doi: 10.1002/mrm.25709

Herrera, S. L., Sheft, M., Mercredi, M. E., Buist, R., Matsuda, K. M., and Martin, M. (2022). Axon diameter inferences in the human corpus callosum using oscillating gradient spin echo sequences. *Magn. Reson. Imaging* 85, 64–70. doi: 10.1016/J.MRI.2021.10.014

Hofer, S., Wang, X., Roeloffs, V., and Frahm, J. (2015). Single-shot T1 mapping of the corpus callosum: A rapid characterization of fiber bundle anatomy. *Front. Neuroanat.* 9:57. doi: 10.3389/FNANA.2015.00057

Hoffman, P. N., Cleveland, D. W., Griffin, J. W., Landes, P. W., Cowan, N. J., and Price, D. L. (1987). Neurofilament gene expression: A major determinant of axonal caliber. *Proc. Natl. Acad. Sci. U. S. A.* 84, 3472–3476. doi: 10.1073/PNAS.84.10.3472

Horowitz, A., Barazany, D., Tavor, I., Bernstein, M., Yovel, G., and Assaf, Y. (2015). In vivo correlation between axon diameter and conduction velocity in the human brain. *Brain Struct. Funct.* 220, 1777–1788. doi: 10.1007/s00429-014-0871-0

Houzel, J. -C., Milleret, C., and Innocenti, G. (1994). Morphology of callosal axons interconnecting areas 17 and 18 of the cat. *Eur. J. Neurosci.* 6, 898–917. doi: 10.1111/J.1460-9568.1994.TB00585.X

Huang, C. C., Hsu, C. C. H., Zhou, F. L., Kusmia, S., Drakesmith, M., Parker, G. J. M., et al. (2021). Validating pore size estimates in a complex microfiber environment on a human MRI system. *Magn Reson Med.* 86, 1514–1530.

Huang, S. Y., Nummenmaa, A., Witzel, T., Duval, T., Cohen-Adad, J., Wald, L. L., et al. (2015). The impact of gradient strength on *in vivo* diffusion MRI estimates of axon diameter. *Neuroimage* 106, 464–472. doi: 10.1016/j.neuroimage.2014.12.008

Hubbard, P. L., Zhou, F. L., Eichhorn, S. J., and Parker, G. J. M. (2015). Biomimetic phantom for the validation of diffusion magnetic resonance imaging. *Magn. Reson. Med.* 73, 299–305.

Hurlimann, M. D., Latour, L. L., and Sotak, C. H. (1994). Diffusion measurement in sandstone core: NMR determination of surface-to-volume ratio and surface relaxivity. *Magn Reson Imaging* 12, 325–327.

Hursh, J. B. (1939). Conduction velocity and diameter of nerve fibers. *Am. J. Physiol. Content* 127, 131–139. doi: 10.1152/ajplegacy.1939.127.1.131

Innocenti, G. M., Caminiti, R., Rouiller, E. M., Knott, G., Dyrby, T. B., Descoteaux, M., et al. (2019). Diversity of cortico-descending projections: Histological and diffusion MRI characterization in the monkey. *Cereb. Cortex* 29, 788–801. doi: 10.1093/CERCOR/BHX363

Innocenti, G. M., Vercelli, A., and Caminiti, R. (2014). The diameter of cortical axons depends both on the area of origin and target. *Cereb. Cortex* 24, 2178–2188. doi: 10.1093/cercor/bht070

Jelescu, I. O., Palombo, M., Bagnato, F., and Schilling, K. G. (2020). Challenges for biophysical modeling of microstructure. *J. Neurosci. Methods* 344:108861. doi: 10.1016/J.JNEUMETH.2020.108861

Jensen, J. H., Russell Glenn, G., and Helpern, J. A. (2016). Fiber ball imaging. *Neuroimage* 124, 824–833. doi: 10.1016/j.neuroimage.2015.09.049

Jones, D. K., Alexander, D. C., Bowtell, R., Cercignani, M., Dell'Acqua, F., McHugh, D. J., et al. (2018). Microstructural imaging of the human brain with a "super-scanner": 10 key advantages of ultra-strong gradients for diffusion MRI. *Neuroimage* doi: 10.1016/j.neuroimage.2018.05.047 [Epub ahead of print].

Kaden, E., and Alexander, D. C. (2013). Can T2-spectroscopy resolve submicrometer axon diameters? *Inf. Process Med. Imaging* 2013, 607–618.

Kaden, E., Kelm, N. D., Carson, R. P., Does, M. D., and Alexander, D. C. (2016a). Multi-compartment microscopic diffusion imaging. *Neuroimage* 139, 346–359. doi: 10.1016/j.neuroimage.2016.06.002

Kaden, E., Kruggel, F., and Alexander, D. C. (2016b). Quantitative mapping of the per-axon diffusion coefficients in brain white matter. *Magn. Reson. Med.* 75, 1752–1763. doi: 10.1002/mrm.25734

Kiselev, V. G., and Novikov, D. S. (2018). Transverse NMR relaxation in biological tissues. *Neuroimage* 182:149. doi: 10.1016/J.NEUROIMAGE.2018.06.002

Klein, A., Andersson, J., Ardekani, B. A., Ashburner, J., Avants, B., Chiang, M. C., et al. (2009). Evaluation of 14 nonlinear deformation algorithms applied to human brain MRI registration. *Neuroimage* 46, 786–802.

Knight, M. J., and Kauppinen, R. A. (2016). Diffusion-mediated nuclear spin phase decoherence in cylindrically porous materials. *J. Magn. Reson.* 269, 1–12. doi: 10.1016/J.JMR.2016.05.007

Knight, M. J., Damion, R. A., and Kauppinen, R. A. (2018). Observation of angular dependence of T1 in the human white matter at 3T. *Biomed. Spectrosc. Imaging* 7, 125–133. doi: 10.3233/BSI-180183

Knight, M. J., Dillon, S., Jarutyte, L., and Kauppinen, R. A. (2017). Magnetic resonance relaxation anisotropy: Physical principles and uses in microstructure imaging. *Biophys. J.* 112, 1517–1528. doi: 10.1016/J.BPJ.2017.02.026

Labadie, C., Lee, J. H., Rooney, W. D., Jarchow, S., Aubert-Frécon, M., Springer, C. S., et al. (2014). Myelin water mapping by spatially regularized longitudinal relaxographic imaging at high magnetic fields. *Magn. Reson. Med.* 71, 375–387. doi: 10.1002/mrm.24670

Lamantia, A.-S., and Rakic, P. (1990). Cytological and quantitative characteristics of four cerebral commissures in the rhesus monkey. *J. Comp. Neurol.* 291, 520–537. doi: 10.1002/cne.902910404

Lampinen, B., Szczepankiewicz, F., Novén, M., van Westen, D., Hansson, O., Englund, E., et al. (2019). Searching for the neurite density with diffusion MRI: Challenges for biophysical modeling. *Hum. Brain Mapp.* 40, 2529–2545.

Lancaster, J. L., Andrews, T., Hardies, L. J., Dodd, S., and Fox, P. T. (2003). Three-pool model of white matter. *J. Magn. Reson. Imaging* 17, 1–10. doi: 10.1002/jmri.10230

Langkammer, C., Krebs, N., Goessler, W., Scheurer, E., Ebner, F., Yen, K., et al. (2010). Quantitative MR imaging of brain iron: A postmortem validation study. *Radiology* 257, 455–462. doi: 10.1148/RADIOL.10100495

Lasiè, S., Szczepankiewicz, F., Eriksson, S., Nilsson, M., and Topgaard, D. (2014). Microanisotropy imaging: Quantification of microscopic diffusion anisotropy and orientational order parameter by diffusion MRI with magic-angle spinning of the q-vector. *Front. Phys.* 2:11. doi: 10.3389/fphy.2014.00011

Le Bihan, D. (2007). The "wet mind": Water and functional neuroimaging. *Phys. Med. Biol.* 52, R57–R90.

Levy, Y., and Onuchic, J. N. (2004). Water and proteins: A love-hate relationship. *Proc. Natl. Acad. Sci. U. S. A.* 101, 3325–3326.

Lindblom, G., Wennerström, H., and Arvidson, G. (1977). Translational diffusion in model membranes studied by NMR. *Int. J. Quant. Chem.* 12, 153–158.

LoPachin, R. M., Castiglia, C. M., and Saubermann, A. J. (1991). Elemental composition and water content of myelinated axons and glial cells in rat central nervous system. *Brain Res.* 549, 253–259. doi: 10.1016/0006-8993(91)90465-8

Lunn, M. P. T., Crawford, T. O., Hughes, R. A. C., Griffin, J. W., and Sheikh, K. A. (2002). Anti-myelin-associated glycoprotein antibodies alter neurofilament spacing. *Brain* 125, 904–911. doi: 10.1093/BRAIN/AWF072

Mackay, A., Whittall, K., Adler, J., Li, D., Paty, D., and Graeb, D. (1994). *In vivo* visualization of myelin water in brain by magnetic resonance. *Magn. Reson. Med.* 31, 673–677. doi: 10.1002/mrm.1910310614

Manjon, J. V., Coupe, P., Concha, L., Buades, A., Collins, D. L., and Robles, M. (2013). Diffusion weighted image denoising using overcomplete local PCA. *PLoS One* 8:e73021. doi: 10.1371/journal.pone.0073021

McConnell, H. M. (1958). Reaction rates by nuclear magnetic resonance. *J. Chem. Phys.* 28:430. doi: 10.1063/1.1744152

McHugh, D. J., Zhou, F. L., Wimpenny, I., Poologasundarampillai, G., Naish, J. H., Hubbard Cristinacce, P. L., et al. (2018). A biomimetic tumor tissue phantom for validating diffusion-weighted MRI measurements. *Magn. Reson. Med.* 80, 147–158.

McKinnon, E. T., and Jensen, J. H. (2019). Measuring intra-axonal T2 in white matter with direction-averaged diffusion MRI. *Magn. Reson. Med.* 81, 2985–2994. doi: 10.1002/MRM.27617

Mohnke, O., and Hughes, B. (2014). Jointly deriving NMR surface relaxivity and pore size distributions by NMR relaxation experiments on partially desaturated rocks. *Water Resour. Res.* 50, 5309–5321. doi: 10.1002/2014WR015282

Mordhorst, L., Morozova, M., Papazoglou, S., Fricke, B., Oeschger, J. M., Tabarin, T., et al. (2022). Towards a representative reference for MRI-based human axon radius assessment using light microscopy. *Neuroimage* 249:118906. doi: 10.1016/J.NEUROIMAGE.2022.118906

Müller-Petke, M., Dlugosch, R., Lehmann-Horn, J., and Ronczka, M. (2015). Nuclear magnetic resonance average pore-size estimations outside the fast-diffusion regime. *GEOPHYSICS* doi: 10.1190/geo2014-0167.1 [Epub ahead of print].

Nilsson, M., Lasič, S., Drobnjak, I., Topgaard, D., Westin, C.-F. F., Lasi?, S., et al. (2017). Resolution limit of cylinder diameter estimation by diffusion MRI: The impact of gradient waveform and orientation dispersion. *NMR Biomed.* 30:e3711. doi: 10.1002/nbm.3711

Ning, L., Westin, C., and Rathi, Y. (2022). Characterization of b-value dependent T_2 relaxation rates for probing neurite microstructure. *bioRxiv* [Preprint]. doi: 10.1101/2022.09.02.506440

Novikov, D. S., Fieremans, E., Jespersen, S. N., and Kiselev, V. G. (2019). *Quantifying brain microstructure with diffusion MRI: Theory and parameter estimation*. Hoboken, NJ: John Wiley & Sons, Ltd.

Nunes, D., Cruz, T. L., Jespersen, S. N., and Shemesh, N. (2017). Mapping axonal density and average diameter using non-monotonic time-dependent gradient-echo MRI. *J. Magn. Reson.* 277, 117–130. doi: 10.1016/J.JMR.2017.02.017

Oh, S. H., Kim, Y. B., Cho, Z. H., and Lee, J. (2013). Origin of B0 orientation dependent R2* (=1/T2*) in white matter. *Neuroimage* 73, 71–79. doi: 10.1016/j.neuroimage.2013.01.051

Pizzolato, M., Andersson, M., Canales-Rodríguez, E. J., Thiran, J. P., and Dyrby, T. B. (2022). Axonal T2 estimation using the spherical variance of the strongly diffusion-weighted MRI signal. *Magn. Reson. Imaging* 86, 118–134.

Pizzolato, M., Canales-Rodríguez, E. J., Andersson, M., and Dyrby, T. B. (2023). Axial and radial axonal diffusivities and radii from single encoding strongly diffusion-weighted MRI. *Med. Image Anal.* 86:102767. doi: 10.1016/J.MEDIA.2023.102767

Pykett, I. L., Rosen, B. R., Buonanno, F. S., and Brady, T. J. (1983). Measurement of spin-lattice relaxation times in nuclear magnetic resonance imaging. *Phys. Med. Biol.* 28:723. doi: 10.1088/0031-9155/28/6/012

Rao, M. V., Houseweart, M. K., Williamson, T. L., Crawford, T. O., Folmer, J., and Cleveland, D. W. (1998). Neurofilament-dependent radial growth of motor axons and axonal organization of neurofilaments does not require the neurofilament heavy subunit (NF-H) or its phosphorylation. *J. Cell Biol.* 143, 171–181. doi: 10.1083/JCB.143.1.171

Riise, J., and Pakkenberg, B. (2011). Stereological estimation of the total number of myelinated callosal fibers in human subjects. *J. Anat.* 218, 277–284. doi: 10.1111/J.1469-7580.2010.01333.X

Romascano, D., Barakovic, M., Rafael-Patino, J., Dyrby, T. B., Thiran, J. P., and Daducci, A. (2020). ActiveAxADD: Toward non-parametric and orientationally invariant axon diameter distribution mapping using PGSE. *Magn. Reson. Med.* 83, 2322–2330. doi: 10.1002/MRM.28053

Rushton, W. A. H. (1951). A theory of the effects of fibre size in medullated nerve. *J. Physiol.* 115:101. doi: 10.1113/JPHYSIOL.1951.SP004655

Schyboll, F., Jaekel, U., Petruccione, F., and Neeb, H. (2020). Origin of orientation-dependent R1 (=1/T1) relaxation in white matter. *Magn. Reson. Med.* 84, 2713–2723. doi: 10.1002/MRM.28277

Schyboll, F., Jaekel, U., Weber, B., and Neeb, H. (2018). The impact of fibre orientation on T1-relaxation and apparent tissue water content in white matter. *Magn. Reson. Mater. Phys. Biol. Med.* 31, 501–510. doi: 10.1007/s10334-018-0678-8

Sepehrband, F., Alexander, D. C., Kurniawan, N. D., Reutens, D. C., and Yang, Z. (2016b). Towards higher sensitivity and stability of axon diameter estimation with diffusion-weighted MRI. *NMR Biomed.* 29, 293–308. doi: 10.1002/nbm.3462

Sepehrband, F., Alexander, D. C., Clark, K. A., Kurniawan, N. D., Yang, Z., and Reutens, D. C. (2016a). Parametric probability distribution functions for axon diameters of corpus callosum. *Front. Neuroanat.* 10:59. doi: 10.3389/FNANA.2016.00059/BIBTEX

Slijkerman, W. F. J., and Hofman, J. P. (1998). Determination of surface relaxivity from NMR diffusion measurements. *Magn. Reson. Imaging* 16, 541–544. doi: 10.1016/S0730-725X(98)00058-7

Smith, S. M., Jenkinson, M., Woolrich, M. W., Beckmann, C. F., Behrens, T. E. J., Johansen-Berg, H., et al. (2004). Advances in functional and structural MR image analysis and implementation as FSL. *Neuroimage* 23, S208–S219.

Sørland, G. H., Djurhuus, K., Widerøe, H. C., Lien, J. R., and Skauge, A. (2007). "Absolute pore size distribution from NMR," in *Proceedings of the International Symposium of the Society of Core Analysts*, Trondheim.

Stikov, N., Boudreau, M., Levesque, I. R., Tardif, C. L., Barral, J. K., and Pike, G. B. (2015). On the accuracy of T1 mapping: Searching for common ground. *Magn. Reson. Med.* 73, 514–522. doi: 10.1002/MRM.25135

Stüber, C., Morawski, M., Schäfer, A., Labadie, C., Wähnert, M., Leuze, C., et al. (2014). Myelin and iron concentration in the human brain: A quantitative study of MRI contrast. *Neuroimage* 93, 95–106. doi: 10.1016/j.neuroimage.2014.02.026

Tax, C. M. W., Kleban, E., Chamberland, M., Baraković, M., Rudrapatna, U., and Jones, D. K. (2021). Measuring compartmental T2-orientational dependence in

human brain white matter using a tiltable RF coil and diffusion-T2 correlation MRI. *Neuroimage* 236:117967. doi: 10.1016/j.neuroimage.2021.117967

van Gelderen, P., Despres, D., van Zijl, P. C., Moonen, C. T. W. T., Vangelderen, P., Despres, D., et al. (1994). Evaluation of restricted diffusion in cylinders. Phosphocreatine in rabbit leg muscle. *J. Magn. Reson. B* 103, 255–260. doi: 10.1006/JMRB.1994.1038

Veraart, J., Novikov, D. S., and Fieremans, E. (2018). TE dependent Diffusion Imaging (TEdDI) distinguishes between compartmental T2 relaxation times. *Neuroimage* 182, 360–369.

Veraart, J., Novikov, D. S., Christiaens, D., Ades-aron, B., Sijbers, J., and Fieremans, E. (2016). Denoising of diffusion MRI using random matrix theory. *Neuroimage* 142, 394–406. doi: 10.1016/j.neuroimage.2016.08.016

Veraart, J., Nunes, D., Rudrapatna, U., Fieremans, E., Jones, D. K., Novikov, D. S., et al. (2020). Noninvasive quantification of axon radii using diffusion MRI. *eLife* 9:49855. doi: 10.7554/eLife.49855

Veraart, J., Raven, E. P., Edwards, L. J., Weiskopf, N., and Jones, D. K. (2021). The variability of MR axon radii estimates in the human white matter. *Hum. Brain Mapp.* 42, 2201–2213. doi: 10.1002/HBM.25359

Virtanen, P., Gommers, R., Oliphant, T. E., Haberland, M., Reddy, T., Cournapeau, D., et al. (2020). SciPy 1.0: Fundamental algorithms for scientific computing in Python. *Nat. Methods* 17, 261–272. doi: 10.1038/s41592-019-0686-2

Waxman, S. G., and Bennett, M. V. I. (1972). Relative conduction velocities of small myelinated and non-myelinated fibres in the central nervous system. *Nat. New Biol.* 238, 217–219. doi: 10.1038/newbio238217a0

Wegiel, J., Kaczmarski, W., Flory, M., Martinez-Cerdeno, V., Wisniewski, T., Nowicki, K., et al. (2018). Deficit of corpus callosum axons, reduced axon diameter and decreased area are markers of abnormal development of interhemispheric connections in autistic subjects. *Acta Neuropathol. Commun.* 6:143. doi: 10.1186/S40478-018-0645-7

Xu, J., Li, H., Harkins, K. D., Jiang, X., Xie, J., Kang, H., et al. (2014). Mapping mean axon diameter and axonal volume fraction by MRI using temporal diffusion spectroscopy. *Neuroimage* 103, 10–19. doi: 10.1016/j.neuroimage.2014.09.006

Yu, T., Canales-Rodríguez, E. J., Pizzolato, M., Piredda, G. F., Hilbert, T., Fischi-Gomez, E., et al. (2020). *Model-informed machine learning for multi-component T2 relaxometry*. Amsterdam: Elsevier, doi: 10.1016/j.media.2020.101940

Zhang, H., Hubbard, P. L., Parker, G. J., and Alexander, D. C. (2011). Axon diameter mapping in the presence of orientation dispersion with diffusion MRI. *Neuroimage* 56, 1301–1315.

Zhang, L., Wang, L., Kao, Y. T., Qiu, W., Yang, Y., Okobiah, O., et al. (2007). Mapping hydration dynamics around a protein surface. *Proc. Natl. Acad. Sci. U. S. A.* 104, 18461–18466. doi: 10.1073/PNAS.0707647104/SUPPL_FILE/IMAGE882.GIF

Zhou, F. L., McHugh, D. J., Li, Z., Gough, J. E., Williams, G. R., and Parker, G. J. M. (2021). Coaxial electrospun biomimetic copolymer fibres for application in diffusion magnetic resonance imaging. *Bioinspir. Biomim.* 16:46016. doi: 10.1088/1748-3190/ABEDCF

Zimmerman, J. R., and Brittin, W. E. (1957). Nuclear magnetic resonance studies in multiple phase systems: Lifetime of a water molecule in an adsorbing phase on silica gel. *J. Phys. Chem.* 61, 1328–1333. doi: 10.1021/j150556a015

frontiers | Frontiers in Neuroscience

TYPE Original Research
PUBLISHED 25 October 2023
DOI 10.3389/fnins.2023.1178473

OPEN ACCESS

EDITED BY
André Döring,
Cardiff University, United Kingdom

REVIEWED BY
Alaka Acharya,
College of Biomedical Engineering and Applied Sciences, Nepal
Fuyuki Karube,
Hokkaido University, Japan

*CORRESPONDENCE
Jeff L. Waugh
✉ jeff.waugh@utsouthwestern.edu

†These authors share senior authorship

RECEIVED 02 March 2023
ACCEPTED 04 September 2023
PUBLISHED 25 October 2023

CITATION
Funk AT, Hassan AAO, Brüggemann N, Sharma N, Breiter HC, Blood AJ and Waugh JL (2023) In humans, striato-pallido-thalamic projections are largely segregated by their origin in either the striosome-like or matrix-like compartments.
Front. Neurosci. 17:1178473.
doi: 10.3389/fnins.2023.1178473

In humans, striato-pallido-thalamic projections are largely segregated by their origin in either the striosome-like or matrix-like compartments

Adrian T. Funk[1], Asim A. O. Hassan[2], Norbert Brüggemann[3†], Nutan Sharma[4†], Hans C. Breiter[5,6†], Anne J. Blood[5,7,8,9†] and Jeff L. Waugh[1,8,9*†]

[1]Division of Pediatric Neurology, Department of Pediatrics, University of Texas Southwestern, Dallas, TX, United States, [2]Department of Natural Sciences and Mathematics, University of Texas at Dallas, Richardson, TX, United States, [3]Department of Neurology and Institute of Neurogenetics, University of Lübeck, Lübeck, Germany, [4]Department of Neurology, Massachusetts General Hospital, Harvard University, Boston, MA, United States, [5]Laboratory of Neuroimaging and Genetics, Massachusetts General Hospital, Charlestown, MA, United States, [6]Warren Wright Adolescent Center, Department of Psychiatry and Behavioral Sciences, Northwestern University Feinberg School of Medicine, Chicago, IL, United States, [7]Department of Psychiatry, Massachusetts General Hospital, Harvard University, Boston, MA, United States, [8]Mood and Motor Control Laboratory, Massachusetts General Hospital, Charlestown, MA, United States, [9]Martinos Center for Biomedical Imaging, Massachusetts General Hospital, Charlestown, MA, United States

Cortico-striato-thalamo-cortical (CSTC) loops are fundamental organizing units in mammalian brains. CSTCs process limbic, associative, and sensorimotor information in largely separated but interacting networks. CTSC loops pass through paired striatal compartments, striosome (aka patch) and matrix, segregated pools of medium spiny projection neurons with distinct embryologic origins, cortical/subcortical structural connectivity, susceptibility to injury, and roles in behaviors and diseases. Similarly, striatal dopamine modulates activity in striosome and matrix in opposite directions. Routing CSTCs through one compartment may be an anatomical basis for regulating discrete functions. We used differential structural connectivity, identified through probabilistic diffusion tractography, to distinguish the striatal compartments (striosome-like and matrix-like voxels) in living humans. We then mapped compartment-specific projections and quantified structural connectivity between each striatal compartment, the globus pallidus interna (GPi), and 20 thalamic nuclei in 221 healthy adults. We found that striosome-originating and matrix-originating streamlines were segregated within the GPi: striosome-like connectivity was significantly more rostral, ventral, and medial. Striato-pallido-thalamic streamline bundles that were seeded from striosome-like and matrix-like voxels transited spatially distinct portions of the white matter. Matrix-like streamlines were 5.7-fold more likely to reach the GPi, replicating animal tract-tracing studies. Striosome-like connectivity dominated in six thalamic nuclei (anteroventral, central lateral, laterodorsal, lateral posterior, mediodorsal-medial, and medial geniculate). Matrix-like connectivity dominated in seven thalamic nuclei (centromedian, parafascicular, pulvinar-anterior, pulvinar-lateral, ventral lateral-anterior, ventral lateral-posterior, ventral posterolateral). Though we mapped all thalamic nuclei independently, functionally-related nuclei were matched for compartment-level bias. We validated these results with prior thalamostriate tract tracing studies in non-human primates and other species; where reliable data was available, all agreed with our measures of structural connectivity. Matrix-like connectivity was lateralized (left > right hemisphere)

in 18 thalamic nuclei, independent of handedness, diffusion protocol, sex, or whether the nucleus was striosome-dominated or matrix-dominated. Compartment-specific biases in striato-pallido-thalamic structural connectivity suggest that routing CSTC loops through striosome-like or matrix-like voxels is a fundamental mechanism for organizing and regulating brain networks. Our MRI-based assessments of striato-thalamic connectivity in humans match and extend the results of prior tract tracing studies in animals. Compartment-level characterization may improve localization of human neuropathologies and improve neurosurgical targeting in the GPi and thalamus.

KEYWORDS

striatum, thalamus, striosome and matrix compartments, patch, classification targets tractography, probabilistic diffusion tractography, cortico-striato-thalamo-cortical circuit, globus pallidus interna

1. Introduction

The mammalian thalamus projects to every cortical area, and each cortical area projects through intermediate structures to specific thalamic nuclei (Jones, 1998; Dufour et al., 2003). However, the thalamus is much more than a passive relay for cortical information; the thalamus integrates information from diverse cortical inputs to stabilize and reshape cortical networks (Hwang et al., 2017) and mediates direct information transfer between cortical areas (Sherman and Guillery, 2013). Precise characterization of connectivity with the thalamus is therefore essential to understanding the organization and functions of higher-order central nervous systems.

Delineating distinct thalamic nuclei has been accomplished based on histologic features (Krauth et al., 2010), structural connectivity (Behrens et al., 2003), resting state functional connectivity (Jones, 1998), and combinations of these methods (Iglesias et al., 2018; Iglehart et al., 2020). These methods have defined between 10 and 26 anatomically and functionally distinct thalamic nuclei (Iglesias et al., 2018; Ilinsky et al., 2018; Mai and Majtanik, 2018). The complexity of thalamic nuclear organization underpins the multimodal functions of cortico-striatal-thalamo-cortical (CSTC) loops (Alexander et al., 1986), anatomically segregated networks that mediate information transfer among functionally linked structures. CSTC loops modulate function beyond the cortex, striatum, and thalamus as well, through projections to the cerebellum, brainstem, and spinal cord (Haber, 2003). Identifying the afferent and efferent patterns of structural connectivity with each thalamic nucleus is essential to understanding the clinical impact of focal thalamic lesions (Hwang et al., 2017, 2020) and extrathalamic lesions that disrupt thalamic networks (Kim et al., 2021; Kletenik et al., 2022).The importance of CSTC loops in normal function and dysfunction in humans necessitates a more granular inspection of striatothalamic connectivity patterns (Joel, 2001).

Connectivity between the striatum and thalamus can be further specified based on the projections of two anatomically and functionally distinct compartments of the mammalian striatum, the striosome (aka patch) and matrix. Tract tracing studies in cats, rodents, and primates describe thalamostriate projections that are biased toward one striatal compartment (Nauta et al., 1974; Veening et al., 1980; Berendse and Groenewegen, 1990; Ragsdale and Graybiel, 1991; Féger et al., 1994). While thalamo-striate projections have been extensively mapped through tracer injections, and one study (Aoki et al., 2019) mapped multi-synaptic CSTC circuits using retrograde tracers, we found no prior reports that mapped compartment-specific multi-synaptic striato-pallido-thalamic projections. Therefore, the contributions of striosome and matrix to the regulation of specific thalamic nuclei, and specific CSTC loops, remain unknown.

While striosome and matrix are indistinguishable by routine histologic stains, the compartments can be readily identified using immunohistochemical methods in animal and human post-mortem tissue (Graybiel and Ragsdale, 1978; Holt et al., 1997). Both striatal compartments are comprised of medium spiny neurons (MSNs), but the two populations migrate from the lateral ganglionic eminence at different times in development (Graybiel and Hickey, 1982; Kelly et al., 2018). They have largely distinct patterns of afferent and efferent connectivity (Lévesque and Parent, 2005; reviewed in Waugh et al., 2022), segregated vascular supplies (Feekes and Cassell, 2006), and distinct expression of >60 surface proteins (Morigaki and Goto, 2015). Similar to other primate and non-primate mammals, in the human striatum the striosome is enriched in the medial, rostral, and ventral striatum – while the matrix is more common in the lateral, caudal, and dorsal striatum (Graybiel and Ragsdale, 1978; Goldman-Rakic, 1982; Donoghue and Herkenham, 1986; Graybiel, 1990; Desban et al., 1993; Eblen and Graybiel, 1995). They appear to fill opposing roles in behavior, with distinct influences on cost–benefit assessments, multiple models of learning, and motor action selection (Joel et al., 2002; Stephenson-Jones et al., 2013; Bloem et al., 2022).

We recently demonstrated that diffusion tensor imaging (DTI) methods can identify voxels with striosome-like and matrix-like patterns of connectivity in living humans (Waugh et al., 2022). Parcellating the striatal compartments based on differential structural connectivity replicated many anatomic features demonstrated through immunohistochemistry – their relative abundance, the anatomic sites where striosome or matrix are differentially enriched, their somatotopic organization, and their connectivity with extrastriate regions that were not utilized for parcellation. Test–retest reliability of this method was high: in humans scanned twice (1 month between scans), only 0.14% of voxels changed compartment-specific identity (Waugh et al., 2022). In regions where prior tract tracing studies in animals identified a robust compartment-specific bias in connectivity, our method replicated those findings in 93% of regions. An important

limitation of this method is the size mismatch between the human striosome and a diffusion voxel, the unit of signal acquisition in our technique. We estimate that the diameter of the typical human striosome in coronal sections ranges from 0.5–1.25 mm [based on histology presented by Graybiel and Ragsdale (1978) and Holt et al. (1997)]. In contrast, the resolution of diffusion voxels in the present study was 1.5 or 2.0 mm isotropic, ensuring that even the most striosome-enriched striatal voxel will include a mix of striosome and matrix tissue. Readers should bear in mind that connection probabilities at each voxel are an average of both compartments, and that the majority of striatal voxels will therefore have indeterminate or weakly-biased compartment-specific connectivity profiles. For this reason, we restrict our assessments to the most-biased voxels, those that exceed 1.5 standard deviations beyond the mean for structural connectivity. Since our connectivity-based parcellations are inferential, we identify these voxels as "striosome-like" and "matrix-like" to remind readers that we have not directly identified striosome and matrix.

The organization of the striatum into striosome and matrix is conserved across all mammalian species investigated to date. Moreover, development of MSNs into striosome or matrix appears to be more fundamental than development of the direct and indirect pathways, a later-arising and less-distinct striatal organizational schema (Crittenden and Graybiel, 2011; Kelly et al., 2018). Projections from most cortical areas (80.0%) are significantly segregated toward one compartment (striosome-favoring or matrix-favoring, Waugh et al., 2022) suggesting that most CSTC loops follow a bifurcated path through striosome or matrix. While it is plausible that thalamic nuclei receive a combination of striosome-originating and matrix-originating projections, we hypothesize that the striato-pallido-thalamic projections to a specific thalamic nucleus may be biased toward one compartment. Striosome and matrix differ in many clinically-relevant ways: they have differential susceptibility to hypoxic–ischemic injury (Burke and Baimbridge, 1993) and to dopamine-mediated excitotoxicity (Saka et al., 2004; Granado et al., 2010; Jaquins-Gerstl et al., 2021); electrical stimulation promotes reward-mediated learning, but only when electrodes are placed in the striosome (White and Hiroi, 1998); dopaminergic D1 stimulation prolongs neuronal activation in matrix but shortens neuronal activation in striosome (Prager et al., 2020); and more than a dozen diseases have been hypothesized to have a compartment-specific neuropathology (Crittenden and Graybiel, 2011; Kuo and Liu, 2020). These observations suggest that characterizing compartment-specific biases in striato-pallido-thalamic projections may be important for understanding why diseases that affect the striatum or thalamus produce specific constellations of symptoms. To the best of our knowledge, such biases in compartment-level striatal projections to the thalamus as a whole, or to individual thalamic nuclei, have not been mapped previously in any species.

Much of our knowledge of the functions of thalamic nuclei in humans is based on correlation from animal studies, from observations in neurologic diseases [e.g., stroke (Schmahmann, 2003; Li et al., 2018), epilepsy (Leiguarda et al., 1992; Sánchez Fernández et al., 2012), traumatic brain injury (Snider et al., 2020; Mofakham et al., 2021], and from the response to focal treatments of neurological diseases, such as deep brain stimulation (DBS, Kundu et al., 2018; Morishita et al., 2019) and high intensity focused ultrasound (Shah et al., 2020). These studies demonstrate that specific thalamic nuclei, mechanisms of injury, and neuropsychiatric symptoms are linked, and that these thalamic dysfunctions can result from primary dysfunction within the thalamus or can result from extrathalamic sites impinging on the thalamus (Morton et al., 1993; Hedreen and Folstein, 1995; Chung et al., 1996; Miyai et al., 2000; Kumral et al., 2001). We hypothesize that the striosome and matrix, through their divergent roles in striatal function, may contribute to the specificity of thalamic nuclear functions. A non-invasive, *in vivo* assessment of compartment-specific thalamic connectivity may provide additional targets and more precise placement for neuromodulation (e.g., DBS), and may provide a nuanced understanding of complex brain injuries in which both striatum and thalamus are injured (Aravamuthan and Waugh, 2016).

In this study, we mapped the structural connectivity of thalamic nuclei with the striosome-like and matrix-like compartments of the striatum in living humans using probabilistic diffusion tractography. We utilized a relatively large (221 individuals) and racially diverse cohort of healthy adults, with equal representation of female and male subjects, and robust representation of ages from 20 to 65 years. This broad representation allowed us to assess for demographic influences on striato-pallido-thalamic connectivity. We cross validated our results against measures of structural connectivity in non-human primates, cats, and rats that used injected tract tracers. Our results suggest that the functional specialization of CSTC loops involves distinct paths through the striosome and matrix compartments of the striatum, and that these loops may be reliably assessed in living humans using probabilistic diffusion tractography.

2. Methods

2.1. Participants

All research was conducted in accordance with the principles set forth in the Declaration of Helsinki. We included subjects from multiple institutions. All data collection was approved by the Institutional Review Board for the respective institution where the subject was recruited. We utilized four separate cohorts of healthy subjects, totaling 221 participants (442 hemispheres). Of these 221 participants, 218 were determined to have connectivity data in at least one hemisphere that met our internal quality control assessments, and were therefore utilized for connectivity analyses (423 hemispheres). The pre-set criteria used to determine whether connectivity data was sufficient for inclusion is explained in section 2.6. We previously described the demographic variables of three of these cohorts (Waugh et al., 2022), which included 121 subjects (Cohorts 1–3). Briefly, 106 of these participants were right-handed (90%), 58 self-reported as female (49%), and the mean age of these cohorts was 35 years (range: 18–74). The remaining 100 subjects (Cohort 4, not previously described) were derived from the Human Connectome Project (HCP), accessed through the National Institute of Mental Health Data Archive (NDA, van Essen et al., 2013). We assembled a diverse cohort of HCP subjects, balancing subjects for age, sex, and self-identified race. To create the HCP cohort, we identified 10 HCP subjects (with a goal of five male, five female) at each five-year increment starting from 20 years old and ending at 65 years old (20, 25, 30, etc.). When there were insufficient numbers of HCP subjects at a particular age target, we selected

subjects at surrounding ages, as close as possible to our target age, never infringing on the adjacent age targets. If there were fewer than five male or female subjects available at a specific age block, we rebalanced the sex ratio in another age block. For example, if only four male subjects were available at 30 years, we identified six female subjects at 30 years, and then at 35 years included six male and four female subjects. Among each group of five subjects (male or female, at a specific age), we attempted to produce a diverse and representative cohort by including at least one Asian subject, and at least one Black subject. We filled the remainder of each block of five with White subjects or those who listed their race as Other/Not reported. These participants were screened as healthy, with no reported history of neurological or psychiatric conditions. Of the 100 HCP subjects, the self-reported race was Asian (13%), Black (28%), White (52%), and Other/Not reported (7%). 90 of the HCP subjects were right-handed (90%) and 10 of the subjects were left-handed or ambidextrous (10%) based on the Edinburgh Handedness Inventory (Oldfield, 1971). The HCP cohort was evenly split between females and males (50:50). Subjects that comprise the HCP cohort can be accessed through the NDA via a study-specific identifier (DOI 10.15154/1528201). For our final, combined cohort (221 subjects), the mean age was 38.2 years old. The self-reported race of subjects was 39 Asian (22%), 37 Black (17%), 121 White (56%), and 10 Other/Not reported (5%). 113 participants were male (52%), and 105 were female (48%). Note that none of the included studies assessed gender identity; whether gender differed from the sex assigned at birth for any subject is unknown. The cohort included 196 right-handed subjects (90%), 21 left-handed or ambidextrous subjects (10%), and one subject who lacked handedness data.

2.2. Imaging data acquisition

All subjects were scanned at 3 T using whole-brain diffusion tensor imaging (DTI) and T1 (MPRAGE) protocols. For all subjects, MRI data was collected in a single scan session. We previously described the imaging acquisition for cohorts A, B, and C (Waugh et al., 2022). Briefly, these subjects were scanned at 2 mm isotropic resolution, using 70 direction (cohorts A and C, 10 B_0 volumes and 60 volumes at non-colinear directions) or 33 direction (cohort B, one B_0 volume and 32 volumes at non-colinear directions) DTI protocols. Data for HCP subjects was collected at three sites in the United States on Siemens Prisma scanners running Syngo MR E11 software and using harmonized protocols. Briefly, DTI for HCP subjects was acquired at 1.5 mm isotropic resolution using 200 directions (14 B_0 volumes, 186 volumes at non-colinear directions) with the following parameters: repetition time = 3.23 s; echo time = 0.0892. Given these differences in DTI acquisition, we included both scanner type and number of diffusion directions as covariates in our subsequent analyses. T1 scans were collected at 1 mm isotropic resolution for cohorts A–C, and 0.80 × 0.76 × 0.76 mm for HCP subjects. The imaging volumes acquired for Cohorts A, B, C, and HCP were: A, 256x256x256mm; B, 180 × 240 × 240 mm; C, 128 × 128 × 128 mm; HCP, 208 × 300 × 320 mm. We utilized the Freesurfer utility *recon-all* to perform whole-brain segmentation. Regardless of the original resolution and imaging volume for each subject, *recon-all* standardized the resolution of all T1 images to 1 mm isotropic.

2.3. Thalamic parcellations

We utilized the automated method of Iglesias et al. (2018) to produce individualized segmentations of the thalamus in native T1 space. Briefly, we completed whole brain segmentation using *recon-all* (Reuter et al., 2012), utilizing each subject's MPRAGE scan. We visually inspected the results of *recon-all* for each subject. Next, we utilized the Iglesias add-on to *recon-all* to further segment the thalamus into 25 nuclei. We planned to use these thalamic segmentations to extract connectivity estimates from probabilistic tractography (after registering tractographic probability maps into native T1 space) but recognized that image registration and partial volume inaccuracies might compromise accurate data extraction. Therefore, we established, *a priori,* a minimum volume threshold for including data from a thalamic nucleus. We set a lower volume limit of four DTI-space voxels (32mm^3 for cohorts A–C; 13.5mm^3 for our HCP cohort) when registered into T1 space, which excluded seven nuclei for cohorts A–C: central lateral, laterodorsal, limitans (suprageniculate), reuniens (medial ventral), paracentral, paratenial, and ventromedial. Note that the thresholds of 32mm^3 for cohorts A–C and the 13.5mm^3 for our HCP cohort are actually the same voxel-based threshold – four native-space voxels, adjusted for the resolution of each diffusion protocol. In addition, we excluded the lateral geniculate and limitans nuclei, given that (1) the white matter architecture surrounding these nuclei made grey/white segregation and accurate segmentation inconsistent in our datasets, and (2) we could identify no prior animal literature documenting afferent or efferent projections between the striatum and either nucleus.

Our exclusion criteria left 17 thalamic nuclei for final analysis in all 221 subjects: anteroventral (AV), central medial (CeM), centromedian (CM), lateral posterior (LP), mediodorsal-lateral (MDl), mediodorsal-medial (MDm), medial geniculate (MGN), parafascicular (Pf), pulvinar-anterior (PuA), pulvinar-inferior (PuI), pulvinar-lateral (PuL), pulvinar-medial (PuM), ventral anterior (VA), ventral anterior magnocellular (VAmc), ventral lateral anterior (VLa), ventral lateral posterior (VLp), and ventral posterolateral (VPL). Given the higher resolution of DTI scans in our HCP cohort (1.5 vs. 2.0 mm isotropic), three additional nuclei met volumetric criteria when assessed only in the HCP cohort: central lateral (CL), laterodorsal (LD), and reuniens (Reu). We therefore assessed CL, LD, and Reu only in the 100 subjects of the HCP cohort.

2.4. DTI processing

Our A, B, and C cohorts had only anterior-to-posterior imaging, whereas the HCP group had both anterior-to-posterior and posterior-to-anterior DTI volumes. Therefore, only HCP subjects were eligible for susceptibility-induced distortion correction using the FSL utility *topup*. We performed skull stripping using the FSL Brain Extraction Tool (*bet2*). We utilized the FSL tool *eddy* to correct for eddy current-induced distortions and subject motion. We fit local diffusion tensors using *dtifit*, creating a 3D FA image at the same resolution as the original diffusion images. Finally, we generated diffusion parameters at each voxel using *bedpostx* (Behrens et al., 2007). We completed preprocessing and probabilistic tractography steps in each subject's native space.

2.5. Probabilistic diffusion tractography

We carried out four separate iterations of probabilistic tractography for this study, each with a distinct purpose. *First*, we completed striatal parcellation using classification targets tractography (CTT) to quantify structural connectivity, as we described previously (Waugh et al., 2022). Briefly, we utilized a series of striosome-favoring or matrix-favoring cortical "bait" regions to identify voxels whose patterns of connectivity with extra-striate targets matched those identified in animals – and thus were "striosome-like" or "matrix-like." We identified these bait regions from our comprehensive review of prior tract tracing studies in animals (Waugh et al., 2022). Unlike traditional probabilistic tractography, which focuses on streamlines after they exit a seed voxel, CTT quantifies the structural connectivity at each seed voxel with a predefined set of targets. Therefore, the output of CTT is a series of probability distributions – in this case, two superimposable maps of the striatum, one measuring connectivity to striosome-favoring regions, the other measuring connectivity to matrix-favoring regions. The ratio of those two probability distributions quantifies the degree to which a voxel is connected in a striosome-like or matrix-like manner. *Second*, we executed traditional streamline tractography (non-CTT) to quantify and localize the streamline bundles that connect striosome-like and matrix-like striatal voxels with the thalamus. *Third*, we performed CTT with the thalamus as seed and the sets of parcellated striosome-like and matrix-like voxels as competing targets (the second round of CTT described here). We used this third iteration of tractography to quantify connectivity between specific thalamic nuclei and each striatal compartment. *Fourth*, we conducted two *post-hoc* iterations of striatal parcellation to assess the importance of precision in selecting striatal voxels. These parcellations utilized "N-1" (aka "leave-one-out") approaches, in which we used five matrix-favoring regions as bait, but only four striosome-favoring regions as bait. This allowed us to quantify connectivity with the left-out region, as we demonstrated previously (Waugh et al., 2022). For all four iterations of tractography, we ran left and right hemispheres independently. Our striatal parcellations (tractography iteration one) and post-hoc assessments of precision (tractography iteration four) utilized a whole-hemisphere bounding mask. Iterations two and three utilized a subcortical bounding mask, described below.

The bait regions we utilized for striatal parcellation were similar to those we described previously (Waugh et al., 2022). However, as the present analysis included the globus pallidus interna (GPi) and thalamus as waypoint or seed regions, respectively, we could not utilize these regions in striatal parcellation – one cannot define striatal compartment identity based on connectivity to a region and subsequently quantify connectivity with that region. Therefore, we replaced three bait regions from our prior work with three cortical regions whose striatal connectivity was significantly biased toward one compartment: (i) superior parietal (matrix-favoring), (ii) the superior portion of the inferior frontal gyrus, pars opercularis (matrix-favoring), and (iii) the posterior portion of the temporal fusiform cortex (striosome-favoring). We selected these cortical regions for their high degree of compartment selectivity and substantial reproducibility across imaging cohorts. However, we were unable to identify any prior tract tracing studies in animals that mapped connectivity with these three regions. Notably, the temporal fusiform cortex is present only in hominids, and the superior parietal lobule and inferior frontal gyrus are present only in primates, precluding their study in the animal species commonly utilized in tract tracing studies (Waugh et al., 2022). We aimed to validate this group of bait regions by assessing whether selecting striatal voxels based on biased connectivity would reproduce other features of the striatal compartments demonstrated through histology, such as the relative location of each compartment within the striatum. Striosome and matrix are not distributed randomly within the striatum [both in animal (Goldman-Rakic, 1982; Gerfen, 1984) and human histology (Graybiel and Ragsdale, 1978; Faull et al., 1989)]. We tested the intra-striate position of striosome-like and matrix-like voxels to learn whether identifying voxels based on biases in connectivity could also match the spatial patterns expected from histology. For the most-biased voxels in the striosome-like and matrix-like distribution (those used as the seed or targets of subsequent rounds of tractography), we measured their cartesian location relative to the centroid of the nucleus it occupied (left or right hemisphere, caudate or putamen).

All standard space regions of interest (ROI) utilized in this study are provided in our Supplemental Materials. These standardized masks, when registered into a subject's native diffusion space, served as seed, waypoint, target, inclusion, or exclusion masks for probabilistic diffusion tractography, which we carried out with the FSL tool *probtractx2* (Behrens et al., 2007). We used *fslview* to manually segment left and right thalamic masks, encompassing only the thalamus and excluding the surrounding white matter. Our striatal ROI did not include the nucleus accumbens, which does not share the striosome/matrix architecture observed in the rest of the striatum, and excluded the posterior half of the caudate tail, as we found that this small structure led to registration errors and frequent partial volume effects (Waugh et al., 2022). We generated a subcortical inclusion mask, which encompassed the caudate, putamen, globus pallidus (interna and externa), thalamus, and the white matter immediately surrounding these structures. This mask eliminated all streamlines that extended beyond its boundaries, excluding corticostriate, thalamocortical, and subcortical-brainstem projections. We utilized this subcortical inclusion mask to refine tractography iterations two and three (mapping striato-pallido-thalamic streamline bundles, and quantifying connectivity at the level of specific thalamic nuclei, respectively). Seven of the cortical ROI masks used for striatal parcellations and our GPi mask were defined in our prior work (Waugh et al., 2022). We segmented the three new cortical ROIs on the MNI152_T1_1mm standard brain utilizing the human brain atlas of Mai et al. (1997) based on prior MRI assessments of the superior parietal (Passarelli et al., 2021), fusiform (Rajimehr et al., 2009), and inferior frontal (Hammers et al., 2007) gyri. We registered all standard-space ROIs into each subject's native space using the FSL tools *flirt* and *fnirt*.

The results of probabilistic tractography can be influenced by the size of the target masks utilized, with larger volume increasing the probability of any given streamline ending at the target mask. Therefore, we assured that striosome-like and matrix-like masks from the same hemistriatum always had equal volume in order to minimize this source of bias, as previously described (Waugh et al., 2022). To create these matched-volume striatal masks, we selected the N most-biased voxels in each probability distribution (striosome-like and matrix like), retaining the voxels that were 1.5 standard deviations above the mean. Since our experimental cohorts included diffusion images with two different resolutions, we set two different volume

thresholds to match this 1.5 standard deviation target. For cohorts A–C (2 mm isotropic voxels), we utilized an 83 voxel threshold. For our HCP cohort (1.5 mm isotropic voxels), we utilized a 180 voxel threshold. Striosome-like and matrix-like voxels cannot overlap; our method for selecting biased voxels precludes the same voxel being selected to represent both compartments. The overlap between compartment-like voxels within a subject was zero.

We utilized these equal-volume striatal compartment masks in tractography iterations two and three; iterations one and four (striatal parcellation) utilized the whole-striatum mask. For tractography iteration one (CTT, striatal parcellation), we utilized the striatum as seed, 10 cortical ROIs (5 striosome-favoring, 5 matrix-favoring) as targets, and included streamline paths from the whole hemisphere. For tractography iteration two (mapping the path of striato-pallido-thalamic streamlines) we utilized equal-volume striatal masks (striosome-like or matrix-like) as seeds, the GPi as a waypoint (streamlines were rejected if they did not contact the GPi), and the thalamus as a termination mask (streamlines terminated upon contacting any thalamic voxel, preventing loopbacks). For tractography iteration three (CTT, quantifying connectivity with each thalamic nucleus) we utilized the thalamus as seed, GPi as waypoint, and striosome-like and matrix-like masks as targets. Note that since the streamlines of probabilistic tractography have no directionality, this round of CTT selected for the same striato-pallido-thalamic streamlines generated using the traditional streamline tractography (iteration two) but allowed us to quantify connectivity at each thalamic voxel.

For tractography iteration four (striatal parcellation followed by quantitative CTT), we parcellated the striatum as described for iteration one, but used 9 cortical ROIs (4 striosome-favoring, 5 matrix-favoring) as targets. We carried out this N-1 parcellation twice, once each for two regions that were among the strongest striosome-favoring biases from our prior work (Waugh et al., 2022): anterior insula and basal operculum. We then performed quantitative CTT with these left-out regions as seed and the N-1 parcellated striatal voxels as targets. As our aim for this iteration of tractography was to assess the influence of precise voxel location on compartment-level bias, we ran parallel versions of quantitative CTT with imprecise striatal voxels as targets. To generate these imprecise masks, we shifted the position of each voxel in our precise, matched-volume masks, at random, by +/− 0–3 voxels in each plane. Note that this randomization step shifted the location by only a few voxels – these imprecise voxels were near-neighbors of the precise matched-volume masks. We measured the amplitude of this location shift for 40 hemispheres, selected at random: five striosome-like and five matrix-like masks for each of our four experimental cohorts. We measured the change in location (root-mean-square distance) for all 4,026 voxels in these 40 hemispheres.

We completed striatal parcellation and mapped the path of striato-thalamic streamlines (tractography iterations one and four, and two, respectively) using the standard *probtrackx2* settings: curvature threshold = 0.2; steplength = 0.5 mm; number of steps per sample = 2,000; number of streamlines/voxels = 5,000. For quantifying striato-thalamic tractography at the level of individual thalamic nuclei, however, increasing the depth of sampling by 10× (50,000 streamlines/voxel) yielded a more accurate probability distribution. Specifically, increasing the number of streamline trials provided a more robust mapping of each compartment's connection probability and thereby decreased the number of thalamic voxels that had no streamlines that met our anatomic and tractographic criteria. This increase in streamlines/voxel reduced the impact of "floor effects," locations where we otherwise could not distinguish between low-connectivity and no-connectivity voxels. This allowed connectivity estimates to derive from a larger fraction of the voxels in each thalamic nucleus. For the MGN, we found that a further increase to 500,000 streamlines per seed voxel was necessary to adequately sample the probability distribution. Therefore, we ran tractography and quantification for MGN separately from all other thalamic nuclei. In all three iterations of probabilistic tractography, streamlines were corrected for length to prevent the proximity to a target from influencing the strength of connection. We visually inspected the results of *dtifit*, *bedpostx*, native space registrations, and both CTT and streamline tractography, for each subject, to assure that DTI processing was complete and accurate.

The regional segmentations and Linux scripts utilized to parcellate the striatum are accessible here: github.com/jeff-waugh/Striatal-Connectivity-based-Parcellation.

2.6. Localizing compartment-specific streamlines

Our goals for tractography iteration two were (1) to map the paths of striato-pallido-thalamic connectivity, and (2) determine the relative abundance of streamlines seeded by striosome-like vs. matrix-like voxels. We sought to determine whether the streamlines seeded from striosome-like and matrix-like voxels traversed different routes to reach their pallidal and thalamic targets. Therefore, we utilized normalized streamline bundles to reduce the impact of tract amplitude on mean location: we divided each subject/hemisphere/compartment's tractography volume by its maximum value within the GPi. The averaged images and *randomise* testing results discussed below utilized these normalized tracts. After registering each subject's tractography into standard space, we used two distinct approaches to assess the overlap of streamlines seeded by striosome-like vs. matrix-like voxels. First, we used *fslstats* to determine the site of maximum value of striato-pallido-thalamic projections within the GPi (independent striosome-like and matrix-like streamline bundles). We quantified the location difference between compartment-specific bundles by calculating the root-mean-square difference in the site of the peak streamline amplitude (striosome-like vs. matrix-like bundles, in each individual and hemisphere). Further, we compared the x-, y-, and z-plane coordinates of these maximum value sites between striosome-like and matrix-like bundles in each individual and hemisphere. To correct for the intrinsic differences in location of the GPi in left and right hemispheres, we matched the center of mass for left and right GPi by mirroring right hemisphere x-coordinates into the left hemisphere and bringing y- and z-coordinates to the mean y- and z-coordinates for left and right GPi. Second, we quantified the overlap in streamlines using the averaged striato-pallido-thalamic tractograms from all subjects, for each hemisphere and compartment-specific seed mask, both within and outside the GPi. For each hemisphere and compartment-specific seed we isolated the core of the tract at high- (uppermost 25% of voxels by amplitude), mid- (uppermost 50%), and low-stringency (uppermost 90%) amplitude thresholds. We previously identified these high- and mid-stringency thresholds as sufficient to isolate the tract core (Waugh et al., 2019).

We then calculated the Dice Similarity Coefficient (DSC) at high-, mid-, and low-stringency to assess the overlap in striosome-like and matrix-like streamlines, both within and outside the GPi, for each hemisphere. We then quantified the overlap of streamlines for individual subjects with the mean streamline bundle (uppermost 50%) to assess location variance within each streamline bundle. Finally, we assessed the number of streamlines per seed voxel (non-normalized), comparing streamline bundles seeded by striosome-like vs. matrix-like voxels.

2.7. Quality assurance and quantification of thalamic connectivity

We registered each subject's thalamic probability maps (tractography iteration three) into native T1 space. This allowed us to utilize each individual's *recon-all* thalamic segmentation to generate nucleus-specific masks for extracting connectivity data from striosome-like and matrix-like probability distributions. For native space probability maps, at every voxel the striosome-like and matrix-like probability distributions summed to one. After registration to T1 space, partial volume and edge effects led some voxels to lose this "sum to one" property. Therefore, we renormalized the probability distributions on a voxel-by-voxel basis. We trimmed edge voxels whose summed value was <0.5, which reduced partial volume effects at the edges of the thalamus. For each thalamic nucleus, we quantified the number of suprathreshold voxels (value ≥0.55) in striosome-favoring and matrix-favoring normalized probability distributions. For each nucleus we expressed connectivity as the percent of suprathreshold voxels dominated by each compartment (N_{voxels}, striosome-like or matrix-like)/(N_{voxels}, striosome-like + N_{voxels}, matrix-like).

Next, we assessed each thalamic nucleus for connectivity differences between left and right hemispheres. For any nucleus whose compartment-specific connectivity (1) was significantly different between left and right hemispheres and (2) was biased toward different compartments in the two hemispheres, we reported results for left and right hemispheres independently. For the four nuclei that met these criteria, bias was significant in one hemisphere and neutral in the other; we did not find significant differences in compartment-by-hemisphere bias (e.g., left hemisphere biased toward matrix-like, and right hemisphere biased toward striosome-like voxels) for any thalamic nucleus. For the remaining 16 nuclei we combined left and right hemispheres for quantifying striosome-like vs. matrix-like patterns of connectivity.

Prior to any statistical comparisons, we imposed a data quality threshold to reduce inaccuracies resulting from inadequate sampling of the thalamic probability distributions. First, we summed the volume of suprathreshold voxels from the striosome-favoring and matrix-favoring probability distributions (the maps resulting from whole-thalamus CTT). As we were concerned that paucity of data might reduce the accuracy of quantification, we eliminated all subject-hemispheres whose suprathreshold total volume was below 10% of the mean volume for that hemisphere. This elimination removed the left hemisphere for 13 participants and the right hemisphere for 6 participants. Next, we eliminated all subject-hemispheres that had no data for one compartment, as this led to a binarization of data that skewed bias calculations. For example, two subjects with very different bias counts would result in the same volume percent calculation (subject 1: 0 matrix-favoring voxels, 99 striosome-favoring voxels; subject 2: 0 matrix-favoring voxels, 1 striosome-favoring voxel; both result in bias estimates of 100% striosome-favoring). Note that increasing the streamlines/voxel during CTT (from 5,000 to 50,000 per seed voxel) substantially reduced the number of under-sampled subject hemispheres. Following this quality control step, we assessed thalamic connectivity in 210 left and 214 right hemispheres. For all subject-hemispheres eliminated based on under-sampling of thalamic CTT (tractography iteration three), we also removed those subjects from assessments of tractography iteration two.

Finally, we compared our MRI-based results with previously published tract tracing studies in animals. For every prior study, we recorded the tracing methods, species utilized, the number of animals assessed, and whether compartment assessment directly visualized tracing material in either striosome or matrix, or indirectly suggested compartment-specific connectivity. We noted compartment-specific assessments as-described by the original authors; we did not reinterpret findings.

2.8. Statistical analyses

All statistical tests on data extracted from tractography volumes were performed using STATA (van Essen et al., 2013, Stata Statistical Software: Release 13, College Station, TX). We performed voxelwise nonparametric permutation testing on tractography volumes using the FSL tool *randomise*. We measured the location of each voxel in our striosome-like and matrix-like masks (the cartesian position relative to the centroid of caudate or putamen) for each subject and hemisphere, producing a dataset of 103,688 parcellated voxels. We assessed the effect of striatal compartment and nucleus of origin (caudate or putamen) on voxel location using two-factor ANOVAs (one each for the x-, y-, and z-planes). Within the same ANOVAs we assessed the effect of cohort, and subject identity nested within cohort. To the best of our knowledge, no interhemispheric differences in matrix and striosome location have been described previously. Therefore, we did not treat hemisphere as a separate factor. We previously demonstrated that scanner type, subject sex, and self-identified race had no influence on the location of parcellated striatal voxels (Waugh et al., 2022), and we therefore did not include these factors in our model. We performed identical ANOVAs for the x-, y-, and z-planes, and therefore used a significance threshold of $p < 0.017$ (0.05/3 comparisons). We performed post-hoc analyses of simple main effects for all factor interactions using the SME utility developed by the UCLA ATS Statistical Consulting Group (Ender, 2017). We utilized the simultaneous test procedure for estimating the critical value of F, the most conservative method provided in this utility.

We evaluated the influence of precise location on compartment-level bias by comparing the results of CTT with precisely-selected versus neighboring (imprecise) striatal voxels. We performed paired samples t-tests for the mean probability of connection, volume projecting to striosome-like voxels, and volume projecting to matrix-like voxels, for two striosome-favoring seed regions, the anterior insula and the basal operculum. We therefore used a significance threshold of $p < 8.3 \times 10^{-3}$ (0.05/6 comparisons).

We utilized paired-samples t-tests to compare the location of the peak value within the GPi for streamline bundles that originated in striosome-like or matrix-like voxels. As we tested location in the x-, y-,

and z-planes, we utilized a significance threshold of $p < 1.7\times10^{-2}$ (Bonferroni correction for three tests, 0.05/3). We utilized a single paired-samples t-test to compare the number of streamlines per voxel originating from striosome-like and matrix-like voxels. Our significance threshold was $p < 0.05$. We compared thalamic nucleus-specific connectivity in the left and right hemispheres using *t*-tests, two samples with equal variance. As we tested 20 thalamic nuclei for hemispheric differences, our significance threshold was $p < 2.5\times10^{-3}$ (Bonferroni correction for 20 tests, 0.05/20). We performed a post-hoc series of ANCOVAs to identify any subject factors that were drivers of interhemispheric difference. Factors assessed included age, number of diffusion directions, scanner type, handedness, hemisphere, self-identified race, and sex. As Cohorts A and B were unbalanced for sex, and Cohort B was also unbalanced for self-identified race, we also assessed the interaction between sex, self-identified race, diffusion directions, and scanner type. Data from different thalamic nuclei was colinear, precluding our use of MANCOVA to combine these tests. Therefore, we performed 20 independent ANCOVAs, resulting in a significance threshold for these ANCOVAs of $p < 2.5\times10^{-3}$ (Bonferroni correction for 20 tests, 0.05/20). We assessed compartment-specific bias in each thalamic nucleus using *t*-tests, two samples with equal variance. As we measured the bias in combined hemispheres in 16 nuclei, our significance threshold for these comparisons was $p < 3.1\times10^{-3}$ (Bonferroni correction for 16 tests, 0.05/16). Finally, we performed voxelwise nonparametric permutation testing of striato-pallido-thalamic streamlines (*randomise*) with the following parameters: 5,000 permutations; variance smoothing = 2 mm; threshold-free cluster enhancement mode; masked by one of two conditions in separate iterations of *randomise*. The two masks utilized for *randomise* were (1) the same GPi mask used as a waypoint for tractography, or (2) the subcortical bounding mask utilized for tractography with all grey matter structures removed (to restrict testing to only the subcortical white matter). For both iterations of randomise, we used the familywise error corrected, threshold-free cluster enhanced test statistics. Since we performed two related tests using randomise, we set our significance threshold at $p < 0.025$ (0.05/2).

3. Results

3.1. Overview of experimental aims

We aimed to identify the thalamic nuclei whose striato-pallido-thalamic structural connectivity was significantly biased toward striosome-like or matrix-like voxels – the striatal voxels whose corticostriate connectivity profiles matched the biases demonstrated in prior tract tracing studies in animals. These striatal parcellations are highly stable: in subjects scanned twice, with 1 month between scans, only 0.14% of striatal voxels switched compartment identity (Waugh et al., 2022). We first measured the locations of our parcellated striatal voxels to assure that our method identified voxels with striosome-like and matrix-like distributions within the striatum, in addition to their striosome-like and matrix-like patterns of connectivity. We next assessed the precision of our striatal parcellations by comparing quantitative tractography when striatal target voxels were either precisely selected or were randomly selected from among the nearest neighbors of those precise voxels. Then, we assessed whether our tractographic approach produced distinct and anatomically plausible streamline bundles by quantifying streamline amplitude and intra-pallidal location of streamline bundles. Next, for all thalamic nuclei whose volume was sufficient to allow for reliable assessment, we tested whether thalamic nuclei in the left and right hemispheres had the same or different biases in striato-pallido-thalamic connectivity. Finally, we evaluated each of these thalamic nuclei for compartment-specific biases in structural connectivity.

3.2. Compartment-specific voxel location

Prior histologic studies in humans (Graybiel and Ragsdale, 1978; Faull et al., 1989; Holt et al., 1997) and animals (Graybiel and Ragsdale, 1978; Goldman-Rakic, 1982; Gerfen, 1984; Donoghue and Herkenham, 1986; Malach and Graybiel, 1986) described medio-lateral, rostro-caudal, and dorsal-ventral gradients in the predominant locations of each compartment. Though striosomes can be found throughout the striatum, they are enriched in medial, rostral, and ventral sites. Our connectivity-based parcellation method identified a similar pattern: striosome-like voxels are located more medial, more rostral, and more ventral than matrix-like voxels. Two-factor ANOVA, examining the effects of striatal compartment and striatal nucleus (caudate or putamen), identified a significant influence of both factors, and their interaction, on voxel location.

The mean location of striosome-like voxels was 0.9 mm more medial ($F[1, 223] = 2{,}668$, $p < 4.6\times10^{-126}$), 4.1 mm more rostral ($F[1, 223] = 8{,}468$, $p < 2.3\times10^{-179}$), and 4.9 mm more ventral ($F[1, 223] = 44{,}277$, $p < 1.9\times10^{-258}$) than the mean location of matrix-like voxels. Whether a voxel was found within the caudate or putamen also had a significant influence on voxel location. Matrix-like voxels in the putamen were more lateral ($F[1, 223] = 90.8$, $p < 2.8\times10^{-18}$), more caudal ($F[1, 223] = 38.8$, $p < 2.3\times10^{-9}$), and more dorsal ($F[1, 223] = 1{,}309.9$, $p < 2.6\times10^{-95}$) than matrix-like voxels in the caudate. Note that since individual voxels were assessed relative to the centroid of either caudate or putamen, the relative positioning of each nucleus within the hemisphere did not drive these differences in location. However, differences in the geometry and size of the caudate and putamen may have allowed voxels to reside at greater distance from the centroid of the putamen.

The interaction of compartment and nucleus had a significant effect on voxel location in the x-plane (sagittal, $F[1, 223] = 1{,}084.7$, $p < 1.3\times10^{-87}$), y-plane (coronal, $F[1, 223] = 53.9$, $p < 3.9\times10^{-12}$), and z-plane (axial, $F[1, 223] = 15.6$, $p < 1.1\times10^{-4}$). Simple main effects analysis of the compartment-nucleus interaction showed that in the x-plane, only putamen has a significant effect on voxel location ($F[1, 103{,}464] = 7{,}667.3$, $p < 1.9\times10^{-305}$). In the y- and z-planes, both caudate and putamen had a significant effect on voxel location: y {caudate, ($F[1, 103{,}464] = 1{,}519.8$, $p < 1.1\times10^{-153}$)}; putamen, ($F[1, 103{,}464] = 10{,}205.5$, $p < 7.0\times10^{-321}$); z {caudate, ($F[1, 103{,}464] = 15{,}341.4$, $p < 2.7\times10^{-322}$)}; putamen, ($F[1, 103{,}464] = 40{,}976.3$, $p < 5.4\times10^{-322}$). Variance from individual subjects and experimental cohort factors (Supplemental Figure 1) were not significant contributors to voxel location in any plane.

3.3. Compartment-specific bias depends on precise selection of striatal voxels

Biases in compartment-specific connectivity were highly influenced by precise voxel location. We performed N-1 parcellation,

leaving out either the anterior insula or basal operculum in successive iterations of CTT, which allowed us to then perform quantitative tractography with each of these two striosome-favoring regions in turn. After generating matched-volume masks for each N-1 parcellation (the precise voxels with the highest degree of striosome-like or matrix-like bias in connectivity), we created parallel, imprecise masks with the location randomly shifted by up to 3 voxels in each plane. We sampled these random shifts in location for 40 hemispheres (4,026 voxels relocated). For both striosome-like and matrix-like masks, this randomization step led to a mean shift in location of 1.8 voxels (SEM, ±0.01 voxel). Importantly, these relocated voxels were among the nearest neighbors of our precisely selected voxels. In our control conditions (anterior insula or basal operculum as seed, precise striatal masks as target), both regions were highly biased toward striosome-like voxels. Of seed voxels with substantial bias (those with compartment-specific connection probability ≥0.87), 82.1% (SEM, ±1.2%) of anterior insular voxels and 91.5% (SEM, ±0.95%) of basal opercular voxels favored striosome-like target voxels. When precise compartment-like targets were shifted to neighboring voxels, the mean volume of anterior insula that favored striosome-like targets fell by 5.1-fold (from 1,438 to 279 voxels; $p < 2.0\times10^{-118}$; Supplemental Figure 2). Similarly, basal opercular voxels that favored striosome-like targets fell by 3.6-fold (from 1,213 to 339 voxels; $p < 1.3\times10^{-111}$). Targeting less-precise striatal voxels also led to an increase in the percentage of seed voxels that favored matrix-like connectivity, increasing by 19.0% in the anterior insula ($p < 3.0\times10^{-3}$) and 49.3% in the basal operculum ($p < 3.6\times10^{-4}$). Mean connectivity bias within the seed regions was also substantially reduced by shifting precise targets to neighboring voxels. The probability of connection to striosome-like voxels reduced by 35.8% in the anterior insula ($p < 1.0\times10^{-101}$) and reduced by 54.8% in the basal operculum ($p < 2.7\times10^{-35}$) when striatal targets were imprecise. Relocating striosome-like and matrix-like targets even 1–2 voxels from their precise location markedly reduced compartment-specific biases in connectivity.

3.4. Streamlines seeded by striosome-like and matrix-like voxels rarely colocalize

Streamline bundles originating in striosome-like and matrix-like voxels occupied distinct locations within the GPi and approached the GPi from different orientations (Figure 1). This GPi organization was qualitatively symmetric between hemispheres (Figures 1F–I). The maximum values of bundles from the two compartments had significantly different locations in the x-, y- and z-planes ($p < 1.1\times10^{-35}$, 1.3×10^{-53}, and 3.8×10^{-42}, respectively), with streamlines seeded by striosome-like voxels situated more rostrally, ventrally, and laterally. Intra-pallidal location was highly similar within each bundle: coefficients of variation (CVs) for striosome-like streamlines (x-, y-, and z-planes) were 3.8, 2.6, and 2.9%, respectively; for matrix-like streamline locations, CVs were 1.8, 1.8, and 3.1%, respectively. The root-mean-square difference in the sites of peak value (striosome-like vs. matrix-like) within the GPi was 4.6 mm (SEM ± 0.089). Intra-pallidal streamlines in the core of the striosome-like and matrix-like bundles (the uppermost 25% of the amplitude distribution, Waugh et al., 2019) did not overlap in either hemisphere (DSC, 0%). At a mid-stringency threshold (the uppermost 50% of the amplitude distribution), streamlines were segregated (DSC, left GPi: 15.3% overlap; right GPi: 13.7% overlap). At a low-stringency threshold (the uppermost 90% of the amplitude distribution), streamlines were still largely segregated (DSC, left GPi: 34.1% overlap; right GPi: 32.8% overlap). Comparison of streamlines at the voxelwise level (with *randomise*, Figure 1H) yielded similar results: for the majority of pallidal voxels (left hemisphere, 83.0%; right hemisphere, 79.0%), streamline counts seeded by one compartment were significantly greater than those seeded by the other compartment, in a similar pattern demonstrated through DSC.

Striato-pallido-thalamic streamline bundles seeded from striosome-like and matrix-like voxels arrived at and occupied distinct parts of the GPi (Figures 1A–G,I). A dense band of streamlines that originated in matrix-like voxels reached the dorsoposterior GPi. Lower density bands of streamlines that originated in striosome-like voxels approached from rostral and caudal orientations; both approached the ventrolateral GPi. Streamlines were highly segregated outside the GPi as well. Streamlines from the uppermost 25% of the amplitude distribution did not overlap, in either hemisphere (DSC, 0%). Streamline bundles from the uppermost 50% of the distribution were highly segregated (DSC, left hemisphere: 2.7% overlap; right: 4.4% overlap). Even at a low-stringency amplitude threshold (the uppermost 90% of the distribution), extra-pallidal streamlines were largely segregated (DSC, left hemisphere: 31.0% overlap; right: 41.4% overlap). Among our 221 subjects, compartment-specific streamline bundles were highly colocalized: the core of each individual's streamline bundle overlapped with the core of the average streamline bundle in 95.7 and 93.9% of our subjects (streamlines seeded by matrix-like and seeded by striosome-like voxels, respectively).

3.5. Abundance of compartment-specific streamlines reaching the GPi

Streamlines seeded from matrix-like voxels were 5.7-fold more likely to reach the thalamus (*via* the GPi) than streamlines seeded by striosome-like voxels (2,291 streamlines per matrix-like seed voxel vs. 401 streamlines per striosome-like seed voxel; $p < 8.7\times10^{-31}$). Within the GPi, streamlines seeded by matrix-like voxels were 7- to 9-fold more abundant than streamlines seeded by striosome-like voxels (left matrix-like: 727.3, SEM ±73.3; left striosome-like: 79.2, SEM ±27.1; right matrix-like: 536.6, SEM ± 89.8; right striosome-like: 70.0, SEM ± 14.3). Note that for each subject and hemisphere, striosome-like and matrix-like seed masks always had equal volume (the uppermost 1.5 standard deviation of each probability distribution) and were seeded with equal numbers of streamlines. Therefore, streamline counts were independent of the relative volume of striosome-like and matrix-like voxels in the whole striatum. The dominance of matrix-like voxels in the GPi is consistent with previous connectivity assessments by tract tracing in squirrel monkeys, cats, and rats (Gimenez-Amaya and Graybiel, 1990; Flaherty and Graybiel, 1993; Rajakumar et al., 1993).

3.6. Compartment-specific biases in striato-pallido-thalamic tractography

Our thalamic CTT (Methods 2.5, tractography iteration three) measured striato-pallido-thalamic connectivity between the striatal

10.3389/fnins.2023.1178473

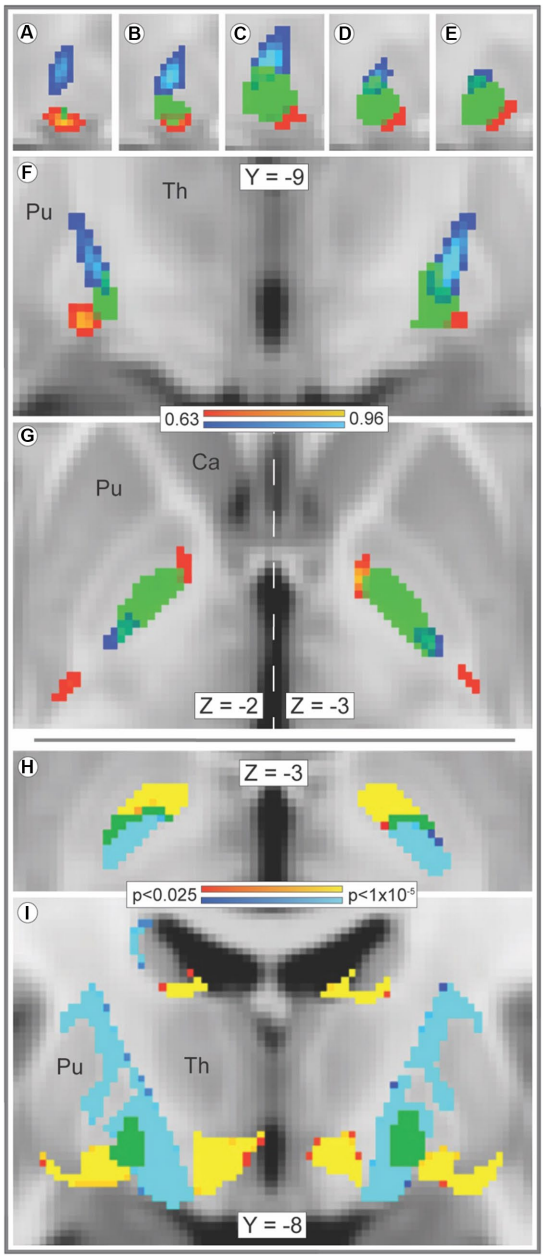

FIGURE 1
Streamline bundles originating in striosome-like or matrix-like voxels reach and traverse the GPi by different paths. Tracts seeded by matrix-like or striosome-like striatal voxels follow distinct paths through the globus pallidus interna (GPi). The averaged streamlines (**A–G**, range: 0.63–0.96) for all subjects are visualized in red-yellow (striosome-like seeds) and blue-light blue (matrix-like seeds) overlaid by the GPi mask (green). The GPi mask is shown at 50% opacity to visualize overlap with streamline bundles. In the x-plane (panels **A–E**), views of the right GPi (from x = 23–19) demonstrate segregation of the two streamline bundles at all lateral-to-medial (left to right) points. The bundles remain segregated in the y- **(F)**, and z-planes **(G)** as well. The locations of peak amplitude for averaged matrix-like and striosome-like streamlines had significantly different locations in each plane (x plane, $p < 1.1 \times 10^{-35}$; y plane, $p < 1.3 \times 10^{-53}$; z plane, $p < 3.8 \times 10^{-42}$). The core of streamline bundles that originated in matrix-like and striosome-like voxels (the uppermost 25% of each bundle, by amplitude) do not overlap in any GPi voxel. Voxelwise significance testing with *randomise* **(H,I)** demonstrated this segregation of streamlines seeded by striosome-like and matrix-like voxels as well (significance threshold, $p < 0.025$, corrected for multiple comparisons; visualized range: 0.025–0.00001). Bundles seeded by striosome-like voxels (red-yellow) and matrix-like voxels (blue-light blue) occupy distinct zones of the GPi **(H)** and the subcortical white matter **(I)**. In H, green voxels illustrate the few pallidal voxels where bundles were not significantly different. In **(I)**, green voxels illustrate the whole of the GPi, as significance testing in this panel included only white matter voxels. Optimal visualization in the z-plane **(G)** was offset by 1 mm in the left and right hemispheres (vertical dashed line). Images follow radiologic convention. Coordinates follow MNI convention. Ca, caudate; Pu, putamen; Th, thalamus.

compartments and each thalamic voxel. Though we assessed each thalamic voxel independently, compartment-specific biases in connectivity mirrored the large-scale anatomic organization of the thalamus (Figure 2). Similarly, while we performed CTT separately in left and right hemispheres, the patterns of structural connectivity in the two hemispheres were strikingly similar. Likewise, the mean

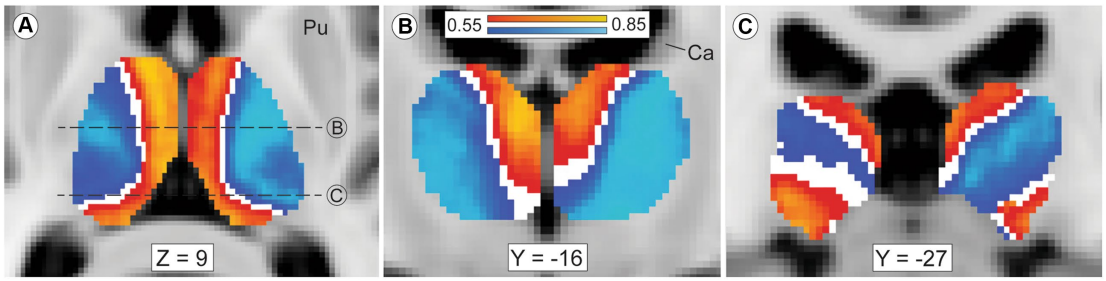

FIGURE 2
Mean probability of striato-pallido-thalamic connectivity for striosome-originating and matrix-originating streamlines. Compartment-specific biases in structural connectivity parallel the anatomic organization of the thalamus. In axial **(A)** and coronal **(B,C)** views, probability maps that favored striosome-like voxels (red-yellow) or matrix-like voxels (blue-light blue) were overlaid on the MNI_152_1mm template brain. Larger biases can be seen in yellow voxels (striosome-like) and light blue voxels (matrix-like). The coronal planes of section in B and C are indicated by dashed lines in A. Maps are the averaged probabilities from all subjects, with left and right hemispheres run independently. These views demonstrate probability values between 0.55–0.85, voxels with substantial compartment-specific bias in structural connectivity. Voxels with indeterminate bias (those with connection probabilities of 0.45–0.55) do not appear in either probability map (white voxels). The anterior and medial nuclear groups have strong bias towards striosome-like striatal voxels, while the lateral nuclear group is mostly biased towards matrix-like voxels. Voxels with indeterminate bias closely approximate the internal medullary lamina. The pulvinar nucleus, the caudal-most portion of the thalamus, has a divided pattern of connectivity, with some pulvinar zones biased towards matrix-like voxels and other zones biased towards striosome-like voxels (panel **C**). Note that in this mode of tractography (classification targets) each thalamic voxel was mapped individually – the similarity of these probability maps to prior histology-based divisions of thalamic nuclei underscores the fact that probabilistic tractography follows the intrinsic anatomic and functional anatomy of the thalamus. Images follow radiologic convention. Coordinates follow MNI convention. Ca, caudate; Pu, putamen.

connection probability for striosome-favoring and matrix-favoring thalamic voxels was highly similar in the left and right hemispheres (favoring matrix-like voxels: left, 0.72 SEM ± 0.024; right, 0.67 SEM ± 0.024 – favoring striosome-like voxels: left, 0.64 SEM ± 0.023; right, 0.67 SEM ± 0.022). Thalamic voxels whose connectivity was biased towards the matrix-like compartment were predominantly located within the lateral nuclear group. Thalamic voxels with bias towards the striosome- like compartment largely occupied the anterior, medial, and midline nuclear groups. Thalamic voxels with sub-threshold bias closely approximated the internal medullary lamina (white voxels in Figures 2A,B), though all measured intralaminar nuclei had biased connectivity. The pulvinar was unique in not conforming to this pairing of nuclear group and striato-thalamic connectivity (Figure 2C). Striosome-like and matrix-like connectivity cut across the pulvinar in orientations that did not match the pulvinar subdivisions we utilized (PuA, PuI, PuL, PuM). Note that while these qualitative patterns utilized the averaged probability maps (which included all subjects), our subsequent quantitative assessments of connectivity measured each nucleus in individual subjects.

Given the visual similarity of left and right hemispheres (Figure 2), we sought to identify whether thalamic nuclei in the left and right hemispheres shared the same patterns of striatal compartment connectivity. While hemispheric specialization in thalamic connectivity was interesting as a primary question, this assessment was also necessary to determine whether hemispheres could be combined for subsequent analyses or should be analyzed separately. We quantified striato-pallido-thalamic connectivity bilaterally for 20 thalamic nuclei (Figure 3, organized from maximum to minimum interhemispheric difference). For two nuclei (Pf, VLa), connectivity was significantly different between left and right hemispheres, but both were biased towards matrix-like voxels; the left hemisphere was simply more matrix-biased than the right (means - Pf: 0.78 vs. 0.63, $p < 7.3\times10^{-5}$; VLa: 0.66 vs. 0.55, $p < 4.5\times10^{-4}$). Note that striosome-like and matrix-like connectivity measures always summed to one. Therefore, we have presented only the measures of matrix-like connectivity. Four nuclei had significant differences in compartment-specific connectivity in one hemisphere, but neutral connectivity in the other hemisphere (presented as mean matrix-like connectivity in the left vs. right hemisphere - CeM: 0.55 vs. 0.36, $p < 1.8\times10^{-6}$; MDl: 0.52 vs. 0.40, $p < 8.5\times10^{-4}$; Reu: 0.54 vs. 0.04, $p < 2.2\times10^{-6}$; VAmc: 0.71 vs. 0.45, $p < 1.4\times10^{-8}$). Note that Reu values were derived only from the 100 subjects in our HCP cohort.

We performed post-hoc ANCOVA testing to identify demographic or experimental factors that contributed to interhemispheric differences in connectivity with the striatal compartments. We tested the following factors for all 20 thalamic nuclei: age, number of diffusion directions, scanner type, handedness, hemisphere, self-identified race, sex, and interactions between sex, race, diffusion directions, and scanner type. No demographic or experimental factor, and no interaction between factors, was a significant contributor to interhemispheric bias.

Sixteen thalamic nuclei did not differ significantly in their compartment bias between left and right hemispheres, and we therefore combined the hemispheres for subsequent analyses (Figure 4; Table 1): AV, CL, CM, LD, LP, MDm, MGN, Pf, PuA, PuI, PuL, PuM, VLa, VLp, and VLP. Note that CL and LD values were derived only from the 100 subjects in our HCP cohort. Six nuclei showed significant connectivity bias toward striosome-like voxels (mean connectivity of 0.5 indicated no bias, with 0 and 1 indicating complete bias towards striosome-like or matrix-like voxels, respectively): AV – 0.29, $p < 9.6\times10^{-43}$; CL – 0.09, $p < 4.6\times10^{-155}$; LD – 0.08, $p < 2.1\times10^{-114}$; LP – 0.42, $p < 7.2\times10^{-8}$; MDm – 0.41, $p < 1.6\times10^{-11}$; MGN – 0.38, $p < 4.7\times10^{-14}$. Seven regions showed significant connectivity bias towards matrix-like voxels: CM – 0.76, $p < 2.0\times10^{-83}$; Pf – 0.70, $p < 1.0\times10^{-42}$; PuA – 0.62, $p < 7.2\times10^{-20}$; PuL – 0.65, $p < 3.8\times10^{-27}$; VLa – 0.61, $p < 4.6\times10^{-20}$; VLp – 0.69, $p < 2.4\times10^{-58}$; VPL – 0.71, $p < 1.7\times10^{-61}$. The three remaining thalamic nuclei were not significantly biased toward either striatal compartment: PuI – 0.49, $p < 0.37$; PuM – 0.49, $p < 0.31$; VA – 0.48, $p < 0.08$. Upon visual assessment

10.3389/fnins.2023.1178473

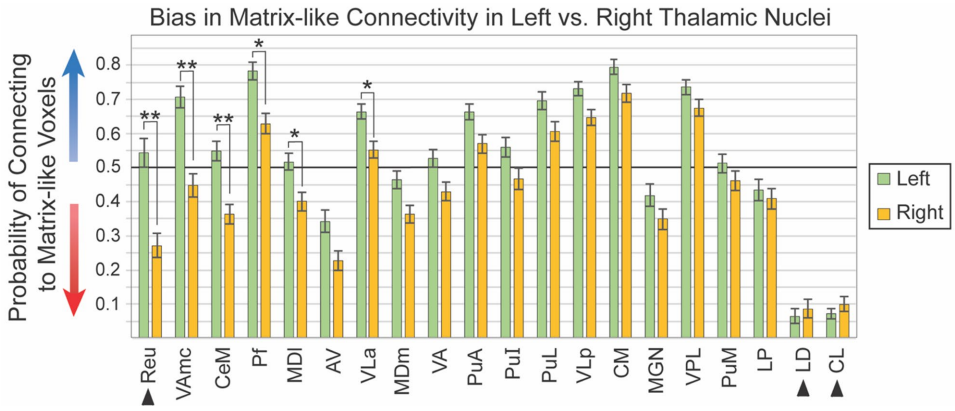

FIGURE 3
Connectivity to matrix-like voxels is stronger in the left hemisphere for most thalamic nuclei. Biased connectivity from the matrix-like compartment is larger in the left hemisphere. While this bias was significant in only six of 20 nuclei, bias was larger in the left for 18 of the 20 nuclei assessed. Note that the darker horizontal line (0.5) indicates the point of equal connectivity between thalamic seed voxels and matrix- or striosome-like target voxels. Higher values on the y axis indicate greater matrix-like connectivity (blue arrow), with lower values indicating greater striosome-like connectivity (red arrow). For any given nucleus, the values for matrix-like and striosome-like connectivity sum to one. Therefore, we present only the matrix-like connectivity for left and right hemispheres. Error bars indicate the standard error of the mean. Three nuclei whose data originated from the HCP cohort alone are indicated by arrowheads. Significance threshold: **, $p < 2.5\times10^{-6}$; *, $p < 2.5\times10^{-3}$.

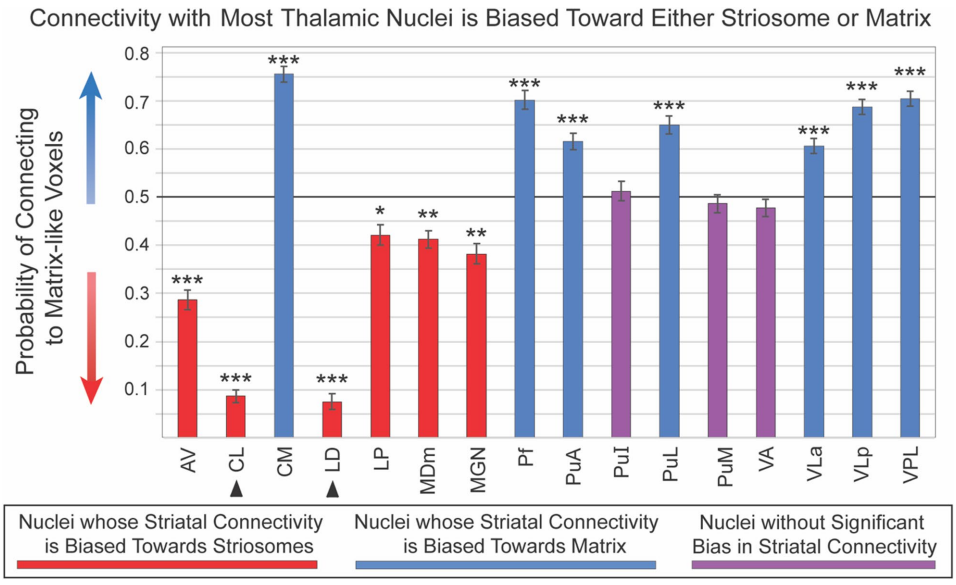

FIGURE 4
Connectivity with most thalamic nuclei is biased toward either striosome-like or matrix-like voxels. Disynaptic projections from striatum to thalamus (via the globus pallidus interna) are biased: streamlines that originate in striosome-like or matrix-like voxels largely reach different thalamic nuclei. Seven nuclei were dominated by projections from matrix-like voxels (blue bars), six nuclei were dominated by striosome-like projections (red bars), and three nuclei had no compartment bias (purple bars). Note that the darker horizontal line (0.5) indicates the point of neutral connectivity. Higher values on the y axis indicate greater matrix-like connectivity (blue arrow), with lower values indicating greater striosome-like connectivity (red arrow). For any given nucleus, the values for matrix-like and striosome-like connectivity sum to one. Therefore, we present only the matrix-like connectivity for each thalamic nucleus. Error bars indicate the standard error of the mean. Two nuclei whose data originated from the HCP cohort alone are indicated by arrowheads. Significance thresholds: *, $p < 3.1\times10^{-3}$; **, $p < 3.1\times10^{-9}$; ***, $p < 3.1\times10^{-15}$.

of individual subjects' probability distributions, it was clear that the segmentations of PuI and PuM paralleled the division between striosome-favoring and matrix-favoring connectivity, but straddled the boundary between them. Assessment of these two pulvinar areas may therefore require more subtle thalamic nuclear segmentations.

3.7. Mapping of striato-thalamic structural connectivity: human vs. model animals

Fourteen thalamic nuclei had (1) significant compartment-specific bias in striato-pallido-thalamic connectivity and (2)

TABLE 1 Probability of striato-pallido-thalamic connectivity with matrix-like voxels.

Nucleus	Mean	Standard Error	99.7% CI	*p* value
AV	0.29	0.021	[0.229, 0.345]	9.6×10^{-43}
CL	0.09	0.013	[0.047, 0.125]	4.6×10^{-155}
CM	0.76	0.017	[0.706, 0.806]	2.0×10^{-83}
LD	0.08	0.017	[0.025, 0.125]	2.1×10^{-114}
LP	0.42	0.020	[0.361, 0.482]	7.2×10^{-8}
MDm	0.41	0.018	[0.358, 0.467]	1.6×10^{-11}
MGN	0.38	0.022	[0.321, 0.444]	4.7×10^{-14}
Pf	0.70	0.020	[0.645, 0.760]	1.0×10^{-42}
PuA	0.62	0.018	[0.563, 0.669]	7.2×10^{-20}
PuI	0.51	0.020	[0.454, 0.572]	0.37
PuL	0.65	0.019	[0.593, 0.707]	3.8×10^{-27}
PuM	0.49	0.018	[0.431, 0.543]	0.31
VA	0.48	0.018	[0.422, 0.532]	0.077
VLa	0.61	0.016	[0.557, 0.656]	4.6×10^{-20}
VLp	0.69	0.015	[0.642, 0.735]	2.4×10^{-58}
VPL	0.71	0.016	[0.657, 0.753]	1.7×10^{-61}

Structural connectivity with matrix-like voxels for the 16 thalamic voxels for which we combined left and right hemispheres. The confidence interval (CI) provided here (99.7%) matches the significance threshold utilized for this set of *t*-tests.

histology-based mapping in published animal studies with high-probability bias towards either striosome-like or matrix-like voxels (Table 2). In all 14 nuclei, our MRI-based method in humans matched the findings of histology-based studies in animals: AV, CL, CM, LD, MDl, MDm, MGN, Pf, PuA, PuL, Reu, VLa, VLp, VPL. We identified a bias toward striosome-like voxels in CeM, but prior animal studies were mixed, with some reporting a matrix bias (Berendse et al., 1988; Ragsdale and Graybiel, 1991) and others reporting a striosome bias (Prensa and Parent, 2001). Connectivity in the VAmc has not been mapped in animals, to the best of our knowledge. While thalamostriate connectivity was mapped for LP in rat, in an unfortunate mixing of terms between species, the rodent LP is the homologue of the pulvinar nucleus in primates (Funaki et al., 1998; Kamishina et al., 2008; Foik et al., 2020). Connectivity with the primate LP has not been described previously, to the best of our knowledge.

4. Discussion

In this study we aimed to identify biases in striato-pallido-thalamic structural connectivity by assessing probabilistic tractography between parcellated striatal compartments (striosome-like and matrix-like voxels) and segmented thalamic nuclei. Prior studies in primate and non-primate species demonstrated that striosome and matrix have distinct functions, pharmacology, and extra-striate connectivity. Therefore, we propose that biases in compartment-specific structural connectivity may be a mode for regulating specific thalamic nuclei and cortico-striato-pallido-thalamo-cortical loops. If this same bifurcation in thalamostriate organization is present in humans, compartment-level regulation may be an anatomical basis for focused regulation of human motor and behavioral functions. We validated our compartment-specific biases in structural connectivity in humans (*in vivo*) with supporting anatomic findings (somatotopy and compartment bias) from previous animal studies, where available. Our findings concur with decades of tract tracing studies in animals and argue that in humans, striato-thalamic structural connectivity is biased towards either striosome-like or matrix-like voxels in most thalamic nuclei. Though it is encouraging that our MRI-based assessments were in agreement with prior animal and human histology and imaging studies, we remind readers that our striatal parcellations were inferential and based on differential connectivity – we did not distinguish striosome and matrix through immunohistochemical staining, the gold standard for identifying the striatal compartments.

It is important to consider the limitations of our tractography-based study. Probabilistic tractography is susceptible to false positive and negative streamline estimations, tract-specific biases based on orientation and degree of curvature, inter-individual variance in total streamline counts, and other potential confounds (Campbell and Pike, 2014). Given these risks, we validated our tractography results with animal and/or human histology, where available. Identifying voxels solely by their differential connectivity replicated the spatial distribution, abundance, extra-striate connectivity, and somatotopy demonstrated previously in animal and human tissue (Waugh et al., 2022). Further, we demonstrated that the precision of our striatal parcellations was essential for assessing compartment-like connectivity. Neighboring voxels (shifted by a mean of 1.8 voxels from their original, precise position) had either a complete loss or a marked reduction in compartment-specific connectivity. Finally, we refined our tractography to select for striato-pallido-thalamic connectivity by excluding streamlines that extended outside our subcortical bounding mask, and by imposing an obligatory waypoint (the GPi). We thereby reduced the contributions of false positive projections, such as thalamostriate projections and fibers of passage in the internal capsule. Since we included subjects from four distinct research cohorts, and measured voxel location at many sites in each subject, we assessed for the impact of repeated measures within each subject and the influence of experimental cohort. These factors did not influence intra-striate voxel location or compartment-specific bias. Finally, we quantified location and connectivity exclusively through within-subject comparisons to reduce the impact of inter-individual variance in streamline propagation. Our MRI-based measures of striato-pallido-thalamic connectivity in humans replicated and extended the findings of injected tract tracer studies in experimental animals. It is likely that streamlines we seeded within one thalamic nucleus propagated through other nuclei en route to our pallidal waypoint and striatal targets. Double-counts of a given streamline have the potential to inflate absolute measures of connectivity, and to inflate streamline counts in voxels closer to edges or the internal medullary lamina (as streamlines transit grey matter to reach white matter). However, it is not clear that double-counts would alter the bias in connectivity toward one striatal compartment. That is, two streamlines, seeded from the same thalamic voxel but bound for opposing striatal compartments, would progress through the same probability space in their egress from the thalamus, leading to double-counts for both compartments. As our method explicitly assesses bias in connectivity, not absolute numbers of streamlines, potential double-counts would not skew quantification toward one compartment. To avoid potential

TABLE 2 Comparison of compartment-specific thalamic projections, animal and human assessments.

Thalamic nuclei	MRI-based results (striato-pallido-thalamic)	Animal Literature (thalamostriate and corticostriate)	Species utilized	Number of animals tested	Agree/Disagree/ Unknown
CM	Matrix-biased	Matrix-biased	Cat[1] Rat[2] Squirrel Monkey[3]	29 93 4	Agree
Pf	Matrix-biased	Matrix-biased	Cat[1] Squirrel Monkey[3] Rat[2]	29 4 93	Agree
PuA	Matrix-biased	Matrix-biased	Tree Shrew[4]	9	Agree
VLa	Matrix-biased	Matrix-biased	Rat[5] Cat[6] Pig-Tailed Macaque[7]	36 6 5 (i)	Agree
VLp	Matrix-biased	Matrix-biased	Rat[5] Cat[6] Pig-Tailed Macaque[7]	36 6 5 (i)	Agree
VPL	Matrix-biased	Matrix-biased	Rat[5] Cat[6]	36 6	Agree
PuL	Matrix-biased	Matrix-biased	Cat[6] Tree Shrew[4]	6 9	Agree
AV	Striosome-biased	Striosome-biased	Cat[1]	29	Agree
CL	Striosome-biased	Striosome-biased	Cat[1] Rat[2] Rat[12] Cat[6]	29 93 11 (i) 6	Agree
LD	Striosome-biased	Striosome-biased	Rat[8]	1	Agree
MDm	Striosome-biased	Striosome-biased	Cat[6]	6	Agree
MGN	Striosome-biased	Striosome-biased	Rat[9]	10 (i)	Agree
PuI	Neutral	Matrix-biased (central pulvinar)	Tree Shrew[4]	9	Unknown
PuM	Neutral	Matrix-biased (central pulvinar)	Tree Shrew[4]	9	Unknown
VA	Neutral	Matrix-biased Matrix-biased	Cat[6] Cat[1]	9 29	Unknown
LP	Striosome-favoring	Unknown	None	None	Unknown
MDl	Striosome-biased	Striosome-biased	Monkey[10] Rat[11] Rat[2]	12 (i) 16 (i) 93	Agree
Reu	Striosome-biased	Striosome-biased	Rat[2]	93	Agree
CeM	Striosome-biased	Striosome-biased Matrix-biased	Rat[13] Rat[2]	45 93	Mixed
VAmc	Matrix-biased	Unknown	None	None	Unknown

Comparison of our MRI-based findings in humans with histology-based assessments in animals. For 14 of 20 nuclei, our measures agree with prior animal literature. For the remaining six nuclei, bias is either mixed or unknown. For CeM, some tract tracing studies found a matrix-favoring bias and others found a striosome-favoring bias ("Mixed"). In LP and VAmc, we could identify no comparable study in animals (recorded as "Unknown" and "None"). In PuI, PuM, and VA, our method did not identify a compartment-specific bias ("Unknown"). We assessed the last four thalamic nuclei (blue) as separate hemispheres. The listed biases for these four nuclei are the mean of left and right hemispheres. Note that our MRI-based method utilized striatal voxels with striosome-like and matrix-like patterns of connectivity. While this inferential parcellation method replicates the compartment-specific spatial distribution, relative abundance, somatotopic organization, and connectivity profiles of striosome and matrix from animal and human histology, our use of living human subjects precluded the use of histologic confirmation of compartment identity. Superscripted numbers ("Species Utilized" column) correspond to the following citations, found in full form in the References Section: (1) Ragsdale and Graybiel (1991); (2) Unzai et al. (2017); (3) Sadikot et al. (1992); (4) Day-Brown et al. (2010); (5) Kincaid and Wilson (1996); (6) Avendano et al. (2006); (7) Pimenta et al. (2001); (8) Kamishina et al. (2008); (9) Barry et al. (2017); (10) Eblen and Graybiel (1995); (11) van Vulpen and Verwer (1989); (12) Wang and Pickel (1998); (13) Prensa and Parent (2001). The (i) designation ("Number of Animals" column) corresponds to the indirect association of compartment bias, as explained in the Discussion section.

distortions by double-counting, we chose to quantify compartment-specific streamlines at each voxel, and always relative to the connectivity with the opposite striatal compartment. We observed no regional trends suggesting that strength or direction of connectivity bias was driven simply by proximity or location. Edge nuclei and embedded nuclei were equally likely to have compartment-specific biases in connectivity (Figures 2, 4). Two of our most-biased nuclei, CM and CL, are both intralaminar but were biased toward matrix-like and striosome-like voxels, respectively. While we cannot exclude the possibility that double-counts impacted our measures of compartment-specific bias, the agreement between our findings and prior tract tracing studies in multiple species (Table 2) argues that this potential limitation did not meaningfully alter our results.

Striatal parcellation – and thus, the entirety of our efforts to map striato-pallido-thalamic connectivity – depends on injected tract tracing studies in animals for both guidance and validation. It is therefore essential to consider the breadth and depth of these histologic studies when judging the veracity of our own findings. The strength of the evidence for compartment-specific connectivity varies considerably among the thalamic nuclei. Some thalamic nuclei were assessed in multiple studies, several species, and using multiple techniques to identify compartment-specific connectivity bias. Nuclei with the strongest evidence included CL, CM, Pf, PuA, PuL, VPL, LD, and AV. Other thalamic nuclei had limited numbers of investigations and generally mapped connectivity in only single species. These included the PuI, PuM, Reu, MDl, MDm, VL, and CeM. A few thalamic nuclei had never been mapped previously, to the best of our knowledge, or were mapped only inferentially by demonstrating thalamocortical connectivity with regions whose compartment-specific bias was demonstrated elsewhere. Nuclei with thin or absent evidence of compartment selectivity included the LP, MGN, VA, and VAmc. Further histologic mapping of striatothalamic, thalamostriate, and thalamocortical projections will be essential to validating our findings in these under-investigated thalamic nuclei. In an inversion of the typical relationship between animal and human studies, such MRI-based investigations in humans, with hundreds of subjects, may bolster the findings of histologic studies that included single or small numbers of animals.

An additional limitation for relating our results to prior histologic studies is the difficulty in comparing connectivity between techniques and across species. Our MRI-based measures of striato-pallido-thalamic connectivity are not a direct comparison to prior tracer-based techniques that assessed thalamostriate and corticostriate connectivity in animals. However, if the striatal limbs of CSTC loops are segregated through either striosome or matrix, we hypothesized that these compartment-specific biases would be shared among the multiple limbs of the CSTC loop (Unzai et al., 2017) – that striato-pallido-thalamic projections (MRI in humans) would match the biases of thalamostriate projections (injected tracers in animals).

Studies of compartment-level striatal projections to the globus pallidus in cats, rats, and squirrel monkeys showed that axons originating from matrix dominate striatopallidal connectivity (Gimenez-Amaya and Graybiel, 1990; Flaherty and Graybiel, 1993; Rajakumar et al., 1993). Our results replicated those findings: streamlines seeded from matrix-like voxels were 5.7-fold more likely to reach the GPi, despite the fact that striosome-like and matrix-like masks seeded equal numbers of streamlines. We previously demonstrated that streamlines seeded by striosome-like voxels contacted 16.1% *more* extra-striate voxels than streamlines seeded by matrix-like voxels (Waugh et al., 2022). Therefore, the dominance of streamlines seeded by matrix-like voxels in striato-pallidal projections is not due to a general reduction in connectivity of striosome-like voxels.

We found that streamlines from striosome- and matrix-like voxels occupied distinct parts of the GPi, with little overlap. This anatomic segregation was qualitatively symmetric between hemispheres, even though we produced left and right hemisphere tractography independently. Our findings align with the tractography-based findings of Bertino et al., who demonstrated that limbic cortices (striosome-favoring) selectively project to the rostral GPi, while sensorimotor cortices (matrix-favoring) selectively project to the caudo-medial GPi (Bertino et al., 2020). This compartment-specific somatotopy in humans matches that demonstrated in both primate and non-primate species. General topographic organization of striato-pallidal synaptic connectivity has been demonstrated in the rat (Sloot and Gramsbergen, 1994; Fujiyama et al., 2011), squirrel monkey (Johnson and Rosvold, 1971; Smith and Parent, 1986), and macaque (Saleem et al., 2002), with striosome and matrix projections partially overlapping but impinging on neurochemically distinct zones (Rajakumar et al., 1993, 1994; Stephenson-Jones et al., 2013). Similarly, in mice the afferents from striosome and matrix MSNs to the entopeduncular nucleus (EP, the rodent equivalent of the GPi) synapse on different subclasses of EP neuron that release different neurotransmitters, have different firing patterns, and project to different targets (Wallace et al., 2017). If humans share these intermixed but functionally distinct populations of GPi neurons, segregating projections from striosome and matrix MSNs to different somatotopic zones may provide the architecture for separable functional roles for the two compartments in humans. The similarity of our tractography-based findings to the histology-based findings in animals supports the validity of using these methods to map striatal compartment-level structural connectivity in human health and disease.

Thalamic nuclei are often assessed at the level of anatomic groups, most commonly as anterior, medial, midline, lateral, and intralaminar nuclei. Thalamostriate projections are often mapped within this schema, with multiple nuclei within a group mapped in parallel, such as all midline (Unzai et al., 2017), lateral (Avendano et al., 2006), or intralaminar nuclei (Ragsdale and Graybiel, 1991). The biases in striato-pallido-thalamic connectivity we demonstrated closely mirror that group-level organization, both qualitatively (Figure 2) and quantitatively (Figure 4). It is important to note, however, that the traditional nuclear groups are not uniform in their functions. Among the intralaminar group, animal and human histologic characterization demonstrated that rostral and caudal intralaminar nuclei have distinct patterns of connectivity, they are engaged in disparate functions, and they have different vulnerability to neurodegeneration (Henderson et al., 2000; Galvan and Smith, 2011; Cover and Mathur, 2021). In cats, the rostral intralaminar nuclei (especially CL and paracentral nuclei) preferentially innervate the striosome, while the caudal intralaminar nuclei (CM and Pf) primarily project to the matrix (Ragsdale and Graybiel, 1991; Fujiyama et al., 2019). Other authors found that the rostral intralaminar nuclei had a mixed pattern of connectivity (Fujiyama et al., 2019). Our measures of striato-pallido-thalamic connectivity in the intralaminar nuclei match these prior findings: CL (the sole rostral intralaminar nucleus large enough to measure here) was markedly biased towards striosome-like voxels, while CM and Pf strongly favored matrix-like connectivity. Our CTT-based parcellation of the thalamus – carried out at the level of individual voxels

– recapitulates the organization of thalamic nuclei into nuclear groups. This emergent property suggests that striatal voxels identified by their differential connectivity are embedded within distinct striato-thalamic structural networks, and potentially, are embedded within distinct CSTC loops.

Thalamostriate projections originating in the CM, Pf, VPL, pulvinar, and ventrolateral (VL) favored the matrix compartment, or other regions highly biased toward the matrix compartment, in anterograde tracing studies in squirrel monkey, rat, cat, and tree shrew (Sadikot et al., 1992; Kincaid and Wilson, 1996; Avendano et al., 2006; Unzai et al., 2017). Our striato-pallido-thalamic connectivity data matches these matrix-biased thalamostriate findings. Tract tracing studies in the rat, cat, and squirrel monkey demonstrated that the VL projects primarily to matrix and receives projections from matrix-favoring portions of the EP (Rajakumar et al., 1993; Pimenta et al., 2001; Avendano et al., 2006). These VL tracing studies also support our findings of distinct, compartment-specific zones within the EP/GPi. Similarly, multiple types of histologic characterization in animals have demonstrated striosome-specific connectivity with particular thalamic nuclei. Anterograde tract tracing studies demonstrate that the medial and midline nuclei (such as Reu) generally project to striosome in animals (Goldman-Rakic and Porrino, 1985; Berendse et al., 1988; Ragsdale and Graybiel, 1991; Avendano et al., 2006; Unzai et al., 2017; Phillips et al., 2019). Injection of tracer in LD (rat) produced terminal labeling exclusively in the striosome compartment (Kamishina et al., 2008). In cats, radiolabeled amino acid injections in the rostral thalamic pole (primarily AV) elicited strong labelling of the lateral striosome (Ragsdale and Graybiel, 1991). In addition to direct evidence for compartment-specific projections, inferential evidence also supports compartment-specific thalamostriate projections. The CL has a robust projection to the dorsal striatum and has afferent and efferent connections with limbic cortices that also preferentially innervate the striosome compartment (Groenewegen, 1988; Eblen and Graybiel, 1995; Wang and Pickel, 1998). Similarly, the striatum receives convergent projections from the MGN and the auditory cortices (Chen et al., 2019). Electrical stimulation of the prelimbic and infralimbic cortices, areas shown to project primarily to striosome (Donoghue and Herkenham, 1986; Gerfen, 1989; Nisenbaum et al., 1998; McGregor et al., 2019), directly alters the neuronal activity of the MGN (Barry et al., 2017). Given the shared structural connectivity between these nuclei and cortical areas with strong striosome biases, these animal histology studies strongly suggest that CL and MGN project primarily to the striosome. The biases of streamlines seeded by striosome-like voxels that we demonstrated here agreed with these thalamostriate projections identified in animals. While the concurrence of our human and prior animal connectivity measures is reassuring, it is important to note that these findings are supportive of, but are not a direct test of our hypothesis. It may be possible to determine whether compartment-specific biases in striato-pallido-thalamic connectivity match the compartment selectivity of thalamostriate projections through colocalized injection of anterograde and retrograde tracers.

We identified one prior study that utilized multi-synaptic tracing to investigate striato-pallido-thalamic connectivity in rodents. Aoki et al. (2019) paired retrograde and anterograde tracing to demonstrate that limbic and motor cortices project through distinct striato-pedunculo-thalamo-cortical circuits. Likewise, they identified spatially distinct limbic and motor zones in the thalamus and striatum. However, they did not assess projections for compartment selectivity. Therefore, comparison of our findings to prior histology-based assessments in animals is limited to single-synapse tracing studies. While animal studies that analyzed single steps in the striato-pallido-thalamic projection (e.g., striatopallidal, or pallidothalamic) lend support to our compartment-specific findings, these isolated segments do not sum to a full tracing of compartment-specific striato-pallido-thalamic connectivity. In a parallel limitation, the probabilistic nature of tractography, coupled with the millimeter-scale resolution of diffusion imaging, ensures that our results will obscure less-abundant tracts and potentially merge tracts that are adjacent but distinct. Despite these limitations, our methods were sufficient to demonstrate that projections from striosome-like and matrix-like voxels occupy different paths to the GPi, occupy different volumes within the GPi, and have significant and substantial biases in their connectivity with thalamic nuclei that match the results of prior histologic assessments in animals. Future multi-synaptic tract tracing studies in animals will be necessary to validate our findings and more fully map the contributions of each striatal compartment to striato-pallido-thalamic arm of CSTC loops. While multi-synapse tracing poses an increased challenge relative to single-synapse tracing, this type of connectivity mapping has previously been accomplished for striato-pedunculo-thalamo-cortical circuits and even with projections from visceral organs to the brain (Bostan et al., 2010; Aoki et al., 2019; Dum et al., 2019; Foster et al., 2021).

The connectivity biases we localized in humans may not compare directly with findings in animals. For example, tract tracing studies did not subdivide the VL or pulvinar nuclei into subnuclei, as we did (Ragsdale and Graybiel, 1991). We found that projections to both VLa and VLp were highly biased toward matrix-like voxels, similar to the biases of the combined VL described in animals. However, in tree shrews the pulvinar was divided into two subdivisions, both of which projected to the matrix compartment (Day-Brown et al., 2010). In humans the pulvinar can be divided into four or more subdivisions. The anatomic correlation between human and tree shew pulvinar is therefore uncertain. In primates, the LP and pulvinar have distinct anatomic boundaries, peptide expression, and neurotransmitter profiles (Pérez-Santos et al., 2021), but these distinctions are not clearly established in non-primate species. Therefore, translating these posterior thalamic findings to human LP and pulvinar is problematic. For other thalamic nuclei, histologic mapping in animals is insufficient to identify a clear pattern of connectivity. Anterograde tracers injected into CeM predominantly reach the matrix (Berendse et al., 1988; Ragsdale and Graybiel, 1991). However, Prensa and Parent found that nigral neurons with dense projections to striosome also send collaterals to CeM (Prensa and Parent, 2001). We found no prior mapping of compartment-specific connectivity of the lateral mediodorsal (MDl), distinct from the other parts of the mediodorsal nucleus. However, the entire mediodorsal thalamus has prominent connectivity with cortical areas that selectively project to striosome, so MDl may also share striosome-favoring bias (Vogt et al., 1987; van Vulpen and Verwer, 1989; Eblen and Graybiel, 1995; O'Muircheartaigh et al., 2015; Phillips et al., 2019). Tract tracing results for Reu are limited but trend strongly toward striosome. In a single cat, a large injection of tracer that included both Reu and the ventromedial nucleus produced "marked" striosome labeling (Ragsdale and Graybiel, 1991). Reu is strongly interconnected with limbic structures (Vertes et al., 2022), which predominantly project to striosome (Donoghue and Herkenham, 1986; Gerfen, 1989; Graybiel, 1990). In contrast, mapping of a *single* Reu neuron identified a mixed, but matrix-dominated pattern of thalamostriate projections (Unzai et al., 2017). We could find no example of compartment-specific mapping

of the VAmc. Greater characterization in animal models, especially primates, will be necessary to understand the thalamostriate and striatothalamic connectivity of the CeM, LP, MDl, pulvinar, Reu, and VAmc nuclei.

Each of the 20 thalamic nuclei we assessed had a particular bias in striatal connectivity: favoring striosome-like voxels, favoring matrix-like voxels, or neutral. However, for 18 out of 20 thalamic nuclei, the left hemisphere was more biased towards matrix than the right (Figure 2). This consistent bias was independent of the type of connectivity that dominated (i.e., present in both striosome-favoring and matrix-favoring nuclei), and was not influenced by handedness, type of diffusion protocol, or any demographic variable. While we executed tractography in each hemisphere independently, all experimental parameters (seed volume, number of streamlines seeded, waypoint and exclusion masks, etc.) were identical in left and right hemisphere tractography. Our hand-segmented thalamic masks were slightly larger on the left (6.6%), but as the targets of tractography (striosome-like and matrix-like striatal masks) were of equal volume, we cannot detect a reason this would skew connectivity from most thalamic nuclei toward matrix-like voxels. This asymmetry in thalamic volume likely reflects neuroanatomic reality – our findings are similar to those of Ahsan et al., who determined that the left thalamus in healthy adults was significantly larger than the right (Ahsan et al., 2007). This asymmetry in compartment bias was independent of a nucleus' position within the thalamus (medial vs. lateral, rostral vs. ventral, embedded vs. edge). It is unclear how asymmetries in the edges of our left and right thalamic masks would produce such widespread, near-universal asymmetries in striatal connectivity. This left-sided bias towards matrix-like voxels was significant in 6 of 20 nuclei. Twelve additional nuclei were more biased in the left but not to a significant degree. The probability of 18/20 nuclei sharing a hemispheric bias by chance is 1 in 5,519. These structural asymmetries may also reflect laterality in function. Previous studies demonstrated that motor performance (speed, precision) was better in children whose functional connectivity was dominated by the left hemisphere (Barber et al., 2012). Likewise, increased motor control (manual dexterity) correlates with the degree of hemispheric lateralization for language (Hodgson et al., 2021). In contrast, abnormalities in lateralization may contribute to the movement disorder dystonia, in which both functional (Blood et al., 2004) and structural (Blood et al., 2019) asymmetries in motor control regions correlate with symptoms. Prior studies that utilized injected tract tracers to assess thalamic connectivity generally did so qualitatively. To fully address the possibility that the left thalamus is more biased toward matrix than the right, we suggest that future studies utilizing injected tract tracers in animals should *quantitatively* compare striatothalamic projections between the hemispheres.

Thalamic asymmetries have been identified in clinical neurology, in human brain mapping through neuroimaging and histology, and in animal neuroscience. The bias of the left thalamus towards the matrix-like compartment may be another example of these widespread thalamic asymmetries. Cerebral infarction, when limited to the thalamus, appears to have equal frequency in the left and right hemisphere. However, left thalamic infarctions are significantly more likely to produce clinically impactful symptoms (Rangus et al., 2022), leading left-sided thalamic infarction to be diagnosed at double the rate of right-sided thalamic infarction (Schaller-Paule et al., 2021). In healthy adolescents, thalamocortical structural connectivity was 24% greater in the left than the right thalamus (Alkonyi et al., 2011). Similarly, pallido-thalamic structural connectivity is significantly higher in the left thalamus, an asymmetry that is present in nuclei at every part of the rostro-caudal extent of the thalamus (Pelzer et al., 2017). During both innocuous and painful thermal stimulation, the right thalamus is significantly more activated than the left, regardless of which side of the body is stimulated (Coghill et al., 2001). Concentrations of the metabolite phosphocreatine, hypothesized to be a "substrate of wakefulness," decline significantly from morning to afternoon, and are restored to morning levels by an afternoon nap – but this metabolic change occurs only in the left thalamus, not the right (Gordji-Nejad et al., 2018). Neurotransmitters are also lateralized in the human thalamus. The right thalamus has more μ-opioid receptor availability than the left, an asymmetry that is greater in the thalamus than in 15 other brain regions (Kantonen et al., 2020). Tissue norepinephrine is strongly lateralized in the postmortem human thalamus (Oke et al., 1978). In healthy rats, 98% of the brain's mast cells are found in the thalamus. At most points in the rostro-caudal extent of the thalamus, the left thalamus has significantly more mast cells – up to 30% more (Goldschmidt et al., 1984). Asymmetries in mast cells number may have implications for human neuroinflammatory disorders, but as mast cell activation is also associated with improved goal-oriented behaviors and learning (Fitzpatrick and Morrow, 2017), asymmetries in humans, if present, may induce a lateralization in the motivational value of rewarding stimuli. These wide-ranging asymmetries in the anatomy, pharmacology, and metabolism of the thalamus provide context for the left-sided bias toward higher connectivity with matrix-like voxels, present in 18 of 20 thalamic nuclei. Our asymmetric findings may reflect a common feature of the mammalian thalamus.

Our method for parcellating the striatum into striosome-like and matrix-like compartments allowed us to map striato-pallido-thalamic connectivity *in vivo* in healthy humans. These techniques may also be useful for mapping striato-pallido-thalamic projections in developmental and degenerative disease states. Numerous disorders that were hypothesized to have a compartment-specific element to their pathology and progression may be more completely understood when studied in a compartment-specific approach, rather than at the whole-striatum level (Crittenden and Graybiel, 2011). For example, early in the clinical course of Huntington disease (HD) MSNs in the striosome degenerate more than those in matrix (Hedreen and Folstein, 1995; Matsushima, 2022). Striosome-dominated degeneration also holds true in later stages of HD for individuals whose symptoms were mood-predominant (Tippett et al., 2007). Selective degeneration of thalamic projections neurons has also been identified in HD, especially in the CM/Pf complex (Heinsen et al., 1996) and mediodorsal nucleus (Heinsen et al., 1999). These thalamic nuclei have opposing patterns of striatal compartment selectivity (CM/Pf, matrix-like; mediodorsal, striosome-like; Figure 4), suggesting that interpretating thalamic neurodegeneration in HD may require both symptom-specific (mood vs. motor) and compartment-specific assessments. Similarly, in both idiopathic Parkinson disease (PD) and progressive supranuclear palsy, thalamic neurodegeneration is relatively selective for the caudal intralaminar thalamic nuclei (CM, Pf; Henderson et al., 2000; Halliday, 2009). Though beyond the scope of this publication, we propose that denervation within compartment-specific CSTC loops may correlate with symptom type in PD as it appears to do for HD.

Abnormalities in the striatal compartments may be a feature of developmental disorders, in addition to the noted neurodegenerative disorders. For some developmental disorders, matrix- or striosome-specific neuropathologies are likely at the ultrastructural or

interneuron level [e.g., schizophrenia (Roberts et al., 2005), Tourette syndrome (Kataoka et al., 2010)]. Such abnormalities are almost certainly below the resolution of diffusion MRI, a limitation of our striatal parcellation method. Other developmental disorders may have discernable structural abnormalities at MRI scale. Children with autism spectrum disorder were found to have increased ratios of matrix:striosome volume (identified by both immunohistochemical stains and mRNA expression, Kuo and Liu, 2020), an intriguing finding that will require repetition in larger cohorts. Habitual motor movements (stereotypies) have been hypothesized to arise from hyperactivation of striosomal neurons, based on studies in rats and squirrel monkeys (Canales and Graybiel, 2000; Saka et al., 2004). Stereotypies are common in autism and developmental disability (Goldman et al., 2009), but are also found among typically developing children (Singer, 2009; Oakley et al., 2015). Stereotypies are remarkably persistent throughout childhood (Tan et al., 1997; Valente et al., 2019) and frequently co-occur with a range of other childhood neurological disorders (e.g., motor developmental delay, attention-deficit hyperactivity disorder, obsessive compulsive disorder, Tourette syndrome), suggesting an anatomic susceptibility within this cohort of neurodevelopmental disorders (Tan et al., 1997; Valente et al., 2019). Whether these disorders are related to striosome or matrix dysfunction in humans has never been investigated, to the best of our knowledge. Anatomic relationships between each striatal compartment and particular symptoms can now be explored in living humans, and longitudinally through the course of diseases, for disorders associated with abnormal development, degeneration, or injury in specific CSTC loops. Identifying which thalamic nuclei have connectivity biases toward striosome-like or matrix-like voxels is an essential step in characterizing the role of the striatal compartments in specific CSTC loops, and thus in understanding the functions of striosome and matrix in human health and disease.

Data availability statement

Publicly available datasets were analyzed in this study. This data can be found here: NIMH Data Archive, Data Object Identifier: 10.15154/1528201.

Ethics statement

All research was conducted in accordance with the principles set forth in the Declaration of Helsinki. All data collection was approved by, and experimental oversight was conducted by, the Institutional Review Board for the respective institution where the subject was recruited. Oversight of the secondary analysis of MRI data was conducted by the Institutional Review Board of the University of Texas Southwestern. The participants provided their written informed consent to participate in the original studies that generated the MRI data presented here.

Author contributions

AF: acquisition and analysis of data, original draft of the manuscript, and critical revising of the manuscript. AH, NB, NS, HB, and AB: acquisition of data and critical revising of the manuscript. JW: acquisition, analysis and interpretation of data, original draft of the manuscript, and critical revising of the manuscript. All authors contributed to the article and approved the submitted version.

Funding

JW was supported by: the Clinical Research Training Fellowship and Career Development Award, American Academy of Neurology; the Collaborative Center for X-linked Dystonia Parkinsonism; and NINDS grant 1K23NS124978-01A1. NB was supported by: the DFG (BR4328.2-1 and GRK1957); the Michael J Fox Foundation; the Collaborative Center for X-linked Dystonia-Parkinsonism and the EU Joint Programme - Neurodegenerative Disease Research (JPND). HB and AB were supported by DABK39-03-0098 and DABK39-03-C-0098; The Phenotype Genotype Project in Addiction and Mood Disorder from the ONDCP - CTAC, Washington, D.C. NS was supported by NINDS grant P01 NS087987. Shared computer resources and storage were made possible by the MGH Shared Instrumentation Grants 1S10RR023043 and 1S10RR023401. Dr. Waugh's funding line: Clinical and Translational Science Award - Pilot Grant.

Acknowledgments

Data used in the preparation of this manuscript was obtained from the National Institute of Mental Health (NIMH) Data Archive (NDA). NDA is a collaborative informatics system created by the National Institutes of Health to provide a national resource to support and accelerate research in mental health. Dataset identifiers can be accessed through a study-specific NDA Data Object Identifier: 10.15154/1528201. This manuscript reflects the views of the authors and may not reflect the opinions or views of the NIH or of the Submitters submitting original data to NDA.

Conflict of interest

The authors declare that the research was conducted in the absence of any commercial or financial relationships that could be construed as a potential conflict of interest.

Publisher's note

Supplementary material

The Supplementary material for this article can be found online at: https://www.frontiersin.org/articles/10.3389/fnins.2023.1178473/full#supplementary-material

References

Ahsan, R. L., Allom, R., Gousias, I. S., Habib, H., Turkheimer, F. E., Free, S., et al. (2007). Volumes, spatial extents and a probabilistic atlas of the human basal ganglia and thalamus. *NeuroImage* 38, 261–270. doi: 10.1016/j.neuroimage.2007.06.004

Alexander, G. E., DeLong, M. R., and Strick, P. L. (1986). Parallel organization of functionally segregated circuits linking basal ganglia and cortex. *Annu. Rev. Neurosci.* 9, 357–381. doi: 10.1146/annurev.ne.09.030186.002041

Alkonyi, B., Juhasz, C., Muzik, O., Behen, M. E., Jeong, J. W., and Chugani, H. T. (2011). Thalamocortical connectivity in healthy children: asymmetries and robust developmental changes between ages 8 and 17 years. *AJNR Am. J. Neuroradiol.* 32, 962–969. doi: 10.3174/ajnr.A2417

Aoki, S., Smith, J. B., Li, H., Yan, X., Igarashi, M., Coulon, P., et al. (2019). An open cortico-basal ganglia loop allows limbic control over motor output via the nigrothalamic pathway. *elife* 8:e49995. doi: 10.7554/eLife.49995

Aravamuthan, B. R., and Waugh, J. L. (2016). Localization of basal ganglia and thalamic damage in Dyskinetic cerebral palsy. *Pediatr. Neurol.* 54, 11–21. doi: 10.1016/j.pediatrneurol.2015.10.005

Avendano, C., de Las Heras, S., and Gimenez-Amaya, J. M. (2006). Striatal projections from the lateral and posterior thalamic complexes. An anterograde tracer study in the cat. *Histochem. Cell Biol.* 125, 265–271. doi: 10.1007/s00418-005-0054-4

Barber, A. D., Srinivasan, P., Joel, S. E., Caffo, B. S., Pekar, J. J., and Mostofsky, S. H. (2012). Motor "dexterity"?: evidence that left hemisphere lateralization of motor circuit connectivity is associated with better motor performance in children. *Cereb. Cortex* 22, 51–59. doi: 10.1093/cercor/bhr062

Barry, K. M., Robertson, D., and Mulders, W. (2017). Medial geniculate neurons show diverse effects in response to electrical stimulation of prefrontal cortex. *Hear. Res.* 353, 204–212. doi: 10.1016/j.heares.2017.07.002

Behrens, T. E., Berg, H. J., Jbabdi, S., Rushworth, M. F., and Woolrich, M. W. (2007). Probabilistic diffusion tractography with multiple fibre orientations: what can we gain? *NeuroImage* 34, 144–155. doi: 10.1016/j.neuroimage.2006.09.018

Behrens, T. E., Johansen-Berg, H., Woolrich, M. W., Smith, S. M., Wheeler-Kingshott, C. A., Boulby, P. A., et al. (2003). Non-invasive mapping of connections between human thalamus and cortex using diffusion imaging. *Nat. Neurosci.* 6, 750–757. doi: 10.1038/nn1075

Berendse, H. W., and Groenewegen, H. J. (1990). Organization of the thalamostriatal projections in the rat, with special emphasis on the ventral striatum. *J. Comp. Neurol.* 299, 187–228. doi: 10.1002/cne.902990206

Berendse, H. W., Voorn, P., te Kortschot, A., and Groenewegen, H. J. (1988). Nuclear origin of thalamic afferents of the ventral striatum determines their relation to patch/matrix configurations in enkephalin-immunoreactivity in the rat. *J. Chem. Neuroanat.* 1, 3–10.

Bertino, S., Basile, G. A., Bramanti, A., Anastasi, G. P., Quartarone, A., Milardi, D., et al. (2020). Spatially coherent and topographically organized pathways of the human globus pallidus. *Hum. Brain Mapp.* 41, 4641–4661. doi: 10.1002/hbm.25147

Bloem, B., Huda, R., Amemori, K. I., Abate, A. S., Krishna, G., Wilson, A. L., et al. (2022). Multiplexed action-outcome representation by striatal striosome-matrix compartments detected with a mouse cost-benefit foraging task. *Nat. Commun.* 13:1541. doi: 10.1038/s41467-022-28983-5

Blood, A. J., Flaherty, A. W., Choi, J. K., Hochberg, F. H., Greve, D. N., Bonmassar, G., et al. (2004). Basal ganglia activity remains elevated after movement in focal hand dystonia. *Ann. Neurol.* 55, 744–748. doi: 10.1002/ana.20108

Blood, A. J., Kuster, J. K., Waugh, J. L., Levenstein, J. M., Multhaupt-Buell, T. J., Sudarsky, L. R., et al. (2019). White matter changes in cervical dystonia relate to clinical effectiveness of botulinum toxin treatment. *Front. Neurol.* 10:265. doi: 10.3389/fneur.2019.00265

Bostan, A. C., Dum, R. P., and Strick, P. L. (2010). The basal ganglia communicate with the cerebellum. *Proc. Natl. Acad. Sci. U. S. A.* 107, 8452–8456. doi: 10.1073/pnas.1000496107

Burke, R. E., and Baimbridge, K. G. (1993). Relative loss of the striatal striosome compartment, defined by calbindin-D28k immunostaining, following developmental hypoxic-ischemic injury. *Neuroscience* 56, 305–315. doi: 10.1016/0306-4522(93)90333-B

Campbell, J. S., and Pike, G. B. (2014). Potential and limitations of diffusion MRI tractography for the study of language. *Brain Lang.* 131, 65–73. doi: 10.1016/j.bandl.2013.06.007

Canales, J. J., and Graybiel, A. M. (2000). A measure of striatal function predicts motor stereotypy. *Nat. Neurosci.* 3, 377–383. doi: 10.1038/73949

Chen, L., Wang, X., Ge, S., and Xiong, Q. (2019). Medial geniculate body and primary auditory cortex differentially contribute to striatal sound representations. *Nat. Commun.* 10:418. doi: 10.1038/s41467-019-08350-7

Chung, C. S., Caplan, L. R., Han, W., Pessin, M. S., Lee, K. H., and Kim, J. M. (1996). Thalamic haemorrhage. *Brain* 119, 1873–1886. doi: 10.1093/brain/119.6.1873

Coghill, R. C., Gilron, I., and Iadarola, M. J. (2001). Hemispheric lateralization of somatosensory processing. *J. Neurophysiol.* 85, 2602–2612. doi: 10.1152/jn.2001.85.6.2602

Cover, K. K., and Mathur, B. N. (2021). Rostral Intralaminar thalamus engagement in cognition and behavior. *Front. Behav. Neurosci.* 15:652764. doi: 10.3389/fnbeh.2021.652764

Crittenden, J. R., and Graybiel, A. M. (2011). Basal ganglia disorders associated with imbalances in the striatal striosome and matrix compartments. *Front. Neuroanat.* 5:59. doi: 10.3389/fnana.2011.00059

Day-Brown, J. D., Wei, H., Chomsung, R. D., Petry, H. M., and Bickford, M. E. (2010). Pulvinar projections to the striatum and amygdala in the tree shrew. *Front. Neuroanat.* 4:143. doi: 10.3389/fnana.2010.00143

Desban, M., Kemel, M. L., Glowinski, J., and Gauchy, C. (1993). Spatial organization of patch and matrix compartments in the rat striatum. *Neuroscience* 57, 661–671. doi: 10.1016/0306-4522(93)90013-6

Donoghue, J. P., and Herkenham, M. (1986). Neostriatal projections from individual cortical fields conform to histochemically distinct striatal compartments in the rat. *Brain Res.* 365, 397–403. doi: 10.1016/0006-8993(86)91658-6

Dufour, A., Seibt, J., Passante, L., Depaepe, V., Ciossek, T., Frisén, J., et al. (2003). Area specificity and topography of thalamocortical projections are controlled by ephrin/Eph genes. *Neuron* 39, 453–465. doi: 10.1016/s0896-6273(03)00440-9

Dum, R. P., Levinthal, D. J., and Strick, P. L. (2019). The mind-body problem: circuits that link the cerebral cortex to the adrenal medulla. *Proc. Natl. Acad. Sci. U. S. A.* 116, 26321–26328. doi: 10.1073/pnas.1902297116

Eblen, F., and Graybiel, A. M. (1995). Highly restricted origin of prefrontal cortical inputs to striosomes in the macaque monkey. *J. Neurosci.* 15, 5999–6013. doi: 10.1523/JNEUROSCI.15-09-05999.1995

Ender, P. (2017). How can I do tests of simple main effects in STATA? Institute for Digital Research and Education. Available at: https://stats.idre.ucla.edu/stata/faq/how-can-i-do-tests-of-simple-main-effects-in-stata/ (Accessed March 2, 2022).

Faull, R. L., Dragunow, M., and Villiger, J. W. (1989). The distribution of neurotensin receptors and acetylcholinesterase in the human caudate nucleus: evidence for the existence of a third neurochemical compartment. *Brain Res.* 488, 381–386. doi: 10.1016/0006-8993(89)90735-X

Feekes, J. A., and Cassell, M. D. (2006). The vascular supply of the functional compartments of the human striatum. *Brain* 129, 2189–2201. doi: 10.1093/brain/awl158

Féger, J., Bevan, M., and Crossman, A. R. (1994). The projections from the parafascicular thalamic nucleus to the subthalamic nucleus and the striatum arise from separate neuronal populations: a comparison with the corticostriatal and corticosubthalamic efferents in a retrograde fluorescent double-labelling study. *Neuroscience* 60, 125–132. doi: 10.1016/0306-4522(94)90208-9

Fitzpatrick, C. J., and Morrow, J. D. (2017). Thalamic mast cell activity is associated with sign-tracking behavior in rats. *Brain Behav. Immun.* 65, 222–229. doi: 10.1016/j.bbi.2017.05.003

Flaherty, A. W., and Graybiel, A. M. (1993). Output architecture of the primate putamen. *J. Neurosci.* 13, 3222–3237. doi: 10.1523/jneurosci.13-08-03222.1993

Foik, A. T., Scholl, L. R., Lean, G. A., and Lyon, D. C. (2020). Visual response characteristics in lateral and medial subdivisions of the rat pulvinar. *Neuroscience* 441, 117–130. doi: 10.1016/j.neuroscience.2020.06.030

Foster, N. N., Barry, J., Korobkova, L., Garcia, L., Gao, L., Becerra, M., et al. (2021). The mouse cortico-basal ganglia-thalamic network. *Nature* 598, 188–194. doi: 10.1038/s41586-021-03993-3

Fujiyama, F., Sohn, J., Nakano, T., Furuta, T., Nakamura, K. C., Matsuda, W., et al. (2011). Exclusive and common targets of neostriatofugal projections of rat striosome neurons: a single neuron-tracing study using a viral vector. *Eur. J. Neurosci.* 33, 668–677. doi: 10.1111/j.1460-9568.2010.07564.x

Fujiyama, F., Unzai, T., and Karube, F. (2019). Thalamostriatal projections and striosome-matrix compartments. *Neurochem. Int.* 125, 67–73. doi: 10.1016/j.neuint.2019.01.024

Funaki, S., Meguro, R., Abe, H., and Norita, M. (1998). The organization of the thalamostriatal projection from the lateral posterior thalamic nuclear complex (LP) in the pigmented rat. *Neurobiology* 6, 273–294.

Galvan, A., and Smith, Y. (2011). The primate thalamostriatal systems: anatomical organization, functional roles and possible involvement in Parkinson's disease. *Basal Ganglia* 1, 179–189. doi: 10.1016/j.baga.2011.09.001

Gerfen, C. R. (1984). The neostriatal mosaic: compartmentalization of corticostriatal input and striatonigral output systems. *Nature* 311, 461–464.

Gerfen, C. R. (1989). The neostriatal mosaic: striatal patch-matrix organization is related to cortical lamination. *Science* 246, 385–388. doi: 10.1126/science.2799392

Gimenez-Amaya, J. M., and Graybiel, A. M. (1990). Compartmental origins of the striatopallidal projection in the primate. *Neuroscience* 34, 111–126. doi: 10.1016/0306-4522(90)90306-O

Goldman, S., Wang, C., Salgado, M. W., Greene, P. E., Kim, M., and Rapin, I. (2009). Motor stereotypies in children with autism and other developmental disorders. *Dev. Med. Child Neurol.* 51, 30–38. doi: 10.1111/j.1469-8749.2008.03178.x

Goldman-Rakic, P. S. (1982). Cytoarchitectonic heterogeneity of the primate neostriatum: subdivision into island and matrix cellular compartments. *J. Comp. Neurol.* 205, 398–413. doi: 10.1002/cne.902050408

Goldman-Rakic, P. S., and Porrino, L. J. (1985). The primate mediodorsal (MD) nucleus and its projection to the frontal lobe. *J. Comp. Neurol.* 242, 535–560. doi: 10.1002/cne.902420406

Goldschmidt, R. C., Hough, L. B., Glick, S. D., and Padawer, J. (1984). Mast cells in rat thalamus: nuclear localization, sex difference and left-right asymmetry. *Brain Res.* 323, 209–217. doi: 10.1016/0006-8993(84)90291-9

Gordji-Nejad, A., Matusch, A., Li, S., Kroll, T., Beer, S., Elmenhorst, D., et al. (2018). Phosphocreatine levels in the left thalamus decline during wakefulness and increase after a nap. *J. Neurosci.* 38, 10552–10565. doi: 10.1523/jneurosci.0865-18.2018

Granado, N., Ares-Santos, S., O'Shea, E., Vicario-Abejon, C., Colado, M. I., and Moratalla, R. (2010). Selective vulnerability in striosomes and in the nigrostriatal dopaminergic pathway after methamphetamine administration: early loss of TH in striosomes after methamphetamine. *Neurotox. Res.* 18, 48–58. doi: 10.1007/s12640-009-9106-1

Graybiel, A. M. (1990). Neurotransmitters and neuromodulators in the basal ganglia. *Trends Neurosci.* 13, 244–254. doi: 10.1016/0166-2236(90)90104-I

Graybiel, A. M., and Hickey, T. L. (1982). Chemospecificity of ontogenetic units in the striatum: demonstration by combining [3H]thymidine neuronography and histochemical staining. *Proc. Natl. Acad. Sci. U. S. A.* 79, 198–202. doi: 10.1073/pnas.79.1.198

Graybiel, A. M., and Ragsdale, C. W. Jr. (1978). Histochemically distinct compartments in the striatum of human, monkeys, and cat demonstrated by acetylthiocholinesterase staining. *Proc. Natl. Acad. Sci. U. S. A.* 75, 5723–5726. doi: 10.1073/pnas.75.11.5723

Groenewegen, H. J. (1988). Organization of the afferent connections of the mediodorsal thalamic nucleus in the rat, related to the mediodorsal-prefrontal topography. *Neuroscience* 24, 379–431. doi: 10.1016/0306-4522(88)90339-9

Haber, S. N. (2003). The primate basal ganglia: parallel and integrative networks. *J. Chem. Neuroanat.* 26, 317–330. doi: 10.1016/j.jchemneu.2003.10.003

Halliday, G. M. (2009). Thalamic changes in Parkinson's disease. *Parkinsonism Relat. Disord.* 15, S152–S155. doi: 10.1016/s1353-8020(09)70804-1

Hammers, A., Chen, C. H., Lemieux, L., Allom, R., Vossos, S., Free, S. L., et al. (2007). Statistical neuroanatomy of the human inferior frontal gyrus and probabilistic atlas in a standard stereotaxic space. *Hum. Brain Mapp.* 28, 34–48. doi: 10.1002/hbm.20254

Hedreen, J. C., and Folstein, S. E. (1995). Early loss of neostriatal striosome neurons in Huntington's disease. *J. Neuropathol. Exp. Neurol.* 54, 105–120. doi: 10.1097/00005072-199501000-00013

Heinsen, H., Rüb, U., Bauer, M., Ulmar, G., Bethke, B., Schüler, M., et al. (1999). Nerve cell loss in the thalamic mediodorsal nucleus in Huntington's disease. *Acta Neuropathol.* 97, 613–622. doi: 10.1007/s004010051037

Heinsen, H., Rüb, U., Gangnus, D., Jungkunz, G., Bauer, M., Ulmar, G., et al. (1996). Nerve cell loss in the thalamic centromedian-parafascicular complex in patients with Huntington's disease. *Acta Neuropathol.* 91, 161–168. doi: 10.1007/s004010050408

Henderson, J. M., Carpenter, K., Cartwright, H., and Halliday, G. M. (2000). Loss of thalamic intralaminar nuclei in progressive supranuclear palsy and Parkinson's disease: clinical and therapeutic implications. *Brain* 123, 1410–1421. doi: 10.1093/brain/123.7.1410

Hodgson, J. C., Richardson, D., and Hudson, J. M. (2021). The relationship between lateralization patterns from sequence based motor tasks and hemispheric speech dominance. *Neuropsychology* 35, 157–171. doi: 10.1037/neu0000702

Holt, D. J., Graybiel, A. M., and Saper, C. B. (1997). Neurochemical architecture of the human striatum. *J. Comp. Neurol.* 384, 1–25. doi: 10.1002/(SICI)1096-9861(19970721)384:1<1::AID-CNE1>3.0.CO;2-5

Hwang, K., Bertolero, M. A., Liu, W. B., and D'Esposito, M. (2017). The human thalamus is an integrative hub for functional brain networks. *J. Neurosci.* 37, 5594–5607. doi: 10.1523/jneurosci.0067-17.2017

Hwang, K., Bruss, J., Tranel, D., and Boes, A. D. (2020). Network localization of executive function deficits in patients with focal thalamic lesions. *J. Cogn. Neurosci.* 32, 2303–2319. doi: 10.1162/jocn_a_01628

Iglehart, C., Monti, M., Cain, J., Tourdias, T., and Saranathan, M. (2020). A systematic comparison of structural-, structural connectivity-, and functional connectivity-based thalamus parcellation techniques. *Brain Struct. Funct.* 225, 1631–1642. doi: 10.1007/s00429-020-02085-8

Iglesias, J. E., Insausti, R., Lerma-Usabiaga, G., Bocchetta, M., Van Leemput, K., Greve, D. N., et al. (2018). A probabilistic atlas of the human thalamic nuclei combining ex vivo MRI and histology. *NeuroImage* 183, 314–326. doi: 10.1016/j.neuroimage.2018.08.012

Ilinsky, I., Horn, A., Paul-Gilloteaux, P., Gressens, P., Verney, C., and Kultas-Ilinsky, K. (2018). Human motor thalamus reconstructed in 3D from continuous sagittal sections with identified subcortical afferent territories. *eNeuro* 5, ENEURO.0060–ENEU18.2018. doi: 10.1523/eneuro.0060-18.2018

Jaquins-Gerstl, A., Nesbitt, K. M., and Michael, A. C. (2021). In vivo evidence for the unique kinetics of evoked dopamine release in the patch and matrix compartments of the striatum. *Anal. Bioanal. Chem.* 413, 6703–6713. doi: 10.1007/s00216-021-03300-z

Joel, D. (2001). Open interconnected model of basal ganglia-thalamocortical circuitry and its relevance to the clinical syndrome of Huntington's disease. *Mov. Disord.* 16, 407–423. doi: 10.1002/mds.1096

Joel, D., Niv, Y., and Ruppin, E. (2002). Actor-critic models of the basal ganglia: new anatomical and computational perspectives. *Neural Netw.* 15, 535–547. doi: 10.1016/S0893-6080(02)00047-3

Johnson, T. N., and Rosvold, H. E. (1971). Topographic projections on the globus pallidus and the substantia nigra of selectively placed lesions in the precommissural caudate nucleus and putamen in the monkey. *Exp. Neurol.* 33, 584–596. doi: 10.1016/0014-4886(71)90129-4

Jones, E. G. (1998). A new view of specific and nonspecific thalamocortical connections. *Adv. Neurol.* 77, 49–71.

Kamishina, H., Yurcisin, G. H., Corwin, J. V., and Reep, R. L. (2008). Striatal projections from the rat lateral posterior thalamic nucleus. *Brain Res.* 1204, 24–39. doi: 10.1016/j.brainres.2008.01.094

Kantonen, T., Karjalainen, T., Isojärvi, J., Nuutila, P., Tuisku, J., Rinne, J., et al. (2020). Interindividual variability and lateralization of μ-opioid receptors in the human brain. *NeuroImage* 217:116922. doi: 10.1016/j.neuroimage.2020.116922

Kataoka, Y., Kalanithi, P. S., Grantz, H., Schwartz, M. L., Saper, C., Leckman, J. F., et al. (2010). Decreased number of parvalbumin and cholinergic interneurons in the striatum of individuals with Tourette syndrome. *J. Comp. Neurol.* 518, 277–291. doi: 10.1002/cne.22206

Kelly, S. M., Raudales, R., He, M., Lee, J. H., Kim, Y., Gibb, L. G., et al. (2018). Radial glial lineage progression and differential intermediate progenitor amplification underlie striatal compartments and circuit organization. *Neuron* 99, 345–361.e4. doi: 10.1016/j.neuron.2018.06.021

Kim, N. Y., Hsu, J., Talmasov, D., Joutsa, J., Soussand, L., Wu, O., et al. (2021). Lesions causing hallucinations localize to one common brain network. *Mol. Psychiatry* 26, 1299–1309. doi: 10.1038/s41380-019-0565-3

Kincaid, A. E., and Wilson, C. J. (1996). Corticostriatal innervation of the patch and matrix in the rat neostriatum. *J. Comp. Neurol.* 374, 578–592. doi: 10.1002/(SICI)1096-9861(19961028)374:4<578::AID-CNE7>3.0.CO;2-Z

Kletenik, I., Ferguson, M. A., Bateman, J. R., Cohen, A. L., Lin, C., Tetreault, A., et al. (2022). Network localization of unconscious visual perception in Blindsight. *Ann. Neurol.* 91, 217–224. doi: 10.1002/ana.26292

Krauth, A., Blanc, R., Poveda, A., Jeanmonod, D., Morel, A., and Székely, G. (2010). A mean three-dimensional atlas of the human thalamus: generation from multiple histological data. *NeuroImage* 49, 2053–2062. doi: 10.1016/j.neuroimage.2009.10.042

Kumral, E., Evyapan, D., Balkir, K., and Kutluhan, S. (2001). Bilateral thalamic infarction. Clinical, etiological and MRI correlates. *Acta Neurol. Scand.* 103, 35–42. doi: 10.1034/j.1600-0404.2001.00141.x

Kundu, B., Brock, A. A., Englot, D. J., Butson, C. R., and Rolston, J. D. (2018). Deep brain stimulation for the treatment of disorders of consciousness and cognition in traumatic brain injury patients: a review. *Neurosurg. Focus.* 45:E14. doi: 10.3171/2018.5.Focus18168

Kuo, H. Y., and Liu, F. C. (2020). Pathological alterations in striatal compartments in the human brain of autism spectrum disorder. *Mol. Brain* 13:83. doi: 10.1186/s13041-020-00624-2

Leiguarda, R., Nogués, M., and Berthier, M. (1992). Gyratory epilepsy in a patient with a thalamic neoplasm. *Epilepsia* 33, 826–828. doi: 10.1111/j.1528-1157.1992.tb02189.x

Lévesque, M., and Parent, A. (2005). The striatofugal fiber system in primates: a reevaluation of its organization based on single-axon tracing studies. *Proc. Natl. Acad. Sci. U. S. A.* 102, 11888–11893. doi: 10.1073/pnas.0502710102

Li, S., Kumar, Y., Gupta, N., Abdelbaki, A., Sahwney, H., Kumar, A., et al. (2018). Clinical and neuroimaging findings in thalamic territory infarctions: a review. *J. Neuroimaging* 28, 343–349. doi: 10.1111/jon.12503

Mai, J. K., and Majtanik, M. (2018). Toward a common terminology for the thalamus. *Front. Neuroanat.* 12:114. doi: 10.3389/fnana.2018.00114

Mai, J., Paxinos, G., and Voss, T. (1997). *Atlas of the human brain. Third Edn.* Cambridge, MA, USA: Academic Press.

Malach, R., and Graybiel, A. M. (1986). Mosaic architecture of the somatic sensory-recipient sector of the cat's striatum. *J. Neurosci.* 6, 3436–3458. doi: 10.1523/JNEUROSCI.06-12-03436.1986

Matsushima, A. (2022). Huntington's disease produces multiplexed transcriptional vulnerabilities of striatal D1-D2 and Striosome-matrix neurons. bioRxiv.

McGregor, M. M., McKinsey, G. L., Girasole, A. E., Bair-Marshall, C. J., Rubenstein, J. L. R., and Nelson, A. B. (2019). Functionally distinct connectivity of developmentally targeted striosome neurons. *Cell Rep.* 29, 1419–1428.e5. doi: 10.1016/j.celrep.2019.09.076

Miyai, I., Suzuki, T., Kang, J., and Volpe, B. T. (2000). Improved functional outcome in patients with hemorrhagic stroke in putamen and thalamus compared with those with

stroke restricted to the putamen or thalamus. *Stroke* 31, 1365–1369. doi: 10.1161/01.str.31.6.1365

Mofakham, S., Fry, A., Adachi, J., Stefancin, P. L., Duong, T. Q., Saadon, J. R., et al. (2021). Electrocorticography reveals thalamic control of cortical dynamics following traumatic brain injury. *Commun. Biol.* 4:1210. doi: 10.1038/s42003-021-02738-2

Morigaki, R., and Goto, S. (2015). Postsynaptic density protein 95 in the striosome and matrix compartments of the human neostriatum. *Front. Neuroanat.* 9:154. doi: 10.3389/fnana.2015.00154

Morishita, T., Higuchi, M. A., Kobayashi, H., Abe, H., Higashi, T., and Inoue, T. (2019). A retrospective evaluation of thalamic targeting for tremor deep brain stimulation using high-resolution anatomical imaging with supplementary fiber tractography. *J. Neurol. Sci.* 398, 148–156. doi: 10.1016/j.jns.2019.01.025

Morton, A. J., Nicholson, L. F., and Faull, R. L. (1993). Compartmental loss of NADPH diaphorase in the neuropil of the human striatum in Huntington's disease. *Neuroscience* 53, 159–168. doi: 10.1016/0306-4522(93)90294-P

Nauta, H. J., Pritz, M. B., and Lasek, R. J. (1974). Afferents to the rat caudoputamen studied with horseradish peroxidase. An evaluation of a retrograde neuroanatomical research method. *Brain Res.* 67, 219–238. doi: 10.1016/0006-8993(74)90274-1

Nisenbaum, L. K., Webster, S. M., Chang, S. L., McQueeney, K. D., and LoTurco, J. J. (1998). Early patterning of prelimbic cortical axons to the striatal patch compartment in the neonatal mouse. *Dev. Neurosci.* 20, 113–124. doi: 10.1159/000017307

Oakley, C., Mahone, E. M., Morris-Berry, C., Kline, T., and Singer, H. S. (2015). Primary complex motor stereotypies in older children and adolescents: clinical features and longitudinal follow-up. *Pediatr. Neurol.* 52, 398–403.e1. doi: 10.1016/j.pediatrneurol.2014.11.002

Oke, A., Keller, R., Mefford, I., and Adams, R. N. (1978). Lateralization of norepinephrine in human thalamus. *Science* 200, 1411–1413. doi: 10.1126/science.663623

Oldfield, R. C. (1971). The assessment and analysis of handedness: the Edinburgh inventory. *Neuropsychologia* 9, 97–113. doi: 10.1016/0028-3932(71)90067-4

O'Muircheartaigh, J., Keller, S. S., Barker, G. J., and Richardson, M. P. (2015). White matter connectivity of the thalamus delineates the functional architecture of competing thalamocortical systems. *Cereb. Cortex* 25, 4477–4489. doi: 10.1093/cercor/bhv063

Passarelli, L., Gamberini, M., and Fattori, P. (2021). The superior parietal lobule of primates: a sensory-motor hub for interaction with the environment. *J. Integr. Neurosci.* 20, 157–171. doi: 10.31083/j.jin.2021.01.334

Pelzer, E. A., Melzer, C., Timmermann, L., von Cramon, D. Y., and Tittgemeyer, M. (2017). Basal ganglia and cerebellar interconnectivity within the human thalamus. *Brain Struct. Funct.* 222, 381–392. doi: 10.1007/s00429-016-1223-z

Pérez-Santos, I., Palomero-Gallagher, N., Zilles, K., and Cavada, C. (2021). Distribution of the noradrenaline innervation and adrenoceptors in the macaque monkey thalamus. *Cereb. Cortex* 31, 4115–4139. doi: 10.1093/cercor/bhab073

Phillips, J. M., Fish, L. R., Kambi, N. A., Redinbaugh, M. J., Mohanta, S., Kecskemeti, S. R., et al. (2019). Topographic organization of connections between prefrontal cortex and mediodorsal thalamus: evidence for a general principle of indirect thalamic pathways between directly connected cortical areas. *NeuroImage* 189, 832–846. doi: 10.1016/j.neuroimage.2019.01.078

Pimenta, A. F., Strick, P. L., and Levitt, P. (2001). Novel proteoglycan epitope expressed in functionally discrete patterns in primate cortical and subcortical regions. *J. Comp. Neurol.* 430, 369–388. doi: 10.1002/1096-9861(20010212)430:3<369::AID-CNE1037>3.0.CO;2-C

Prager, E. M., Dorman, D. B., Hobel, Z. B., Malgady, J. M., Blackwell, K. T., and Plotkin, J. L. (2020). Dopamine oppositely modulates state transitions in Striosome and matrix direct pathway striatal spiny neurons. *Neuron* 108, 1091–1102.e5. doi: 10.1016/j.neuron.2020.09.028

Prensa, L., and Parent, A. (2001). The nigrostriatal pathway in the rat: a single-axon study of the relationship between dorsal and ventral tier nigral neurons and the striosome/matrix striatal compartments. *J. Neurosci.* 21, 7247–7260. doi: 10.1523/JNEUROSCI.21-18-07247.2001

Ragsdale, C. W. Jr., and Graybiel, A. M. (1991). Compartmental organization of the thalamostriatal connection in the cat. *J. Comp. Neurol.* 311, 134–167. doi: 10.1002/cne.903110110

Rajakumar, N., Elisevich, K., and Flumerfelt, B. A. (1993). Compartmental origin of the striato-entopeduncular projection in the rat. *J. Comp. Neurol.* 331, 286–296. doi: 10.1002/cne.903310210

Rajakumar, N., Rushlow, W., Naus, C. C., Elisevich, K., and Flumerfelt, B. A. (1994). Neurochemical compartmentalization of the globus pallidus in the rat: an immunocytochemical study of calcium-binding proteins. *J. Comp. Neurol.* 346, 337–348. doi: 10.1002/cne.903460303

Rajimehr, R., Young, J. C., and Tootell, R. B. (2009). An anterior temporal face patch in human cortex, predicted by macaque maps. *Proc. Natl. Acad. Sci. U. S. A.* 106, 1995–2000. doi: 10.1073/pnas.0807304106

Rangus, I., Fritsch, M., Endres, M., Udke, B., and Nolte, C. H. (2022). Frequency and phenotype of thalamic aphasia. *J. Neurol.* 269, 368–376. doi: 10.1007/s00415-021-10640-4

Reuter, M., Schmansky, N. J., Rosas, H. D., and Fischl, B. (2012). Within-subject template estimation for unbiased longitudinal image analysis. *NeuroImage* 61, 1402–1418. doi: 10.1016/j.neuroimage.2012.02.084

Roberts, R. C., Roche, J. K., and Conley, R. R. (2005). Synaptic differences in the patch matrix compartments of subjects with schizophrenia: a postmortem ultrastructural study of the striatum. *Neurobiol. Dis.* 20, 324–335. doi: 10.1016/j.nbd.2005.03.015

Sadikot, A. F., Parent, A., Smith, Y., and Bolam, J. P. (1992). Efferent connections of the centromedian and parafascicular thalamic nuclei in the squirrel monkey: a light and electron microscopic study of the thalamostriatal projection in relation to striatal heterogeneity. *J. Comp. Neurol.* 320, 228–242. doi: 10.1002/cne.903200207

Saka, E., Goodrich, C., Harlan, P., Madras, B. K., and Graybiel, A. M. (2004). Repetitive behaviors in monkeys are linked to specific striatal activation patterns. *J. Neurosci.* 24, 7557–7565. doi: 10.1523/jneurosci.1072-04.2004

Saleem, K. S., Pauls, J. M., Augath, M., Trinath, T., Prause, B. A., Hashikawa, T., et al. (2002). Magnetic resonance imaging of neuronal connections in the macaque monkey. *Neuron* 34, 685–700. doi: 10.1016/s0896-6273(02)00718-3

Sánchez Fernández, I., Takeoka, M., Tas, E., Peters, J. M., Prabhu, S. P., Stannard, K. M., et al. (2012). Early thalamic lesions in patients with sleep-potentiated epileptiform activity. *Neurology* 78, 1721–1727. doi: 10.1212/WNL.0b013e3182582ff8

Schaller-Paule, M. A., Oeckel, A. M., Schüre, J. R., Keil, F., Hattingen, E., Foerch, C., et al. (2021). Isolated thalamic stroke - analysis of clinical characteristics and asymmetry of lesion distribution in a retrospective cohort study. *Neurol. Res. Pract.* 3:49. doi: 10.1186/s42466-021-00148-7

Schmahmann, J. D. (2003). Vascular syndromes of the thalamus. *Stroke* 34, 2264–2278. doi: 10.1161/01.Str.0000087786.38997.9e

Shah, B. R., Lehman, V. T., Kaufmann, T. J., Blezek, D., Waugh, J., Imphean, D., et al. (2020). Advanced MRI techniques for transcranial high intensity focused ultrasound targeting. *Brain* 143, 2664–2672. doi: 10.1093/brain/awaa107

Sherman, S. M., and Guillery, R. W. (2013). *Functional connections of cortical areas: A new view from the thalamus*. Cambridge, MA, USA: The MIT Press.

Singer, H. S. (2009). Motor stereotypies. *Semin. Pediatr. Neurol.* 16, 77–81. doi: 10.1016/j.spen.2009.03.008

Sloot, W. N., and Gramsbergen, J. B. (1994). Axonal transport of manganese and its relevance to selective neurotoxicity in the rat basal ganglia. *Brain Res.* 657, 124–132. doi: 10.1016/0006-8993(94)90959-8

Smith, Y., and Parent, A. (1986). Differential connections of caudate nucleus and putamen in the squirrel monkey (*Saimiri sciureus*). *Neuroscience* 18, 347–371. doi: 10.1016/0306-4522(86)90159-4

Snider, S. B., Bodien, Y. G., Frau-Pascual, A., Bianciardi, M., Foulkes, A. S., and Edlow, B. L. (2020). Ascending arousal network connectivity during recovery from traumatic coma. *Neuroimage Clin.* 28:102503. doi: 10.1016/j.nicl.2020.102503

Stephenson-Jones, M., Kardamakis, A. A., Robertson, B., and Grillner, S. (2013). Independent circuits in the basal ganglia for the evaluation and selection of actions. *Proc. Natl. Acad. Sci. U. S. A.* 110, E3670–E3679. doi: 10.1073/pnas.1314815110

Tan, A., Salgado, M., and Fahn, S. (1997). The characterization and outcome of stereotypical movements in nonautistic children. *Mov. Disord.* 12, 47–52. doi: 10.1002/mds.870120109

Tippett, L. J., Waldvogel, H. J., Thomas, S. J., Hogg, V. M., van Roon-Mom, W., Synek, B. J., et al. (2007). Striosomes and mood dysfunction in Huntington's disease. *Brain* 130, 206–221. doi: 10.1093/brain/awl243

Unzai, T., Kuramoto, E., Kaneko, T., and Fujiyama, F. (2017). Quantitative analyses of the projection of individual neurons from the midline thalamic nuclei to the Striosome and matrix compartments of the rat striatum. *Cereb. Cortex* 27, bhv295–bhv1181. doi: 10.1093/cercor/bhv295

Valente, F., Pesola, C., Baglioni, V., Teresa Giannini, M., Chiarotti, F., Caravale, B., et al. (2019). Developmental motor profile in preschool children with primary stereotypic movement disorder. *Biomed. Res. Int.* 2019, 1427294–1427296. doi: 10.1155/2019/1427294

van Essen, D., Smith, S. M., Barch, D. M., Behrens, T. E., Yacoub, E., Ugurbil, K., et al. (2013). The Wu-Minn human connectome project: an overview. *NeuroImage* 80, 62–79. doi: 10.1016/j.neuroimage.2013.05.041

van Vulpen, E. H., and Verwer, R. W. (1989). Organization of projections from the mediodorsal nucleus of the thalamus to the basolateral complex of the amygdala in the rat. *Brain Res.* 500, 389–394. doi: 10.1016/0006-8993(89)90337-5

Veening, J. G., Cornelissen, F. M., and Lieven, P. A. (1980). The topical organization of the afferents to the caudatoputamen of the rat. A horseradish peroxidase study. *Neuroscience* 5, 1253–1268. doi: 10.1016/0306-4522(80)90198-0

Vertes, R. P., Linley, S. B., and Rojas, A. K. P. (2022). Structural and functional organization of the midline and intralaminar nuclei of the thalamus. *Front. Behav. Neurosci.* 16:964644. doi: 10.3389/fnbeh.2022.964644

Vogt, B. A., Pandya, D. N., and Rosene, D. L. (1987). Cingulate cortex of the rhesus monkey: I. Cytoarchitecture and thalamic afferents. *J. Comp. Neurol.* 262, 256–270. doi: 10.1002/cne.902620207

Wallace, M. L., Saunders, A., Huang, K. W., Philson, A. C., Goldman, M., Macosko, E. Z., et al. (2017). Genetically distinct parallel pathways in the entopeduncular nucleus for limbic and sensorimotor output of the basal ganglia. *Neuron* 94, 138–152.e5. doi: 10.1016/j.neuron.2017.03.017

Wang, H., and Pickel, V. M. (1998). Dendritic spines containing mu-opioid receptors in rat striatal patches receive asymmetric synapses from prefrontal corticostriatal afferents. *J. Comp. Neurol.* 396, 223–237. doi: 10.1002/(SICI)1096-9861(19980629)396:2<223::AID-CNE7>3.0.CO;2-2

Waugh, J. L., Hassan, A., Kuster, J. K., Levenstein, J. M., Warfield, S. K., Makris, N., et al. (2022). An MRI method for parcellating the human striatum into matrix and striosome compartments in vivo. *NeuroImage* 246:118714. doi: 10.1016/j.neuroimage.2021.118714

Waugh, J. L., Kuster, J. K., Makhlouf, M. L., Levenstein, J. M., Multhaupt-Buell, T. J., Warfield, S. K., et al. (2019). A registration method for improving quantitative assessment in probabilistic diffusion tractography. *NeuroImage* 189, 288–306. doi: 10.1016/j.neuroimage.2018.12.057

White, N. M., and Hiroi, N. (1998). Preferential localization of self-stimulation sites in striosomes/patches in the rat striatum. *Proc. Natl. Acad. Sci. U. S. A.* 95, 6486–6491. doi: 10.1073/pnas.95.11.6486

10.3389/fnins.2023.1178473

Glossary

AP	Anterior to posterior
CSTC	Cortico striatal thalamo cortical
CTT	Classification targets tractography
DBS	Deep brain stimulation
DSC	Dice similarity coefficient
DTI	Diffusion tensor imaging
EP	Entopeduncular nucleus
FA	Fractional anisotropy
GPi	Globus pallidus interna
HCP	Human connectome project
HD	Huntington disease
MOR	Mu opioid receptor
MSNs	Medium spiny neurons
NDA	National Institute of Mental Health Data Archive
PA	Posterior to anterior
PD	Parkinson disease
ROI	Region of interest
SEM	Standard error of the mean
Thalamic nuclei were abbreviated in the convention of Iglesias et al. (2018):	
AV	Anteroventral
CeM	Central medial
CL	Central lateral
CM	Centromedian
LD	Laterodorsal
LP	Lateral posterior
MDl	Mediodorsal-lateral
MDm	Mediodorsal-medial
MGN	Medial geniculate nucleus
Pf	Parafascicular
PuA	Pulvinar-anterior
PuI	Pulvinar-inferior
PuL	Pulvinar-lateral
PuM	Pulvinar-medial
Reu	Reuniens-medial ventral
VA	Ventral anterior
VAmc	Ventral anterior magnocellular
VLa	Ventral lateral anterior
VLp	Ventral lateral posterior
VPL	Ventral posterolateral

frontiers | Frontiers in Neuroscience

TYPE Original Research
PUBLISHED 07 December 2023
DOI 10.3389/fnins.2023.1258408

OPEN ACCESS

EDITED BY
Yi Zhang,
Zhejiang University, China

REVIEWED BY
Min Wang,
Zhejiang University, China
Yanqin Lin,
Xiamen University, China

*CORRESPONDENCE
Christopher W. Davies-Jenkins
✉ cdavies9@jh.edu

RECEIVED 14 July 2023
ACCEPTED 03 November 2023
PUBLISHED 07 December 2023

CITATION
Davies-Jenkins CW, Döring A, Fasano F, Kleban E, Mueller L, Evans CJ, Afzali M, Jones DK, Ronen I, Branzoli F and Tax CMW (2023) Practical considerations of diffusion-weighted MRS with ultra-strong diffusion gradients.
Front. Neurosci. 17:1258408.
doi: 10.3389/fnins.2023.1258408

Practical considerations of diffusion-weighted MRS with ultra-strong diffusion gradients

Christopher W. Davies-Jenkins[1,2,3]*, André Döring[3,4], Fabrizio Fasano[3,5], Elena Kleban[3,6], Lars Mueller[3,7], C. John Evans[3], Maryam Afzali[3,7], Derek K. Jones[3], Itamar Ronen[8], Francesca Branzoli[9,10] and Chantal M. W. Tax[11,12]

[1]The Russell H. Morgan Department of Radiology and Radiological Science, Johns Hopkins University School of Medicine, Baltimore, MD, United States, [2]Kirby Research Center for Functional Brain Imaging, Kennedy Krieger Institute, Baltimore, MD, United States, [3]Cardiff University Brain Research Imaging Centre, Cardiff University, Cardiff, United Kingdom, [4]CIBM Center for Biomedical Imaging, EPFL CIBM-AIT, EPFL Lausanne, Lausanne, Switzerland, [5]Siemens Healthcare Ltd., Camberly, United Kingdom, [6]Department of Radiology, Universität Bern, Bern, Switzerland, [7]Leeds Institute of Cardiovascular & Metabolic Medicine, University of Leeds, Leeds, United Kingdom, [8]Clinical Sciences Institue, Brighton and Sussex Medical School, Brighton, United Kingdom, [9]Center for NeuroImaging Research (CENIR), Paris Brain Institute (ICM), Pitié-Salpêtrière Hospital, Paris, France, [10]Inserm U1127, CNRS U7225, Sorbonne Universités, Paris, France, [11]Brain Research Imaging Centre, School Physics and Astronomy, Cardiff University, Cardiff, United Kingdom, [12]Image Sciences Institute, University Medical Center Utrecht, Utrecht, Netherlands

Introduction: Diffusion-weighted magnetic resonance spectroscopy (DW-MRS) offers improved cellular specificity to microstructure—compared to water-based methods alone—but spatial resolution and SNR is severely reduced and slow-diffusing metabolites necessitate higher *b*-values to accurately characterize their diffusion properties. Ultra-strong gradients allow access to higher *b*-values per-unit time, higher SNR for a given *b*-value, and shorter diffusion times, but introduce additional challenges such as eddy-current artefacts, gradient non-uniformity, and mechanical vibrations.

Methods: In this work, we present initial DW-MRS data acquired on a 3T Siemens Connectom scanner equipped with ultra-strong (300 mT/m) gradients. We explore the practical issues associated with this manner of acquisition, the steps that may be taken to mitigate their impact on the data, and the potential benefits of ultra-strong gradients for DW-MRS. An in-house DW-PRESS sequence and data processing pipeline were developed to mitigate the impact of these confounds. The interaction of TE, *b*-value, and maximum gradient amplitude was investigated using simulations and pilot data, whereby maximum gradient amplitude was restricted. Furthermore, two DW-MRS voxels in grey and white matter were acquired using ultra-strong gradients and high *b*-values.

Results: Simulations suggest T_2-based SNR gains that are experimentally confirmed. Ultra-strong gradient acquisitions exhibit similar artefact profiles to those of lower gradient amplitude, suggesting adequate performance of artefact mitigation strategies. Gradient field non-uniformity influenced ADC estimates by up to 4% when left uncorrected. ADC and Kurtosis estimates for tNAA, tCho, and tCr align with previously published literature.

Discussion: In conclusion, we successfully implemented acquisition and data processing strategies for ultra-strong gradient DW-MRS and results indicate that confounding effects of the strong gradient system can be ameliorated, while achieving shorter diffusion times and improved metabolite SNR.

KEYWORDS

diffusion-weighted MRS, ultra-strong gradients, gradient non-uniformity, eddy currents, metabolites

1 Introduction

Diffusion-weighted magnetic resonance imaging (DW-MRI) is usually sensitized to the displacement of water, and provides a myriad of tissue microstructure metrics that aid in the study of many neuropathologies, including traumatic brain injury (Hutchinson et al., 2018), neurodegeneration (Goveas et al., 2015), and measuring treatment response in cancer therapy (Patterson et al., 2008), to name a few. However, the ubiquity of water molecules—present in both intra- and extracellular spaces—complicates the modeling of water diffusion as a measure of cellular microstructure. Magnetic resonance spectroscopy (MRS) is a non-invasive technique providing quantitative measures of metabolites and neurotransmitters which are present in the brain at millimolar concentrations. Diffusion-weighted MRS (DW-MRS) introduces diffusion gradients into MRS sequences, utilising MRS as a filter to sensitize the MR signal to different metabolites which are almost exclusively intra-cellular, with some considered predominantly glial—myo-inositol (mI) and choline compounds (tCho)—and others predominantly neuronal—N-acetyl-aspartate (NAA) and glutamate (Glu) (Choi et al., 2007). While the signal-to-noise ratio (SNR) and spatial resolution are reduced compared to conventional water-based imaging, the specificity afforded by DW-MRS greatly simplifies diffusion modeling and interpretation, and provides a valuable non-invasive window into metabolism and cellular microstructure, complimentary to water-based diffusion imaging (Ronen et al., 2014; Najac et al., 2016; Palombo et al., 2018; Ligneul et al., 2019; Genovese et al., 2021b).

The apparent diffusion coefficients (ADCs) of metabolites are at least five times smaller than those of water (Ellegood et al., 2011), which necessitates higher *b*-values to adequately characterize metabolite diffusion properties. A common approach is to employ a DW-STEAM sequence, whereby metabolite diffusion occurs during the mixing time (TM), with the diffusion time uncoupled from the echo time (TE). However, this comes with the caveat that STEAM generates a stimulated echo, reducing the available SNR compared to spin-echo localisation methods by a factor of two. The shorter TE of STEAM can ameliorate this, but the long diffusion times required to achieve adequate diffusion weighting may be undesired. If the goal is to probe short diffusion times and/or high *b*-values, then the spin-echo-based diffusion-weighted Point RESolved Spectroscopy sequence (Bottomley, 1987) (DW-PRESS) provides an alternative, offering better SNR than STEAM, without the additional TE restrictions imposed by adiabatic pulse pairing required for a diffusion-weighted semi-LASER (DW-sLASER) sequence. Larger *b*-values can be achieved by increasing the DW-gradient amplitude (limited by the gradient system) and/or by increasing the diffusion time. Achieving the latter with DW-PRESS can be challenging. With the diffusion time coupled to the choice of TE, the available SNR at high *b*-value is restricted by metabolite T_2 relaxation. The introduction of ultra-strong gradient systems can mitigate this. The Siemens Connectom scanner is fitted with a gradient system capable of reaching 300 mT/m per axis. This provides larger *b*-values for a given TE, and access to shorter diffusion times while maintaining the required *b*-value range. Shorter diffusion times can reduce the variability resulting from motion artefacts and, crucially, can provide additional cell-specific microstructural properties of highly-restrictive compartments (e.g., subcellular organelles) and cellular viscosity (Setsompop et al., 2013; Palombo et al., 2017; Jones et al., 2018).

However, the introduction of ultra-strong gradients poses additional practical challenges. Specifically, eddy currents become increasingly prevalent at larger gradient amplitudes. Switched gradient fields induce eddy currents which produce time-varying magnetic fields, distorting the lineshape of MR spectra and hampering MRS modeling attempts. Moreover, eddy current correction in conventional MRS relies on acquiring a water-unsuppressed reference scan (Klose, 1990); however, in DW-MRS, the water signal is heavily attenuated at high *b*-values, complicating the extraction of the relevant phase information. In addition to eddy current effects, it becomes increasingly difficult to maintain uniform gradient fields on ultra-strong gradient systems. This leads to a deviation in the applied gradient field from the nominal gradient field, which is of particular relevance for diffusion studies (Mesri et al., 2020). These gradient non-uniformities will spatially modulate the *b*-matrix and image geometry, and must be corrected in order to obtain reliable estimates (Bammer et al., 2003). Finally, mechanical vibrations—caused by Lorentz forces generated during rapid gradient switching—can cause anomalous signal loss in diffusion experiments (Gallichan et al., 2010; Weidlich et al., 2019, 2020), and is a particular concern for strong gradient systems.

At the time of writing, only one full study has been published on DW-MRS with ultra-strong gradients in humans, which focused on utilising the hardware to measure macromolecular background profiles for MRS (Şimşek et al., 2022). Despite increasing community interest in strong gradients for diffusion encoding (Setsompop et al., 2013; Jones et al., 2018; Jenkins et al., 2020; Şimşek et al., 2020, 2021; Huang et al., 2021; Jenkins, 2021; Fan et al., 2022; Döring et al., 2023), no studies have specifically addressed the challenges of ultra-strong gradients in the context of DW-MRS. Furthermore, data processing software specific to DW-MRS data is limited, and variation between existing methods has been previously shown (Najac et al., 2022). With increased accessibility of high performance scanner gradient systems, it is crucial to develop open-source software that broaches the challenges posed by this hardware.

In this work, we present initial data acquired using a 3T Connectom—a research-only scanner equipped with a 300 mT/m gradient system. We introduce the practical issues associated with this manner of acquisition and steps that may be taken to mitigate their impact on the data. In this study, we limited the scope of our investigation specifically to the diffusion-weighted PRESS sequence, which was implemented with a flexible bipolar diffusion gradient scheme. A DW-MRS data processing pipeline was implemented and evaluated against pilot DW-PRESS data. Phantom experiments were conducted and *in vivo* data were acquired from a small cohort of individuals in order to validate the measurements and demonstrate the capabilities of ultra-strong gradients compared to more conventional gradient settings.

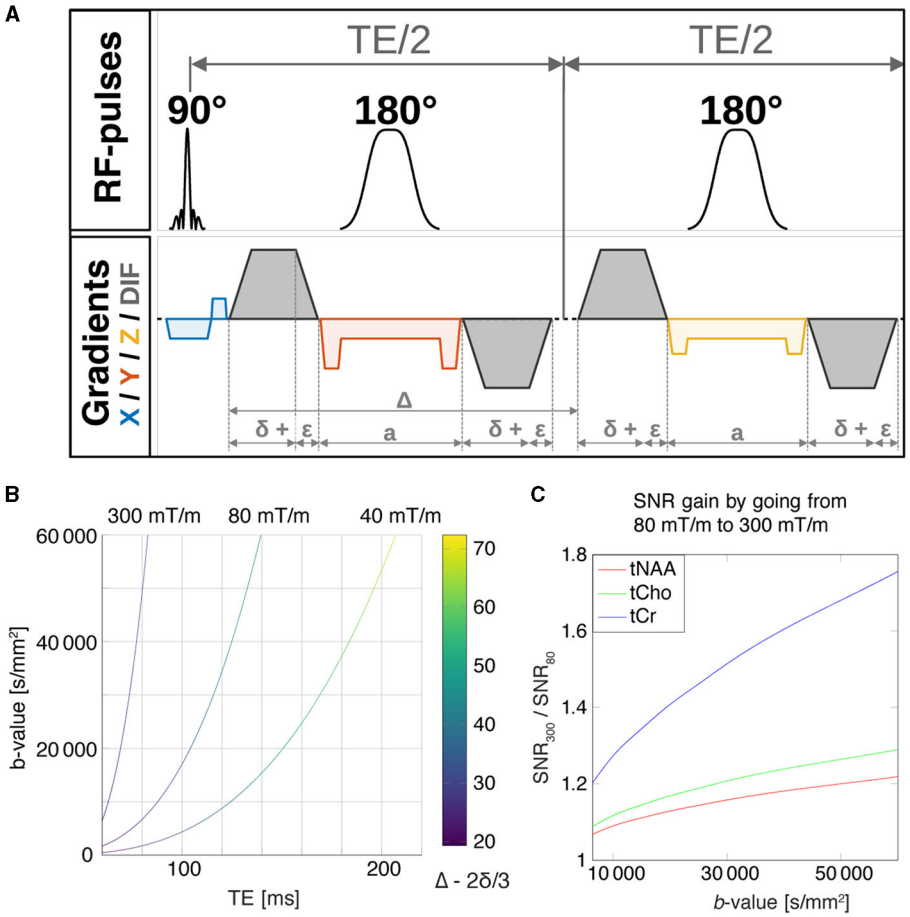

FIGURE 1
(A) Pulse sequence diagram for the DW-PRESS sequence. Slice-select gradients are shown for each dimension, x (blue), y (red), z (yellow), and diffusion gradients are shown in gray. **(B)** The maximum achievable *b*-value as a function of the echo time for the DW-PRESS sequence, which is limited by the maximum achievable diffusion-gradient strengths. The curves were calculated for maximal gradient amplitudes of 40, 80, and 300 mT/m corresponding to the Siemens TRIO, Prisma, and Connectom scanner configurations, respectively. **(C)** For a given *b*-value, reduction of the echo time by going from 80 mT/m to 300 mT/m will result in SNR gain. SNR gains were estimated for tNAA, tCho and tCr using their relaxation times T_2 (Ke et al., 2002; Ganji et al., 2012).

2 Materials and methods

For the DW-MRS acquisition, an in-house developed DW-PRESS sequence with bipolar diffusion gradients (Branzoli, 2015) was adapted for use on the 300 mT/m Connectom scanner. The full pulse sequence diagram is shown in Figure 1A.

2.1 SNR simulations

We first conducted simulations to explore the relationship between TE, maximum *b*-value, and diffusion time for the DW-PRESS sequence, and subsequently, the potential TE-based SNR improvements possible with ultra-strong gradients. The maximum-achievable *b*-value is constrained by the gradient characteristics, and has a corresponding minimum-achievable TE. We investigated this relationship at three maximum gradient amplitudes: 40, 80, and 300 mT/m. The maximum achievable *b*-value was calculated numerically using in-house code written in Matlab. The slew rates—corresponding to each of the maximum gradient amplitudes—were 200 T/m/s, 200 T/m/s and 83 T/m/s, respectively.

For a given maximum *b*-value, the minimum-achievable TE will define the magnitude of T_2-based signal attenuation, with short TE implying higher SNR. We investigated the expected SNR increase when moving from a Siemens Prisma gradient system (80 mT/m) to a Connectom gradient system (300 mT/m) for three major metabolite measures—creatine + phosphocreatine (tCr), tCho, and NAA+N-acetyl-aspartyl-glutamate (tNAA). The ratio of SNR values between the 300 mT/m and 80 mT/m gradient systems was calculated using previously-published metabolite T_2 values (Ke et al., 2002; Ganji et al., 2012):

$$S(\mathrm{TE}) \sim S_0 e^{-\mathrm{TE}/T_{2,\mathrm{metabolite}}} \tag{1}$$

$$\frac{\mathrm{SNR}_{300}}{\mathrm{SNR}_{80}}(b) = \frac{S\left(\mathrm{TE}_{min,300}(b)\right)}{S\left(\mathrm{TE}_{min,80}(b)\right)} = \exp\frac{-\mathrm{TE}_{min,300}(b) + \mathrm{TE}_{min,80}(b)}{T_{2,\mathrm{metabolite}}} \tag{2}$$

where, $\frac{SNR_{300}}{SNR_{80}}(b)$ is the ratio of TE-dependent SNR values corresponding to the respective gradient systems, S is the signal amplitude, S_0 is the signal amplitude before T_2-weighting, and $T_{2,\text{metabolite}}$ is the metabolite-specific T_2. Note that the SNR ratio is independent of S_0. The SNR ratio was calculated for a range of maximum b-values (and hence, TEs) for each metabolite. Apart from the pure T_2 relaxation-driven reduction in SNR at longer TE, J-evolution contributes to metabolite dephasing and increases fitting uncertainties as well (Landheer et al., 2020); however, these effects were not included in our simple model, as we focused on the major singlet resonances.

2.2 Data acquisition

In order to evaluate measurement procedures and data processing strategies pilot data were acquired in small test group of 3 healthy participants—1 female; age 33 ± 10 years (mean ± standard deviation). Spectroscopic and structural data were collected on a research-only 3 T Connectom MRI scanner, a modified 3 T MAGNETOM Skyra system equipped with 300 mT/m gradients (Siemens Healthcare, Erlangen, Germany) and a 32-channel receive array head coil (Nova Medical, Wilmington, United States). The study was performed with ethics approval from the Cardiff University School of Psychology ethics review board and written informed consent was obtained from all participants. Additional Supplementary material were acquired on an isotropic diffusion phantom (NIST) (Palacios et al., 2017).

2.2.1 Structural MRI

Each *in vivo* MR protocol included a Magnetization Prepared Rapid Acquisition Gradient Echoes (MPRAGE) (Mugler III and Brookeman, 1990) scan. Scanning parameters for the MPRAGE sequence were: 1 mm isotropic resolution, TR = 2.3 s, TE = 2 ms, TI = 837 ms, Flip-angle = 9°, field-of-view=256 × 256.

2.2.2 DW-MRS

To reduce the impact of pulsation artefacts, all *in vivo* DW-MRS scans were cardiac triggered to avoid systolic pulsation using a pulse oximeter placed on the participant's forefinger. DW-MRS voxels were positioned using the T_1-weighted MPRAGE.

In order to avoid cross-term effects from gradient overlap, diffusion gradients were applied along the physical single-gradient axes. To facilitate this, no rotations were applied to the voxels and the dimensions were adjusted to maximize the coverage of the relevant tissue volume in each case.

2.2.2.1 300 mT/m vs. 80 mT/m maximum gradient strength

The DW-PRESS sequence's functionality was extended to allow precise specification of the gradients applied. This allowed us to simulate different gradient configurations on the Connectom scanner by selecting appropriate minimum rise times and the maximum gradient amplitudes, G_{max}. While this single-scanner experimental design limited the conclusions we could draw about the performance of the Connectom compared to a different system with lower maximum gradient strength, our approach allowed comparisons to be drawn between different gradient strengths without the confounding impact of certain experimental influences. Specifically, this approach removed the risk of different voxel placement, ensured the equivalence of scanner calibrations, and allowed us to study gradient-strength differences without introducing differences in gradient non-uniformities. Here, we considered conservative limits for the gradient characteristics [slightly below the hardware and physiological limits (Setsompop et al., 2013)] for the Connectom system, which can be potentially extended and thus the maximum-achievable b-values increased.

For the DW-MRS protocol, we selected TEs of 116 ms and 74 ms for G_{max} = 80 mT/m (Prisma-like setting) and G_{max} = 300 mT/m, respectively. Diffusion weighting was applied along a single gradient axis. The diffusion-gradient configurations provided as {δ, ϵ, a, Δ [ms]} and shown in Figure 1A were {20.7, 0.5, 9.2, 56.2} and {7.1, 3.6, 9.2, 35.2} for 80 mT/m and 300 mT/m, respectively, giving a maximum b-value of ≈ 30 000 s/mm^2. Further specification of the sequence parameters are listed in Table 1. TEs and flat-top gradient durations were rounded to the nearest *ms* by the sequence implementation, resulting in unavoidable differences in b-values between the two conditions. However, these deviations were minimized to the greatest extent possible, and less than 1.5% in all cases. For each gradient setting, 24 transients were acquired with water suppression, along with 8 water-unsuppressed transients. A single 22 × 20 × 22 mm^3 DW-MRS voxel was acquired for both gradient conditions in the grey-matter rich occipital lobe (OCC) of one participant in a single scan session.

2.2.2.2 Gray matter vs. white matter

To compare tissue-type specific differences, DW-MRS voxels were acquired in grey matter (GM) and white matter (WM) rich brain regions of the other two participants with a modified protocol. In one participant, a 24 × 20 × 25 mm^3 voxel was placed in the OCC, centred on the mid-line and as posterior as possible without including the sagittal sinus or skull, maximising the GM fraction. In a second participant, a 27 × 16 × 16 mm^3 voxel was placed in the sub-cortical white matter of the corona radiata (CR) in the left hemisphere, maximising the WM fraction. Contrary to the previous section, three diffusion weightings were applied along each of the physical gradient axes with a single maximum gradient amplitude (295 mT/m), and reduced TE of 70 ms giving a gradient configuration of {7.1, 3.6, 9.2, 31.2} and a reduced maximum b-value of 21763 s/mm^2. The 8 nominal b-values were 0, 557.8, 1266.2, 2260.6, 5107.4, 9099.3, 14237, and 21763 s/mm^2 along each of the three orthogonal single-gradient axes. Both DW-MRS acquisitions otherwise used the same parameters: TR_{min} = 2, 500 ms, spectral width = 4, 000Hz, 24 water-suppressed, and 8 water-unsuppressed transients.

2.2.2.3 Table vibration phantom scans

In order to investigate table vibrations induced by the gradient system, we acquired non-water-suppressed DW-MRS spectra in an isotropic diffusion phantom with a volume fraction of 50% polyvinylpyrrolidone (PVP, NIST). Spectra were acquired for the 300 mT/m and 80 mT/m gradient settings, with three diffusion directions, along each of the three orthogonal single-gradient

TABLE 1 Sequence parameters for the 300 and 80 mT/m gradient conditions.

	g_{max}=300 mT/m		g_{max}=80 mT/m	
	g [mT/m]	b [s/mm^2]	g [mT/m]	b [s/mm^2]
Gradient amplitudes and corresponding b-values	59	1,257	16	1,245
	89	2,838	24	2,801
	118	4,989	32	4,980
	177	11,226	48	11,204
	236	19,957	64	19,918
	295	31,183	80	31,122
TE [ms]	74		116	
δ [ms]	7.1		21.4	
Rise time [ms·m/T]	12		6 (5)	

Nominal b-values were calculated for the echo-times 74 ms and 116 ms for g_{max}=300 mT/m and g_{max}=80 mT/m, respectively.

physical axes. For each b-value, 4 transients were acquired, as well as 4 corresponding transients with inverted gradient polarity i.e., $g = [0, \pm59, \pm89, \pm118, \pm177, \pm236, \pm290]$ mT/m. The inverted scans facilitated eddy current correction for the non-water-suppressed data, as described in the following section.

2.3 Data processing

2.3.1 MRS data processing

A DW-MRS pre-processing pipeline—conforming to MRS consensus recommendations (Near et al., 2021)—was implemented using the Matlab-based MRS toolkit, FID-A (Simpson et al., 2017)[1]. Relative coil phasing was applied using the water-unsuppressed $b = 0$ acquisition, weighting individual coil elements based on signal-to-noise ratio (Hall et al., 2014). Motion-corrupted transients were identified using a likeliness metric, comparing FIDs to the first acquisition for each respective diffusion condition (Simpson et al., 2017). Transients which varied by more than 2 standard deviations were omitted prior to averaging to reduce the impact of motion on the final results. To minimize signal losses due to phase and frequency drift, spectral registration (Near et al., 2015) was used to align individual transients for each diffusion condition, separately. The resulting spectra were then manually inspected for residual water/lipid or motion contamination, automated data quality cutoffs were used for tNAA full-width at half-maximum greater than 0.1 PPM and metabolite SNR less than 3 (Wilson et al., 2019).

Tarquin (Wilson et al., 2011) V4.3.10 was used for linear-combination modeling (LCM), with TE-specific simulated basis sets including -CrCH2 (relaxation correction basis function), alanine (Ala), aspartate (Asp), creatine (Cr), GABA, glycerophosphocholine (GPC), glucose (Glc), glutamine (Gln), glutathione (GSH), Glu, glycine (Gly), mI, lactate (Lac), NAA, N-acetylaspartylglutamate (NAAG), phosphocholine (PCh), phosphocreatine (PCr), phosphorylethanolamine (PE), scyllo-inositol (sI), and taurine (Tau). Reported metabolites are total creatine (tCr = Cr + PCr), total NAA (tNAA = NAA + NAAG), and total choline (tCho = Cho + GPC). Additional basis functions were incorporated for macromolecular and lipid resonances, with the baseline approximated by a Gaussian window function. The extracted metabolite amplitudes and Cramér-Rao lower bounds (CRLBs) were then used for diffusion modeling. Water phantom scans were processed without LCM, with the water signal amplitude quantified by taking the magnitude of the first point of the complex FID.

2.3.2 Eddy current correction

While the DW-PRESS sequence was designed to minimize eddy current artefacts using a bipolar gradient scheme (Branzoli, 2015), further eddy-current correction was required, particularly for the highest b-values. For *in vivo* data, we performed eddy current correction using a non-water-suppressed reference scan. The signal of the water-suppressed scan, $S_{met}(t)$ can be divided by the signal of the non-water-suppressed reference $S_{ref}(t)$ to remove the eddy-current-related phase, ϕ_{eddy}, (Klose, 1990):

$$S_{met}(t) = |S_{met}|\, e^{i(\phi_{met}(t)+\phi_{eddy}(t))} \quad (3)$$

$$S_{ref}(t) = |S_{ref}|\, e^{i\phi_{eddy}(t)} \quad (4)$$

where the phase information of the MR spectrum, ϕ_{met}, is retained. To mitigate issues resulting from the attenuation of the water signal at higher b-values, the relevant phase correction term, ϕ_{eddy} was extracted from the reference scan using an LPSVD (Vanhamme et al., 1998), improving robustness to the noisier high-b-value water transients.

The Klose et al. method was used for all *in vivo* data in our study. Testing revealed satisfactory performance, even at high b-value; however, this might not be the case for all types of acquisition. To supplement this approach, we also demonstrate a second method of *post-hoc* eddy current correction in a nickel-doped water phantom, using gradient polarity inversion (Lin et al., 1994), whereby alternating transients of a particular diffusion gradient

1 Full code available https://github.com/CWDAVIESJENKINS/FIDA-Tarquin-Processing/tree/main/PipeLines/DWMRS.

strength are acquired with opposite gradient polarity. This reverses the phase development due to eddy currents, such that:

$$S_{\text{invert}}(t) = \left|S(t)\right| e^{i\phi(t) - i\phi_{\text{eddy}(t)}} \quad (5)$$

$$S(t)S_{\text{invert}}(t) = \left|S(t)\right|^2 e^{i\phi(t)} \quad (6)$$

where, ϕ is the phase, ϕ_{eddy} is the phase specifically resulting from eddy currents, and S and S_{invert} are the signals resulting from the initial and inverted gradient polarities, respectively. Multiplying the resulting time-domain signals removes phase evolution due to eddy currents.

2.3.3 Gradient non-uniformity correction

A mask representing the DW-MRS voxel was created in the anatomical image space using SPM12 (Penny et al., 2011; Edden et al., 2014). A vendor-supplied spherical harmonic description of the spatial dependence of the field generated by each gradient coil was used to assess geometric deviations of the voxel. A coil tensor, $\boldsymbol{L}$, was computed by taking the partial derivatives of the field—normalized by the nominal gradient strength—where the elements of the coil tensor contain the spatially varying deviations for each of the gradient axes. The coil tensor was subsequently used to compute the effective b-matrix and b-value from the nominal ones, i.e., $\boldsymbol{B}_{eff} = \boldsymbol{LBL}^T$ and $b_{eff} = \text{trace}(\boldsymbol{B}_{eff})$ (Bammer et al., 2003). Nominal b-values were estimated using in-house software written in Matlab (Mathworks, Natick, MA, USA), then subsequently, the nominal b-values were corrected for gradient non-uniformities (Bammer et al., 2003). This gave rise to a distribution of corrected b-values for each diffusion condition—rather than the single nominal value. The corrected mask was used in conjunction with the corrected b-values, to ascertain the effective b-value within the DW-MRS voxel.

2.3.4 Diffusion measures

Data were fitted in the low ($b < 3,000 smm^{-2}$) and intermediate ($b < 9,500 smm^{-2}$) b-value range with a mono-exponential and kurtosis diffusion representation, respectively, and over the full b-value range with an astrocylinder model (fully dispersed cylinders). All diffusion fitting was performed in Matlab 2021b using trust-region reflective optimisation. The inverse of the metabolite CRLBs was used to weight each data point, to reduce the impact of individual poorly-fit spectra on quantification.

2.3.4.1 Diffusion representation

Metabolite ADCs were estimated for each direction independently. The reported metabolite amplitudes for each b-value were modeled using two approaches. Firstly, all b-values below 3,000 s/mm^2 were fit using a mono-exponential decay:

$$\ln(S) = \ln(S_0) - b \cdot ADC_e \quad (7)$$

where $\ln(S)$ is the natural logarithm of the fitted metabolite amplitude, and b is the b-value. S_0 and ADC_e are the non-diffusion-weighted signal amplitude and apparent diffusion coefficient (where $_e$ indicates the ADC from a mono-exponential fit), respectively. Non-mono-exponential behavior was observed beyond this b-value range, so b-values up to 9,500 s/mm^2 were fit using the diffusion kurtosis representation (Jensen et al., 2005; Yablonskiy and Sukstanskii, 2010):

$$\ln(S) = \ln(S_0) - b \cdot ADC_k + \frac{1}{6}\left(b \cdot ADC_k\right)^2 \cdot K \quad (8)$$

where ADC_k is the apparent diffusion coefficient from the kurtosis representation and k is the kurtosis. To stabilize fitting, ADC_e estimates from the mono-exponential representation were used to initiate the fit of the kurtosis representation.

Following gradient non-uniformity correction, each single nominal b-value, b_i, is replaced with a distribution of corrected b-values (denoted b_{i,eff_j}). To investigate the impact this had on metabolite diffusion measures, we estimated mono-exponential fits considering the distribution of b-values within the DW-MRS voxel:

$$\begin{bmatrix} \ln S(b_1) \\ \vdots \\ \ln S(b_1) \\ \vdots \\ \ln S(b_N) \end{bmatrix} = \begin{bmatrix} 1 & -b_{1,\text{eff}_1} \\ \vdots & \\ 1 & -b_{1,\text{eff}_M} \\ \vdots & \\ 1 & -b_{N,\text{eff}_M} \end{bmatrix} \cdot \begin{bmatrix} \ln S_0 \\ ADC_{\text{d}} \end{bmatrix} \quad (9)$$

where ADC_{d} is the apparent diffusion coefficient ($_d$ indicates that it is estimated from a distribution of b-values), and the signal of the i^{th} b-value, $S(b_i)$, is repeated across M voxels at 1 mm^3 isotropic resolution (i.e., the resolution of the MPRAGE).

2.3.4.2 Diffusion modeling

Code adapted from the Multidimensional diffusion MRI (MDdMRI) analysis framework was used to implement a single-compartment model of fully-dispersed cylinders (astrocylinders) for bipolar diffusion encoding, in agreement with DW-MRS recommendation (Nilsson et al., 2017, 2018; Ligneul et al., 2023). To rate model performance and investigate ultra-high b-values with Connectom settings (higher SNR, shorter TE, and diffusion-time) the corrected Akaike information criterion (AICc) was used. The model parameters include the signal amplitude S_0 at $b = 0$, the free diffusivity D_0 and the cylinder radius R_C with boundaries $0 \leq R_C \leq 20\mu m$. Moreover, fitting included outlier detection to remove data-points potentially affected by motion by iteratively removing a single b-value from the fitting and identify the fit with the lowest root-mean-square-error (c.f., Supplementary Figures S3, S4). In the case of multi-directional data, the directional average of the signal was used for fitting to mitigate effects from tissue anisotropy. The fitting uncertainties of the parameters were estimated by residual bootstrapping with 250 random noise realizations (Jelescu et al., 2022).

3 Results

3.1 SNR simulations

Figures 1B, C shows the results of the theoretical investigation into the relationship between maximum-achievable b-value and minimum-achievable TE for the DW-PRESS sequence, as well as the related SNR simulation results. As anticipated, ultra-strong gradients allow for a far shorter TE for a given b-value, a benefit

which becomes even more apparent as the required maximum *b*-value increases. Moreover, one can see from the color bar that the minimum achievable diffusion time for a given maximum *b*-value is strongly related to the maximum gradient strength. In terms of SNR, we found that tCr—with the shortest T_2 of the metabolites considered—had the largest SNR gains. For a maximum *b*-value of 31 000 s/mm^2, our simulations suggest a potential SNR improvement of 50%. Likewise, for tNAA and tCho, our simulations suggest an expected SNR gain of about 10% and 21% moving from 80 mT/m to 300 mT/m, respectively.

3.2 Eddy currents

Figure 2 shows a summary of sequence validation results, including examples of gradient-polarity-inversion eddy current correction (ECC) in a phantom (Figure 2A), and examples of water-reference-based ECC *in vivo* (Figure 2B). Although bipolar diffusion gradients were applied in the water PVP phantom, Figure 2A shows clear eddy current artifacts for both positive and negative gradient polarity configurations. However, by combining both datasets, effects from eddy currents can be largely prevented. Apart from the benefits of limiting eddy-current artifacts, combining consecutive transients with inverted gradient polarity also reduces contributions from linear gradient cross-terms. This allows for an accurate estimation of the *b*-value, even without taking slice-selection, and crushing gradients into account. If no gradient polarity inversion is used, one has to calculate the real *b*-value directly from the full gradient chronograms (Mattiello et al., 1997). For the *in vivo* acquisitions, where only a single gradient polarity configuration was used, the effects from eddy currents are clearly visible from Figure 2B (red line, Before ECC). This effect is more pronounced at higher *b*-values, where steeper gradients give rise to stronger induction currents. However, when the acquired water reference is used for ECC (black line, After ECC) non-linear phase distortions from eddy-currents can be widely prevented. Despite large differences in diffusion gradient characteristics, MRS fit residuals were comparable between the 80 mT/m and 300 mT/m acquisitions (Supplementary Figure S1). The mean ratio between the fit residual and the noise level—as reported by Tarquin—was 2.98 and 3.04 for the 300 and 80 mT/m acquisitions, respectively. The comparability of the residuals alludes to a lack of significant differences in modeling performance, despite the larger eddy current artifacts induced when ultra-strong gradients are applied.

3.3 Gradient non-uniformities

Deviations in the voxel mask geometry and *b*-values due to gradient non-uniformities were corrected by taking the nonlinear spatial gradient profiles into account. While voxel deformations made little-to-no difference to the voxel volume and position ($<$ 1% deviation), *b*-values were affected significantly. This is perhaps expected, as unlike spatial encoding, *b*-values are driven by the squared gradient amplitude. Figure 3 shows the magnitude and spatial distribution of deviations from the nominally-specified *b*-value due to gradient non-uniformities. While the fractional deviation from the nominal *b*-value is constant, the actual deviation increased with gradient strength. A relatively narrow distribution is observed about zero at the lowest non-zero *b*-value and a much wider, non-zero-centered distribution is seen for the highest *b*-value. For the smallest nominal *b*-value of 567 s/mm^2, the mean (standard deviation) of the distributions of corrected *b*-values in *x*, *y*, and *z* were 563 (5), 567 (5), and 559 (5) s/mm^2, respectively, and for the largest nominal *b*-value of 22,107 s/mm^2–21,948 (198), 22,137 (185), 21,802 (199) s/mm^2, respectively. The mean deviation—calculated by taking subtracting nominal *b*-value from the corrected one—were −4, 0, and −8 s/mm^2 for 557.8 s/mm^2, and –159, 30, and –305 s/mm^2 for a nominal value of 21,763 s/mm^2.

Figure 4 shows *in vivo* mono-exponential fitting results if *b*-values were not corrected for non-uniformity (blue); corrected for non-uniformity, fitting the the full in-voxel distribution (red); and corrected for non-uniformity using the median of the distribution for fitting (green). After correction, we observed no significant difference in the estimated ADCs when either using the full *b*-value distribution or the median of that distribution, but overestimated ADCs in the absense of non-uniformity correction (approximately 4% faster diffusion). Thus, in the subsequent analysis, the median *b*-value was used to inform ADC, kurtosis, and microstructural fitting.

3.4 Comparison of 80 and 300 mT/m acquisitions

Figure 5A shows the individual *in vivo* spectra and LCM fitting results left with the Connectom ($G_{max} = 300\ mT/m$) and right with the Prisma ($G_{max} = 80\ mT/m$) settings. Overall spectral SNR of all acquisitions was well above minimum consensus recommendations, even for the highest *b*-value. The mean SNR gain for tNAA—calculated by taking the ratio of the metabolite peak amplitude to the standard deviation of the noise—was 1.16, with a 16% increase in SNR when ultra-strong gradients are used. Likewise, for the other major metabolites, we found an SNR gain of 1.36 for tCr, and 1.27 for tCho. To further elucidate the results, we expanded our SNR calculations to examine J-coupled metabolites—Glu and mI (Wyss et al., 2018)—and found similar SNR gains: a predicted 30% improvement for Glu was experimentally verified, and a 29% improvement was observed for mI, compared to the expected 31%.

The mean full-width half-maximum of tNAA was found to be 6.2 Hz across both acquisitions, indicating a good shimming and linewidth for LCM quantification. The tNAA CRLBs were all less than 27%—even including the highest *b*-values—with a mean value of 17% across all *b*-values. Similarly, the mean CRLB for tCr was 14%, with all-but-one value falling below 22% . CRLBs were higher for tCho with 4 acquisitions greater than 27%. Only a single transient was rejected by the motion corruption metric—for the 300 mT/m acquisition at the highest *b*-value. Full data quality measures are reported in Supplementary Table S2.

Figure 5B shows the tNAA diffusion decay fitted to a mono-exponential for the single diffusion direction acquired in the OCC. For the mono-exponential representation, the apparent diffusion

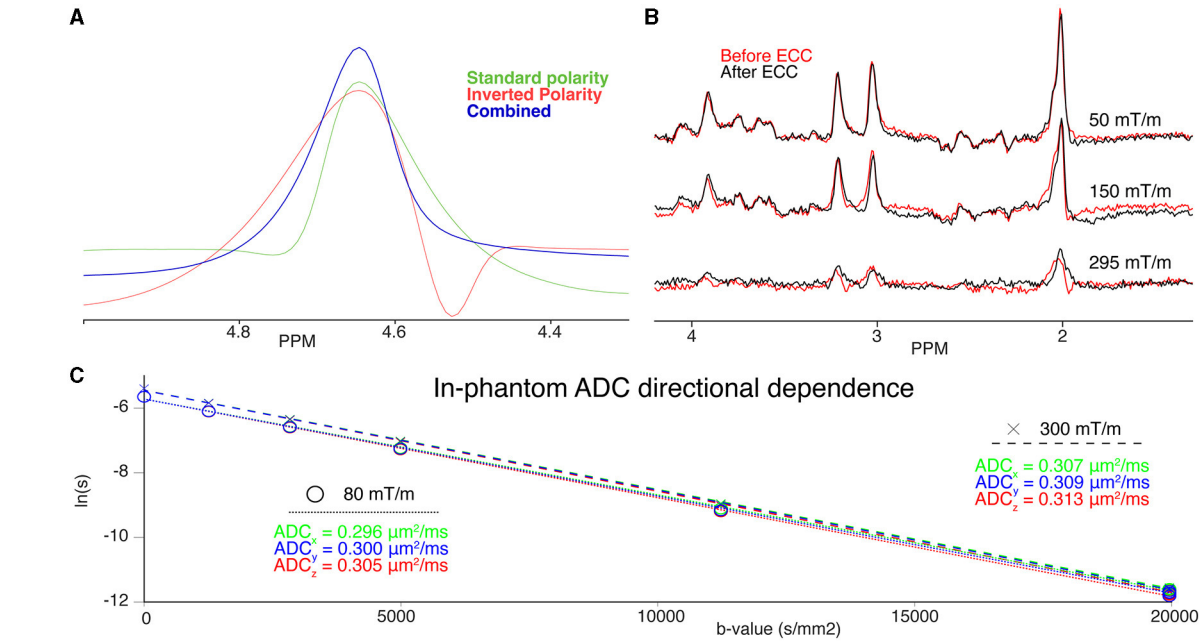

FIGURE 2
(A) Phantom water spectra acquired with a given gradient polarity (green), inverted gradient polarity (red), and the combined, eddy-current corrected spectrum (blue) **(B)** Three examples of spectra before (red) and after Klose eddy-current correction (black) at 50 mT/m (top), 150 mT/m (middle), and 295 mT/m (bottom). **(C)** DW-MRS quantification of the isotropic diffusion phantom. Individual diffusion directions (x, green; y, blue;, z, red) are plotted on top of each other for the 300 mT/m (dashed fit line above, "x") and 80 mT/m (dotted fit line below, "o") acquisitions. The individual quantified ADCs are also noted in the colour corresponding to the direction acquired. Note the strong overlap between directions, and vertical offset between gradient conditions.

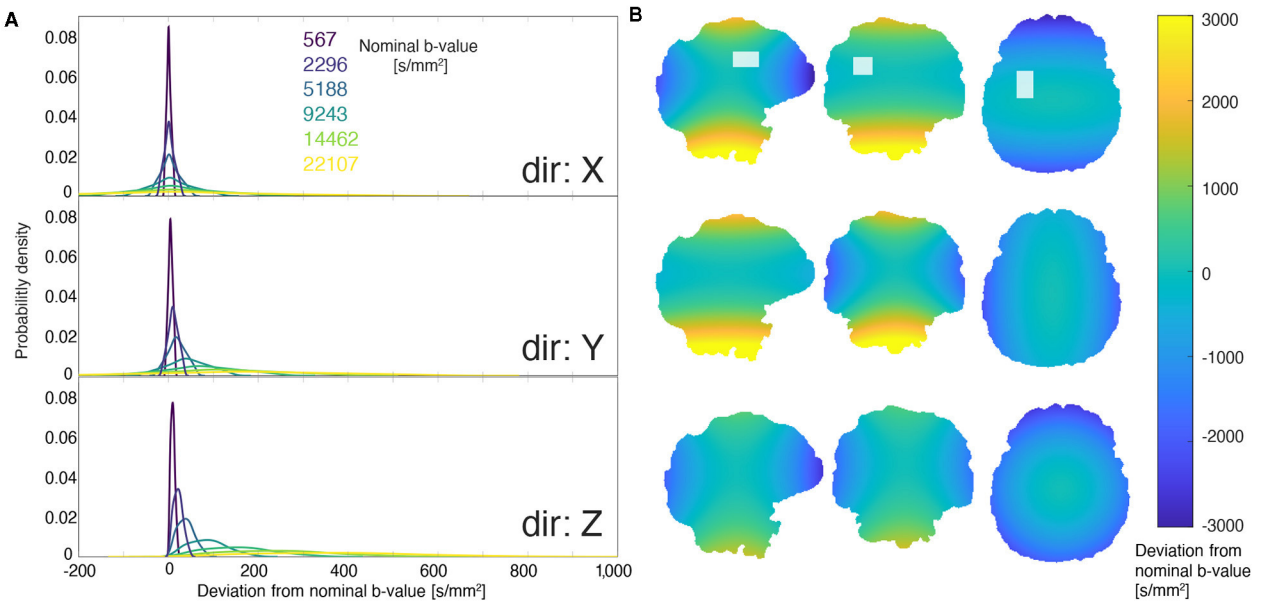

FIGURE 3
Deviation from nominally specified *b*-values due to gradient non-uniformity. **(A)** The distribution of deviation from the nominal *b*-value within the voxel. From dark blue to yellow, the distributions correspond to nominal *b*-values of 567, 2,296, 5,188, 9,243, 14,462, and 22,107 s/mm^2. Higher *b*-values exhibit broader distributions of deviations. **(B)** An example of the spatial distribution of deviations from a nominal *b*-value of 22,107 s/mm^2. The rows correspond to different gradient directions (consistent with the first panel), and the columns represent orthogonal slices. The images in the top row are overlaid with the DW-MRS voxel location used to determine the distributions shown in the left panel.

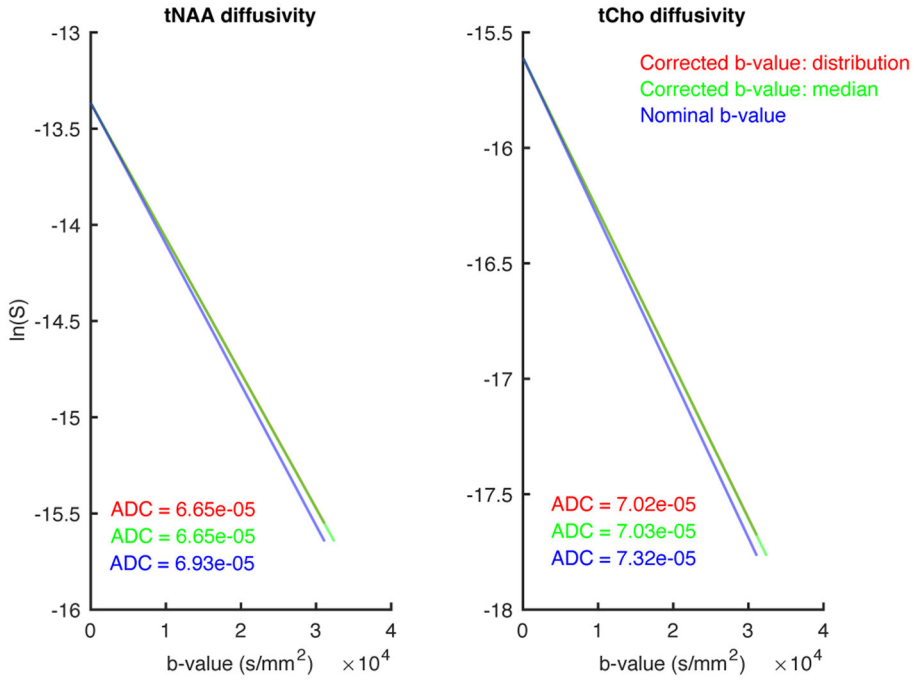

FIGURE 4
This figure shows three different approaches to representing the *b*-value during mono-exponential modelling. Directly fitting using the nominally-specified *b*-value (blue), fitting using the median of the distribution of gradient-non-linearity-corrected *b*-values (green), and fitting using the full distribution of corrected *b*-values (red). The resulting ADCs are shown in their respective colours. The **(left)** shows the tNAA diffusivity, while the **(right)** shows tCho.

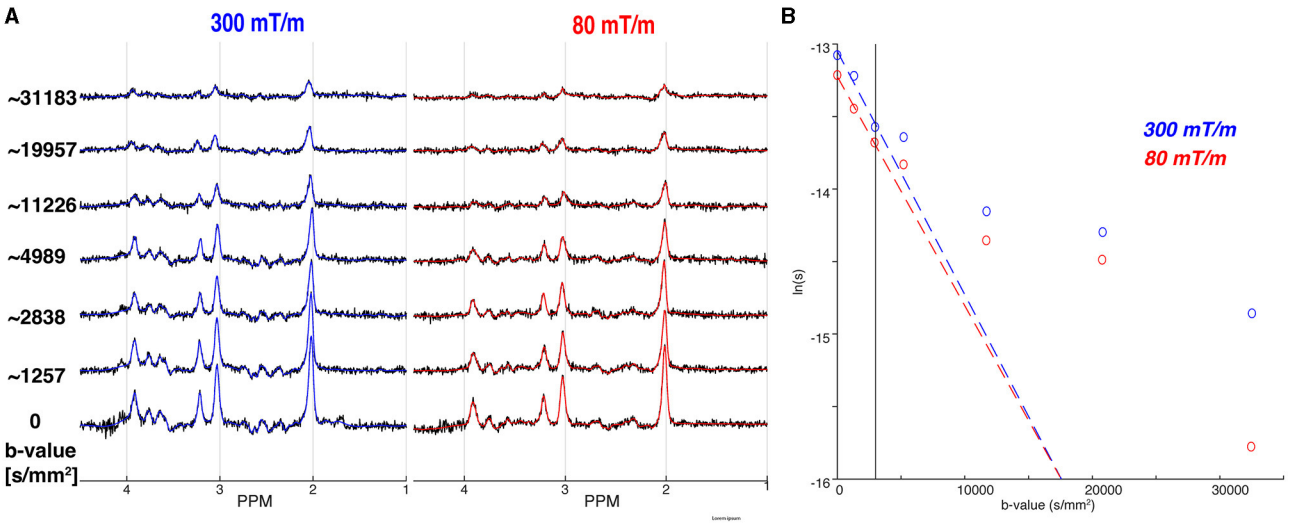

FIGURE 5
Comparison of the 300 mT/m acquisition to the 80 mT/m acquisition. **(A)** The individual spectra (black) for all *b*-values are overlaid by the corresponding MRS fits for the 300 mT/m (blue) and 80 mT/m (red), respectively. The approximate *b*-values are noted on the left, with full details in Table 1. **(B)** The mono-exponential (dashed coloured line) fits for the 300 mT/m (blue) and 80 mT/m acquisition (red) for tNAA. The vertical line indicates the *b*-value data exclusion threshold for mono-exponential modeling.

coefficients of tNAA were $ADC_{e,300}$ = 0.168 μm^2/ms, and $ADC_{e,80}$ = 0.158 μm^2/ms for 300 and 80 mT/m, respectively. Results for the other metabolites—tCho and tCr—are reported in Table 2. The Kurtosis representation was not included for these data, as only a single data point fell in the intermediate *b*-value range of 3, 000–9, 500 s/mm^2.

Table 3 lists, in the upper rows, the estimated microstructural properties derived from the astrocylinder model comparing the 300 and 80 mT/m settings acquired in the OCC . The estimated AICc's are similar between 80 and 300 mT/m settings. It is interesting to note that D_0 is, by average, higher for the Prisma settings, which is also apparent from the signal attenuation at low

TABLE 2 Listing of the *in vivo* results applying a mono-exponential and kurtosis representation for the three major metabolites.

Experiment	Metabolite	ADC_e [$\mu m^2/ms$]	adj.R_e^2	ADC_k [$\mu m^2/ms$]	K	adj.R_k^2
300mT/m	$tNAA_Z$	0.168	0.94	-	-	-
	$tCho_Z$	0.116	0.93	-	-	-
	tCr_Z	0.125	0.73	-	-	-
80mT/m	$tNAA_Z$	0.158	0.99	-	-	-
	$tCho_Z$	0.184	0.69	-	-	-
	tCr_Z	0.184	0.75	-	-	-
CR voxel	$tNAA_X$	0.146	0.99	0.142	2.226	0.98
	$tNAA_Y$	0.122	0.99	0.170	1.855	0.98
	$tNAA_Z$	0.153	0.97	0.166	1.622	1.00
	$tCho_X$	0.223	1.00	0.204	1.466	0.96
	$tCho_Y$	0.185	0.81	0.211	1.758	0.97
	$tCho_Z$	0.112	0.45	0.101	0.192	0.94
	tCr_X	0.191	0.97	0.231	1.589	0.99
	tCr_Y	0.158	0.89	0.167	1.383	0.99
	tCr_Z	0.177	0.89	0.136	1.014	0.96
OCC voxel	$tNAA_X$	0.128	0.93	0.180	1.569	0.98
	$tNAA_Y$	0.153	0.42	0.194	2.147	0.82
	$tNAA_Z$	0.096	0.79	0.122	1.542	0.98
	$tCho_X$	0.079	0.47	0.104	1.913	0.94
	$tCho_Y$	0.211	0.77	0.154	1.557	0.84
	$tCho_Z$	0.209	0.92	0.160	1.518	0.93
	tCr_X	0.181	0.78	0.204	1.477	0.96
	tCr_Y	0.202	0.36	0.231	1.628	0.80
	tCr_Z	0.156	0.89	0.173	1.070	0.99

The Experiment column delineates the acquisition and the metabolite column specifies the metabolite considered, with the subscript indicating the diffusion direction. The obtained-R^2 for each model is included to evaluate the overall fitting quality of the diffusion decay.

b-values in Supplementary Figure S3, and in line with the estimated ADCs. Moreover, R_C tends toward zero for tNAA for the Prisma configuration.

3.5 Grey matter and white matter

Figure 6A shows the voxel positions and tissue segmentation in the OCC and CR estimated from 3D T_1 MPRAGE (Penny et al., 2011; Edden et al., 2014). The OCC voxel contained predominantly grey matter (GM/WM/CSF: 75/17/8 %) and the CR voxel contained predominantly white matter (GM/WM/CSF: 15/83/2 %). Spectral quality was generally high for both voxels. The minimum SNR—as measured by the maximum point of tNAA—was 10.9 in the OCC and 8.9 in the CR at $b = 0$. The mean FWHM across the DW-MRS acquisitions was 5.65 Hz for the OCC voxel, and 6.31 Hz for the CR voxel, well within consensus recommended limits (Wilson et al., 2019). The tNAA CRLBs ranged from 3.4–9.7% for the OCC, and 5.1–51.9% for the CR, with difference between voxels likely driven by the lower SNR in the CR voxel, or perhaps reflects increased variability due to the proximity of the CR voxel to the ventricles, as previously reported (Genovese et al., 2021a). We also noted lower data quality for the OCC voxel in the y-direction, which exhibited lower SNR and increased CRLBs, compared to the other two directions. Regarding motion-corruption, we excluded a greater number of transients in the data sets for the GM/WM comparison than in the previous analysis. In all cases, no more than 2 transients were removed per diffusion weighting, with one exception for the CR voxel, where 3 transients were removed for a single diffusion condition. All spectra and fits are shown in Supplementary Figure S2. Figure 6B shows the fitting results for tNAA in the OCC and CR voxels. Full data quality measures are reported in Supplementary Table S2.

Metabolite ADC_e for the mono-exponential representation and ADC_K and K for the kurtosis representation are reported in Table 2 in the lower rows for each individual diffusion-encoding direction. The mean directional-averaged ADC_es for

TABLE 3 Listing of the *in vivo* results of microstructural measures (free diffusivity D_0, cylinder radius R_C) estimated from an astrocylinder model.

Experiment	Metabolite	D_0 $[\mu m^2 ms^{-1}]$	R_C $[\mu m]$	AICc
300 mT/m	$tNAA_Z$	0.33 ± 0.09	2.2 ± 0.1	−51.1
	$tCho_Z$	0.39 ± 0.06	1.4 ± 0.3	−59.4
	tCr_Z	0.41 ± 0.07	1.6 ± 0.4	−57.8
80 mT/m	$tNAA_Z$	0.52 ± 0.08	0.0 ± 0.0	−59.0
	$tCho_Z$	0.92 ± 0.14	2.4 ± 0.9	−56.4
	tCr_Z	0.72 ± 0.16	2.7 ± 1.0	−55.3
CR voxel	$tNAA_{avg}$	0.43 ± 0.07	2.2 ± 0.4	−73.1
	$tCho_{avg}$	0.48 ± 0.06	1.6 ± 0.7	−76.1
	tCr_{avg}	0.46 ± 0.05	2.6 ± 0.2	−82.1
OCC voxel	$tNAA_{avg}$	0.39 ± 0.05	1.5 ± 0.3	−76.5
	$tCho_{avg}$	0.36 ± 0.04	0.0 ± 0.7	−72.3
	tCr_{avg}	0.57 ± 0.07	1.9 ± 0.2	−74.6

The double-lined-column delineation shows, in the upper half, the comparison of the 300 and 80 mT/m settings where diffusion-encoding was applied only along the z-direction, and in the lower half, the comparison of the averaged diffusion metrics over three orthogonal diffusion-directions in the white matter rich corona radiata (CR) and grey matter rich occipital lobe (OCC) using the 300 mT/m setting. The fitting results can be found in Supplementary Figure S3.

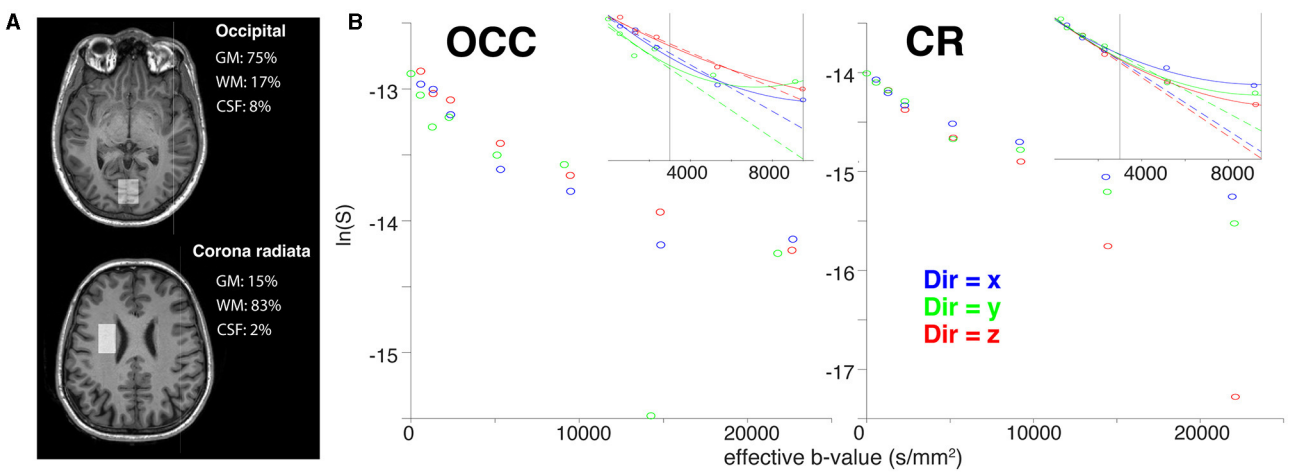

FIGURE 6
Results of the *in vivo* grey and white matter acquisitions. **(A)** T_1-weighted images are overlaid with tissue-specific segmentation masks for grey matter (GM), white matter (WM), and CSF in the occipital (above) and white matter (below) voxels. Grey matter, white matter, and CSF voxel fractions are reported in the corresponding text. **(B)** The three tNAA diffusion decays for the OCC and CR voxels. Mono-exponential (dashed lines) and kurtosis (solid lines) fits are shown for the x (blue), y (green), and z (red) directions. The vertical lines indicate the *b*-value thresholds of data exclusion for mono-exponential and kurtosis modelling, respectively.

tNAA/tCho/tCr are $0.14/0.17/0.18\,\mu m^2 ms^{-1}$ in the CR and $0.13/0.17/0.18\,\mu m^2 ms^{-1}$ in the OCC. For ADC_K slightly higher values were found with $0.16/0.17/0.18\,\mu m^2 ms^{-1}$ in the CR and $0.17/0.14/0.20\,\mu m^2 ms^{-1}$ in the OCC, and corresponding Kurtosis values of 1.90/1.14/1.33 in the CR and 1.75/1.66/1.39 in the OCC.

The estimated microstructural properties for the astrocylinder model are listed in Table 3 in the lower rows for the voxels placed in the WM-rich CR and GM-rich OCC acquired with Connectom settings. The AICc's are comparable between these two brain regions and do not indicate greater model validity in either WM or GM.

3.6 Table vibration

Figure 2C shows the signal decay for the isotropic diffusion phantom acquired along the three orthogonal directions x, y, and z for the Connectom and Prisma settings. The ADC for both settings only shows a slightly faster diffusion along the z-direction, which may point to stronger table vibrations along z. However, the overall estimated ADCs are well in line with the calibration value of 0.293 μm^2/ms at 22°C. Considering our results *in vivo* shown in Figure 6 we found a stronger signal decay for tNAA, but also tCr and tCho (not shown), in the CR when diffusion-encoding is applied along the z-direction at ultra-high b-values.

4 Discussion

In this study, we investigated the practical feasibility of DW-MRS on a Connectom MR scanner equipped with 300 mT/m gradients to measure metabolite diffusion at ultra-high *b*-values in the human brain. By comparing these results between clinical and ultra-high gradient amplitudes, we show the benefits of new gradient systems for DW-MRS, but also present strategies to mitigate the impact of methodological challenges.

4.1 SNR simulations

Simulated SNR benefits of applying ultra-strong gradients were mostly in line with experimental measurements *in vivo*. Comparing the Prisma (G_{max} = 80 mT/m) and Connectom (G_{max} = 300 mT/m) settings, the theoretical SNR gain of 10% for tNAA was even exceeded experimentally and a 16% improvement was achieved. A similar pattern is observed for tCho, where experimental SNR gains exceed predictions by 7 percentage points. J-coupled metabolites mI and Glu were approximately in-line with expectations. For tCr, while we still report an increase in the SNR at 300 mT/m, the magnitude of the SNR increase is not as large as predicted by simulation—36% vs. the expected 50%. This variation from expected SNR gains is attributed to inaccuracies in the assumed T_2, but further verification would require acquisition of T_2 relaxometry alongside the DW-MRS. Interestingly, two studies that investigated this—in humans and mice respectively—found that tCr was the only metabolite that showed a slight dependence of ADC on TE (Branzoli et al., 2014; Mougel et al., 2022).

In general, SNR should be carefully considered in the context of diffusion imaging (Ellegood et al., 2011). The SNR dependence of MRS reconstruction and fitting methods can lead to anomalous signal decay, particularly at higher *b*-values, making it an important consideration for high-*b*-value DW-MRS. The shorter TE afforded by ultra-strong gradients improved SNR and reduced CRLBs, but strict consideration of SNR and MRS fit uncertainty is still necessary.

4.2 *In vivo* results

Previous work (Ronen et al., 2014) found tNAA diffusivity values of 0.076 and 0.34 μm^2/ms for diffusion gradients orthogonal and parallel to the main fibre orientation of the corpus callosum, respectively. The DW-MRS voxels considered in this study were arranged to contain predominantly grey or white matter, but inevitably contained mixed fibre orientations. Our measured ADCs fell within the range reported by Ronen et al. (2014), with our lowest ADC reported in grey matter (0.096 μm^2/ms) and the highest in kurtosis model of white matter (0.194 μm^2/ms).

Furthermore, higher ADCs in GM compared to WM have been previously reported (Ellegood et al., 2011; Kan et al., 2012; Najac et al., 2016) and this finding is confirmed by our results for tNAA in our grey-white matter comparison, where we find a mean ADC of 0.126 μm^2/ms for the OCC GM voxel, and 0.140 μm^2/ms for the CR WM voxel. Kurtosis value ranges for tNAA (1.5–2.2), tCr (1.0–1.6), and—excluding one low-kurtosis fit (0.192)—tCho (1.5–1.9) fall within previously reported diffusion-time-dependent ranges for metabolites (Döring et al., 2023). Lower AICc values were found in the data averaged over multiple diffusion directions. This difference could potentially be attributed to a higher SNR or better agreement with the model, resulting from powder averaging. Furthermore, we examined the data to assess the feasibility of employing more extensive modeling strategies, specifically using a two-compartment model as described in Supplementary Figure S4 and Supplementary Table S1. However, the estimated AICc values were consistently were higher.

We report a 6% decrease in the tNAA ADC of 80 mT/m acquisition, compared to the 300 mT/m acquisition. Conversely, a significant increase was noted for the other two metabolites (tCho, tCr), in line with an even more pronounced increase in the free diffusivity D_0. Although the goodness-of-fit was lower for the 80 mT/m configuration, a possible explanation could be that the longer TE reduces signal contributions from restricted compartments—such as organelles—and consequently increases ADCs and D_0s. Previous studies within a TE range of 35 to 70 ms have not found a correlation between metabolite diffusion and T_2 relaxation, but others at 7T and longer TE report on faster diffusion with increasing TE (Branzoli et al., 2014; Ligneul et al., 2023). This is in line with our results for tCho and tCr indicating faster diffusion when TE increases from 74 to 116 ms, although T_2s were different due to the lower field-strength and diffusion-times due to different maximum gradient amplitudes. Moreover, despite the higher SNR, shorter TE, and shorter diffusion-times achieved with the 300 mT/m settings, AICc's indicate similar model support.

It is important to note that the relatively small size of our volunteer group limits the confidence with which we can draw conclusions about our quantitative analyses. Uncertainty in the MRS modeling procedures—due to a myriad of factors, including lineshape distortion, motion, uncharacterized signals from macromolecules, and issues in baseline characterisation—will affect the measured diffusion properties necessitating a larger participant population to achieve sufficient statistical power. Here, we utilize the Cramer-Rao lower bounds, and weight the fitting accordingly in an attempt to mitigate this. However, in the future it might be beneficial to use metabolite-cycling to further reduce motion and eddy-current artifacts (Döring et al., 2018), and expanding the sample size of the study.

4.3 Eddy currents

Diffusion-weighted imaging and spectroscopy use strong gradients to achieve the desired diffusion weighting. Eddy currents generated during ramp up and down times can cause time-dependent frequency variations in the time domain and consequently distort the MR spectra. Correcting for eddy-current effects is vital in MRS—and particularly so for DW-MRS—in order to accurately reflect lineshape distortions while modeling MR spectra. Furthermore, as per Faraday's law, the magnitude of the induced eddy-current effects increase with the applied gradient strength, further compounding their relevance in the context of ultra-strong gradient DW-MRS. Thankfully, in the particular

case of the Siemens Connectom scanner, the shield coil design minimizes the relative size of eddy current effects. Setsompop et al. (2013) reported that a 7.5-fold increase in gradient amplitude on the Connectom scanner corresponded to just a 2–3-fold eddy current increase, in absolute terms. Our sequence, acquisition scheme, and post processing pipeline further reduce the impact of eddy currents. Our DW-PRESS sequence utilized a bipolar diffusion gradient scheme, which has the potential to reduce eddy current effects on the acquired DW-MR spectra (Alexander et al., 1997; Branzoli, 2015). We further applied two methods of post-hoc eddy current correction.

Our *in vivo* DW-MRS protocols included unsuppressed water-signal, which we used to correct for eddy-current-induced phase and frequency shifts (Klose, 1990). Though this method requires acquisition of only few additional spectra, faster water diffusion may have reduced the effectiveness of this method at the highest *b*-values applied in this work. Therefore, we also demonstrate a second approach (Lin et al., 1994). For this, we inverted the polarity of diffusion-weighting gradients for half of metabolite spectra acquired at the highest *b*-values. The inversion of diffusion gradient polarities inverts the phase of the generated eddy currents, while the intrinsic signal phase and the magnitude of the diffusion-weighting are expected to remain unchanged. No additional acquisitions are required in this case. However, it should be noted that motion corruption of individual transients would necessitate the pairwise removal of the corresponding inverted diffusion condition, potentially doubling motion-related transient exclusions. Furthermore, our implementation of the method did not include the inversion of slice-selective gradients, which may explain the residual asymmetry of the lineshapes in our combined spectra.

The quality of eddy current correction of the above methods relies on the quality of the acquired water and metabolite spectra. A lot of work has been done to monitor the field perturbations in presence of diffusion gradients and their effect of the readout trajectory and the consequent deterioration in image quality in DW-MRI (Chan et al., 2014; Wilm et al., 2015). External probes could be a valuable tool in characterizing and correcting for the eddy current effects present in the FID. The existing DW-PRESS sequence would require a trigger event prior the FID acquisition and a careful temporal and spatial alignment between the FID from the spectroscopy voxel and the estimated eddy current effects from FIDs measured by the probes.

4.4 Gradient non-uniformities

Gradient coils are often designed with a limited field of view (FOV) to minimize nerve stimulation caused by rapidly changing magnetic fields over time. However, this design choice will increase gradient spatial non-uniformity, which becomes more noticeable as one moves away from the isocenter. In high-performance gradient systems like the one used here, gradient uniformity is often further compromized to achieve better performance. There is increased awareness of the importance of correcting for gradient deviations in diffusion MRI studies (Bammer et al., 2003; Guo et al., 2020; Mesri et al., 2020; Morez et al., 2021), but the specification of a gradient system is commercially sensitive information and not widely available.

Two strategies to represent the effective *b*-value were tested, i.e., incorporating the distribution of *b*-values, and representing that distribution using the median. Both strategies show similar deviations of the estimated ADC in DW-MRS, but both varied from the uncorrected nominal *b*-value, it is thus important to take into account the effective *b*-values when this information is available. Also, at lower gradient strength, and lower *b*-values—where the absolute signal change as a function of *b*-value is typically largest—gradient non-uniformities can bias quantitative estimates. In addition to *b*-value deviations, gradient non-uniformities will also result in distortions of the slice profile and thus voxel geometry. While the distortions we observed were small, it should be a consideration when placing voxels close to tissue boundaries, and conservative placement within the relevant tissue is advised, particularly when deviating far from the isocenter, where gradient non-uniformities are larger. Furthermore, there will likely be a small impact on chemical shift displacement error (CSDE). While CSDE is typically a linear chemical-shift-dependent translation of the effective voxel, when gradient non-uniformities are substantial, this effect is no longer a simple translation, and will result in metabolite-specific voxel deformation. This is an area that requires further study; however, we expect this effect to be minimal due to the lower amplitude of the imaging gradients, and the linear—rather than quadratic—effect that non-uniformities have on slice-selective gradients.

4.5 Table vibrations

The switching of strong diffusion gradients can cause mechanical vibrations at low frequencies within the scanner system and table. These vibrations could then be transmitted to the subject being scanned, resulting in artificial signal decay (Hiltunen et al., 2006) which artificially increases the measured ADC. While the Connectom scanner does, indeed, provide access to stronger gradients, it is not trivial how this may manifest as mechanical vibration. Interestingly, Setsompop et al. (2013) reported that the effects of acoustic noise generated by a 300 mT/m Connectom scanner were, in fact, lower than those at more conventional gradient strengths (40 mT/m). They postulated that the thicker, larger, and heavier gradient system of the Connectom scanner somewhat offset the larger amplitude of vibrational forces it generated (Setsompop et al., 2013).

Although the relatively lower directional variance of ADCs measured in the NIST phantom at the $G_{max} = 300$ mT/m setting was surprising, it is important to note that *in vivo* tissue stiffness and composition is different and likely more prone to vibration-induced artifacts. Indeed, our measurements in the CR show a particularly strong signal decay when diffusion-encoding is applied along z-direction. This might originate from tissue anisotropy and major white-matter tracts pointing along z (e.g., cortico-spinal or cortico-pontine tract) when diffusion of tNAA is considered. However, tCho shows consistent signal dropouts and diffusion in the low *b*-value range remains unaffected, which could point to effects related to table vibrations at high gradient amplitudes.

Our hypothesis is that the CR—further away from the contact point between the head and the coil—is more strongly affected by random rotations induced by table vibrations than the OCC. This would be in line with previous observations of largest vibrations on the Connectom when diffusion-encoding is applied along the z-direction (Mueller et al., 2019). However, additional dedicated investigations with different sequence parameters (voxel position, diffusion-time) are required to elucidate this further.

In general, this artefact will be hardware- and sequence-specific but can be mitigated at the hardware level through careful consideration of the coil/gradient mounting (Ogura et al., 2006; Mueller et al., 2019), or even participant positioning, as different placement of padding around the head can lead to differing vibrational coupling between the brain and RF coil housing (Gallichan et al., 2010).

4.6 Other considerations

4.6.1 Macromolecules

The macromolecular background is a potential confound to DW-MRS quantification (Ronen and Valette, 2007), with slowly-diffusing signal components persistent throughout the diffusion conditions. The impact of macromolecules is mitigated in this study as we acquired data at a longer TE, and parameterized the MM background during modeling. Experimentally acquired MM backgrounds are preferable—and can be acquired with ultra-strong gradient DW-MRS (Şimşek et al., 2022)—but are parameterization dependent, and are perhaps best-acquired at the cohort level in larger studies (Zöllner et al., 2023).

4.6.2 Other sequences

While our study focused on a DW-PRESS implementation, the methodological considerations we identified are transferable to other DW-MRS localisation methods. The gradient non-uniformities can be corrected using the same principles, with simple modifications made to account for the specific gradient profile. Similarly, both of the eddy current correction methods considered here are also applicable to other single-shot localization schemes, and DW-PRESS might actually present a particularly challenging example. PRESS localization is known to be more susceptible to chemical shift displacement error than STEAM or sLASER, and this—coupled with the strong spatiotemporal dependence of eddy currents—can adversely affect the efficacy of the eddy-current correction in a metabolite-specific manner. The T_2-based SNR gains provided by ultra-strong gradients are also transferable to other sequences with some caveats. Both DW-STEAM and DW-sLASER will benefit from the T_2-based SNR gains, but are less sensitive to anomalous J-modulation effects than PRESS; however, our data suggest that this has a minimal effect on our DW-PRESS data. DW-STEAM also benefits from the decoupling of diffusion time from the TE, and this can be used to circumvent some of the T_2 limitations to achieve high *b*-values. However, when short diffusion times are required—for example, to probe shorter length scales and/or minimize motion artefacts—ultra-strong gradients can still provide benefits. Furthermore, when measuring metabolite diffusion in small anatomical structures such as thalamus, hippocampus, brainstem, or spinal cord, higher gradient amplitudes combined with DW-STEAM or DW-sLASER localization can enhance an accurate localization (with a minimal CSDE) and should be prefered over DW-PRESS [2].

Another practical consideration that we didn't directly investigate in this work is the effect of concomitant gradient fields. These are nonlinear transverse components to an applied gradient field that arise from Maxwell's equations, and are typically more prominent at lower static field strengths and higher gradient field strengths (Baron et al., 2012). Our DW-PRESS sequence implementation utilized symmetric gradient timing to mitigate the impact of this effect, but for non-symmetric gradient implementations—for example, free gradient waveforms—this effect becomes an important consideration that should be corrected in a prospective manner (Baron et al., 2012; Szczepankiewicz et al., 2019).

4.6.3 Other preprocessing steps

In this study, a retrospective outlier rejection method was used to identify and remove suspected motion-corrupted transients by comparing subsequent transients to the first. While 3 transients were removed in one such case—at the highest *b*-value—this did not impact the ADC estimations using the mono-exponential and kurtosis representations, which were performed using lower *b*-values. However, this may be adversely affect the SNR of highest *b*-value acquisitions in the other models. Weighting using the CRLBs mitigated the impact this had on model performance. Furthermore, if the initial transient of a given series is corrupted by motion, a high rate of outlier rejection would be observed. While this case wasn't encountered in these data, a secondary process—perhaps comparing to the median spectrum—would circumvent this issue. Our approach was conservative, and an alternative approach could be to monitor bulk motion in a prospective manner (Andrews-Shigaki et al., 2011; Saleh et al., 2020).

We have previously investigated the impact of phase and frequency correction methods on DW-MRS data (Jenkins, 2021), and the inherent SNR-dependent performance of such methods. Signal denoising techniques could mitigate this somewhat, and show promise for DW-MRS data (Mosso et al., 2022); however, care must be taken not to invalidate assumptions about noise characteristics during further modeling steps (Dziadosz et al., 2023).

4.6.4 Modeling

While we focused on the practical considerations here, alternative DW-MRS modeling procedures could be beneficial, particularly leveraging high *b*-values and/or the higher SNR to further disentangle compartments (i.e., cylinders and spheres, Supplementary Figure S4, Supplementary Table S1). With the current data, sufficient support was not found for a more complex model, but future work could investigate this with specifically-acquired data.

2 At ultra-high field (≥ 7T) PRESS localization is severely compromised by CSD, and STEAM or sLASER localization is recommended.

Multi-spectrum modeling of MRS data—fitting the frequency and *b*-value dimensions in a single step, rather than independently—is another promising avenue which improves model parsimony and the stability of diffusion measures to experimental variation (Tal, 2023), and notably, allows stable parameterization of the macromolecules and baseline. Several groups have worked to develop this methodology in recent years e.g., FitAid (Chong et al., 2011; Adalid et al., 2017), FSL-MRS (Clarke et al., 2021), and Osprey (Oeltzschner et al., 2020).

4.7 Limitations

We were able to demonstrate the SNR improvement of incorporating ultra-strong gradients. However, cardiac and nerve stimulation limits place firm lower bounds on gradient ramp time and restrict the achievable gradient amplitudes at shorter TE. As a result, at TEs below 70 ms, the maximum gradient amplitude of the Connectom scanner is not achievable within the echo time, at least with the DW-PRESS sequence and diffusion gradient configuration we used. This limits the potential benefit provided by the ultra-strong gradient system. However, in practice, the ultra-high *b*-values we achieved in this study might not be necessary for all applications, and sacrificing diffusion weighting in favour of the improved SNR brought by lower TE might be preferable. This would be particularly beneficial when smaller voxel sizes or shorter scan times are a necessity. Moreover, for DW-PRESS, shorter TE also reduces the diffusion time, probing smaller length scales and different aspects of cell morphology. In practice, lower *b*-values and shorter TE might be preferable for detecting cell morphology changes in order to reduce scan time and/or voxel size.

Our relatively small cohort of volunteers limits the interpretability of the reported ADCs. A larger study is required to elucidate the effects of diffusion time, and systematically validate microstructure across tissue types. Moreover, while our multiple-gradient-condition acquisition allowed reasonable comparisons with conventional gradient systems, a systematic repeatability study using independent gradient systems would be necessary to fully vindicate these results. Indeed, the Connectom gradient design differs from that of a lower-gradient system, affecting gradient non-uniformity even at low gradient amplitudes, and cross-scanner comparisons would automatically include such differences (Gudino and Littin, 2023).

Furthermore, while our focus in this work was in the implementation of DW-MRS with ultra-strong gradients, and circumvention of major artefacts, we primarily limited our analysis to the major metabolites.

5 Conclusion

We successfully implemented acquisition and data processing strategies for ultra-strong gradient DW-MRS. We report diffusion coefficients which conform with the existing literature. Simulated SNR gains are experimentally confirmed, and results indicate that confounding effects of the strong gradient system can be ameliorated.

Data availability statement

The datasets presented in this article are not readily available because we do not have ethical consent to make the *in-vivo* datasets acquired for this study publicly available. Requests to access the datasets should be directed to TaxC@cardiff.ac.uk.

Ethics statement

The studies involving humans were approved by Cardiff University School of Psychology. The studies were conducted in accordance with the local legislation and institutional requirements. The participants provided their written informed consent to participate in this study.

Author contributions

CD-J: Data curation, Formal analysis, Investigation, Methodology, Software, Visualization, Writing – original draft, Writing – review & editing. AD: Formal analysis, Investigation, Methodology, Software, Visualization, Writing – original draft, Writing – review & editing. FF: Methodology, Software, Writing – review & editing. EK: Formal analysis, Investigation, Methodology, Software, Visualization, Writing – original draft, Writing – review & editing. LM: Investigation, Methodology, Software, Writing – review & editing. CE: Conceptualization, Methodology, Supervision, Writing – review & editing. MA: Software, Writing – review & editing. DJ: Funding acquisition, Resources, Supervision, Writing – review & editing. IR: Conceptualization, Methodology, Software, Supervision, Writing – review & editing. FB: Conceptualization, Methodology, Software, Supervision, Writing – review & editing. CT: Conceptualization, Formal analysis, Investigation, Methodology, Software, Supervision, Visualization, Writing – original draft, Writing – review & editing.

Funding

The author(s) declare financial support was received for the research, authorship, and/or publication of this article. This research was funded in whole, or in part, by a Wellcome Trust Investigator Award (096646/Z/11/Z) and a Wellcome Trust Strategic Award (104943/Z/14/Z). CT is supported by the Wellcome Trust [215944/Z/19/Z] and a Veni grant (17331) from the Dutch Research Council (NWO). AD is supported by a Swiss National Science Foundation Fellowship (SNSF #202962). FB acknowledges support from Investissements d'avenir [grant Nos. ANR-10-IAIHU-06 and ANR-11-INBS-0006]. MA and LM are supported by a Wellcome Trust Investigator Award (219536/Z/19/Z). For the purpose of open access, the author has applied a CC BY public copyright licence to any Author Accepted Manuscript version arising from this submission.

Acknowledgments

The authors would like to acknowledge the contribution of Umesh Rudrapatna whose efforts aided in the development of the DW-MRS sequence and data processing strategies.

Conflict of interest

FF was employed by company Siemens Healthcare Ltd.

The remaining authors declare that the research was conducted in the absence of any commercial or financial relationships that could be construed as a potential conflict of interest.

The author(s) declared that they were an editorial board member of Frontiers, at the time of submission. This had no impact on the peer review process and the final decision.

Publisher's note

All claims expressed in this article are solely those of the authors and do not necessarily represent those of their affiliated organizations, or those of the publisher, the editors and the reviewers. Any product that may be evaluated in this article, or claim that may be made by its manufacturer, is not guaranteed or endorsed by the publisher.

Supplementary material

The Supplementary Material for this article can be found online at: https://www.frontiersin.org/articles/10.3389/fnins.2023.1258408/full#supplementary-material

SUPPLEMENTARY FIGURE S1
Figure showing the MRS fitting residuals for the 300 mT/m **(left)** and 80 mT/m **(right)** acquisitions. Residuals are plotted in red, ascending in b-value from top to bottom.

SUPPLEMENTARY FIGURE S2
This figure shows the individual processed spectra (black) and fits (red) for the OCC **(left)** and CR **(right)** voxels for all b-values. Individual diffusion directions are grouped by diffusion value, and are ordered from top to bottom: x, y, and z, respectively.

SUPPLEMENTARY FIGURE S3
Eddy current phase evolution from three different gradient amplitudes: 295 mT/m (blue), 150 mT/m (red), and 50 mT/m (yellow).

SUPPLEMENTARY FIGURE S4
Fitting results applying an astrocylinder model and the estimated microstructural measures (free diffusivity D0, cylinder radius RC). Outliers were identified by the RMSE when iteratively removing a single data point from fitting.

SUPPLEMENTARY FIGURE S5
Fitting results applying a two-compartment model and the estimated microstructural measures (free diffusivity D0, sphere radius RS, cylinder radius RC). The fraction of cylinders fC was kept fixed at 0.8 and the standard deviation was estimated from bootstrapping. Outliers were identified by the RMSE when iteratively removing a single data point from fitting.

SUPPLEMENTARY TABLE S1
Listing of the *in vivo* results of microstructural measures (free diffusivity D0, sphere radius RS, cylinder radius RC) estimated from a two-compartment model. The double lined column delineation shows in the upper half the comparison of the 300 and 80 mT/m settings where diffusion-encoding was applied only along the z-direction, and in the lower half the comparison of the averaged diffusion metrics over three orthogonal diffusion-directions in the white matter rich corona radiata (CR) and grey matter rich occipital lobe (OCC) using the 300 mT/m setting. The fitting results can be found in Supplementary Figure S4. *Fraction of cylinders fC was kept fixed at 0.8, c.f., text.

SUPPLEMENTARY TABLE S2
Full data quality information for the *in vivo* data. Each section contains entries for the Cramer-Rao lower bound (CRLB) of tNAA, tCho, and tCr, as well as the full width half maximum (FWHM), signal-to-noise ratio (SNR), points excluded by the motion-corruption metric (Excl.), and the mean frequency (Freq-Mean) and phase (Phs-Mean) shifts applied by spectral registration. Entries are ordered by increasing b-value per section.

References

Adalid, V., Döring, A., Kyathanahally, S. P., Bolliger, C. S., Boesch, C., and Kreis, R. (2017). Fitting interrelated datasets: metabolite diffusion and general lineshapes. *Magn. Reson. Mater. Phys. Biol. Med.* 30, 429–448. doi: 10.1007/s10334-017-0618-z

Alexander, A. L., Tsuruda, J. S., and Parker, D. L. (1997). Elimination of eddy current artifacts in diffusion-weighted echo-planar images: the use of bipolar gradients. *Magn. Reson. Med.* 38, 1016–1021. doi: 10.1002/mrm.1910380623

Andrews-Shigaki, B. C., Armstrong, B. S., Zaitsev, M., and Ernst, T. (2011). Prospective motion correction for magnetic resonance spectroscopy using single camera retro-grate reflector optical tracking. *J. Magn. Reson. Imag.* 33, 498–504. doi: 10.1002/jmri.22467

Bammer, R., Markl, M., Barnett, A., Acar, B., Alley, M., Pelc, N., et al. (2003). Analysis and generalized correction of the effect of spatial gradient field distortions in diffusion-weighted imaging. *Magn. Reson. Med.* 50, 560–569. doi: 10.1002/mrm.10545

Baron, C., Lebel, R., Wilman, A., and Beaulieu, C. (2012). The effect of concomitant gradient fields on diffusion tensor imaging. *Magn. Reson. Med.* 68, 1190–1201. doi: 10.1002/mrm.24120

Bottomley, P. A. (1987). Spatial localization in NMR spectroscopy in vivo. *Ann. NY. Acad. Sci.* 508, 333–348. doi: 10.1111/j.1749-6632.1987.tb32915.x

Branzoli, F. (2015). "Diffusion-weighted spectroscopy of n-acetylaspartate: a novel technique to specifically explore neuroaxonal damage in multiple sclerosis, in *Proceedings of the International Social Magnetic Resonance Medicine* 617.

Branzoli, F., Ercan, E., Webb, A., and Ronen, I. (2014). The interaction between apparent diffusion coefficients and transverse relaxation rates of human brain metabolites and water studied by diffusion-weighted spectroscopy at 7 T. *NMR Biomed.* 27, 495–506. doi: 10.1002/nbm.3085

Chan, R. W., von Deuster, C., Giese, D., Stoeck, C. T., Harmer, J., Aitken, A. P., et al. (2014). Characterization and correction of eddy-current artifacts in unipolar and bipolar diffusion sequences using magnetic field monitoring. *J. Magn. Reson.* 244, 74–84. doi: 10.1016/j.jmr.2014.04.018

Choi, J.-K., Dedeoglu, A., and Jenkins, B. G. (2007). Application of MRS to mouse models of neurodegenerative illness. *NMR Biomed.* 20, 216–237. doi: 10.1002/nbm.1145

Chong, D. G., Kreis, R., Bolliger, C. S., Boesch, C., and Slotboom, J. (2011). Two-dimensional linear-combination model fitting of magnetic resonance spectra to define the macromolecule baseline using fitaid, a fitting tool for arrays of interrelated datasets. *Magn. Reson. Mater. Phys. Biol. Med.* 24, 147–164. doi: 10.1007/s10334-011-0246-y

Clarke, W. T., Stagg, C. J., and Jbabdi, S. (2021). FSL-MRS: an end-to-end spectroscopy analysis package. *Magn. Reson. Med.* 85, 2950–2964. doi: 10.1002/mrm.28630

Döring, A., Adalid, V., Boesch, C., and Kreis, R. (2018). Diffusion-weighted magnetic resonance spectroscopy boosted by simultaneously acquired water reference signals. *Magn. Reson. Med.* 80, 2326–2338. doi: 10.1002/mrm.27222

Döring, A., Rösler, F., Şimşek, K., Afzali, M., Kreis, R., Jones, D. K., et al. (2023). "Time dependent diffusion and kurtosis of human brain metabolites, in *Proceedings of the Virtual Conference of ISMRM*.

Dziadosz, M., Rizzo, R., Kyathanahally, S. P., and Kreis, R. (2023). Denoising single MR spectra by deep learning: miracle or mirage? *Magn. Reson. Med*. 90, 1749–1761. doi: 10.1002/mrm.29762

Edden, R. A., Puts, N. A., Harris, A. D., Barker, P. B., and Evans, C. J. (2014). Gannet: a batch-processing tool for the quantitative analysis of gamma-aminobutyric acid-edited mr spectroscopy spectra. *J. Magn. Reson. Imag.* 40, 1445–1452. doi: 10.1002/jmri.24478

Ellegood, J., Hanstock, C. C., and Beaulieu, C. (2011). Considerations for measuring the fractional anisotropy of metabolites with diffusion tensor spectroscopy. *NMR Biomed*. 24, 270–280. doi: 10.1002/nbm.1586

Fan, Q., Eichner, C., Afzali, M., Mueller, L., Tax, C. M., Davids, M., et al. (2022). Mapping the human connectome using diffusion MRI at 300 mt/m gradient strength: methodological advances and scientific impact. *NeuroImage* 254, 118958. doi: 10.1016/j.neuroimage.2022.118958

Gallichan, D., Scholz, J., Bartsch, A., Behrens, T. E., Robson, M. D., and Miller, K. L. (2010). Addressing a systematic vibration artifact in diffusion-weighted MRI. *Hum. Brain Mapp*. 31, 193–202. doi: 10.1002/hbm.20856

Ganji, S. K., Banerjee, A., Patel, A. M., Zhao, Y. D., Dimitrov, I. E., Browning, J. D., et al. (2012). T_2 measurement of J-coupled metabolites in the human brain at 3 T. *NMR Biomed*. 25, 523–529. doi: 10.1002/nbm.1767

Genovese, G., Marjańska, M., Auerbach, E. J., Cherif, L. Y., Ronen, I., Lehéricy, S., et al. (2021a). In vivo diffusion-weighted mrs using semi-laser in the human brain at 3 T: Methodological aspects and clinical feasibility. *NMR Biomed*. 34, e4206. doi: 10.1002/nbm.4206

Genovese, G., Palombo, M., Santin, M. D., Valette, J., Ligneul, C., Aigrot, M.-S., et al. (2021b). Inflammation-driven glial alterations in the cuprizone mouse model probed with diffusion-weighted magnetic resonance spectroscopy at 11.7 T. *NMR Biomed*. 34, e4480. doi: 10.1002/nbm.4480

Goveas, J., O'Dwyer, L., Mascalchi, M., Cosottini, M., Diciotti, S., De Santis, S., et al. (2015). Diffusion-MRI in neurodegenerative disorders. *Magn. Reson. Imag.* 33, 853–876. doi: 10.1016/j.mri.2015.04.006

Gudino, N., and Littin, S. (2023). Advancements in gradient system performance for clinical and research MRI. *J. Magn. Reson. Imag.* 57, 57–70. doi: 10.1002/jmri.28421

Guo, F., de Luca, A., Parker, G., Jones, D., Viergever, M., Leemans, A., et al. (2020). The effect of gradient nonlinearities on fiber orientation estimates from spherical deconvolution of diffusion magnetic resonance imaging data. *Hum. Brain Mapp*. 42, 367–383. doi: 10.1002/hbm.25228

Hall, E. L., Stephenson, M. C., Price, D., and Morris, P. G. (2014). Methodology for improved detection of low concentration metabolites in MRS: optimised combination of signals from multi-element coil arrays. *Neuroimage* 86, 35–42. doi: 10.1016/j.neuroimage.2013.04.077

Hiltunen, J., Hari, R., Jousmki, V., Muller, K., Sepponen, R., and Joensuu, R. (2006). Quantification of mechanical vibration during diffusion tensor imaging at 3T. *NeuroImage* 32, 93–103. doi: 10.1016/j.neuroimage.2006.03.004

Huang, S. Y., Witzel, T., Keil, B., Scholz, A., Davids, M., Dietz, P., et al. (2021). Connectome 2.0: Developing the next-generation ultra-high gradient strength human MRI scanner for bridging studies of the micro-, meso-and macro-connectome. *Neuroimage* 243, 118530. doi: 10.1016/j.neuroimage.2021.118530

Hutchinson, E. B., Schwerin, S. C., Avram, A. V., Juliano, S. L., and Pierpaoli, C. (2018). Diffusion MRI and the detection of alterations following traumatic brain injury. *J. Neurosci. Res*. 96, 612–625. doi: 10.1002/jnr.24065

Jelescu, I. O., de Skowronski, A., Geffroy, F., Palombo, M., and Novikov, D. S. (2022). Neurite exchange imaging (NEXI): a minimal model of diffusion in gray matter with inter-compartment water exchange. *NeuroImage* 256, 119277. doi: 10.1016/j.neuroimage.2022.119277

Jenkins, C., Kleban, E., Mueller, L., Evans, C. J., Rudrapanta, U., Jones, D., et al. (2020). "Dw-MRS with ultra-strong diffusion gradients," in *ISMRM*.

Jenkins, C. W. (2021). "The influence of spectral registration on diffusion-weighted magnetic resonance spectroscopy ADC estimates," in *ISMRM*.

Jensen, J. H., Helpern, J. A., Ramani, A., Lu, H., and Kaczynski, K. (2005). Diffusional kurtosis imaging: the quantification of non-gaussian water diffusion by means of magnetic resonance imaging. *Magn. Reson. Med*. 53, 1432–1440. doi: 10.1002/mrm.20508

Jones, D. K., Alexander, D. C., Bowtell, R., Cercignani, M., Dell'Acqua, F., McHugh, D. J., et al. (2018). Microstructural imaging of the human brain with a super-scanner: 10 key advantages of ultra-strong gradients for diffusion mri. *NeuroImage* 182, 8–38. doi: 10.1016/j.neuroimage.2018.05.047

Kan, H. E., Techawiboonwong, A., Van Osch, M. J., Versluis, M. J., Deelchand, D. K., Henry, P.-G., et al. (2012). Differences in apparent diffusion coefficients of brain metabolites between grey and white matter in the human brain measured at 7 t. *Magn. Reson. Med*. 67, 1203–1209. doi: 10.1002/mrm.23129

Ke, Y., Cohen, B., Lowen, S., Hirashima, F., Nassar, L., and Renshaw, P. (2002). Biexponential transverse relaxation (t2) of the proton mrs creatine resonance in human brain. *Magn. Reson. Med*. 47, 232–238. doi: 10.1002/mrm.10063

Klose, U. (1990). In vivo proton spectroscopy in presence of eddy currents. *Magn. Reson. Med*. 14, 26–30. doi: 10.1002/mrm.1910140104

Landheer, K., Gajdošík, M., and Juchem, C. (2020). A semi LASER, single-voxel spectroscopic sequence with a minimal echo time of 20.1 ms in the human brain at 3 T. *NMR Biomed*. 33, 1–12. doi: 10.1002/nbm.4324

Ligneul, C., Najac, C., Döring, A., Beaulieu, C., Branzoli, F., Clarke, W. T., et al. (2023). Diffusion-weighted MR spectroscopy: consensus, recommendations and resources from acquisition to modelling. *arXiv preprint arXiv:2305.10829*.

Ligneul, C., Palombo, M., Hernández-Garzón, E., Carrillo-de Sauvage, M.-A., Flament, J., Hantraye, P., et al. (2019). Diffusion-weighted magnetic resonance spectroscopy enables cell-specific monitoring of astrocyte reactivity in vivo. *NeuroImage* 191, 457–469. doi: 10.1016/j.neuroimage.2019.02.046

Lin, C., Wendt, R. E., Evans, H. J., Rowe, R. M., Hedrick, T. D., and LeBlanc, A. D. (1994). Eddy current correction in volume-localized MR spectroscopy. *J. Magn. Reson. Imaging* 4, 823–827. doi: 10.1002/jmri.1880040614

Mattiello, J., Basser, P. J., and Le Bihan, D. (1997). The B matrix in diffusion tensor echo-planar imaging. *Magn. Reson. Med*. 37, 292–300. doi: 10.1002/mrm.1910370226

Mesri, H. Y., David, S., Viergever, M. A., and Leemans, A. (2020). The adverse effect of gradient nonlinearities on diffusion MRI: from voxels to group studies. *NeuroImage* 205, 116127. doi: 10.1016/j.neuroimage.2019.116127

Morez, J., Sijbers, J., Vanhevel, F., and Jeurissen, B. (2021). Constrained spherical deconvolution of nonspherically sampled diffusion MRI data. *Hum. Brain Mapp*. 42, 521–538. doi: 10.1002/hbm.25241

Mosso, J., Simicic, D., Şimşek, K., Kreis, R., Cudalbu, C., and Jelescu, I. O. (2022). MP-PCA denoising for diffusion mrs data: promises and pitfalls. *NeuroImage* 263, 119634. doi: 10.1016/j.neuroimage.2022.119634

Mougel, E., Malaquin, S., and Valette, J. (2022). Assessing potential correlation between t2 relaxation and diffusion of lactate in the mouse brain. *Magn. Reson. Med*. 88, 2277–2284. doi: 10.1002/mrm.29395

Mueller, L., Rudrapatna, S. U., Tax, C. M. W., Wise, R. G., and Jones, D. K. (2019). "Diffusion MRI with b = 1000 s/mm2 at te < 22 ms using single-shot spiral readout and ultra-strong gradients: Implications for microstructure imaging, in *Proceedings of the 27th Annual Meeting of ISMRM*.

Mugler III, J. P., and Brookeman, J. R. (1990). Three-dimensional magnetization-prepared rapid gradient-echo imaging (3D mp rage). *Magn. Reson. Med*. 15, 152–157. doi: 10.1002/mrm.1910150117

Najac, C., Branzoli, F., Ronen, I., and Valette, J. (2016). Brain intracellular metabolites are freely diffusing along cell fibers in grey and white matter, as measured by diffusion-weighted mr spectroscopy in the human brain at 7 T. *Brain Struct. Funct*. 221, 1245–1254. doi: 10.1007/s00429-014-0968-5

Najac, C., Döring, A., Clarke, W., Genovese, G., Just, N., Kreis, R., et al. (2022). "Differences in diffusion-weighted mrs processing and fitting pipelines, and their effect on tissue modeling: results from a workshop challenge, in *Proceedings of the International Social Magnetic Resonance in Medicine* 30.

Near, J., Edden, R., Evans, C. J., Paquin, R., Harris, A., and Jezzard, P. (2015). Frequency and phase drift correction of magnetic resonance spectroscopy data by spectral registration in the time domain. *Magn. Reson. Med*. 73, 44–50. doi: 10.1002/mrm.25094

Near, J., Harris, A. D., Juchem, C., Kreis, R., Marjańska, M., Öz, G., et al. (2021). Preprocessing, analysis and quantification in single-voxel magnetic resonance spectroscopy: experts' consensus recommendations. *NMR Biomed*. 34, e4257. doi: 10.1002/nbm.4257

Nilsson, M., Lasič, S., Drobnjak, I., Topgaard, D., and Westin, C.-F. (2017). Resolution limit of cylinder diameter estimation by diffusion MRI: The impact of gradient waveform and orientation dispersion. *NMR Biomed*. 30, e3711. doi: 10.1002/nbm.3711

Nilsson, M., Szczepankiewicz, F., Lampinen, B., Ahlgren, A., de Martins, J. P., Lasic, S., et al. (2018). "An open-source framework for analysis of multidimensional diffusion MRI data implemented in MATLAB, in *Proceedings of the International Social Magnetic Resonance in Medicine* 5355.

Oeltzschner, G., Zöllner, H. J., Hui, S. C., Mikkelsen, M., Saleh, M. G., Tapper, S., et al. (2020). Osprey: Open-source processing, reconstruction estimation of magnetic resonance spectroscopy data. *J. Neurosci. Methods* 343, 108827. doi: 10.1016/j.jneumeth.2020.108827

Ogura, A., Maeda, F., Miyai, A., Hayashi, K., and Hongoh, T. (2006). Effect of vibration caused by time-varying magnetic fields on diffusion-weighted mri. *Nihon Hoshasen Gijutsu Gakkai Zasshi* 62, 565–569. doi: 10.6009/jjrt.62.565

Palacios, E. M., Martin, A. J., Boss, M. A., Ezekiel, F., Chang, Y. S., Yuh, E. L., et al. (2017). Toward precision and reproducibility of diffusion tensor imaging: a multicenter diffusion phantom and traveling volunteer study. *Am. J. Neuroradiol*. 38, 537–545. doi: 10.3174/ajnr.A5025

Palombo, M., Ligneul, C., and Valette, J. (2017). Modeling diffusion of intracellular metabolites in the mouse brain up to very high diffusion-weighting: diffusion in long fibers (almost) accounts for non-monoexponential attenuation. *Magn. Reson. Med*. 77, 343–350. doi: 10.1002/mrm.26548

Palombo, M., Shemesh, N., Ronen, I., and Valette, J. (2018). Insights into brain microstructure from in vivo dw-mrs. *Neuroimage* 182, 97–116. doi: 10.1016/j.neuroimage.2017.11.028

Patterson, D. M., Padhani, A. R., and Collins, D. J. (2008). Technology insight: water diffusion mria potential new biomarker of response to cancer therapy. *Nat. Clin. Pract. Oncol*. 5, 220–233. doi: 10.1038/ncponc1073

Penny, W. D., Friston, K. J., Ashburner, J. T., Kiebel, S. J., and Nichols, T. E. (2011). *Statistical Parametric Mapping: The Analysis of Functional Brain Images*. London: Elsevier.

Ronen, I., Budde, M., Ercan, E., Annese, J., Techawiboonwong, A., and Webb, A. (2014). Microstructural organization of axons in the human corpus callosum quantified by diffusion-weighted magnetic resonance spectroscopy of n-acetylaspartate and post-mortem histology. *Brain Struct. Funct*. 219, 1773–1785. doi: 10.1007/s00429-013-0600-0

Ronen, I., and Valette, J. (2007). Diffusion-weighted magnetic resonance spectroscopy. *EMagRes*. 4, 733–750. doi: 10.1002/9780470034590.emrstm1471

Saleh, M. G., Edden, R. A., Chang, L., and Ernst, T. (2020). Motion correction in magnetic resonance spectroscopy. *Magn. Reson. Med*. 84, 2312–2326. doi: 10.1002/mrm.28287

Setsompop, K., Kimmlingen, R., Eberlein, E., Witzel, T., Cohen-Adad, J., McNab, J. A., et al. (2013). Pushing the limits of in vivo diffusion MRI for the human connectome project. *Neuroimage* 80, 220–233. doi: 10.1016/j.neuroimage.2013.05.078

Simpson, R., Devenyi, G. A., Jezzard, P., Hennessy, T. J., and Near, J. (2017). Advanced processing and simulation of mrs data using the fid appliance (fid-a) an open source, matlab-based toolkit. *Magn. Reson. Med*. 77, 23–33. doi: 10.1002/mrm.26091

Şimşek, K., Döring, A., Pampel, A., Möller, H. E., and Kreis, R. (2020). "Diffusion-weighted mrs at short te using a connectom system: non-gaussian metabolite diffusion and macromolecular signals in human brain," in *Proceedings of the Virtual Conference of ISMRM* 364.

Şimşek, K., Döring, A., Pampel, A., Möller, H. E., and Kreis, R. (2021). "Simultaneous spectral and bi-exponential diffusion modeling of doubly motion-corrected human brain spectra with very high b-values," in *Proceedings of the Annual Meeting of ISMRM* 4263.

Şimşek, K., Döring, A., Pampel, A., Möller, H. E., and Kreis, R. (2022). Macromolecular background signal and non-gaussian metabolite diffusion determined in human brain using ultra-high diffusion weighting. *Magn. Reson. Med*. 88, 1962–1977. doi: 10.1002/mrm.29367

Szczepankiewicz, F., Westin, C.-F., and Nilsson, M. (2019). Maxwell-compensated design of asymmetric gradient waveforms for tensor-valued diffusion encoding. *Magn. Reson. Med*. 82, 1424–1437. doi: 10.1002/mrm.27828

Tal, A. (2023). The future is 2d: spectral-temporal fitting of dynamic mrs data provides exponential gains in precision over conventional approaches. *Magn. Reson. Med*. 89, 499–507. doi: 10.1002/mrm.29456

Vanhamme, L., Fierro, R. D., Van Huffel, S., and de Beer, R. (1998). Fast removal of residual water in proton spectra. *J. Magn. Reson*. 132, 197–203. doi: 10.1006/jmre.1998.1425

Weidlich, D., Honecker, J., Gmach, O., Wu, M., Burgkart, R., Ruschke, S., et al. (2019). Measuring large lipid droplet sizes by probing restricted lipid diffusion effects with diffusion-weighted mrs at 3T. *Magn. Reson. Med*. 81, 3427–3439. doi: 10.1002/mrm.27651

Weidlich, D., Zamskiy, M., Maeder, M., Ruschke, S., Marburg, S., and Karampinos, D. C. (2020). Reduction of vibration-induced signal loss by matching mechanical vibrational states: Application in high b-value diffusion-weighted mrs. *Magn. Reson. Med*. 84, 39–51. doi: 10.1002/mrm.28128

Wilm, B. J., Nagy, Z., Barmet, C., Vannesjo, S. J., Kasper, L., Haeberlin, M., et al. (2015). Diffusion MRI with concurrent magnetic field monitoring. *Magn. Reson. Med*. 74, 925–933. doi: 10.1002/mrm.25827

Wilson, M., Andronesi, O., Barker, P. B., Bartha, R., Bizzi, A., Bolan, P. J., et al. (2019). Methodological consensus on clinical proton mrs of the brain: review and recommendations. *Magn. Reson. Med*. 82, 527–550. doi: 10.1002/mrm.27742

Wilson, M., Reynolds, G., Kauppinen, R. A., Arvanitis, T. N., and Peet, A. C. (2011). A constrained least-squares approach to the automated quantitation of in vivo 1h magnetic resonance spectroscopy data. *Magn. Reson. Med*. 65, 1–12. doi: 10.1002/mrm.22579

Wyss, P. O., Bianchini, C., Scheidegger, M., Giapitzakis, I. A., Hock, A., Fuchs, A., et al. (2018). In vivo estimation of transverse relaxation time constant (t2) of 17 human brain metabolites at 3T. *Magn. Reson. Med*. 80, 452–461. doi: 10.1002/mrm.27067

Yablonskiy, D. A., and Sukstanskii, A. L. (2010). Theoretical models of the diffusion weighted mr signal. *NMR Biomed*. 23, 661–681. doi: 10.1002/nbm.1520

Zöllner, H. J., Davies-Jenkins, C. W., Murali-Manohar, S., Gong, T., Hui, S. C., Song, Y., et al. (2023). Feasibility and implications of using subject-specific macromolecular spectra to model short echo time magnetic resonance spectroscopy data. *NMR Biomed*. 36, e4854. doi: 10.1002/nbm.4854

frontiers | Frontiers in Neuroscience

TYPE Original Research
PUBLISHED 30 January 2024
DOI 10.3389/fnins.2023.1320296

OPEN ACCESS

EDITED BY
André Döring,
Center for Biomedical Imaging (CIBM), Switzerland

REVIEWED BY
Marius Mader,
Stanford University, United States
Yande Ren,
Qingdao University Affiliated Hospital, China

*CORRESPONDENCE
Xiaoyue Ma
✉ maxiaoyue0822@163.com
Jingliang Cheng
✉ fccchengjl@zzu.edu.cn

†These authors share first authorship

RECEIVED 12 October 2023
ACCEPTED 19 December 2023
PUBLISHED 30 January 2024

CITATION
Zhao K, Gao A, Gao E, Qi J, Chen T, Zhao G, Zhao G, Wang P, Wang W, Bai J, Zhang Y, Zhang H, Yang G, Ma X and Cheng J (2024) Multiple diffusion metrics in differentiating solid glioma from brain inflammation. *Front. Neurosci.* 17:1320296. doi: 10.3389/fnins.2023.1320296

Multiple diffusion metrics in differentiating solid glioma from brain inflammation

Kai Zhao[1†], Ankang Gao[1†], Eryuan Gao[1], Jinbo Qi[1], Ting Chen[1], Guohua Zhao[1], Gaoyang Zhao[1], Peipei Wang[1], Weijian Wang[1], Jie Bai[1], Yong Zhang[1], Huiting Zhang[2], Guang Yang[3], Xiaoyue Ma[1*] and Jingliang Cheng[1*]

[1]Department of Magnetic Resonance Imaging, The First Affiliated Hospital of Zhengzhou University, Zhengzhou, China, [2]MR Research Collaboration, Siemens Healthineers Ltd., Wuhan, China, [3]Shanghai Key Laboratory of Magnetic Resonance, East China Normal University, Shanghai, China

Background and purpose: The differential diagnosis between solid glioma and brain inflammation is necessary but sometimes difficult. We assessed the effectiveness of multiple diffusion metrics of diffusion-weighted imaging (DWI) in differentiating solid glioma from brain inflammation and compared the diagnostic performance of different DWI models.

Materials and methods: Participants diagnosed with either glioma or brain inflammation with a solid lesion on MRI were enrolled in this prospective study from May 2016 to April 2023. Diffusion-weighted imaging was performed using a spin-echo echo-planar imaging sequence with five b values (500, 1,000, 1,500, 2000, and 2,500 s/mm^2) in 30 directions for each b value, and one b value of 0 was included. The mean values of multiple diffusion metrics based on diffusion tensor imaging (DTI), diffusion kurtosis imaging (DKI), mean apparent propagator (MAP), and neurite orientation dispersion and density imaging (NODDI) in the abnormal signal area were calculated. Comparisons between glioma and inflammation were performed. The area under the curve (AUC) of the receiver operating characteristic curve (ROC) of diffusion metrics were calculated.

Results: 57 patients (39 patients with glioma and 18 patients with inflammation) were finally included. MAP model, with its metric non-Gaussianity (NG), shows the greatest diagnostic performance (AUC = 0.879) for differentiation of inflammation and glioma with atypical MRI manifestation. The AUC of DKI model, with its metric mean kurtosis (MK) are comparable to NG (AUC = 0.855), followed by NODDI model with intracellular volume fraction (ICVF) (AUC = 0.825). The lowest value was obtained in DTI with mean diffusivity (MD) (AUC = 0.758).

Conclusion: Multiple diffusion metrics can be used in differentiation of inflammation and solid glioma. Non-Gaussianity (NG) from mean apparent propagator (MAP) model shows the greatest diagnostic performance for differentiation of inflammation and glioma.

KEYWORDS

magnetic resonance imaging, non-Gaussian, diffusion-weighted imaging, glioma, brain inflammation

1 Introduction

Glioma is the most common primary brain tumor and requires timely surgical treatment for a better prognosis (Lapointe et al., 2018). Brain inflammation, on the other hand, is a common benign lesion with associated neurologic dysfunction and non-operative therapy as the main treatment (Hodler et al., 2020). Early identification of glioma from inflammation is essential. However, these two types of diseases sometimes overlap in clinical symptoms, signs, and laboratory tests (Han et al., 2021).

Currently, the preoperative diagnosis of glioma relies on magnetic resonance imaging (MRI) examination (Zoccarato et al., 2019). Some cystic or necrotic brain inflammation may exhibit ring-shaped enhancement, making it prone to misdiagnosis as glioblastoma, consequently leading to erroneous treatment decisions (Sabel et al., 2001; Nadal Desbarats et al., 2003). Central necrosis, hemorrhage, and ring-shaped enhancement are considered typical malignant features of high-grade gliomas in advanced stages. These characteristics are associated with rapid tumor cell growth, inadequate blood and oxygen supply to the tumor core, damage to the blood–brain barrier and immature angiogenesis. Several studies (Hiremath et al., 2017; Bo et al., 2021) have advanced imaging analysis methods to distinguish gliomas exhibiting typical malignant features from conditions such as brain abscesses and tumefactive demyelination. On the other hand, gliomas with atypical MRI presentations are prone to misdiagnosis as brain inflammation, resulting in treatment delays and further tumor progression, thereby worsening prognosis (Talathi et al., 2015; Lu et al., 2019), resulting in treatment delays and further progression, thereby worsening prognosis. Some research (Wu et al., 2021; Piao et al., 2022) have defined atypical MRI manifestation of glioma as the absence of an obvious mass effect or enhancement. Gliomas with such atypical manifestations are deemed challenging to differentiate from brain inflammation using conventional MRI, making them a focal point for research. We recognize the importance of choosing cases with comparable imaging presentations for studies on imaging methods that aim to distinguish between gliomas and brain inflammation. This strategy aligns with the pragmatic considerations of clinical practice (Omuro et al., 2006). However, the definition of atypical MRI manifestations in gliomas remains ambiguous and lacks standardized criteria.

Building upon the studies and case reports mentioned above, we advocate for the incorporation of a straightforward and widely applicable set of selection criteria in investigations of novel imaging techniques. This involves including glioma cases based on the identification of either cystic or solid lesions as primary criteria. Additionally, the selection of cases of brain inflammation with comparable imaging presentations is emphasized to establish a homogeneous control group. Specifically, distinguishing cystic/necrotic gliomas from cerebral abscesses, cysticercosis or tumefactive demyelination, and differentiating solid gliomas from brain inflammation with similar imaging presentations.

Accurate diagnosis of solid lesions is paramount, as these manifest in the early stages of the disease. Timely intervention can curtail lesion progression, preserve cerebral function, and enhance overall prognosis. Recent research (Wu et al., 2021; Piao et al., 2022) found that the deep learning and radiomics analysis based on conventional MRI performed well in distinguishing glioma and brain inflammation, but the features extracted by those methods are limited in characterizing the pathophysiological and microstructural differences between two type of lesions due to their complex numerical nature (Abdel Razek et al., 2021). Therefore, the use of advanced MRI techniques to access patients with suspected glioma is in need.

Diffusion-weighted imaging (DWI) is increasingly used because of its ability to quantitatively assess the microstructure of lesion. Advanced diffusion models describe the displacement of the water molecules more accurately, which can illustrate the microstructural information of the tissue better. Several non-Gaussian diffusion models have been used to evaluate glioma, and they performed well in predicting glioma genotyping (Gao et al., 2022) and distinguishing glioblastoma from solitary brain metastasis (Qi et al., 2022; Wang et al., 2022). In this study, we evaluated the performance of 4 diffusion models in differentiating glioma with atypical MRI manifestation from brain inflammation, including diffusion tensor imaging (DTI), diffusion kurtosis imaging (DKI), mean apparent propagator (MAP), and neurite orientation dispersion and density imaging (NODDI) models.

2 Materials and methods

The study was approved by scientific research and clinical trial ethics committee of the first affiliated hospital of Zhengzhou university, and informed consent was waived (Approval Number: 2019-KY-231).

2.1 Patients

This retrospective study involved the collection of imaging data from 62 patients diagnosed with either glioma or inflammation from May 2016 to April 2023. The inclusion criteria were: (1) glioma histopathologically confirmed cerebral gliomas based on the World Health Organization (WHO) 2021 classification criteria or brain inflammation confirmed through pathological biopsy or cerebrospinal fluid analysis; (2) MRI shows a solid lesion without hemorrhagic, ring-shaped enhancement, or patchy heterogeneous signals of necrosis.

The exclusion criteria were: (1) patients who had undergone surgery, anti-tumor therapy, steroids or anti-infective treatment before the MRI examination; (2) MRI images with severe susceptibility artifacts or motion artifacts; (3) lesions located under the tentorium of cerebellum; (4) incomplete imaging data.

2.2 MRI protocol

All patients underwent MRI scans on a 3 T MR scanner (MAGNETOM Prisma, Siemens Healthineers, Erlangen, Germany) with a 64 channel of head–neck coil. The acquisition sequence and parameters were as follows: (1). T1WI: repetition time (TR), 250.0 ms; excitation time (TE), 2.46 ms; number of slices, 20; slice thickness, 5.0 mm; field of view (FOV), $220 \times 220\ mm^2$; acquisition matrix, 314×314; (2). T2WI: TR, 4,090.0 ms; TE, 99.0 ms; number of slices, 20; slice thickness, 5.0 mm; FOV, $220 \times 220\ mm^2$; acquisition matrix, 733×733; (3). T2 dark-fluid: TR, 8,000.0 ms; TE, 81.0 ms; number of slices, 20; slice thickness, 5.0 mm; FOV, $220 \times 220\ mm^2$; acquisition matrix, 314×314; (4). DWI: spin-echo echo-planar imaging sequence,

TR 2,500 ms, TE 71 ms, number of slices, 60; slice thickness, 2.2 mm; FOV, 220 × 220 mm^2, five non-zero b values (500, 1,000, 1,500, 2000, and 2,500 s/mm^2) with 30 directions for every b value, and one zero b value (b = 0 s/mm^2).

2.3 Diffusion-weighted imaging processing

Eddy current and motion correction were conducted on diffusion-weighted data using the Diffusion Kit Eddy tool[1] (Xie et al., 2016). The DWI images were processed by NeuDiLab (Diffusion Imaging in Python)[2] to obtain b = 0 s/mm^2 (b0) image and the metric maps including the DKI-based mean kurtosis (MK), the DTI-based mean diffusivity (MD) and fractional anisotropy (FA), the MAP-based mean squared displacement (MSD), *q*-space inverse variance (QIV), non-Gaussianity (NG) and return-to-origin probability (RTOP), the NODDI-based intracellular volume fraction (ICVF) and orientation dispersion index (ODI).

2.4 Image processing and analysis

The volumes of interest (VOIs) of lesions were delineated using ITK-SNAP software[3] by two neuroradiologists (K.Z. and X.M., 3 and 11 years of experience, respectively) who were blind to the diagnostic information. The VOIs of lesions were defined as abnormal hyperintense signals on the b0 image (Figure 1) and cerebrospinal fluid signals were avoided. Since the b0 images were part of the DWI sequence, it was simple to align VOIs with other metric maps (Huang et al., 2021). The mean value of each metric map was calculated by FAE[4] (Song et al., 2020).

2.5 Statistical analysis

Statistical analyses were all performed by software environment R (v4.2.0).[5] The chi-square test was used to compare the sex distribution of the patients between the two groups. The normality of the data and homogeneity of the variance were evaluated using the Shapiro–Wilk and Levene's tests, respectively. The differences of the metrics and mean age between glioma and inflammation were compared using independent *t*-test or Mann–Whitney *U* test depending on the results of test for normality and homoscedasticity. All data were expressed as the mean ± standard deviation (SD) or median (25th percentile, 75th percentile) depending on the test method. Cohen's d effect sizes were calculated to demonstrate the strength of difference between parameters in inflammation group and glioma group. A value of Cohen's d greater than 0.8 was considered as a large effect size (Ma et al., 2020). The receiver operating characteristic (ROC) curve was drawn and the area under the curve (AUC), sensitivity, specificity and accuracy were calculated to evaluate the diagnostic performance of each metric. The optimal cut-off values were selected based on the best Youden Index. Delong test was used to compare the differential diagnostic performance. Statistical significance was set at $p < 0.05$.

3 Results

3.1 Patients characteristics

The demographic characteristics and the timepoint of imaging in relation to symptom onset of included patients were summarized in Table 1. Overall, 57 participants (34 men, 23 women, mean age, 46 years; age range, 17–73 years) were included in this study (Figure 2). 24 participants were diagnosed with WHO grade 2 glioma (10 astrocytoma, 12 oligodendroglioma, 2 Not Otherwise Specified (NOS)), 11 participants were diagnosed with WHO grade 3 glioma (4 astrocytoma, 5 oligodendroglioma, 2 NOS), 4 participants were diagnosed with WHO grade 4 glioma (4 glioblastoma). 18 participants were diagnosed with brain inflammation. The average age of patients in the inflammation group is significantly higher than that of those in the glioma group ($p < 0.05$). There were no significant differences in gender or onset between two groups ($p > 0.05$).

3.2 Histogram analyses of DWI parameters

Various metrics differed significantly between glioma group and inflammation group (Table 2). MK, NG, FA, RTOP, and ICVF were significantly lower in the glioma compared with those in the inflammation ($p < 0.05$); MD, MSD, QIV were significantly higher in the glioma compared with those in the inflammation ($p < 0.05$). There were no significant differences in ODI between two groups ($p > 0.05$). Corresponding boxplots of metrics were shown in Figure 3.

3.3 Performance of diagnosis

Table 3 and Figure 4 present the results of the ROC curve analyses of diffusion metrics. The NG derived from MAP model had highest AUC value. Based on the Delong test (Table 4), a comparison of the area under the curve (AUC) for the most valuable diagnostic parameters among different models revealed NG demonstrates the highest AUC, significantly surpassing both ICVF and MD. There is no significant difference observed in AUC between NG and MK. MK follows as the second-highest, with a significant increase in AUC compared to MD. There is no significant difference in AUC between MK and ICVF. ICVF exhibits a significantly higher AUC compared to MD.

4 Discussion

Our study aimed to assess the discriminative potential of multiple diffusion metrics of diffusion-weighted imaging (DWI) in distinguishing solid glioma from inflammation. Various diffusion models, including diffusion-tensor imaging (DTI), diffusion-kurtosis imaging (DKI), neurite orientation dispersion and density imaging (NODDI), mean apparent propagator (MAP) were utilized. Our

1 https://diffusionkit.Readthedocs.io
2 http://nipy.org/dipy
3 http://www.itksnap.org/pmwiki/pmwiki.php
4 https://github.com/salan668/FAE
5 http://www.r-project.org

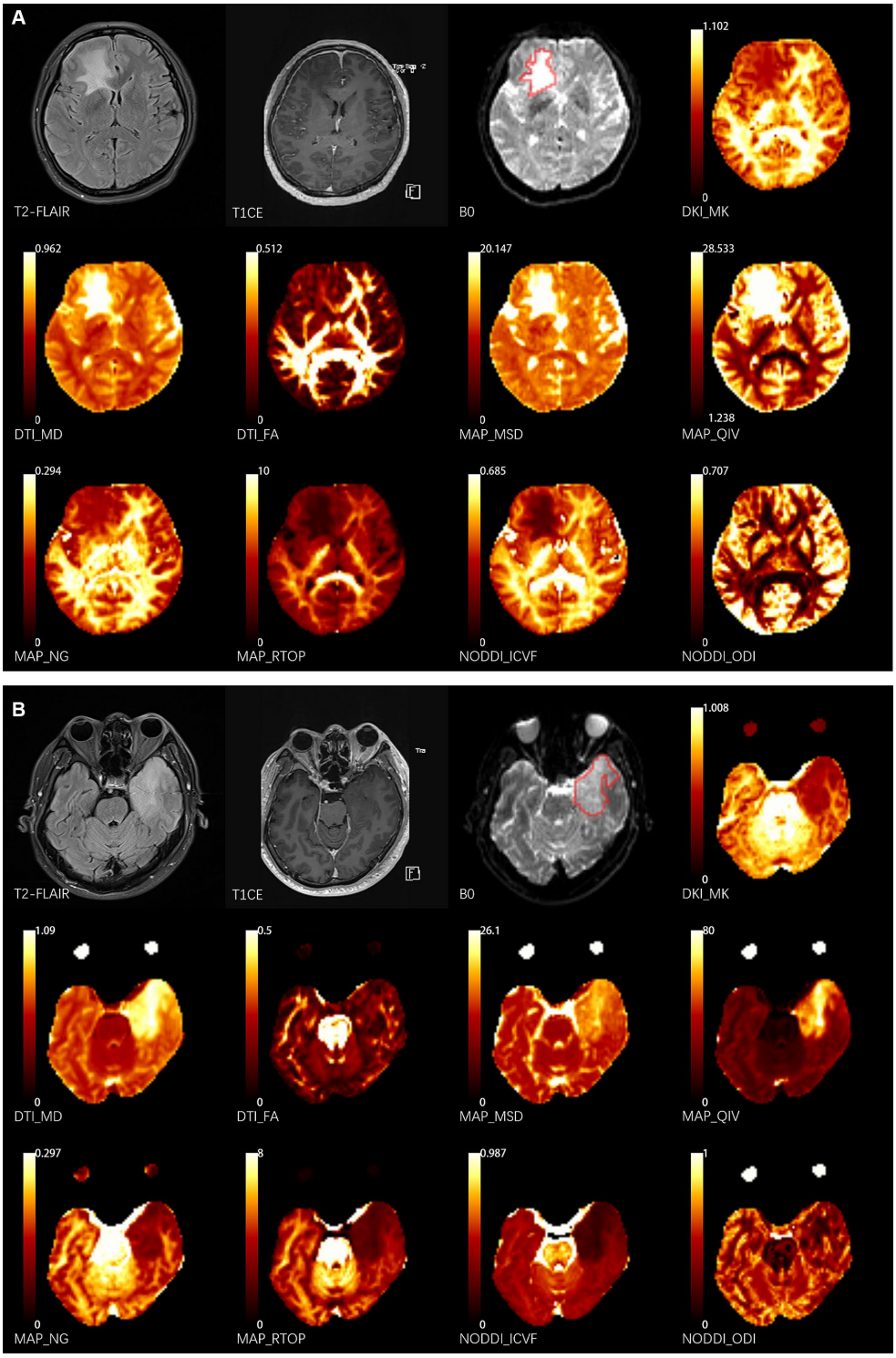

FIGURE 1
Two representative cases. The delineation of the volume of interest (VOI) is shown by the red lines on the b0 images. **(A)** 43-year-old female patient presents with NMDA-IgG positivity autoimmune encephalitis. **(B)** A 52-year-old male patient with left temporal glioblastoma (World Health Organization grade 4). T1CE, T1 weighted contrast enhancement; DKI, diffusion-kurtosis imaging; MK, mean kurtosis; DTI, diffusion-tensor imaging; MD, mean diffusivity; FA, fractional anisotropy; MAP, mean apparent propagator; MSD, Mean squared diffusion; NG, mean non-Gaussianity; RTOP, return-to-origin probability; QIV, *q*-space inverse variance; NODDI, neurite orientation dispersion and density imaging; ICVF, intracellular volume fraction; ODI, orientation dispersion index.

results demonstrated that the non-Gaussianity (NG) from MAP model may hold the greatest potential as a diffusion metric for differentiation of inflammation and glioma with the highest AUC (0.879) as well as the largest effect size (Cohen's d = −1.644).

NG quantifies diffusion heterogeneity by assessing the divergence between the spin displacement probability density function (PDF) and its Gaussian approximation. Similar to NG, mean kurtosis (MK) is a measure of the deviation of water molecule movement from a

TABLE 1 Patient characteristics.

	Total	Inflammation	Glioma	*p*
Age	46 ± 12	52 ± 10	43 ± 13	0.006
Sex				0.112
Male	34	8	26	
Female	23	10	13	
Onset				0.511
Acute (< 2 weeks)	21	7	14	
Subacute (2 weeks–3 months)	18	7	11	
Chronic (> 3 months)	18	4	14	

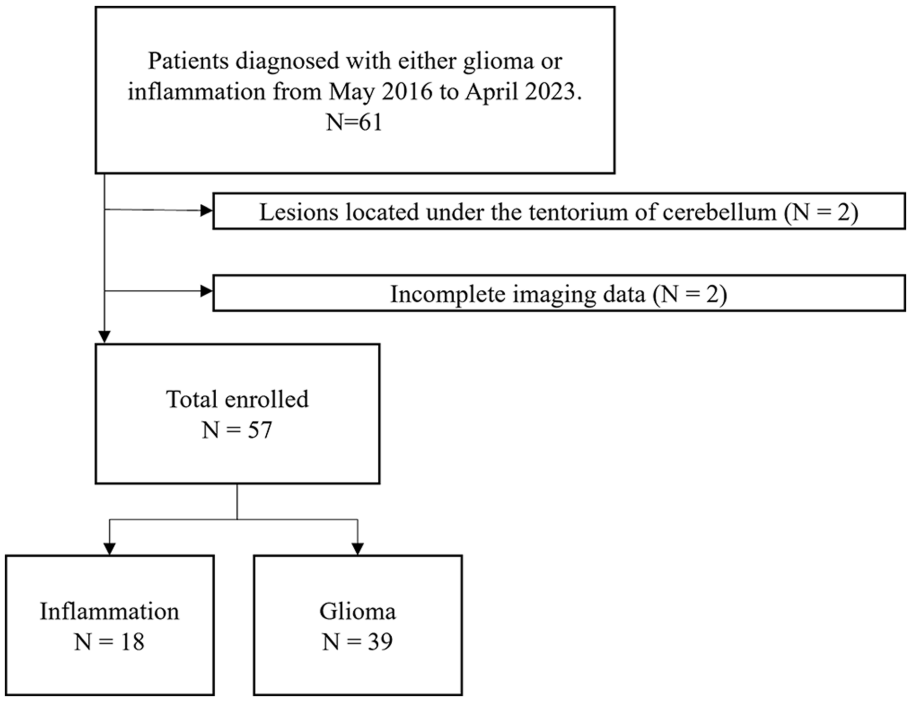

FIGURE 2
Participant selection flowchart.

TABLE 2 Mean values of diffusion metrics of inflammation and glioma.

	Inflammation	Glioma	*t*/z	*p*	Cohen's d
MK	0.669 ± 0.098	0.543 ± 0.066	5.769*	< 0.001	−1.644
FA	0.181 (0.153,0.208)	0.151 (0.126,0.172)	477	0.030	−0.693
MD	0.916 ± 0.169	1.045 ± 0.127	−3.218*	0.002	0.917
MSD	20.208 ± 2.623	21.251 ± 2.142	−1.592*	0.117	0.454
NG	0.169 (0.156,0.191)	0.118 (0.103,0.132)	617	< 0.001	−1.836
QIV	53.126 (35.598,56.28)	67.366 (55.093,81.27)	181	0.003	0.71
RTOP	2.215 (2.041,2.931)	1.699 (1.497,1.881)	558	< 0.001	−1.195
ICVF	0.273 (0.229,0.356)	0.194 (0.164,0.224)	579	< 0.001	−1.422
ODI	0.325 (0.265,0.406)	0.307 (0.289,0.355)	369	0.766	−0.432

*In line with normal distribution, independent *t*-test was adopted.

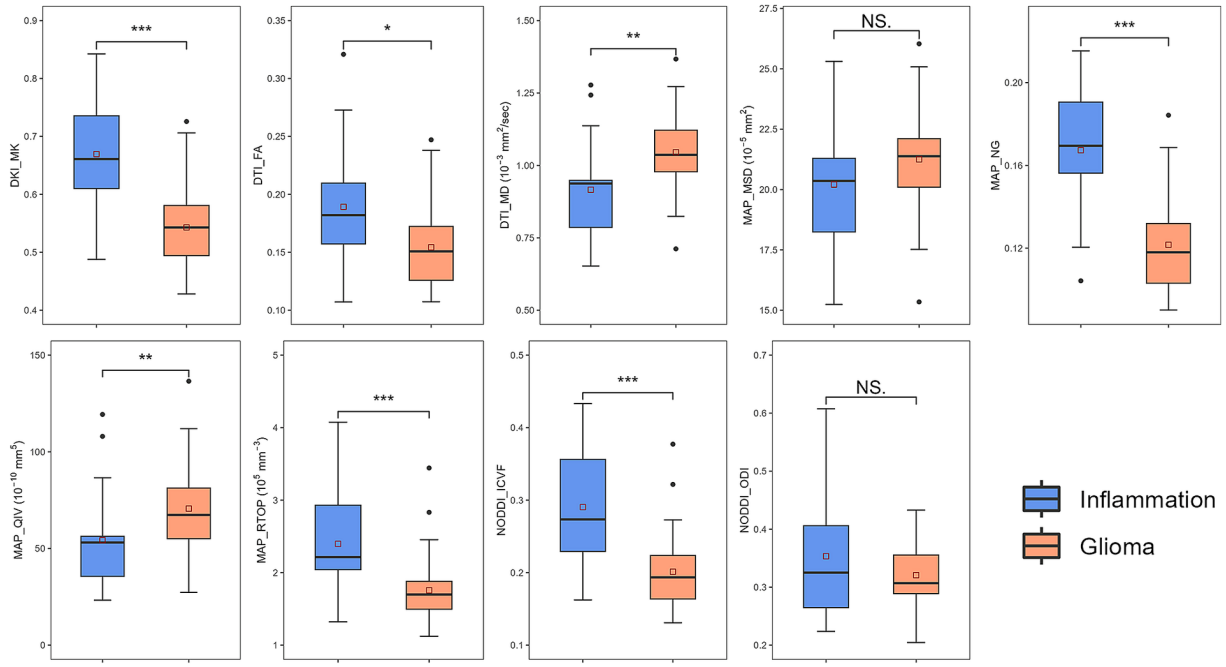

FIGURE 3
Boxplots of diffusion metrics. * represented $p = 0.01 \sim 0.05$, ** represented $p = 0.001 \sim 0.01$, *** represented $p \leq 0.001$. DKI, diffusion-kurtosis imaging; MK, mean kurtosis; DTI, diffusion-tensor imaging; MD, mean diffusivity; FA, fractional anisotropy; MAP, mean apparent propagator; MSD, Mean squared diffusion; NG, mean non-Gaussianity; RTOP, return-to-origin probability; QIV, q-space inverse variance; NODDI, neurite orientation dispersion and density imaging; ICVF, intracellular volume fraction; ODI, orientation dispersion index.

TABLE 3 ROC curve analysis of diffusion metrics for differentiation of inflammation and glioma.

	Cut-off	AUC (95%CI)	*p*	Sensitivity	Specificity	Accuracy
MK	0.600	0.855 (0.737,0.972)	< 0.001	0.778	0.872	0.842
FA	0.171	0.679 (0.516,0.843)	0.016	0.667	0.718	0.702
MD	0.962	0.758 (0.599,0.917)	< 0.001	0.778	0.769	0.772
MSD	21.3	0.647 (0.482,0.812)	0.041	0.778	0.538	0.614
NG	0.150	0.879 (0.776,0.982)	< 0.001	0.778	0.923	0.877
QIV	61.1	0.742 (0.582,0.902)	0.002	0.833	0.692	0.737
RTOP	2.01	0.795 (0.645,0.945)	< 0.001	0.778	0.846	0.825
ICVF	0.221	0.825 (0.698,0.951)	< 0.001	0.833	0.718	0.754
ODI	0.399	0.526 (0.331,0.72)	0.398	0.333	0.923	0.737

Gaussian distribution within a tissue. In biological tissues, the diffusion behavior of water molecules is often influenced by various complex factors such as cell size and membrane permeability, resulting in non-Gaussian diffusion patterns. Both higher NG and MK value indicates a greater deviation from a Gaussian distribution, suggesting a more complex and heterogeneous microstructure of the tissue (Ozarslan et al., 2013). The similar physiological significance between NG and MK may explain the comparable diagnostic performance of the two (AUC of 0.879 and 0.855, Delong test $p = 0.078$). We initially hypothesized NG and MK to be larger in glioma for more diffusion barrier (Raab et al., 2010), as histopathological studies have revealed that due to loss of contact inhibition, gliomas exhibit higher degrees of cellularity and cytological atypia compared to reactive gliosis in brain inflammation (Hewer et al., 2020). However, the results were contrary to such assumption. In glioma, both the smaller NG and MK, as well as the larger MD and MSD, have indicated a smaller diffusion barrier than inflammation. One possible explanation is that the majority of the glioma cases with atypical MRI manifestation involved low-grade glioma (LGG). Tumor cell proliferation in LGG is characterized by larger cell volume, relatively smaller density, and reduced extracellular space due to extrusion between cells (Raab et al., 2010). Consequently, the barrier restricting the diffusion of water molecules including phospholipids and macromolecular proteins becomes less (Goryawala et al., 2018). Conversely, during the course of inflammation, the reparative response of brain tissue to injury may lead to an enhancement of its structural integrity. Zhuo et al. (2012) found that reactive gliosis has been shown to be a prominent feature during recovery from brain inflammation and this process can

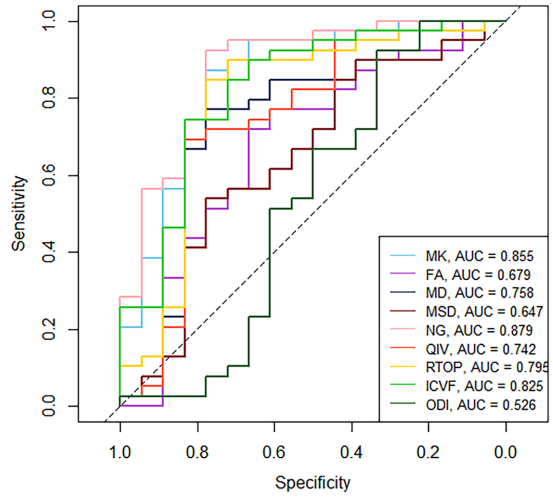

FIGURE 4
ROC curves of the diffusion metrics for distinguishing glioma from brain inflammation. MK, mean kurtosis; MD, mean diffusivity; FA, fractional anisotropy; MSD, Mean squared diffusion; NG, mean non-Gaussianity; RTOP, return-to-origin probability; QIV, q-space inverse variance; ICVF, intracellular volume fraction; ODI, orientation dispersion index.

TABLE 4 Delong test for diffusion metrics with largest AUC in each model for differentiation of inflammation and glioma.

	z	*p*
MK vs. MD	2.927	0.003
MK vs. NG	−1.762	0.078
MK vs. ICVF	1.908	0.056
MD vs. NG	−2.995	0.003
MD vs. ICVF	−2.547	0.011
NG vs. ICVF	2.315	0.021

gradually increase the value of MK, which helps to support our view. Additionally, there is a discernable difference in the cellular morphology of benign and malignant gliosis. Research (Rivera-Zengotita and Yachnis, 2012) utilizing immunohistochemistry targeting glial fibrillary acidic protein (GFAP) have demonstrated that reactive astrocytes are found in an evenly spaced pattern with multiple thin, elongated radiating glial processes that extend into the stroma. In contrast, astrocytoma cells exhibit shorter and thicker processes (Shao et al., 2016). This disparity in astrocytic morphology may result in a higher cell membrane surface area within the voxel of benign glial hyperplasia, leading to the formation of more diffusion barriers that hinder gaussian diffusion of water molecules.

Furthermore, another explanation for the less diffusion restriction in gliomas is the more severe damage inflicted upon brain tissue by gliomas compared to inflammation. ICVF in NODDI model has been confirmed by histological studies (Jespersen et al., 2010) to exhibit a correlation with myelin staining. Our study found a lower ICVF value in glioma, which may be reflective of reduced intracellular diffusivity caused by more severe neuron injury or axonal loss (Chong et al., 2021). Also, the extracellular matrix produced by glioma may be another factor that reduces the density of white matter fibers and axons (Zamecnik, 2005). In DKI model, MK value reflects the complexity and structural integrity of brain tissue (Das et al., 2017). Previous studies on the application of DKI to low-grade gliomas (Goryawala et al., 2018) and inflammation (Liu et al., 2022) have demonstrated lower radial kurtosis (RK) values in lesions in comparison to healthy controls or contralateral normal-appearing white matter, which related to the destructive impact exerted by tumor cells or inflammation on brain tissue. In our research, the values of MK in glioma were lower, suggesting more severe structural damage in glioma than inflammatory lesions. In MAP model, NG has been identified as an indicator of the organizational complexity within tissues (Ozarslan et al., 2013). Meanwhile, RTOP has been shown to decrease in response to damage of neural fibers (Jiang et al., 2021b). Besides, in a recent study by Gao et al. (2022), it was discovered that values of NG and RTOP were significantly smaller in more invasive isocitrate dehydrogenase (IDH) wild-type gliomas compared to those with IDH mutant. Given the stronger invasiveness of IDH wild-type gliomas, these MAP metrics may potentially serve as parameters to characterize differences in lesion invasiveness. The invasion behavior and infiltration of glioma cells is a crucial factor affecting the diffusion metrics.

Fractional anisotropy (FA) is widely utilized to assess the coherence of white matter fiber bundles, our investigation found that FA in glioma was lower, which may represent more severe damage to white matter fiber bundles. A study (Hiremath et al., 2017) utilizing DTI to differentiate demyelination and glioma revealed no significant differences between the solid components and peritumoral regions of the two lesion groups ($p = 0.341$ and 0.052, respectively). These findings contradict our results, which could be attributed to the small sample size employed ($n = 35$). However, the AUC and the effect size of FA in our research were relatively small (AUC = 0.679, Cohen's d = 0.693), indicating a lack of practical value (Ma et al., 2020). It is possible that the gaussian diffusion model-based limitations of FA in elucidating the intricate microstructural features of tissues may have had a bearing on this outcome (Chong et al., 2021). FA is influenced by both white matter fiber reduction and fiber crossing, which are difficult to differentiate using the DTI model, particularly in areas affected by edema (Jiang et al., 2021a). NODDI model is based on the three-compartment theory of non-Gaussian diffusion of water molecules, and it decomposes the physiological significance of FA into ICVF and orientation dispersion index (ODI) (Slattery et al., 2017). Histologically, ODI was found to be more correlated with orientation dispersion than FA, reflecting the dispersion of nerve walking, which could be used to characterize fiber crossing (Schilling et al., 2018). Results in our research showed no significant differences in Orientation Dispersion Index (ODI) between the two groups ($p = 0.766$), suggesting that fiber crossings and distortions occur in both inflammation and glioma, which limited the role of FA in characterizing white matter integrity.

In summary, non-Gaussian diffusion models, including MAP and DKI, have greater potential than NODDI and DTI for characterize the differences of microstructure, the extent of brain tissue damage and invasiveness between inflammation and glioma, thus facilitating their differential diagnosis. However, these advantages are based on technical principles and indirect results rather than direct pathological validation, highlighting the need for further research.

This study has several limitations that should be considered. Firstly, the sample size of cases with inflammation is relatively small, which may

result in biased or inaccurate results. Secondly, the imbalanced proportion of different types of cases included in the study could further exacerbate this issue. Moreover, the VOIs were manually delineated in this study. This approach lacks objectivity and may introduce errors or inconsistencies in the data analysis. Alternative methods for identifying and measuring the VOIs, such as automated segmentation algorithms, might help mitigate this limitation in future studies.

5 Conclusion

Multiple diffusion metrics is a promising approach for distinguish solid glioma from inflammation. Non-Gaussianity (NG) from mean apparent propagator (MAP) model shows the greatest potential for differentiation of inflammation and glioma.

Data availability statement

The raw data supporting the conclusions of this article will be made available by the authors, without undue reservation.

Ethics statement

The studies involving humans were approved by the First Affiliated Hospital of Zhengzhou University. The studies were conducted in accordance with the local legislation and institutional requirements. Written informed consent for participation was not required for this study in accordance with the national legislation and the institutional requirements.

Author contributions

KZ: Writing – original draft, Writing – review & editing. AG: Conceptualization, Funding acquisition, Writing – review & editing. EG: Data curation. TC: Data curation. GuZ: Software. GaZ: Data curation. PW: Software. WW: Funding acquisition. JB: Data curation. YZ: Writing – review & editing. HZ: Software. GY: Software. XM: Writing – review & editing, Funding acquisition. JC: Writing – review & editing.

Funding

The author(s) declare financial support was received for the research, authorship, and/or publication of this article. This study has received funding from the Joint Construction Project of Henan Province Medical Science and Technology Research Program (Grant No. LHGJ20230181), the Youth Project of Henan Medical Science and Technology Research Project (Grant No. SBGJ202103078), the 2021 Henan Province key research and development and promotion of special projects (scientific and technological research) (Grant No. 212102310699), the Joint construction project of Health Commission of Henan Province, China (Grant No. LHGJ20200384), and the Beijing Health Alliance Charitable Foundation, China (Grant No. HN-20201017-004).

Conflict of interest

HZ was employed by Siemens Healthineers Ltd.

The remaining authors declare that the research was conducted in the absence of any commercial or financial relationships that could be construed as a potential conflict of interest.

Publisher's note

References

Abdel Razek, A. A. K., Alksas, A., Shehata, M., Abdelkhalek, A., Abdel Baky, K., El-Baz, A., et al. (2021). Clinical applications of artificial intelligence and Radiomics in neuro-oncology imaging. *Insights Imaging* 12:152. doi: 10.1186/S13244-021-01102-6

Bo, L., Zhang, Z., Jiang, Z., Yang, C., Huang, P., Chen, T., et al. (2021). Differentiation of brain abscess from cystic glioma using conventional Mri based on deep transfer learning features and hand-crafted Radiomics features. *Front Med (Lausanne)* 8:748144. doi: 10.3389/Fmed.2021.748144

Chong, S. T., Liu, X., Kao, H. W., Lin, C. E., Hsu, C. H., Kung, Y. C., et al. (2021). Exploring Peritumoral neural tracts by using neurite orientation dispersion and density imaging. *Front. Neurosci.* 15:702353. doi: 10.3389/Fnins.2021.702353

Das, S. K., Wang, J. L., Bing, L., Bhetuwal, A., and Yang, H. F. (2017). Regional values of diffusional kurtosis estimates in the healthy brain during Normal aging. *Clin. Neuroradiol.* 27, 283–298. doi: 10.1007/S00062-015-0490-Z

Gao, A., Zhang, H., Yan, X., Wang, S., Chen, Q., Gao, E., et al. (2022). Whole-tumor histogram analysis of multiple diffusion metrics for glioma genotyping. *Radiology* 302, 652–661. doi: 10.1148/Radiol.210820

Goryawala, M. Z., Heros, D. O., Komotar, R. J., Sheriff, S., Saraf-Lavi, E., and Maudsley, A. A. (2018). Value of diffusion kurtosis imaging in assessing low-grade gliomas. *J. Magn. Reson. Imaging* 48, 1551–1558. doi: 10.1002/Jmri.26012

Han, Y., Yang, Y., Shi, Z. S., Zhang, A. D., Yan, L. F., Hu, Y. C., et al. (2021). Distinguishing brain inflammation from grade II glioma in population without contrast enhancement: a Radiomics analysis based on conventional MRI. *Eur. J. Radiol.* 134:109467. doi: 10.1016/J.Ejrad.2020.109467

Hewer, E., Phour, J., Gutt-Will, M., Schucht, P., Dettmer, M. S., and Vassella, E. (2020). TERT promoter mutation analysis to distinguish glioma from gliosis. *J. Neuropathol. Exp. Neurol.* 79, 430–436. doi: 10.1093/Jnen/Nlaa004

Hiremath, S. B., Muraleedharan, A., Kumar, S., Nagesh, C., Kesavadas, C., Abraham, M., et al. (2017). Combining diffusion tensor metrics and DSC perfusion imaging: can it improve the diagnostic accuracy in differentiating Tumefactive demyelination from high-grade glioma? *AJNR Am. J. Neuroradiol.* 38, 685–690. doi: 10.3174/Ajnr.A5089

Hodler, J., Kubik-Huch, R. A., and Von Schulthess, G. K. (2020). (Eds.) *Diseases of the brain, head and neck, spine 2020–2023: Diagnostic imaging*. Springer Nature: Cham. doi: 10.1007/978-3-030-38490-6

Huang, Z., Lu, C., Li, G., Li, Z., Sun, S., Zhang, Y., et al. (2021). Prediction of lower grade insular glioma molecular pathology using diffusion tensor imaging metric-based histogram parameters. *Front. Oncol.* 11:627202. doi: 10.3389/Fonc.2021.627202

Jespersen, S. N., Bjarkam, C. R., Nyengaard, J. R., Chakravarty, M. M., Hansen, B., Vosegaard, T., et al. (2010). Neurite density from magnetic resonance diffusion measurements at ultrahigh field: comparison with light microscopy and Electron microscopy. *NeuroImage* 49, 205–216. doi: 10.1016/J.Neuroimage.2009.08.053

Jiang, R., Hu, X., Deng, K., Jiang, S., Chen, W., and Zhang, Z. (2021a). Neurite orientation dispersion and density imaging in evaluation of high-grade glioma-induced corticospinal tract injury. *Eur. J. Radiol.* 140:109750. doi: 10.1016/J.Ejrad.2021.109750

Jiang, R., Jiang, S., Song, S., Wei, X., Deng, K., Zhang, Z., et al. (2021b). Laplacian-regularized mean apparent propagator-MRI in evaluating corticospinal tract injury in patients with brain glioma. *Korean J. Radiol.* 22, 759–769. doi: 10.3348/Kjr.2020.0949

Lapointe, S., Perry, A., and Butowski, N. A. (2018). Primary brain tumours in adults. *Lancet* 392, 432–446. doi: 10.1016/S0140-6736(18)30990-5

Liu, H., Xiang, Y., Liu, J., Feng, J., Du, S., Luo, T., et al. (2022). Diffusion kurtosis imaging and diffusion tensor imaging parameters applied to white matter and gray matter of patients with anti-N-methyl-D-aspartate receptor encephalitis. *Front. Neurosci.* 16:1030230. doi: 10.3389/Fnins.2022.1030230

Lu, J., Zhang, J. H., Miao, A. L., Yin, J. X., Zhu, D. L., Lin, X. J., et al. (2019). Brain astrocytoma misdiagnosed as anti-NMDAR encephalitis: a case report. *BMC Neurol.* 19:210. doi: 10.1186/S12883-019-1436-X

Ma, K., Zhang, X., Zhang, H., Yan, X., Gao, A., Song, C., et al. (2020). Mean apparent propagator-MRI: a new diffusion model which improves temporal lobe epilepsy lateralization. *Eur. J. Radiol.* 126:108914. doi: 10.1016/J.Ejrad.2020.108914

Nadal Desbarats, L., Herlidou, S., De Marco, G., Gondry-Jouet, C., Le Gars, D., Deramond, H., et al. (2003). Differential MRI diagnosis between brain abscesses and necrotic or cystic brain tumors using the apparent diffusion coefficient and normalized diffusion-weighted images. *Magn. Reson. Imaging* 21, 645–650. doi: 10.1016/S0730-725x(03)00084-5

Omuro, A. M., Leite, C. C., Mokhtari, K., and Delattre, J. Y. (2006). Pitfalls in the diagnosis of brain tumours. *Lancet Neurol.* 5, 937–948. doi: 10.1016/S1474-4422(06)70597-X

Ozarslan, E., Koay, C. G., Shepherd, T. M., Komlosh, M. E., Irfanoglu, M. O., Pierpaoli, C., et al. (2013). Mean apparent propagator (MAP) MRI: a novel diffusion imaging method for mapping tissue microstructure. *NeuroImage* 78, 16–32. doi: 10.1016/J.Neuroimage.2013.04.016

Piao, S., Luo, X., Bao, Y., Hu, B., Liu, X., Zhu, Y., et al. (2022). An MRI-based joint model of Radiomics and spatial distribution differentiates autoimmune encephalitis from low-grade diffuse astrocytoma. *Front. Neurol.* 13:998279. doi: 10.3389/Fneur.2022.998279

Qi, J., Wang, P., Zhao, G., Gao, E., Zhao, K., Gao, A., et al. (2022). Histogram analysis based on neurite orientation dispersion and density MR imaging for differentiation between glioblastoma Multiforme and solitary brain metastasis and comparison of the diagnostic performance of two ROI placements. *J. Magn. Reson. Imaging* 57, 1464–1474. doi: 10.1002/Jmri.28419

Raab, P., Hattingen, E., Franz, K., Zanella, F. E., and Lanfermann, H. (2010). Cerebral gliomas: diffusional kurtosis imaging analysis of microstructural differences. *Radiology* 254, 876–881. doi: 10.1148/Radiol.09090819

Rivera-Zengotita, M., and Yachnis, A. T. (2012). Gliosis versus glioma?: Don't grade until you know. *Adv. Anat. Pathol.* 19, 239–249. doi: 10.1097/Pap.0b013e31825c6a04

Sabel, M., Neuen-Jacob, E., Vogt, C., and Weber, F. (2001). Intracerebral Neurocysticercosis mimicking glioblastoma Multiforme: a rare differential diagnosis in Central Europe. *Neuroradiology* 43, 227–230. doi: 10.1007/S002340000474

Schilling, K. G., Janve, V., Gao, Y., Stepniewska, I., Landman, B. A., and Anderson, A. W. (2018). Histological validation of diffusion MRI Fiber orientation distributions and dispersion. *NeuroImage* 165, 200–221. doi: 10.1016/J.Neuroimage.2017.10.046

Shao, Z. H., Wang, G. L., Yi, X. H., and Wang, P. J. (2016). An intracranial gliosis mimicking neoplasm: a dilemma. *Iran. J. Radiol.* 13:E16785. doi: 10.5812/Iranjradiol.16785

Slattery, C. F., Zhang, J., Paterson, R. W., Foulkes, A. J. M., Carton, A., Macpherson, K., et al. (2017). ApoE influences regional white-matter axonal density loss in Alzheimer's disease. *Neurobiol. Aging* 57, 8–17. doi: 10.1016/J.Neurobiolaging.2017.04.021

Song, Y., Zhang, J., Zhang, Y. D., Hou, Y., Yan, X., Wang, Y., et al. (2020). Feature explorer (FAE): a tool for developing and comparing radiomics models. *PLoS One* 15:E0237587. doi: 10.1371/Journal.Pone.0237587

Talathi, S., Gupta, N., Reddivalla, N., Prokhorov, S., and Gold, M. (2015). Anaplastic astrocytoma mimicking herpes simplex encephalitis in 13-year old girl. *Eur. J. Paediatr. Neurol.* 19, 722–725. doi: 10.1016/J.Ejpn.2015.07.007

Wang, P., Gao, E., Qi, J., Ma, X., Zhao, K., Bai, J., et al. (2022). Quantitative analysis of mean apparent propagator-magnetic resonance imaging for distinguishing glioblastoma from solitary brain metastasis. *Eur. J. Radiol.* 154:110430. doi: 10.1016/J.Ejrad.2022.110430

Wu, W., Li, J., Ye, J., Wang, Q., Zhang, W., and Xu, S. (2021). Differentiation of glioma mimicking encephalitis and encephalitis using multiparametric MR-based deep learning. *Front. Oncol.* 11:639062. doi: 10.3389/Fonc.2021.639062

Xie, S., Chen, L., Zuo, N., and Jiang, T. (2016). Diffusionkit: a light one-stop solution for diffusion MRI data analysis. *J. Neurosci. Methods* 273, 107–119. doi: 10.1016/J.Jneumeth.2016.08.011

Zamecnik, J. (2005). The extracellular space and matrix of gliomas. *Acta Neuropathol.* 110, 435–442. doi: 10.1007/S00401-005-1078-5

Zhuo, J., Xu, S., Proctor, J. L., Mullins, R. J., Simon, J. Z., Fiskum, G., et al. (2012). Diffusion kurtosis as an *in vivo* imaging marker for reactive Astrogliosis in traumatic brain injury. *NeuroImage* 59, 467–477. doi: 10.1016/J.Neuroimage.2011.07.050

Zoccarato, M., Valeggia, S., Zuliani, L., Gastaldi, M., Mariotto, S., Franciotta, D., et al. (2019). Conventional brain MRI features distinguishing limbic encephalitis from mesial temporal glioma. *Neuroradiology* 61, 853–860. doi: 10.1007/S00234-019-02212-1

frontiers | Frontiers in Neuroimaging

TYPE Original Research
PUBLISHED 14 March 2024
DOI 10.3389/fnimg.2024.1349415

OPEN ACCESS

EDITED BY
Clemence Ligneul,
University of Oxford, United Kingdom

REVIEWED BY
Jaeseok Park,
Sungkyunkwan University, Republic of Korea
Steven Baete,
New York University, United States

*CORRESPONDENCE
Leevi Kerkelä
✉ leevi.kerkela.17@ucl.ac.uk

RECEIVED 04 December 2023
ACCEPTED 26 February 2024
PUBLISHED 14 March 2024

CITATION
Kerkelä L, Seunarine K, Szczepankiewicz F and Clark CA (2024) Spherical convolutional neural networks can improve brain microstructure estimation from diffusion MRI data. *Front. Neuroimaging* 3:1349415. doi: 10.3389/fnimg.2024.1349415

Spherical convolutional neural networks can improve brain microstructure estimation from diffusion MRI data

Leevi Kerkelä[1]*, Kiran Seunarine[1,2], Filip Szczepankiewicz[3] and Chris A. Clark[1]

[1]UCL Great Ormond Street Institute of Child Health, University College London, London, United Kingdom, [2]Department of Neurosurgery, Great Ormond Street Hospital, London, United Kingdom, [3]Medical Radiation Physics, Clinical Sciences Lund, Lund University, Lund, Sweden

Diffusion magnetic resonance imaging is sensitive to the microstructural properties of brain tissue. However, estimating clinically and scientifically relevant microstructural properties from the measured signals remains a highly challenging inverse problem that machine learning may help solve. This study investigated if recently developed rotationally invariant spherical convolutional neural networks can improve microstructural parameter estimation. We trained a spherical convolutional neural network to predict the ground-truth parameter values from efficiently simulated noisy data and applied the trained network to imaging data acquired in a clinical setting to generate microstructural parameter maps. Our network performed better than the spherical mean technique and multi-layer perceptron, achieving higher prediction accuracy than the spherical mean technique with less rotational variance than the multi-layer perceptron. Although we focused on a constrained two-compartment model of neuronal tissue, the network and training pipeline are generalizable and can be used to estimate the parameters of any Gaussian compartment model. To highlight this, we also trained the network to predict the parameters of a three-compartment model that enables the estimation of apparent neural soma density using tensor-valued diffusion encoding.

KEYWORDS

diffusion magnetic resonance imaging, geometric deep learning, microstructure, spherical convolutional neural network, MRI

1 Introduction

Neuroimaging enables non-invasively measuring functional and structural properties of the brain, and it is essential in modern neuroscience. Diffusion magnetic resonance imaging (dMRI), the most commonly used imaging modality for quantifying microstructural properties of the brain, measures displacements of water molecules at the microscopic level and is thus sensitive to tissue microstructure. dMRI has been used to localize microstructural alterations associated with, for example, learning (Sagi et al., 2012), healthy development (Lebel et al., 2019), aging (Sullivan and Pfefferbaum, 2006), neurodevelopmental disorders (Gibbard et al., 2018), and neurodegenerative diseases (Zhang et al., 2009). However, accurately inferring clinically and scientifically relevant properties of tissue microstructure (e.g., cell morphology or distribution of cell types) from the measured signals remains a highly challenging inverse problem (Kiselev, 2017).

Most dMRI data analysis methods are based on signal models that express the measured signal as a function of parameters of interest and can be fit to data by numerically minimizing an objective function (Novikov et al., 2019). An essential requirement for microstructural neuroimaging methods is low rotational variance (i.e., estimated parameters should not depend on how the subject's head is oriented in the scanner). Furthermore, it is often desirable for the parameter estimates to be independent of the orientation distribution of the microscopic structures (e.g., an estimate of axon density should not depend on whether the axons are aligned or crossing). These two requirements are often achieved by acquiring high-angular resolution diffusion imaging (HARDI) data and averaging over the diffusion encoding directions, which is referred to as "powder-averaging", a term borrowed from the field of solid-state nuclear magnetic resonance (NMR). The number of acquisition directions required for a nearly rotationally invariant powder-averaged signal depends on the properties of tissue microstructure and diffusion encoding (Szczepankiewicz et al., 2019a). Fitting models to powder-averaged signals is often referred to as the "spherical mean technique" (SMT), a term introduced by Kaden et al. (2016b). While powder-averaging enables the estimation of various microstructural parameters (Jespersen et al., 2013; Lasič et al., 2014; Kaden et al., 2016a,b; Szczepankiewicz et al., 2016; Henriques et al., 2020; Palombo et al., 2020; Gyori et al., 2021), a significant amount of information is lost during averaging. Therefore, it may be beneficial to estimate the parameters directly from full data without powder-averaging.

In recent years, microstructural parameter estimation using machine learning (ML) has received significant attention as a potential solution to issues with conventional fitting, such as slow convergence, poor noise robustness, and terminating at local minima (Golkov et al., 2016; Barbieri et al., 2020; Palombo et al., 2020; de Almeida Martins et al., 2021; Elaldi et al., 2021; Gyori et al., 2021, 2022; Karimi et al., 2021; Sedlar et al., 2021a,b; Kerkelä et al., 2022). ML models can be trained to predict microstructural parameter values from data using supervised or self-supervised learning. In the context of dMRI, a particularly promising development has been the invention of spherical convolutional neural networks (sCNNs) (Cohen et al., 2018; Esteves et al., 2018). sCNNs are SO(3)-equivariant (i.e., rotating the input changes the output according to the same rotation) artificial neural networks that perform spherical convolutions with learnable filters. They theoretically enable rotationally invariant classification and regression, making them potentially well-suited for predicting microstructural parameters from dMRI data.

This study aimed to investigate if sCNNs can improve microstructural parameter estimation. We focused on estimating the parameters of a constrained two-compartment model by Kaden et al. (2016a) regularly used in neuroscience to study human white matter *in vivo* (Collins et al., 2019; Toescu et al., 2021; Voldsbekk et al., 2021; Battocchio et al., 2022; Rahmanzadeh et al., 2022). An sCNN implemented according to Esteves et al. (2018) was trained to predict the neurite orientation distribution function (ODF) and scalar parameters (neurite diffusivity and density) from dMRI data. Training and testing were done using simulated data. The sCNN was compared to conventional fitting and a multi-layer perceptron (MLP) in terms of accuracy and orientational variance. The trained model was then applied to MRI data acquired in a clinical setting to generate microstructural maps. Furthermore, to highlight the fact that the sCNN and training pipeline are applicable to any Gaussian compartment model, the network was trained to estimate the parameters of a constrained three-compartment model by Gyori et al. (2021) that enables the estimation of apparent neural soma density using tensor-valued diffusion encoding (Topgaard, 2017).

2 Materials and methods

2.1 Spherical harmonics

Any square-integrable function on the sphere $f : S^2 \to \mathbb{C}$ can be expanded in the spherical harmonic basis:

$$f(\mathbf{x}) = \sum_{l=0}^{b} \sum_{m=-l}^{l} \hat{f}_l^m Y_l^m(\mathbf{x}), \tag{1}$$

where $\mathbf{x}$ is a point on the unit sphere, b is the bandwidth of f, l is the degree, m is the order, $\hat{f}_l^m$ is an expansion coefficient, and Y_l^m is a spherical harmonic defined as

$$Y_l^m(\theta, \phi) = \sqrt{\frac{2l+1}{4\pi} \frac{(l-m)!}{(l+m)!}} P_l^m(\cos\theta) e^{im\phi}, \tag{2}$$

where $\theta \in [0, \pi]$ is the polar coordinate, $\phi \in [0, 2\pi)$ is the azimuthal coordinate, and P_l^m is the associated Legendre function.

The expansion coefficients are given by the spherical Fourier transform (SFT):

$$\hat{f}_l^m = \int_{S^2} \mathrm{d}\mathbf{x} f(\mathbf{x}) \bar{Y}_l^m(\mathbf{x}). \tag{3}$$

SFT of a band-limited function can be computed exactly as a finite sum using a sampling theorem (Driscoll and Healy, 1994). Equation 1 is the inverse spherical Fourier transform (ISFT).

Since reconstructed dMRI signals are real-valued and antipodally symmetric, we use the following basis:

$$S_l^m = \begin{cases} 0 & \text{if } l \text{ is odd} \\ \sqrt{2}\,\Im\left(Y_l^{-m}\right) & \text{if } m < 0 \\ Y_l^0 & \text{if } m = 0 \\ \sqrt{2}\,\Re\left(Y_l^m\right) & \text{if } m > 0 \end{cases}. \tag{4}$$

Considering that diffusion encoding directions do not usually follow a sampling theorem like the one by Driscoll and Healy (1994) that enables SFT to be exactly computed as a finite sum, we use least squares to compute the expansion coefficients: Indexing $j = \frac{1}{2}l(l+1) + m$ assigns a unique index j to every pair l, m. Given f sampled at points $\mathbf{x}_1, \mathbf{x}_2, ..., \mathbf{x}_{n_{\text{points}}}$ stored in a column vector $\mathbf{X}$, the values of the spherical harmonics sampled at the same points are organized in a $n_{\text{points}} \times n_{\text{coefficients}}$ matrix $\mathbf{B}$ where $B_{ij} = S_l^m(\mathbf{x}_i)$. $\left(\mathbf{B}^{\mathrm{T}}\mathbf{B}\right)^{-1}\mathbf{B}^{\mathrm{T}}\mathbf{X}$ gives a vector containing the expansion coefficients minimizing the Frobenius norm (Brechbühler et al., 1995).

2.2 Spherical convolution

Convolution of a spherical signal f by a spherical filter h is defined as

$$(f * h)(\mathbf{x}) = \int_{SO(3)} d\mathbf{R}\, f(\mathbf{R}\hat{\mathbf{e}}_3) h(\mathbf{R}^{-1}\mathbf{x}), \tag{5}$$

where $\hat{\mathbf{e}}_3$ is a unit vector aligned with the z-axis. If f and h are band-limited, the above equation can be evaluated efficiently as a pointwise product in the frequency domain (Driscoll and Healy, 1994). The spherical harmonic coefficients of the convoluted signal y are

$$\hat{y}_l^m = 2\pi \sqrt{\frac{4\pi}{2l+1}} \hat{f}_l^m \hat{h}_l^0. \tag{6}$$

Spherical convolution is equivariant to rotations (i.e., $\mathbf{R}(f*h) = (\mathbf{R}f) * h$ for all $\mathbf{R} \in \mathrm{SO}(3)$) and the filter is marginalized around the z-axis (i.e, for every h, there exists a filter h_z that is symmetric with respect to the z-axis so that $f * h = f * h_z$).

2.3 Compartment models

Compartment models represent the dMRI signal as a sum of signals coming from different microstructural environments (e.g., intra- and extra-axonal water). For details, see, for example, the review by Jelescu and Budde (2017). Here, we focus on models with non-exchanging Gaussian compartments following an ODF. The signal measured along $\hat{\mathbf{n}}$ is expressed as a spherical convolution of the ODF by a microstructural kernel response function K:

$$S(\hat{\mathbf{n}}) = \int_{SO(3)} d\mathbf{R}\, \mathrm{ODF}(\mathbf{R}\hat{\mathbf{e}}_3) K(\mathbf{R}^{-1}\hat{\mathbf{n}}), \tag{7}$$

where K is the microstructural kernel response function:

$$K(\hat{\mathbf{n}}) = S_0 \left[\sum_{i=1}^{N} f_i \exp(-\mathbf{b} : \mathbf{D}_i) \right], \tag{8}$$

where S_0 is the signal without diffusion-weighting, N is the number of compartments, f_i is a signal fraction, $\mathbf{b}$ is the b-tensor corresponding to $\hat{\mathbf{n}}$ and a b-value equal to $\mathrm{Tr}(\mathbf{b})$, : denotes the generalized scalar product ($\mathbf{b} : \mathbf{D} = \sum_{i=1}^{3}\sum_{j=1}^{3} b_{ij}D_{ij}$) (Westin et al., 2016), and $\mathbf{D}_i$ is an axially symmetric diffusion tensor aligned with the z-axis representing Gaussian diffusion in the compartment. The training pipeline presented in this paper is applicable to any compartment model that can be expressed using Equations 7 and 8. Given a different data generation method, the sCNN can be trained to predict the parameters of non-Gaussian models as well.

2.3.1 Two-compartment model

The so-called "standard model" of diffusion in white matter consists of a one-dimensional compartment representing diffusion inside neurites and a coaxial axially symmetric extra-cellular compartment (Novikov et al., 2019). We focus on a constrained version of the model by Kaden et al. (2016a) that enables model parameters to be estimated from powder-averaged data using the SMT. The model contains two parameters: intra-neurite diffusivity d and intra-neurite signal fraction f. Axial and radial diffusivities of the extra-cellular compartment are d and $(1-f)d$, respectively. Inserting this into Equation 8 gives

$$K(\hat{\mathbf{n}}) = S_0 \left[f \exp\left(-\mathbf{b} : \begin{bmatrix} 0 & 0 & 0 \\ 0 & 0 & 0 \\ 0 & 0 & d \end{bmatrix} \right) + (1-f) \exp\left(-\mathbf{b} : \begin{bmatrix} (1-f)d & 0 & 0 \\ 0 & (1-f)d & 0 \\ 0 & 0 & d \end{bmatrix} \right) \right]. \tag{9}$$

2.3.2 Spherical mean technique

Kaden et al. (2016b) observed that for a fixed b-value, the spherical mean of the dMRI signal over the gradient directions does not depend on the ODF. By exploiting this invariance, the constrained two-compartment model can be fit to powder-averaged data, denoted by S_{PA} here, using the following signal equation (Kaden et al., 2016a):

$$S_{\mathrm{PA}} = S_0 \left[f \frac{\sqrt{\pi}\,\mathrm{erf}\left(\sqrt{bd}\right)}{2\sqrt{bd}} + (1-f) e^{-b(1-f)d} \frac{\sqrt{\pi}\,\mathrm{erf}\left(\sqrt{bfd}\right)}{2\sqrt{bfd}} \right]. \tag{10}$$

2.3.3 Three-compartment model

Palombo et al. (2020) added a spherical compartment representing neural soma to the standard model to make it more suitable for gray matter. We use a constrained three-compartment model by Gyori et al. (2021) that uses tensor-valued diffusion encoding to make apparent neural soma imaging more feasible without high-performance gradient hardware. The model contains four parameters: intra-neurite diffusivity d_{i}, intra-neurite signal fraction f_{i}, spherical compartment diffusivity d_{sph}, and spherical compartment signal fraction f_{sph}. Axial and radial diffusivities of the extra-cellular compartment are $d_{\mathrm{i}}(1-f_{\mathrm{i}}-f_{\mathrm{sph}})^{\frac{1}{2}f_{\mathrm{sph}}/(f_{\mathrm{sph}}+f_{\mathrm{i}})}$ and $d_{\mathrm{i}}(1-f_{\mathrm{i}}-f_{\mathrm{sph}})^{(\frac{1}{2}f_{\mathrm{sph}}+f_{\mathrm{i}})/(f_{\mathrm{sph}}+f_{\mathrm{i}})}$, respectively. We omit explicitly writing out the kernel signal equation to save space, but it is trivial to construct from Equation 8.

2.4 Simulations

Simulated training data was generated by evaluating Equation 7 in the frequency domain according to Equation 6. The response function values were evaluated along 3072 directions uniformly distributed over the surface of the sphere according to the hierarchical equal area isolatitude pixelisation (HEALPix) (Gorski et al., 2005; Zonca et al., 2019) and expanded in the spherical harmonics basis. Rician noise was added to the simulated signals:

$$S_{\mathrm{noisy}} = \sqrt{(S+X)^2 + Y^2}, \tag{11}$$

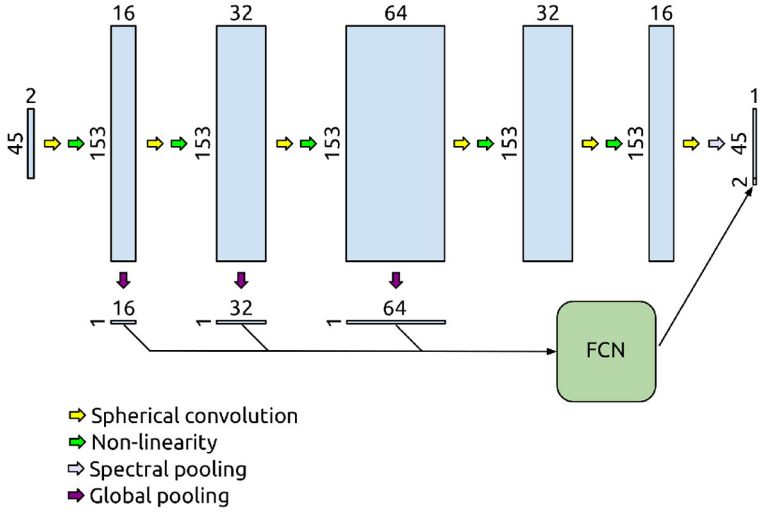

FIGURE 1
Network for two-compartment model parameter prediction. The input is normalized two-shell data expanded using spherical harmonics up to degree eight. The signals undergo spherical convolutions, non-linearities, and spectral pooling to produce the predicted orientation distribution function. After the initial three convolutions, global mean pooling is applied in the signal domain, and the resulting arrays are concatenated to create a nearly rotationally invariant feature vector passed on to the FCN that outputs the predicted scalar parameter.

TABLE 1 Mean squared error of the estimated two-compartment model parameters on the test dataset.

Method	ODF	d (μm^2/ms)	f
sCNN	$2.76 \cdot 10^{-3}$	$3.08 \cdot 10^{-3}$	$\mathbf{3.23 \cdot 10^{-3}}$
sCNN*	$2.75 \cdot 10^{-3}$	$\mathbf{3.07 \cdot 10^{-3}}$	$\mathbf{3.23 \cdot 10^{-3}}$
SMT	$6.47 \cdot 10^{-3}$	$10.92 \cdot 10^{-3}$	$37.50 \cdot 10^{-3}$
MLP	$2.71 \cdot 10^{-3}$	$4.00 \cdot 10^{-3}$	$3.70 \cdot 10^{-3}$
MLP*	$\mathbf{2.70 \cdot 10^{-3}}$	$4.00 \cdot 10^{-3}$	$3.63 \cdot 10^{-3}$

Deep learning-based parameter estimation outperformed the spherical mean technique. The asterisk (*) refers to models trained with randomly rotated training data. The lowest values are highlighted in bold.

where S is the simulated signal without noise and X and Y are sampled from a normal distribution with zero mean and standard deviation of 1/SNR, where SNR is the signal-to-noise ratio. SNR was matched to the mean SNR in the imaging experiments.

2.5 Network architecture

Our sCNN, visualized in Figure 1, consists of six spherical convolution layers implemented according to Esteves et al. (2018) without enforcing localized filters. The network takes the expansion coefficients in the frequency domain as input and outputs the estimated ODF and scalar model parameters. The number of input channels is equal to the number of shells in data. Each spherical convolution layer is followed by a leaky (slope is 0.1 for negative values) rectified linear unit (ReLU) applied in the spatial domain. The conversion between frequency and spatial domains is done using the 3072 HEALPix directions. Spherical harmonics up to degree 16 are used in the network because the non-linearity can increase signal bandwidth. Spectral pooling discards coefficients of the highest degrees. After the initial three convolutions, global mean pooling is applied in the spatial domain, and the resulting arrays are concatenated and passed to the fully connected network (FCN) that outputs the predicted scalar parameter. The FCN consists of three hidden layers with 128 units each. The first two layers of the FCN are followed by batch normalization (Ioffe and Szegedy, 2015) and a ReLU. The sCNN for estimating the two-compartment model parameters has 78,258 trainable parameters.

2.6 Training

Training was done over 10^5 batches of simulated data generated during training. Each batch contained signals from 500 microstructural configurations produced by random sampling ($d \sim U(0, 3\ \mu\text{m}^2/\text{ms})$ and $f \sim U(0, 1)$). ODFs were sampled from five volunteer scans. Validation and test datasets were constructed similarly, except that they contained 10^4 and 10^6 microstructural configurations, respectively, and the ODFs were sampled from different volunteer scans. Training was performed twice: with and without randomly rotating the ODFs. The ODFs in the validation and test datasets were randomly rotated. ADAM (Kingma and Ba, 2014) was the optimizer with an initial learning rate of 10^{-3}, which was reduced by 90% after 50% and 75% into the training. Mean squared error (MSE) was the loss function. ODF MSE was calculated in the spatial domain.

2.7 Baseline methods

The sCNN was compared to the SMT and an MLP that takes the normalized dMRI signals as inputs and outputs the

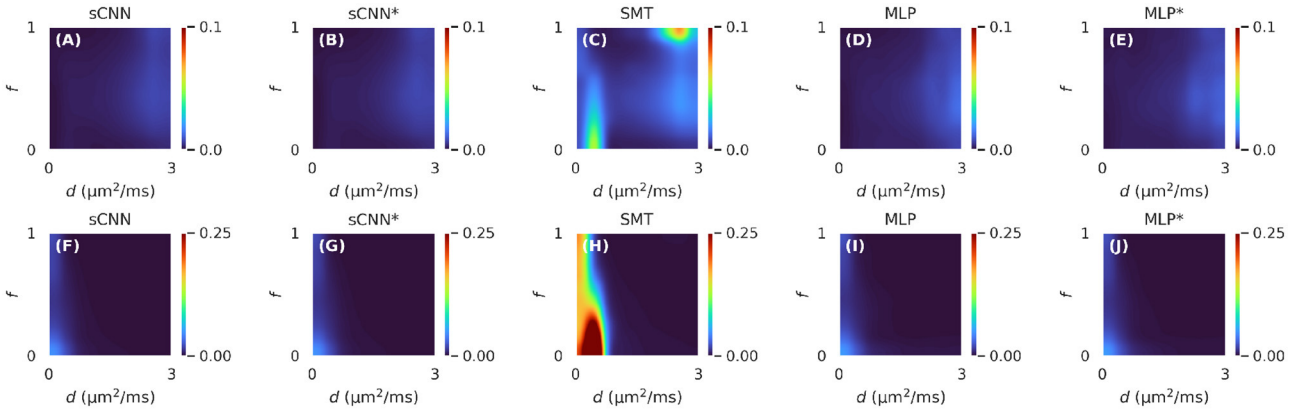

FIGURE 2
Mean squared error of the estimated two-compartment model parameters on the test dataset for different values of intra-neurite diffusivity (d) and intra-neurite signal fraction (f). The first row **(A–E)** shows the results for d and the second row **(F–J)** shows the results for f. Deep learning-based methods outperformed the spherical mean technique in all parts of the parameter space. The asterisk (*) refers to models trained with randomly rotated training data.

TABLE 2 Average standard deviation of the estimated two-compartment model parameters over rotations of the input signals.

Method	d (μm²/ms)	f
sCNN	$0.23 \cdot 10^{-3}$	$0.13 \cdot 10^{-3}$
sCNN*	$0.18 \cdot 10^{-3}$	$\mathbf{0.09 \cdot 10^{-3}}$
SMT	$\mathbf{0.14} \cdot 10^{-3}$	$0.25 \cdot 10^{-3}$
MLP	$20.30 \cdot 10^{-3}$	$14.40 \cdot 10^{-3}$
MLP*	$17.23 \cdot 10^{-3}$	$12.78 \cdot 10^{-3}$

The asterisk (*) refers to models trained with randomly rotated training data. The lowest values are highlighted in bold.

spherical harmonic coefficients of the ODF and the model parameters. The SMT parameter estimation and the subsequent ODF estimation using the estimated microstructural kernel and constrained spherical deconvolution (CSD) was done using Dmipy (Fick et al., 2019). The MLP consisted of three hidden layers with 512 nodes each. The hidden layers were followed by batch normalization and a ReLU. The MLP had 614,447 trainable parameters. It was trained like the sCNN, except ten times more batches were used to account for the higher number of parameters and ensure convergence.

2.8 Imaging data

The brains of eight healthy adult volunteers were scanned on a Siemens Magnetom Prisma 3T (Siemens Healthcare, Erlangen, Germany) at Great Ormond Street Hospital, London, United Kingdom. Data was denoised (Veraart et al., 2016) using MRtrix3 (Tournier et al., 2019) and distortion- and motion-corrected using FSL (Jenkinson et al., 2012; Andersson and Sotiropoulos, 2016). SNR was estimated in each voxel as the inverse of the standard deviation of the normalized signals without diffusion-weighting.

2.8.1 High-angular resolution diffusion imaging

Seven volunteers were scanned using a standard clinical two-shell HARDI protocol with two non-zero b-values of 1 and 2.2 ms/μm^2 with 60 directions over half a sphere each. Other relevant scan parameters were the following: diffusion time (Δ) = 28.7 ms; diffusion encoding time (δ) = 16.7 ms; echo time (TE) = 60 ms; repetition time (TR) = 3,050 ms; field of view (FOV) = 220 × 220 ms; voxel size = 2 × 2 × 2 mm^3; slice gap = 0.2 mm; 66 slices; phase partial Fourier = 6/8; multiband acceleration factor = 2. Fourteen images were acquired without diffusion-weighting, one of which had the phase encoding direction reversed to be used to correct for susceptibility-induced distortions. The total scan time was 7 minutes. Mean SNR in the brain was 50. Neurite ODFs were estimated using multi-tissue CSD (Jeurissen et al., 2014) with $l_{max} = 8$.

2.8.2 Tensor-valued diffusion imaging

One volunteer was scanned using a prototype spin echo sequence that enables tensor-valued diffusion encoding (Szczepankiewicz et al., 2019a). Data was acquired using numerically optimized (Sjölund et al., 2015) and Maxwell-compensated (Szczepankiewicz et al., 2019b) gradient waveforms encoding linear and planar b-tensors. The acquisitions with linear b-tensors were performed with b-values of 0.5, 1, 2, 3.5, and 5 ms/μm^2 with 12, 12, 20, 20, and 30 directions over half a sphere, respectively. The acquisitions with planar b-tensors were performed with b-values of 0.5, 1, and 2 ms/μm^2 with 12, 12, and 20 directions over half a sphere, respectively. Other relevant scan parameters were the following: TE = 82 ms; TR = 4.2 s; FOV = 220 × 220 ms; voxel size = 2 × 2 × 2 mm^3; slice gap = 0.2 mm; 66 slices; phase partial Fourier = 6/8; multiband acceleration factor = 2. Fourteen images were acquired without diffusion-weighting, one of which had the phase encoding direction reversed. The total scan time was 12 minutes. Mean SNR in the brain was 29.

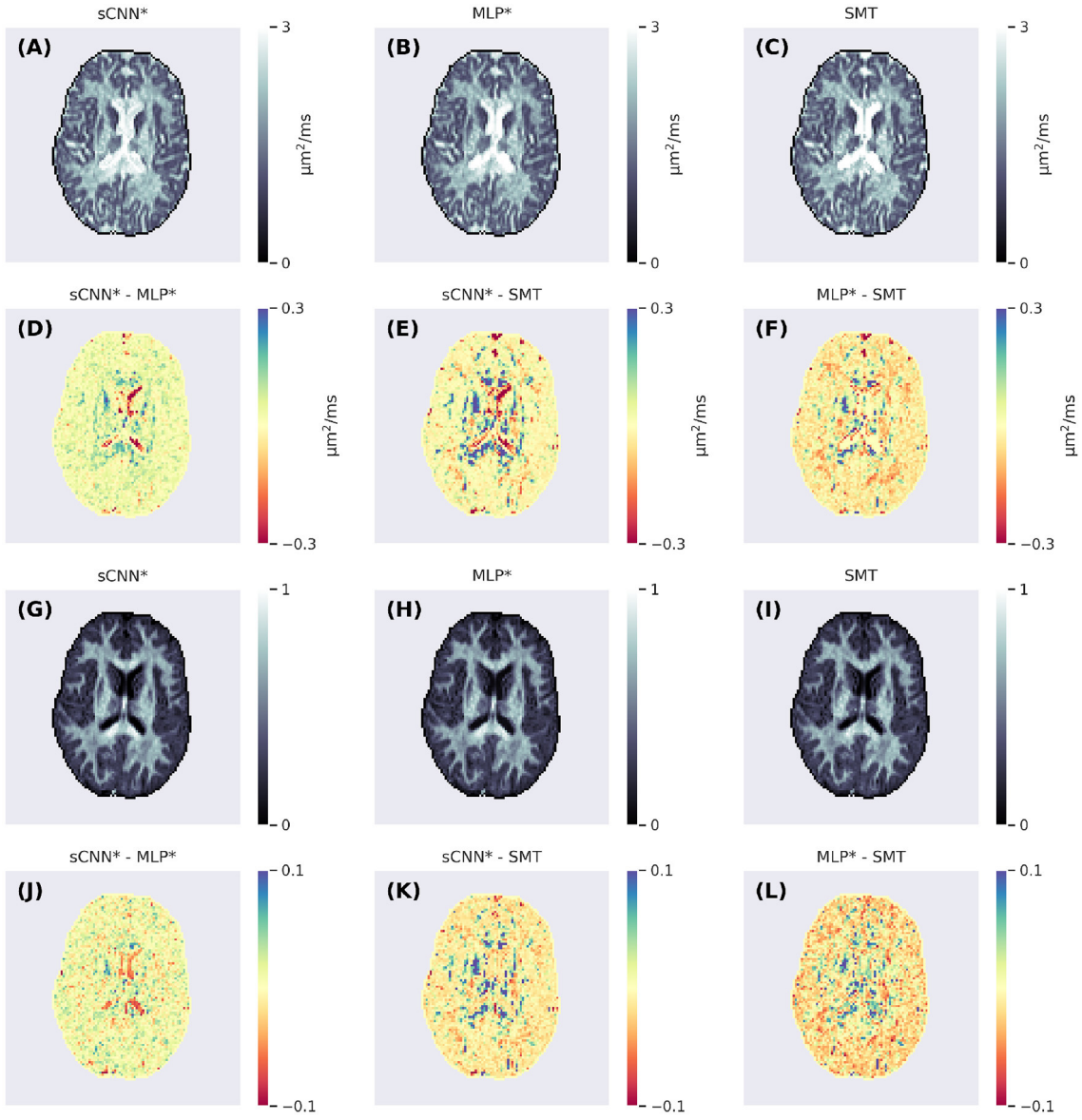

FIGURE 3
Axial slices of the intra-neurite diffusivity **(A–C)** and intra-neurite signal fraction **(G–I)** maps generated using the spherical convolutional neural network, multi-layer perceptron, and spherical mean technique. The second row **(D–F)** shows the differences between the intra-neurite diffusivity maps and the fourth row **(J–L)** shows the differences between the intra-neurite signal fraction maps.

3 Results

3.1 Two-compartment model

3.1.1 Prediction accuracy

MSE on the test dataset is reported in Table 1. The sCNN and MLP outperformed the SMT in estimating the ODF and scalar parameters. The sCNN predicted d and f the best while the MLP was predicted the ODF marginally better than the sCNN. Both the sCNN and MLP benefited slightly from randomly rotating the training data. Figure 2 shows how prediction accuracy depends on the values of d and f. The sCNN and MLP outperformed the SMT in all parts of the parameter space. Although the largest errors with the SMT occurred for values of d and f not typically observed in the brain, ML-based approaches were more accurate for values observed in the brain (i.e., d roughly between 1 and 2 $\mu m^2/ms$).

3.1.2 Rotational variance

The rotational variance of the different methods was assessed by generating signals from 10^3 random microstructural configurations rotated over 729 rotations given by the SO(3) sampling theorem by Kostelec and Rockmore (2008). No noise was added to the signals to exclude the effects of noise. The average standard deviation of the estimated parameters from the rotated data are shown in Table 2. The sCNN and SMT were much less sensitive to rotations than the MLP. The SMT had the lowest

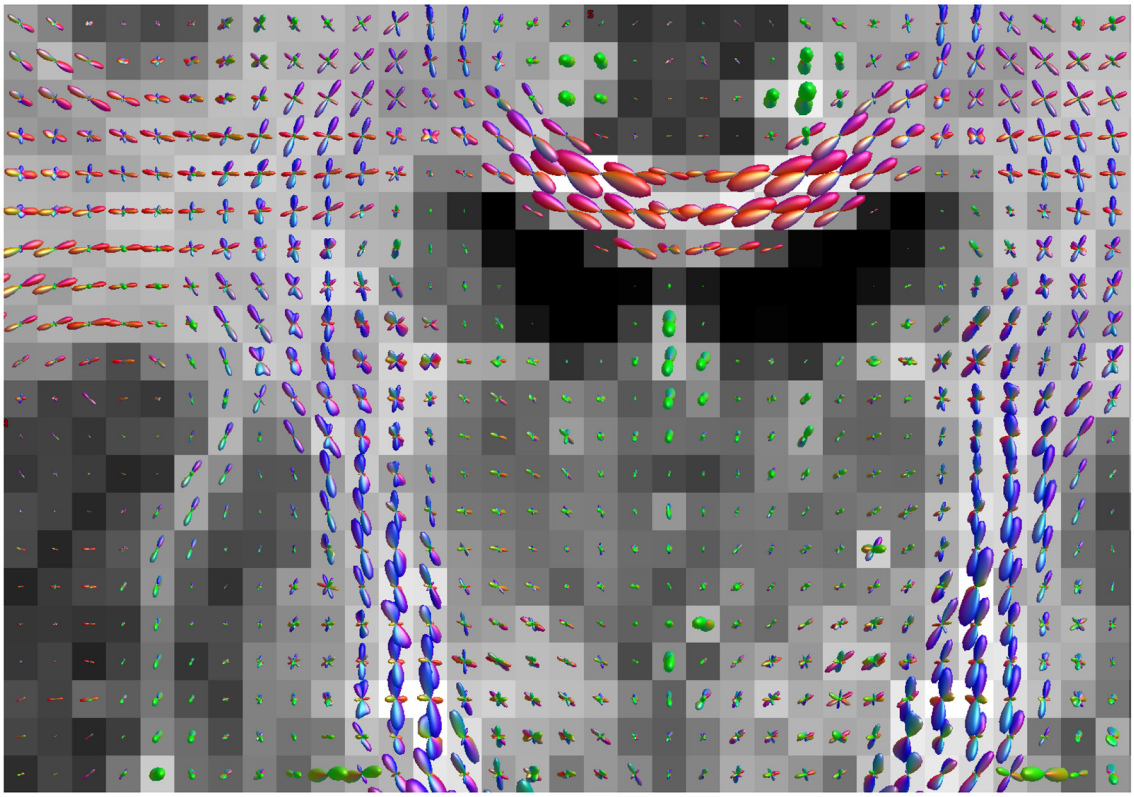

FIGURE 4
Neurite orientation distribution functions overlaid on a map of intra-neurite signal fraction generated by the spherical convolutional neural network trained with randomly rotating the training data. The color represents the principal direction, and the size is scaled according to neurite density. This coronal slice shows the intersection of the corticospinal tract and the corpus callosum.

rotational variance for d, and the sCNN had the lowest rotational variance for f. However, the SMT's non-zero rotational variance was driven by low values of d or f for which the fit is unstable. For values typically observed in white matter, the SMT's estimates' standard deviation was three orders of magnitude smaller than the average. Data augmentation by rotating the input signals improved prediction accuracy for both the sCNN and MLP. However, the sCNN was much less rotationally variant even without data augmentation than the MLP was with data augmentation.

3.1.3 Application on real imaging data

Figure 3 shows parameter maps generated using the three methods. The maps produced by the ML-based methods appear less noisy. Overall, the sCNN estimated d to be greater than the MLP (mean difference = $2.4 \cdot 10^{-2}$ $\mu m^2/ms$; std of difference = $8.1 \cdot 10^{-2}$ $\mu m^2/ms$) and SMT (mean difference = $0.9 \cdot 10^{-2}$ $\mu m^2/ms$; std of difference = $12.7 \cdot 10^{-2}$ $\mu m^2/ms$). However, in the CSF the sCNN tended to estimate d to be less than the MLP or SMT. Overall, the sCNN estimated f to be greater than the MLP (mean difference = $0.5 \cdot 10^{-2}$; std of difference = $3.6 \cdot 10^{-2}$) and SMT (mean difference = $0.1 \cdot 10^{-2}$; std of difference = $4.5 \cdot 10^{-2}$) while exhibiting a similar yet lesser tissue-dependent pattern as d. Figure 4 shows example ODFs generated by the trained sCNN.

3.2 Three-compartment model

To highlight the fact that the network and training pipeline are applicable to any Gaussian compartment models, the sCNN was trained to predict the three-compartment model parameters the same way as with the two-compartment model. Informed by the two-compartment model results, the network was trained with randomly rotated training data. $d_i \sim U(0, 3\ \mu m^2/ms)$, $f_i \sim U(0, 1)$, $d_{sph} \sim U(0, max(d_i, 0.5\ \mu m^2/ms))$, and $f_{sph} \sim U(0, 1 - f_i)$. The upper limit of d_{sph} was chosen to correspond to a sphere with a diameter of 25 μm using the Monte Carlo simulator Disimpy (Kerkelä et al., 2020). Figure 5 shows maps that the sCNN generated from preprocessed dMRI data.

4 Discussion

The primary purpose of this study was to investigate whether sCNNs can improve microstructural parameter estimation from noisy dMRI data, focusing on a constrained two-compartment model widely used in neuroscience research to study human white matter *in vivo*. The sCNN demonstrated superior accuracy with similar rotational variance compared to the SMT, and exhibited similar accuracy but considerably lower rotational variance than the MLP that had significantly more trainable parameters. Our results show that sCNNs can offer substantial benefits over

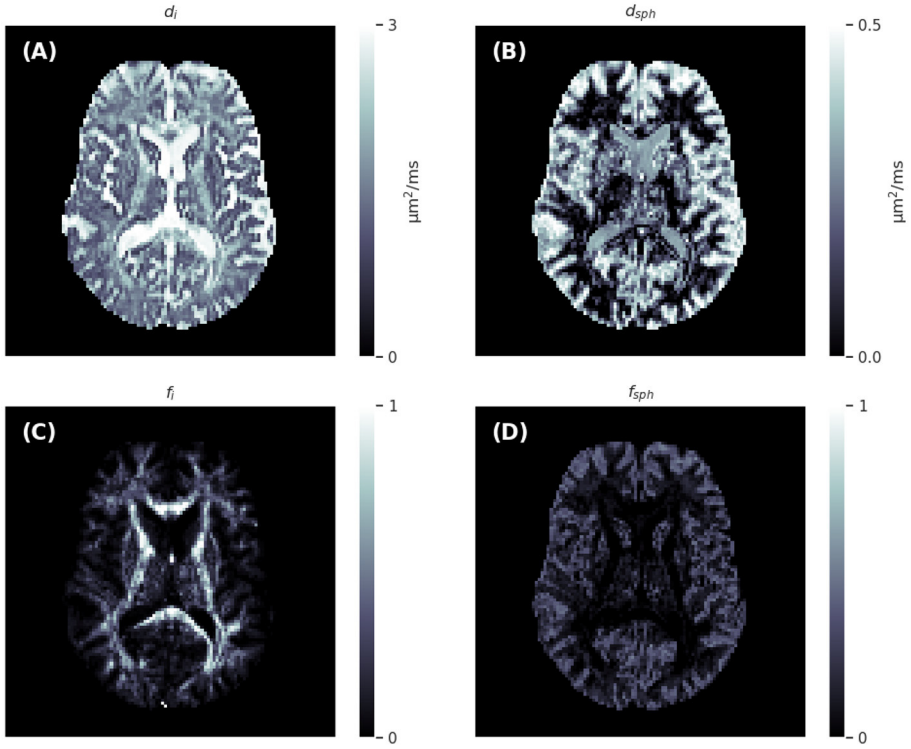

FIGURE 5
Axial slices of the intra-neurite diffusivity **(A)**, spherical compartment diffusivity **(B)**, intra-neurite signal fraction **(C)**, and spherical compartment signal fraction **(D)** maps generated by the spherical convolutional neural network trained with randomly rotating the training data.

simpler artificial neural network architectures for ML-based microstructural parameter estimation from dMRI data.

We focused on comparing neural network architectures with a fixed training strategy, using the SMT as a baseline. Previous research by Gyori et al. (2022) has highlighted the significant impact of training data distribution on neural network predictions, which affects the performance of our sCNN when applied to real imaging data. We are aware of this limitation, and in future work, we aim to optimize the training data distribution. Another relevant key takeaway from the work by Gyori et al. (2022) is that at low SNR, ML-based parameter estimation can suffer from high bias, which manifests as maps that appear exceedingly smooth. Moreover, it is important to note the general limitation of microstructural models that deviations from model assumptions can lead to inaccuracies (Lampinen et al., 2017; Henriques et al., 2019; Kerkelä et al., 2021).

When it comes to training the sCNN, while it is crucial to sample the space of possible ODFs as exhaustively as possible during training, the MLP training requirements are even more demanding since its rotational variance can only be reduced through learning. Changes in b-values or the angular resolution of shells will necessitate retraining our network. Technically, the same network could be used as long as the b-values remain consistent, but the spherical harmonics expansion would vary with different angular resolutions (i.e., the number of b-vectors).

To the best of our knowledge, sCNNs have been used to analyze dMRI data only a few times prior to this. Sedlar et al. (2021a) trained an sCNN to predict 'neurite orientation dispersion and density imaging' (NODDI) (Zhang et al., 2012) parameters from subsampled data, and Goodwin-Allcock et al. (2022) showed that sCNNs can improve the robustness of diffusion tensor estimation from data with just a few directions. sCNNs have also been used to estimate ODFs (Elaldi et al., 2021; Sedlar et al., 2021b). However, this study differs from the aforementioned studies in two important ways. First, our network and simulations were developed to estimate both the ODF and scalar parameters of any Gaussian compartment model. Second, we carefully compared the sCNN to the SMT, a commonly used and nearly rotationally invariant conventional fitting method, thus warranting a comparison with sCNN. Although we implemented spherical convolution layers as described by Esteves et al. (2018), other architectures also exist and warrant investigation in the context of microstructural parameter estimation. For example, the sCNNs by Cohen et al. (2018) use cross-correlation and can learn non-zonal (i.e., not symmetric with respect to the z-axis) filters, Kondor et al. (2018) developed efficient quadratic nonlinearities in the spherical harmonics domain, and the graph-based sCNN by Perraudin et al. (2019) is suitable for spherical data with very high angular resolution. Besides optimizing network architecture, future studies should also focus on optimizing hyperparameters and especially on carefully assessing the effects of and optimizing the training data distribution.

Data availability statement

The raw data supporting the conclusions of this article will be made available by the authors, without undue reservation.

Ethics statement

The studies involving humans were approved by UCL Research Ethics Committee (https://www.ucl.ac.uk/research-ethics/committees-and-governance/about-ucl-research-ethics-committee). The studies were conducted in accordance with the local legislation and institutional requirements. The participants provided their written informed consent to participate in this study.

Author contributions

LK: Conceptualization, Data curation, Formal analysis, Investigation, Methodology, Project administration, Resources, Software, Validation, Visualization, Writing—original draft, Writing—review & editing. KS: Data curation, Writing—review & editing. FS: Resources, Software, Writing—review & editing. CC: Funding acquisition, Writing—review & editing.

Funding

The author(s) declare that no financial support was received for the research, authorship, and/or publication of this article.

Conflict of interest

FS is an inventor on a patent related to the study.

The remaining authors declare that the research was conducted in the absence of any commercial or financial relationships that could be construed as a potential conflict of interest.

Publisher's note

References

Andersson, J. L., and Sotiropoulos, S. N. (2016). An integrated approach to correction for off-resonance effects and subject movement in diffusion mr imaging. *Neuroimage* 125, 1063–1078. doi: 10.1016/j.neuroimage.2015.10.019

Barbieri, S., Gurney-Champion, O. J., Klaassen, R., and Thoeny, H. C. (2020). Deep learning how to fit an intravoxel incoherent motion model to diffusion-weighted mri. *Magn. Reson. Med* 83:312–321. doi: 10.1002/mrm.27910

Battocchio, M., Schiavi, S., Descoteaux, M., and Daducci, A. (2022). Bundle-o-graphy: improving structural connectivity estimation with adaptive microstructure-informed tractography. *Neuroimage* 263, 119600. doi: 10.1016/j.neuroimage.2022.119600

Brechbühler, C., Gerig, G., and Kübler, O. (1995). Parametrization of closed surfaces for 3-d shape description. *Comput. Vis. Image Underst.* 61, 154–170. doi: 10.1006/cviu.1995.1013

Cohen, T. S., Geiger, M., Köhler, J., and Welling, M. (2018). Spherical CNNs. *arXiv [Preprint]*. arXiv:1801.10130. doi: 10.48550/arXiv.1801.10130

Collins, S. E., Spencer-Smith, M., Mürner-Lavanchy, I., Kelly, C. E., Pyman, P., Pascoe, L., et al. (2019). White matter microstructure correlates with mathematics but not word reading performance in 13-year-old children born very preterm and full-term. *NeuroImage.* 24, 101944. doi: 10.1016/j.nicl.2019.101944

de Almeida Martins, J. P., Nilsson, M., Lampinen, B., Palombo, M., While, P. T., Westin, C.-F., et al. (2021). Neural networks for parameter estimation in microstructural mri: application to a diffusion-relaxation model of white matter. *Neuroimage* 244, 118601. doi: 10.1016/j.neuroimage.2021.118601

Driscoll, J. R., and Healy, D. M. (1994). Computing fourier transforms and convolutions on the 2-sphere. *Adv. Appl. Math.* 15, 202–250. doi: 10.1006/aama.1994.1008

Elaldi, A., Dey, N., Kim, H., and Gerig, G. (2021). "Equivariant spherical deconvolution: Learning sparse orientation distribution functions from spherical data," in *International Conference on Information Processing in Medical Imaging* (Cham: Springer), 267–278.

Esteves, C., Allen-Blanchette, C., Makadia, A., and Daniilidis, K. (2018). "Learning so (3) equivariant representations with spherical CNNs," in *Proceedings of the European Conference on Computer Vision (ECCV)*. Available online at: https://openaccess.thecvf.com/content_ECCV_2018/html/Carlos_Esteves_Learning_SO3_Equivariant_ECCV_2018_paper.html

Fick, R. H., Wassermann, D., and Deriche, R. (2019). The dmipy toolbox: diffusion mri multi-compartment modeling and microstructure recovery made easy. *Front. Neuroinform.* 13, 64. doi: 10.3389/fninf.2019.00064

Gibbard, C. R., Ren, J., Skuse, D. H., Clayden, J. D., and Clark, C. A. (2018). Structural connectivity of the amygdala in young adults with autism spectrum disorder. *Hum. Brain Mapp.* 39, 1270–1282. doi: 10.1002/hbm.23915

Golkov, V., Dosovitskiy, A., Sperl, J. I., Menzel, M. I., Czisch, M., Sämann, P., et al. (2016). Q-space deep learning: twelve-fold shorter and model-free diffusion mri scans. *IEEE Trans. Med. Imaging* 35, 1344–1351. doi: 10.1109/TMI.2016.2551324

Goodwin-Allcock, T., McEwen, J., Gray, R., Nachev, P., and Zhang, H. (2022). "How can spherical CNNs benefit ML-based diffusion MRI parameter estimation?" in *International Workshop on Computational Diffusion MRI* (Cham: Springer Nature Switzerland). doi: 10.1007/978-3-031-21206-2_9

Gorski, K. M., Hivon, E., Banday, A. J., Wandelt, B. D., Hansen, F. K., Reinecke, M., et al. (2005). Healpix: a framework for high-resolution discretization and fast analysis of data distributed on the sphere. *Astrophys. J.* 622, 759. doi: 10.1086/427976

Gyori, N. G., Clark, C. A., Alexander, D. C., and Kaden, E. (2021). On the potential for mapping apparent neural soma density via a clinically viable diffusion mri protocol. *Neuroimage* 239, 118303. doi: 10.1016/j.neuroimage.2021.118303

Gyori, N. G., Palombo, M., Clark, C. A., Zhang, H., and Alexander, D. C. (2022). Training data distribution significantly impacts the estimation of tissue microstructure with machine learning. *Magn. Reson. Med* 87, 932–947. doi: 10.1002/mrm.29014

Henriques, R. N., Jespersen, S. N., and Shemesh, N. (2019). Microscopic anisotropy misestimation in spherical-mean single diffusion encoding mri. *Magn. Reson. Med* 81, 3245–3261. doi: 10.1002/mrm.27606

Henriques, R. N., Jespersen, S. N., and Shemesh, N. (2020). Correlation tensor magnetic resonance imaging. *Neuroimage* 211, 116605. doi: 10.1016/j.neuroimage.2020.116605

Ioffe, S., and Szegedy, C. (2015). "Batch normalization: accelerating deep network training by reducing internal covariate shift," in *International Conference on Machine Learning* (PMLR). Available online at: https://proceedings.mlr.press/v37/ioffe15.html

Jelescu, I. O., and Budde, M. D. (2017). Design and validation of diffusion mri models of white matter. *Front. Phys.* 5, 61. doi: 10.3389/fphy.2017.00061

Jenkinson, M., Beckmann, C. F., Behrens, T. E., Woolrich, M. W., and Smith, S. M. (2012). Fsl. *Neuroimage* 62, 782–790. doi: 10.1016/j.neuroimage.2011.09.015

Jespersen, S. N., Lundell, H., Sønderby, C. K., and Dyrby, T. B. (2013). Orientationally invariant metrics of apparent compartment eccentricity from double pulsed field gradient diffusion experiments. *NMR Biomed*. 26, 1647–1662. doi: 10.1002/nbm.2999

Jeurissen, B., Tournier, J.-D., Dhollander, T., Connelly, A., and Sijbers, J. (2014). Multi-tissue constrained spherical deconvolution for improved analysis of multi-shell diffusion mri data. *Neuroimage* 103, 411–426. doi: 10.1016/j.neuroimage.2014.07.061

Kaden, E., Kelm, N. D., Carson, R. P., Does, M. D., and Alexander, D. C. (2016a). Multi-compartment microscopic diffusion imaging. *Neuroimage* 139, 346–359. doi: 10.1016/j.neuroimage.2016.06.002

Kaden, E., Kruggel, F., and Alexander, D. C. (2016b). Quantitative mapping of the per-axon diffusion coefficients in brain white matter. *Magn. Reson. Med* 75, 1752–1763. doi: 10.1002/mrm.25734

Karimi, D., Jaimes, C., Machado-Rivas, F., Vasung, L., Khan, S., Warfield, S. K., et al. (2021). Deep learning-based parameter estimation in fetal diffusion-weighted mri. *Neuroimage* 243, 118482. doi: 10.1016/j.neuroimage.2021.118482

Kerkelä, L., Nery, F., Callaghan, R., Zhou, F., Gyori, N. G., Szczepankiewicz, F., et al. (2021). Comparative analysis of signal models for microscopic fractional anisotropy estimation using q-space trajectory encoding. *Neuroimage* 242, 118445. doi: 10.1016/j.neuroimage.2021.118445

Kerkelä, L., Nery, F., Hall, M. G., and Clark, C. A. (2020). Disimpy: a massively parallel monte carlo simulator for generating diffusion-weighted mri data in python. *J. Open Source Softw*. 5, 2527. doi: 10.21105/joss.02527

Kerkelä, L., Seunarine, K., Henriques, R. N., Clayden, J. D., and Clark, C. A. (2022). Improved reproducibility of diffusion kurtosis imaging using regularized non-linear optimization informed by artificial neural networks. *arXiv [Preprint]*. arXiv:2203.07327. doi: 10.48550/arXiv.2203.07327

Kingma, D. P., and Ba, J. (2014). "Adam: a method for stochastic optimization," in *arXiv*.

Kiselev, V. G. (2017). Fundamentals of diffusion mri physics. *NMR Biomed*. 30, e3602. doi: 10.1002/nbm.3602

Kondor, R., Lin, Z., and Trivedi, S. (2018). Clebsch-gordan nets: a fully fourier space spherical convolutional neural network. *Adv. Neural Inf. Process. Syst*.

Kostelec, P. J., and Rockmore, D. N. (2008). Ffts on the rotation group. *J. Fourier Analy. Appl*. 14, 145–179. doi: 10.1007/s00041-008-9013-5

Lampinen, B., Szczepankiewicz, F., Mårtensson, J., van Westen, D., Sundgren, P. C., and Nilsson, M. (2017). Neurite density imaging versus imaging of microscopic anisotropy in diffusion mri: a model comparison using spherical tensor encoding. *Neuroimage* 147, 517–531. doi: 10.1016/j.neuroimage.2016.11.053

Lasič, S., Szczepankiewicz, F., Eriksson, S., Nilsson, M., and Topgaard, D. (2014). Microanisotropy imaging: quantification of microscopic diffusion anisotropy and orientational order parameter by diffusion mri with magic-angle spinning of the q-vector. *Front. Phys*. 2, 11. doi: 10.3389/fphy.2014.00011

Lebel, C., Treit, S., and Beaulieu, C. (2019). A review of diffusion mri of typical white matter development from early childhood to young adulthood. *NMR Biomed*. 32, e3778. doi: 10.1002/nbm.3778

Novikov, D. S., Fieremans, E., Jespersen, S. N., and Kiselev, V. G. (2019). Quantifying brain microstructure with diffusion mri: theory and parameter estimation. *NMR Biomed*. 32, e3998. doi: 10.1002/nbm.3998

Palombo, M., Ianus, A., Guerreri, M., Nunes, D., Alexander, D. C., Shemesh, N., et al. (2020). Sandi: a compartment-based model for non-invasive apparent soma and neurite imaging by diffusion mri. *Neuroimage* 215, 116835. doi: 10.1016/j.neuroimage.2020.116835

Perraudin, N., Defferrard, M., Kacprzak, T., and Sgier, R. (2019). Deepsphere: efficient spherical convolutional neural network with healpix sampling for cosmological applications. *Astron. Comp*. 27, 130–146. doi: 10.1016/j.ascom.2019.03.004

Rahmanzadeh, R., Galbusera, R., Lu, P.-J., Bahn, E., Weigel, M., Barakovic, M., et al. (2022). A new advanced mri biomarker for remyelinated lesions in multiple sclerosis. *Ann. Neurol*. 92, 486–502. doi: 10.1002/ana.26441

Sagi, Y., Tavor, I., Hofstetter, S., Tzur-Moryosef, S., Blumenfeld-Katzir, T., and Assaf, Y. (2012). Learning in the fast lane: new insights into neuroplasticity. *Neuron* 73, 1195–1203. doi: 10.1016/j.neuron.2012.01.025

Sedlar, S., Alimi, A., Papadopoulo, T., Deriche, R., and Deslauriers-Gauthier, S. (2021a). "A spherical convolutional neural network for white matter structure imaging via dMRI," in *International Conference on Medical Image Computing and Computer-Assisted Intervention* (Cham: Springer), 529–539.

Sedlar, S., Papadopoulo, T., Deriche, R., and Deslauriers-Gauthier, S. (2021b). "Diffusion mri fiber orientation distribution function estimation using voxel-wise spherical u-net," in *Computational Diffusion MRI* (Cham: Springer), 95–106.

Sjölund, J., Szczepankiewicz, F., Nilsson, M., Topgaard, D., Westin, C.-F., and Knutsson, H. (2015). Constrained optimization of gradient waveforms for generalized diffusion encoding. *J. Magne. Res*. 261, 157–168. doi: 10.1016/j.jmr.2015.10.012

Sullivan, E. V., and Pfefferbaum, A. (2006). Diffusion tensor imaging and aging. *Neurosci. Biobehav. Rev*. 30, 749–761. doi: 10.1016/j.neubiorev.2006.06.002

Szczepankiewicz, F., Sjölund, J., Ståhlberg, F., Lätt, J., and Nilsson, M. (2019a). Tensor-valued diffusion encoding for diffusional variance decomposition (divide): technical feasibility in clinical mri systems. *PLoS ONE* 14, e0214238. doi: 10.1371/journal.pone.0214238

Szczepankiewicz, F., van Westen, D., Englund, E., Westin, C.-F., Ståhlberg, F., Lätt, J., et al. (2016). The link between diffusion mri and tumor heterogeneity: mapping cell eccentricity and density by diffusional variance decomposition (divide). *Neuroimage* 142, 522–532. doi: 10.1016/j.neuroimage.2016.07.038

Szczepankiewicz, F., Westin, C.-F., and Nilsson, M. (2019b). Maxwell-compensated design of asymmetric gradient waveforms for tensor-valued diffusion encoding. *Magn. Reson. Med* 82, 1424–1437. doi: 10.1002/mrm.27828

Toescu, S. M., Hales, P. W., Kaden, E., Lacerda, L. M., Aquilina, K., and Clark, C. A. (2021). Tractographic and microstructural analysis of the dentato-rubro-thalamo-cortical tracts in children using diffusion MRI. *Cerebral Cortex* 31, 2595–2609. doi: 10.1093/cercor/bhaa377

Topgaard, D. (2017). Multidimensional diffusion MRI. *J. Magne. Res*. 275:98–113. doi: 10.1016/j.jmr.2016.12.007

Tournier, J.-D., Smith, R., Raffelt, D., Tabbara, R., Dhollander, T., Pietsch, M., et al. (2019). Mrtrix3: A fast, flexible and open software framework for medical image processing and visualisation. *Neuroimage* 202, 116137. doi: 10.1016/j.neuroimage.2019.116137

Veraart, J., Novikov, D. S., Christiaens, D., Ades-Aron, B., Sijbers, J., and Fieremans, E. (2016). Denoising of diffusion mri using random matrix theory. *Neuroimage* 142, 394–406. doi: 10.1016/j.neuroimage.2016.08.016

Voldsbekk, I., Groote, I., Zak, N., Roelfs, D., Geier, O., Due-Tønnessen, P., et al. (2021). Sleep and sleep deprivation differentially alter white matter microstructure: a mixed model design utilising advanced diffusion modelling. *Neuroimage* 226, 117540. doi: 10.1016/j.neuroimage.2020.117540

Westin, C.-F., Knutsson, H., Pasternak, O., Szczepankiewicz, F., Özarslan, E., van Westen, D., et al. (2016). Q-space trajectory imaging for multidimensional diffusion mri of the human brain. *Neuroimage* 135, 345–362. doi: 10.1016/j.neuroimage.2016.02.039

Zhang, H., Schneider, T., Wheeler-Kingshott, C. A., and Alexander, D. C. (2012). Noddi: practical *in vivo* neurite orientation dispersion and density imaging of the human brain. *Neuroimage* 61, 1000–1016. doi: 10.1016/j.neuroimage.2012.03.072

Zhang, Y., Schuff, N., Du, A.-T., Rosen, H. J., Kramer, J. H., Gorno-Tempini, M. L., et al. (2009). White matter damage in frontotemporal dementia and alzheimer's disease measured by diffusion mri. *Brain* 132, 2579–2592. doi: 10.1093/brain/awp071

Zonca, A., Singer, L. P., Lenz, D., Reinecke, M., Rosset, C., Hivon, E., et al. (2019). healpy: equal area pixelization and spherical harmonics transforms for data on the sphere in python. *J. Open Source Softw*. 4, 1298. doi: 10.21105/joss.01298

frontiers | Frontiers in Neuroscience

TYPE Original Research
PUBLISHED 20 March 2024
DOI 10.3389/fnins.2024.1344076

OPEN ACCESS

EDITED BY
Maryam Afzali,
University of Leeds, United Kingdom

REVIEWED BY
Yuhei Takado,
National Institutes for Quantum and Radiological Science and Technology (Japan), Japan
Jens Velde Andersen,
University of Copenhagen, Denmark

*CORRESPONDENCE
Cristina Cudalbu
✉ cristina.cudalbu@epfl.ch

†These authors have contributed equally to this work and share first authorship

RECEIVED 24 November 2023
ACCEPTED 19 February 2024
PUBLISHED 20 March 2024

CITATION
Mosso J, Briand G, Pierzchala K, Simicic D, Sierra A, Abdollahzadeh A, Jelescu IO and Cudalbu C (2024) Diffusion of brain metabolites highlights altered brain microstructure in type C hepatic encephalopathy: a 9.4 T preliminary study. *Front. Neurosci.* 18:1344076. doi: 10.3389/fnins.2024.1344076

Diffusion of brain metabolites highlights altered brain microstructure in type C hepatic encephalopathy: a 9.4 T preliminary study

Jessie Mosso[1,2†], Guillaume Briand[1,2†], Katarzyna Pierzchala[1,2], Dunja Simicic[1,2], Alejandra Sierra[3], Ali Abdollahzadeh[4], Ileana O. Jelescu[5,6] and Cristina Cudalbu[1,2*]

[1]CIBM Center for Biomedical Imaging, Lausanne, Switzerland, [2]Animal Imaging and Technology, École polytechnique fédérale de Lausanne (EPFL), Lausanne, Switzerland, [3]A.I. Virtanen Institute for Molecular Sciences, University of Eastern Finland, Kuopio, Finland, [4]Center for Biomedical Imaging, Department of Radiology, New York University Grossman School of Medicine, New York, NY, United States, [5]Department of Radiology, Lausanne University Hospital (CHUV), Lausanne, Switzerland, [6]Faculty of Biology and Medicine, University of Lausanne, Lausanne, Switzerland

Introduction: Type C hepatic encephalopathy (HE) is a decompensating event of chronic liver disease leading to severe motor and cognitive impairment. The progression of type C HE is associated with changes in brain metabolite concentrations measured by ^{1}H magnetic resonance spectroscopy (MRS), most noticeably a strong increase in glutamine to detoxify brain ammonia. In addition, alterations of brain cellular architecture have been measured *ex vivo* by histology in a rat model of type C HE. The aim of this study was to assess the potential of diffusion-weighted MRS (dMRS) for probing these cellular shape alterations *in vivo* by monitoring the diffusion properties of the major brain metabolites.

Methods: The bile duct-ligated (BDL) rat model of type C HE was used. Five animals were scanned before surgery and 6- to 7-week post-BDL surgery, with each animal being used as its own control. ^{1}H-MRS was performed in the hippocampus (SPECIAL, TE = 2.8 ms) and dMRS in a voxel encompassing the entire brain (DW-STEAM, TE = 15 ms, diffusion time = 120 ms, maximum *b*-value = 25 ms/µm^2) on a 9.4 T scanner. The *in vivo* MRS acquisitions were further validated with histological measures (immunohistochemistry, Golgi-Cox, electron microscopy).

Results: The characteristic ^{1}H-MRS pattern of type C HE, i.e., a gradual increase of brain glutamine and a decrease of the main organic osmolytes, was observed in the hippocampus of BDL rats. Overall increased metabolite diffusivities (apparent diffusion coefficient and intra-stick diffusivity—Callaghan's model, significant for glutamine, myo-inositol, and taurine) and decreased kurtosis coefficients were observed in BDL rats compared to control, highlighting the presence of osmotic stress and possibly of astrocytic and neuronal alterations. These results were consistent with the microstructure depicted by histology and represented by a decline in dendritic spines density in neurons, a shortening and decreased number of astrocytic processes, and extracellular edema.

Discussion: dMRS enables non-invasive and longitudinal monitoring of the diffusion behavior of brain metabolites, reflecting in the present study the globally altered brain microstructure in BDL rats, as confirmed *ex vivo* by histology. These findings give new insights into metabolic and microstructural abnormalities associated with high brain glutamine and its consequences in type C HE.

KEYWORDS

in vivo magnetic resonance spectroscopy, diffusion-weighted magnetic resonance spectroscopy, brain metabolism, hepatic encephalopathy, rat brain, bile duct ligation, ultra high magnetic field

1 Introduction

Diffusion-weighted MRI (dMRI) has emerged as a promising "super-resolution" technique that can provide information about tissue microstructure non-invasively in the order of a micron. dMRI uses the diffusion of water molecules and their interaction with tissue cellular components to generate image contrast. This signal originates from ubiquitous water molecules present in all cell types and extracellular spaces, thus limiting its specificity to any tissue compartment, cell type, or physiological phenomenon. In contrast, brain metabolites measured by magnetic resonance spectroscopy (MRS) are predominantly intracellular, and some metabolites have preferential localization within specific brain cell types (Najac et al., 2016). Myo-inositol (Ins) and glutamine (Gln) concentrations are higher in astrocytes, and N-acetylaspartate (NAA) and glutamate (Glu) concentrations are higher in neurons (Brand et al., 1993; Urenjak et al., 1993; Harris et al., 2015). Although the representation of metabolite localization in one cell type is over-simplistic *in vivo* (Rae, 2014), it constitutes a useful assumption for MRS studies.

The combination between diffusion weighting and MRS, diffusion-weighted MRS (dMRS), enables the measurement of metabolite diffusion properties, which are expected to reflect properties of intracellular space (i.e., cell-type geometry, structure, cytosol viscosity, and molecular crowding). Different dMRS modeling approaches have been proposed to quantify cell microstructure (Ligneul et al., 2024), and, among others, alterations of astrocytic morphology were observed in a mouse model of reactive astrocytes and cuprizone-fed mice as a model of glial inflammation (Ligneul et al., 2019; Genovese et al., 2021).

Type C hepatic encephalopathy (HE) is a severe neurological condition that arises as a consequence of chronic liver disease (Monfort et al., 2009; Dharel and Bajaj, 2015; Häussinger et al., 2022). In type C HE, the high ammonium delivery to the brain, due to impaired urea cycle in the cirrhotic liver, is causing Gln accumulation and the gradual release of other metabolites (Ins, taurine (Tau), total choline (tCho)) as an osmotic response (Rackayova et al., 2016; Lanz et al., 2017; Braissant et al., 2019; Cudalbu and Taylor-Robinson, 2019; Rackayová et al., 2021; Pierzchala et al., 2023). In spite of this apparent osmoregulation, a mild increase in the apparent diffusion coefficient (ADC) of water has sometimes been observed in patients with type C HE (Kale et al., 2006). It has been associated with edema without a clear consensus on its compartmentalization (Cudalbu and Taylor-Robinson, 2019; Pierzchala et al., 2023). The overall interpretation of diffusion data is difficult and sometimes controversial, as extracting quantitative metrics that characterize the underlying tissue microstructure requires modeling of the diffusion signal (Jelescu and Budde, 2017; Jelescu et al., 2020), which has not yet been proposed in type C HE. Furthermore, the presence of brain edema and/or increased brain water content is still controversial in type C HE, as type C HE, in contrast to acute HE, is characterized by lower blood ammonium values and a longer disease time course, allowing for the presence of compensatory mechanisms (Pierzchala et al., 2023). Gln synthesis in the central nervous system is largely confined to astrocytes (the site of glutamine synthetase activity) (Martinez-Hernandez et al., 1977). Thus, it has been postulated that HE is the clinical manifestation of astrocyte swelling and/or astrocyte reactivity due to increased osmotic pressure triggered by Gln accumulation, with Gln acting as an osmolyte driving water into the cells. Although the pathological role of astrocytes in animal models and humans with severe hyperammonemia and liver failure has been confirmed, it has also become clear that additional cell types in the brain are also involved in the pathogenesis of HE. To date, the direct effects of Gln accumulation on astrocytes and potentially on other cell morphology concomitant with the appearance of brain edema in type C HE are not clear, mainly due to a limited number of *in vivo* studies. An increase in brain Gln will eventually lead to cellular microstructural changes despite osmoregulation (i.e., release of other brain osmolytes). Diffusion-weighted MRS is a powerful tool to study these alterations non-invasively and *in vivo* in an animal model of type C HE.

The aim of our study was to follow *in vivo* the longitudinal evolution of brain Gln and other metabolite diffusion properties in a rat model of type C HE using dMRS, thus providing information on potential microstructural alterations during type C HE. Furthermore, histological assessment of the brain tissue was performed to validate the *in vivo* dMRS findings, and short TE ^{1}H-MRS measurements in the hippocampus were performed to validate the well-known metabolic changes in type C HE.

2 Materials and methods

2.1 Animal model of chronic liver disease induced type C HE

All experiments were approved by the Committee on Animal Experimentation for the Canton de Vaud, Switzerland (VD3022.1). Adult male Wistar rats underwent bile duct ligation (BDL; Charles River Laboratories, L'Arbresle, France, 175–200 g at surgery) to create a model of chronic liver disease-induced type C HE, as previously described (Braissant et al., 2019; DeMorrow et al., 2021), and SHAM surgery as controls for histology assessment only. BDL animals were scanned longitudinally under isoflurane anesthesia (~1.5%, in a mixture of 50% oxygen and 50% air). A first scan was performed before surgery (n = 5, "week 0"), and a second scan between 6- and 7-week post-BDL (same animals, n = 5, "week 6"); the long duration of the MRI/MRS experiments did not allow us to scan all animals on the same day. For the MRI/MRS scans, all animals were placed in an in-house-built holder, with the head fixed in a stereotaxic system using a bite bar and a pair of ear bars. A small-animal monitor system (SA Instruments, New York, NY, USA) was used to monitor the body

temperature (maintained at 37.7 ± 0.2°C by warm circulating water and measured with a rectal thermosensor) and the respiration rate. Blood samples of bilirubin (Reflotron Plus system, F. Hoffmann-La Roche Ltd.) and ammonium (PocketChem™ BA PA-4140) were performed before the MRI/MRS scans (before BDL and at week 6–7 post-BDL) to validate the model of chronic liver disease.

2.2 MRI, ^{1}H-MRS and dMRS

All experiments were performed on a 9.4 T, actively shielded MRI system with a 31-cm horizontal bore (Magnex Scientific, Oxford, United Kingdom), featuring a 12-cm gradient coil insert (400 mT/m, 120 µs) interfaced to an Agilent/Varian Direct Drive console (Palo Alto, CA, USA). An in-house-built ^{1}H quadrature transceiver was used (25-mm inner diameter).

Fast T_2-weighted images (multislice turbo-spin-echo sequence, TR = 4,000 ms, TE_{eff} = 52 ms, echo train length = 8, field of view (FOV) = 23 × 23 mm^2, slice thickness = 1 mm, 15 slices, matrix size = 256 × 256, two averages) were acquired in the axial direction to position the volumes of interest (VOIs) for ^{1}H-MRS. First, a ^{1}H-MRS scan was performed in the hippocampus (2 × 2.8 × 2 mm^3, 11.8 µL) using the SPECIAL sequence (TE = 2.8 ms, TR = 4 s, 160 shots) to measure neurometabolism, as previously described (Braissant et al., 2019). Then, dMRS data were acquired using a localized STEAM-based spectroscopic pulse sequence (Kunz et al., 2010; Ligneul et al., 2024) (TE/TM = 15/112 ms, 5 kHz spectral width, 4,096 spectral points, single shot acquisitions) in a voxel ranging from 162 to 245 µL depending on the animal. The dMRS voxel size was increased compared to the hippocampus MRS voxel due to the lower signal-to-noise ratio (SNR) in the diffusion experiments as compared to a simple MRS acquisition. FASTESTMAP (Gruetter, 1993; Gruetter and Tkác, 2000) was used for shimming, leading to water linewidths of 9–10 Hz in the hippocampus and of 18–20 Hz for the dMRS VOI (Figure 1A). Outer volume suppression blocks were interleaved with the VAPOR water suppression module. Diffusion gradients were applied simultaneously along three orthogonal directions (gradient duration δ = 6 ms, diffusion time Δ = 120 ms, direction [1,1,1]). A total of nine *b*-values (in ms/µm^2, corrected for cross-terms (Kunz et al., 2010; Mosso et al., 2024)) with the following number of shots were acquired: 0.4 (160), 1.5 (160), 6.0 (160), 7.6 (160), 9.3 (160), 13.3 (320), 15.6 (480), 20.8 (480), and 25.1 (480).

Spectra were collected as single shots (consecutive ISIS acquisitions from SPECIAL were directly combined, with each combination being labeled as "shot" in this article) and corrected for eddy current distortions and phase and frequency drifts. Outlier shots with manifest signal drops (>50%) were removed, and all shots were averaged. Metabolite signals were quantified using LCModel (Version 6.3-1 N) combined with an *in vitro* measured metabolite basis set for ^{1}H-MRS hippocampus spectra and a simulated metabolite basis set for dMRS spectra using published values of *J*-coupling constants and chemical shifts (Govindaraju et al., 2000; Govind et al., 2015). The following metabolites were included in the basis sets: alanine (Ala), ascorbate (Asc), aspartate (Asp), β-hydroxybutyrate (bHB), glycerophosphocholine (GPC), phosphocholine (PCho), creatine (Cr), phosphocreatine (PCr), glycine (Gly), GABA, glucose (Glc), Gln, glutamate (Glu), glutathione (GSH), Ins, lactate (Lac), N-acetylaspartate (NAA), N-acetylaspartylglutamate (NAAG), phosphoethanolamine (PE), scyllo-inositol (Scyllo), and Tau. In addition, an *in vivo* macromolecule spectrum acquired under the same conditions as *in vivo* ^{1}H-MRS and dMRS data was included in each of the corresponding metabolite basis sets (single inversion recovery, TI = 750 ms, TR = 2,500 ms, no diffusion weighting, and metabolite residuals eliminated as described previously (Cudalbu et al., 2021; Simicic et al., 2021)). For ^{1}H-MRS, metabolites with relative Cramer Rao Lower Bounds (CRLB) below 25% at week 0 for all animals were reported (selecting reported metabolites but not individual values), a purposely loose criterion to avoid filtering out low-concentrated metabolites (Kreis, 2016). For dMRS, to limit error propagation, only metabolites with relative CRLBs below 6% at the lowest *b*-value for all animals were reported.

Metabolite signal decays as a function of *b*-value were then fitted using two different approaches, using a non-linear least squares algorithm in MATLAB (*fit* function, *Trust-Region* method): First, Callaghan's model of randomly oriented sticks (Callaghan et al., 1979) (mimicking neurites or processes) with metabolite diffusivity D_{intra} along the neurite/process:

$$\frac{S}{S_0} = \sqrt{\frac{\pi}{4bD_{intra}}}\,erf\left(\sqrt{bD_{intra}}\right) \quad (1)$$

Second, the cumulant expansion at second order:

$$\ln\left(\frac{S}{S_0}\right) = -bD + \frac{1}{6}(bD)^2 K \quad (2)$$

Yielding the apparent diffusion coefficient D and kurtosis K, where *b* refers to the *b*-value and *erf* refers to the error function. Assuming an underlying isotropic distribution of sticks (Callaghan's model) (Equation 1), the radius of convergence of the cumulant expansion is given by the first zero of the error function in the complex plane (Kiselev and Il'yasov, 2007), whereby assuming a diffusivity of about 0.3 µm^2/ms, b_c = 19 ms/µm^2. *b*-values up to b_c were used for this fit. For each metabolite, the fits were performed on the individual animal diffusion signal decay, and the fitted parameters were reported as mean and SD across animals. The fits were also performed on the group-averaged diffusion signal decay for each metabolite, yielding a mean coefficient.

A detailed table of the acquisition and processing parameters following the experts' consensus recommendations on minimum reporting standards in *in vivo* MRS (Lin et al., 2021) is presented in Supplementary Table S1.

2.3 Histology assessments

2.3.1 Fluorescence and Brightfield microscopy

Animals (SHAM and BDL animals) were sacrificed for histological evaluation between week 6 and 7 post-BDL. The deeply anesthetized (4% isoflurane for 5 min) animals were injected with analgesic (Temgesic [Essex Pharma], 0.1 mg/kg) before transcardiac perfusion with PBS. Due to the complexity of the experiments, additional groups of animals (in addition to the ones scanned by dMRS) were used for histological evaluation and electron microscopy, and SHAM animals were not used for electron microscopy. All animals were controlled for

blood bilirubin and ammonium values to ensure that the presence and evolution of CLD were in fact reflective of the dMRS group.

2.3.2 Immunohistochemistry (IHC)

Brains (SHAM n = 3, BDL n = 3) were fixed in a 4% formaldehyde PBS solution overnight at 4°C, washed with PBS, and cryopreserved in a 30% sucrose PBS solution at 4°C for 48 h. They were then embedded in Tissue-Tek® O.C.T. compound and cut into 16-µm sagittal sections. Astrocyte morphological alterations were depicted using mouse monoclonal anti-GFAP antibody (MAB360 Merck Millipore) (2 h at RT, 1:100 dilution) with secondary Alexa Fluor® 594-AffiniPure+ Rat Anti-Mouse IgG (H + L) antibody (415–585-166 Jackson ImmunoResearch Europe Ltd.) (1 h at RT, 1:200 dilution). Nuclei were stained with DAPI (D1306, Thermo Fisher Scientific). The stained sections were mounted with ProLong™ Diamond Antifade Mountant and covered with coverslip. Morphometric measurements (processes number/cell and processes length) were performed using Sholl analysis, as previously described (Braissant et al., 2019). A total of 200 astrocytes from each group were randomly selected and traced for all processes identified through GFAP staining. An average of 350 astrocytic processes were measured per sample, amounting to approximately 1,000 processes per group (seven slides/rat).

2.3.3 Golgi-cox staining

Golgi-Cox staining was performed to unveil the detailed morphology of the CA1 hippocampus neurons (Zaqout and Kaindl, 2016). Extracted brains were directly immersed in the Golgi-Cox staining solution, then stored in the dark at room temperature for 25 days prior to being washed with PBS, and cryopreserved for 48 h in 30% sucrose in PBS at 4°C. Brains were sliced into 115-µm-thick sagittal sections using a Leica VT1200 S vibratome (25 slides/hemisphere, SHAM n = 3, BDL n = 7). After the staining procedure and dehydration, the slides were mounted with Neo-Mount (EMD Millipore). For quantitative analysis, only uniformly stained tissue with clearly apparent dendritic segments and spines was used. The surface of the neuronal soma was measured, and dendritic spines were manually counted (CA1 neurons: BDL soma ~200 cells, apical and basal dendrites ~100 each; SHAM soma ~120 cells, apical and basal dendrites ~60 each). The images were acquired using a Meiji Techno TC5600 Microscope (INFINITYX-32 camera, picture size: 6,464× 4,864 pixels). The image processing and the quantitative immunohistochemical analysis were performed with INFINITY ANALYZE 7 software (Lumenera, Canada).

2.3.4 Electron microscopy (EM)

Deeply anesthetized BDL rats (n = 3) received an intraperitoneal injection of sodium pentobarbital. Afterward, a cardiac perfusion with 20 mL of isotonic PBS followed immediately with 300 mL of 2.5% glutaraldehyde and 2% formaldehyde in phosphate buffer (0.1 M, pH 7.4) was performed. The brains were removed 2 h after perfusion, and 100-µm-thick coronal sections were cut through the somatosensory cortex, striatum, hippocampus, and cerebellum (vibratome Leica VT1200; Leica Microsystems). Following a cacodylate buffer wash (0.1 m, pH 7.4), the sections were postfixed for 1 h in 1.5% potassium ferrocyanide and 2% osmium tetroxide in 0.13 M ice-cold cacodylate buffer, followed by 30 min in 2% osmium tetroxide alone, each in the same buffer, and then overnight (O/N) at 4°C in 1% uranyl acetate in water. After dehydrating in alcohol, the sections were infiltrated O/N with Durcupan resin (Fluka, Buchs, Switzerland). The sections were flat embedded between glass slides in fresh resin and left O/N at 65°C for the resin to harden. The images were acquired using a Carl ZEISS Merlin With 3View (Gatan) Scanning Electron Microscope (SEM) (current: 300 pA, voltage: 1.6 kV, image size: 6 nm/pixel, and *z*-axis: 50 nm) and analyzed with ImageJ FiJi16.

2.3.4.1 Edema reconstruction

We imaged $21 \times 21 \times 14.75\,\mu m^3$ of the hippocampus using the SEM method with a voxel size of $6 \times 6 \times 50\,nm^3$, $3{,}500 \times 3{,}500 \times 295$ voxel^3. We applied the DeepACSON pipeline (Abdollahzadeh et al., 2021a,b) for the semantic segmentation of the extracellular edema in the acquired 3D-EM dataset. We used a small training set—six 2D planar images manually segmented for edema. The images were tiled into 350×350 voxel^2 non-overlapping patches to initiate the training. To deal with the small training sets, we enhanced the performance of the networks by sequentially giving feedback as manual corrections to the network predictions. The training procedure for the networks follows the description in Abdollahzadeh et al. (2021a,b). For the instance segmentation of the extracellular edema, we applied a bottom-up percentile-based region agglomeration technique to merge over-segmented watersheds to perform instance segmentation of the intra-axonal spaces (Behanova et al., 2022).

2.4 Statistics

Data are presented as mean ± SD. For MRS, differences in metabolite concentration estimates were assessed with a repeated measure two-way analysis of variance (ANOVA) (Prism 5.03, GraphPad, La Jolla, CA, United States), with metabolites and disease (weeks 0 and 6) factors. For dMRS, differences in diffusion parameters based on individual animal fitting were assessed with a repeated measures two-way ANOVA on each parameter individually (ADC, AKC, D_{intra}), with metabolites and disease (weeks 0 and 6) factors. For both MRS and dMRS, Bonferroni's multi-comparisons *post-hoc* test was applied, where the number of comparisons was set to the number of metabolites passing the CRLB criteria (n = 17 comparisons for MRS and n = 7 for dMRS). For the histological measures, a two-way ANOVA with *post-hoc* Tukey HSD was used to test for statistical significance. All tests were two-tailed. The significance level in all tests was attributed as follows: $^*p < 0.05$, $^{**}p < 0.01$, $^{***}p < 0.001$, $^{****}p < 0.0001$.

3 Results

The characteristic ^{1}H-MRS pattern of type C HE, i.e., a gradual increase of Gln as a result of ammonia detoxification and a decrease in the main organic osmolytes as an osmoregulatory response (Rackayova et al., 2016; Flatt et al., 2017; Braissant et al., 2019; Rackayová et al., 2021; Mosso et al., 2022), was present in the rats investigated in the current study. ^{1}H-MRS in the hippocampus showed a significant increase of brain Gln (+178 ± 95%****), a decrease of Ins (−29 ± 14%**), trends of decrease for Tau, tCho, Glu, Asc, tCr (Cr + PCr), and GSH, and no difference for GABA, Lac, PE, tNAA (NAA + NAAG), and the macromolecules (Supplementary Figure S1).

Alanine, aspartate, bHB, glycine, glucose, and scyllo-inositol, often poorly quantified even at high fields, were not reported as they did not survive the ^{1}H-MRS CRLB criterion.

Similar patterns were observed in the dMRS voxel on low *b*-value spectra (qualitative results in Figure 1B): an increase in Gln (2.1 ppm and 3.7 ppm, observed from its relative amplitude compared to NAA), together with a decrease in the main osmolyte Ins (3.5 ppm).

Furthermore, all BDL rats displayed an increase in plasma bilirubin (from undetectable to 9.1 ± 2.1 mg/dL) and blood ammonium (from 25.9 ± 7.5 to 59.3 ± 30.9 µM) at 6-week post-BDL, both validating the BDL surgery and thus the chronic liver disease.

The quality of the acquired dMRS spectra both at week 0 and week 6 (Figure 1A) allowed the estimation of diffusion parameters of Gln, Glu, NAA, Ins, Tau, tCho (GPC + PCho), and tCr (Cr + PCr) and a fair comparison between the two time points. Supplementary Figure S2 displays the quality of the LCModel fits in a representative set of diffusion-weighted spectra acquired in one animal at weeks 0 and 6 post-BDL.

Figure 2 displays the metabolite signal diffusion decays with *b*-value, averaged over the cohort of animals at weeks 0 (green) and 6 (orange) after normalization to $b = 0.4$ ms/µm^2. A good quality fit was obtained with some minor discrepancies for tCho, tCr, and Tau at high *b*-values. To further evaluate data quality, the metabolite signal diffusion decays of individual animals are also plotted in Supplementary Figures S3,S4. The derived metabolites ADC before surgery (Figure 3, first panel, orange, "week 0") were in good agreement with results in the healthy rodent brain (Ligneul et al., 2019). After a 6-week period after surgery, an increase in intra-neurite/process diffusivity D_{intra} was measured for all metabolites (disease effect: **** with +58 ± 16% increase for Gln:**, n = 5 rats), as estimated from the sticks model (Equation 1) (Figure 3). The cumulant expansion fit (Equation 2) confirmed this trend: an increase in ADC (disease effect:****, subject-matching:* with +35 ± 14% increase for Gln:*, +29 ± 21% increase for Ins:*, +17 ± 18% increase for Tau:*, n = 5 rats) and a trend of decrease in kurtosis for some metabolites were observed, although the latter was not significant (Figure 3).

The Sholl analysis of the GFAP-stained astrocytes showed morphological alterations with a significant shortening of the processes (~30%****) and a decrease in the number of processes per

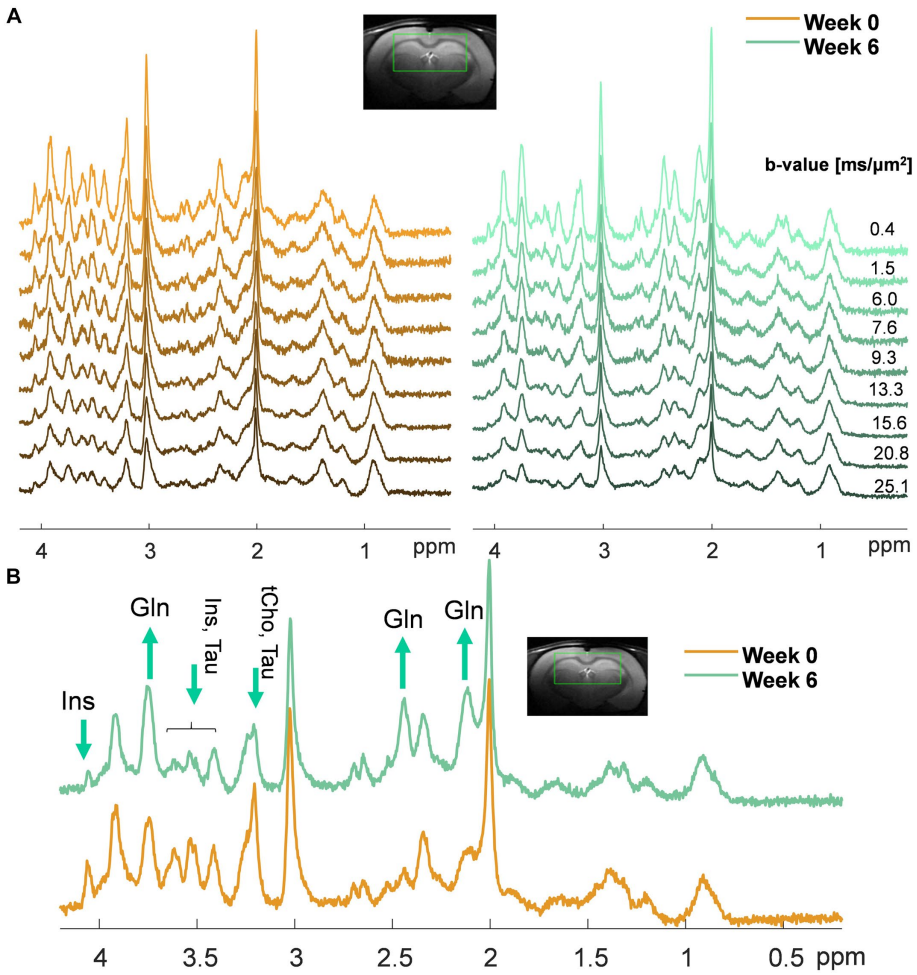

FIGURE 1
(A) Representative sets of diffusion-weighted spectra in one animal at week 0 (orange, left) and week 6 post-BDL surgery (green, right) acquired with diffusion-weighted STEAM. The voxel position and the *b*-values used are displayed at the top. Of note, the differences in noise level among the spectra are due to a different number of shots for each on the *b*-value (less noise at high *b*-values due to more shots); **(B)** Example of spectra acquired in the same animal at week 0 (orange) and week 6 post-BDL surgery (green) at $b = 0.4$ ms/µm^2, highlighting with arrows the increase in brain Gln and decrease of the main brain osmolytes (i.e., Ins, tCho, Tau) observed qualitatively.

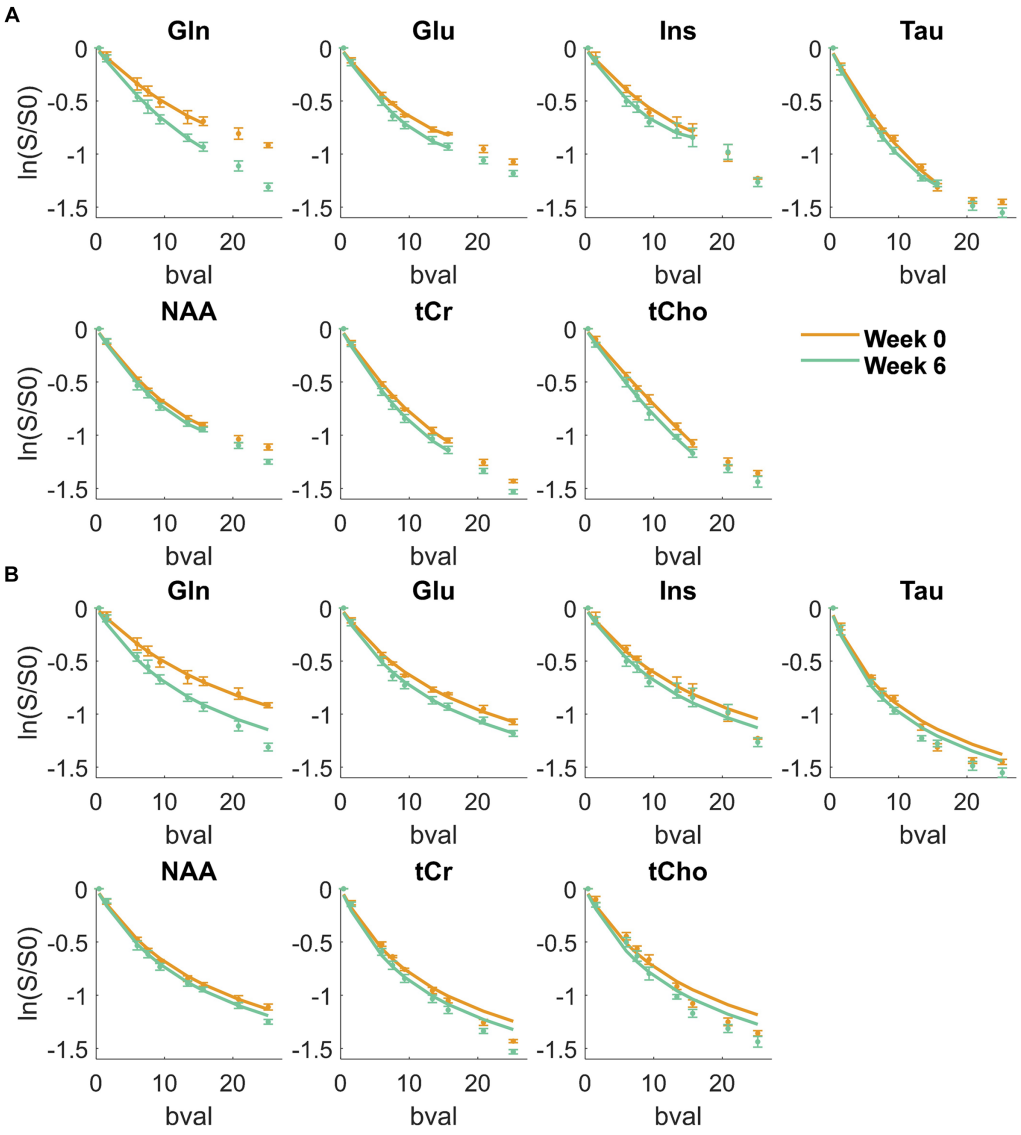

FIGURE 2
Metabolite signal diffusion decay with *b*-value, averaged over the cohort of animals at week 0 (green) and week 6 (orange) after normalization to $b = 0.4\ ms/\mu m^2$. Solid line: kurtosis fit up to $b = 15.7\ ms/\mu m^2$ **(A)** and D_{intra} fit from the randomly oriented sticks model (Equation 1) up to $b = 25\ ms/\mu m^2$ **(B)** Bval are in $ms/\mu m^2$.

cell (~18%****) at week 6 post-BDL (Figure 4A). In addition, the Golgi-Cox staining showed a significant increase in CA1 hippocampal neuronal soma surface (~65%***) and a significant loss of dendritic spines density, both apical and basal (both ~50%***) (Figure 4B). Electron microscopy of the BDL rats' brains revealed changes in the ultrastructure, as shown in Figures 4C,D, which were not observed in the healthy rat brain (Nahirney and Tremblay, 2021). Electron-dense lipofuscin granules were found in the perikaryal cytoplasm of neurons and in the cytoplasm of astrocytes, and aggregates are indicated in Figure 4C, together with elongated/fused mitochondria. A pattern of myelin sheath degeneration/breakdown was also observed (Figure 4C). The hippocampus was characterized by loss of tissue integrity and enlarged extracellular spaces, indicating increased extracellular water content in the area surrounding the astrocytes (Figure 4D). Automatic segmentation of extracellular space allowed reconstruction of the edema volume ($938.743\ \mu m^3$), corresponding to 14.5% of the whole dataset volume ($6504.75\ \mu m^3$).

4 Discussion

The present study describes the first *in vivo* implementation of single-voxel MRS, dMRS, and histology in rats with chronic liver disease-induced HE. It evaluates the potential of dMRS to highlight microstructural changes in the rat brain with type C HE through the measurement of metabolite diffusion properties. ^{1}H-MRS probed an increase in Gln and a decrease in the main osmolytes (Ins) in the hippocampus of BDL rats at 6-week post-surgery, indicating the presence of osmotic stress. The additional use of dMRS in the same animals enabled the characterization of changes in the diffusion behavior of brain Gln, Glu, Ins, Tau, tCr, and tCho (an overall increase

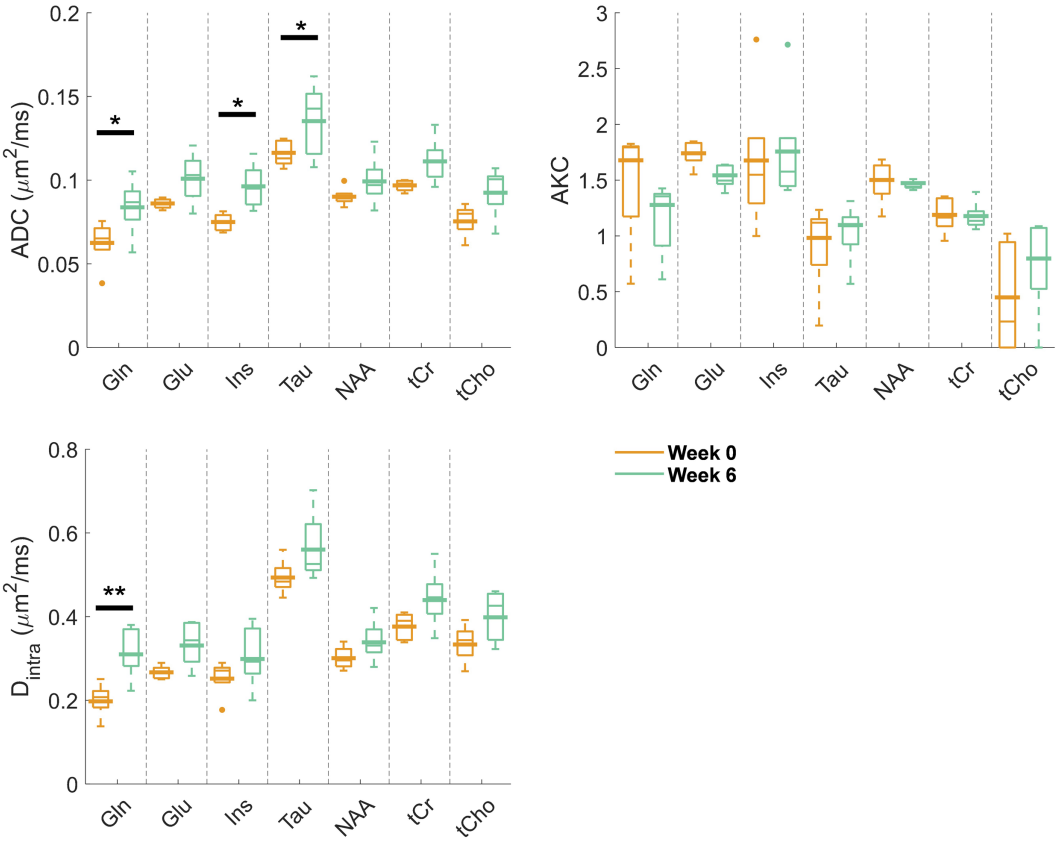

FIGURE 3
Estimated diffusion parameters from the kurtosis fit (ADC and AKC) and from the randomly oriented sticks model (Equation 1) (D_{intra}) for the reliably estimated metabolites (Gln, Glu, Ins, Tau, NAA, tCr, and tCho) at week 0 (orange) and week 6 (green). Box plots: parameters fitted on the individual animal signal decays (line: median, top and bottom edges: 25th and 75th percentiles, whiskers: extreme values, dots: outliers); bold lines: parameters fitted to the mean signal decay as plotted and fitted in Figure 2. Significant differences from a two-way ANOVA (metabolite and disease factors) with a Bonferroni post-hoc test are indicated. $^{**}p < 0.01$, $^{*}p < 0.05$.

as a disease effect, with Gln, Ins, and Tau showing significant changes), highlighting the presence of microstructural changes in this animal model, which were validated by different histological measures (astrocytes: decreased number and length of GFAP-stained intermediate filaments; neurons: decreased density of dendritic spines; and enlarged extracellular spaces). Taken together, our data suggest a loss of tissue integrity, providing new insights into metabolic and microstructural alterations linked to increased brain Gln and its consequences in type C HE. Furthermore, our results confirm that type C HE is characterized by complex and multicellular alterations that go beyond the hypothesis of intracellular edema, with astrocytes being the only target.

4.1 Brain metabolism alterations in the hippocampus

The increase in brain Gln in the hippocampus, mainly due to increased blood ammonium as a consequence of chronic liver disease, led to an osmotic imbalance resulting in a gradual decrease of other brain osmolytes (Ins), and contributed to morphological astrocytic alterations (shortening of process length together with a decrease in their number) (Häussinger et al., 2000), among other mechanisms. Of note, osmotic stress is not the sole mechanism involved in type C HE; oxidative stress and inflammation are complementary mechanisms acting synergistically (Simicic et al., 2022; Andersen and Schousboe, 2023; Pierzchala et al., 2023). Consistent with our previous findings (Braissant et al., 2019), we also identified some trends (not significant) in the changes of other metabolites. These changes included a decrease in Tau and tCho due to the osmotic response, the neurotransmitter Glu, and the antioxidants Asc and GSH. Moreover, the EM-observed intracellular accumulation of lipofuscin aggregates is a sign of lipid peroxidation and thus the presence of oxidative stress, which is in agreement with our previous studies (Pierzchala et al., 2022; Simicic et al., 2022), and we observed herein a decrease in antioxidants, a sign of redox homeostasis alterations. The same trends in metabolite changes were also observed in the bigger VOI used for dMRS. The quantification of these data was not used for characterizing the brain metabolism due to the longer TE of the dMRS sequence and the lack of T_2 corrections for water and metabolites.

4.2 Brain microstructural alterations revealed by dMRS and histology

In the BDL group at week 6, increased diffusivities of brain Gln and of the main brain osmolytes (Ins, Tau) were observed when

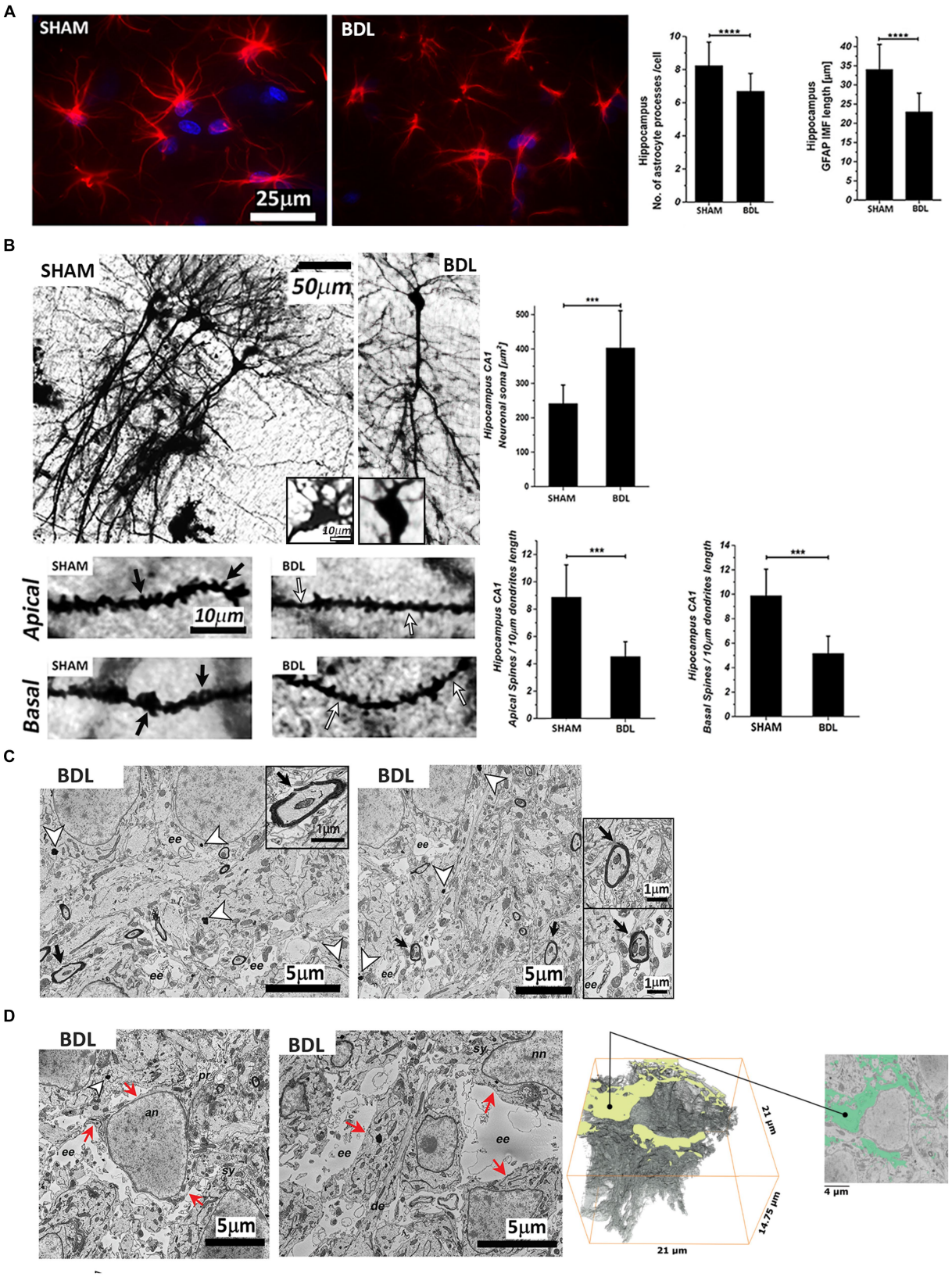

FIGURE 4
Hippocampal sections from SHAM and BDL rats. **(A)** Astrocytes stained with anti-GFAP (red) and DAPI-nuclei (blue) and morphological characterization of the number and length of processes. **(B)** Representative micrographs of Golgi-Cox staining and neuronal morphology analysis of pyramidal CA1 neurons. Black arrows indicate the spines, and the white arrows indicate spine pruning. **(C)** Analysis of the ultrastructure alterations of the hippocampus CA1 area. White arrowheads indicate granular electron-dense lipofuscin, and black arrowheads indicate myelin degeneration. **(D)** Extracellular edema reconstruction. Red arrows indicate the continuity of the plasma membrane. **(C)** and **(D)**: an—astrocyte nuclei; nn—neuronal nuclei; ee—extracellular edema; sy—synapse; se—synaptic edema; pr—processes; de—dendrite. Data are presented as mean±SD and statistical significance (two-way ANOVA with post-hoc Tukey HSD): *p<0.05, **p<0.01, ***p<0.001, ****p<0.0001.

compared to week 0. This observation is a possible consequence of the osmotic stress caused by intra-astrocytic Gln increase: brain osmolytes may be temporarily present in the extracellular space, therein experiencing freer diffusion compared to intracellular space, before being cleared out, as supported by the steady-state net decrease of osmolyte concentrations observed with MRS. The electron microscopy results revealed a loss of tissue integrity and enlarged extracellular spaces in the hippocampus, indicating increased extracellular water content in the area surrounding the astrocytes.

Furthermore, the increased diffusivities of Gln and Ins in the BDL rats, metabolites assumed to be glial markers (Martinez-Hernandez et al., 1977; Häussinger et al., 1994), may also reflect astrocyte alterations following the strong Gln increase. Changes in diffusivity *in vivo* are usually associated with microstructural changes (Najac et al., 2014, 2016; Palombo et al., 2018; Ligneul et al., 2019; Genovese et al., 2021), and the diffusion time used in the present study (120 ms, characteristic 2D diffusion length of $\sqrt{4D\Delta} = 8.5\mu m$, assuming $D = 0.15$ μm²/ms) is likely to probe metabolite diffusion along fibers (astrocytic processes or neuronal dendrites) rather than confinement in cell bodies, as shown with dMRS in the human (Najac et al., 2016) and macaque brain (Najac et al., 2014). These dMRS findings are supported by the GFAP histological observations (i.e., decreased length and number of astrocytic processes) pointing toward a less restricted and ramified cellular architecture, explaining increased diffusivities for astrocytic metabolites in the BDL rats. A recent study showed increased serum GFAP levels in cirrhotic patients (Gairing et al., 2023), suggesting that the presence of astrocyte injury and astrocyte activation are two mechanisms that may lead to increased serum GFAP concentrations. It is worth mentioning that, using dMRS in a model of reactive astrocytes, Ins has been revealed as a specific intra-astrocytic marker whose diffusion closely reflects astrocytic morphology, enabling the non-invasive detection of astrocyte hypertrophy (Ligneul et al., 2019). In addition, the diffusion of astrocytic metabolites can mirror their altered morphology and pro-inflammatory phenotype (de Marco et al., 2022), since, during neuroinflammation, both astrocytes and microglia undergo metabolic, functional, and morphological changes (Heneka et al., 2014). In our previous studies, significantly elevated levels of IL-6 and reactive oxygen species were observed in the brains of BDL rats as compared to the SHAM animals (Pierzchala et al., 2022), suggesting the presence of neuroinflammation. IL-6 levels, together with oxidative stress, have also been associated with increased blood–brain barrier permeability, allowing neurotoxins to enter the brain and impair neurological functions (Simicic et al., 2022). Recent studies promoted dMRS as a tool sensitive to glial cytomorphological changes induced by inflammation following LPS administration in humans (de Marco et al., 2022) or in cuprizone-fed mice (Genovese et al., 2021), where Ins and tCho apparent diffusion coefficients were significantly elevated. Following these studies, tCho diffusivity changes were related to the presence of inflammation, even though tCho has a limited specificity for glial cells. Similarly, an increased diffusivity for tCho (a trend of ~20% increase) was measured in this study, possibly reflecting here also the presence of neuroinflammation, as shown previously in BDL rats *ex vivo* (Pierzchala et al., 2022). Neuroinflammation will impact the astrocyte cytoskeleton, which may lead to an increase in intracellular and extracellular space, as observed in our study. Furthermore, the EM data depicted a breakdown of myelin sheaths and myelin outfolding formation in BDL rats, which could also impact tCho diffusivity as tCho is required for membrane phospholipid synthesis and myelination (Zeisel et al., 1986), although only a few studies have validated the association between myelin status and tCho (Laule et al., 2007; Rae, 2014, Skripuletz et al., 2015).

Glu and NAA, both expected to be preferentially located in neurons (MOFFETT et al., 2007; Fendt and Verstreken, 2017), exhibited a trend of increased diffusivity in BDL rats at week 6 post-BDL. Golgi-Cox measures probed an increased soma surface of CA1 hippocampal neurons and a loss of dendritic spines density (which is made of filamentous actin cytoskeleton; Hering and Sheng, 2001) in BDL rats. Numerical simulations (Palombo et al., 2018) have suggested that decreased dendritic spines density would increase the ADC of neuronal metabolites, consistent with the trend of increased Glu and NAA diffusivity observed herein. Furthermore, additional studies using two-photon microscopy on brain slices (Santamaria et al., 2006, 2011) have shown that the diffusional characteristics of dendrites are greatly affected by the dendritic spines density, being slower in the dendrite with the higher density of spines due to anomalous diffusion, and significantly faster in smooth/low spines density dendrites. Of note, Glu is the main precursor of Gln synthesis in the astrocytes, and the observed increased diffusivity trend can also reflect the reduced number and shortening of astrocyte processes. Total Cr also showed a trend of increased diffusivity in this study. Creatine is located in most cell types, has different roles in energy metabolism and cytoprotection, and also appears to act in osmoregulation and neurotransmission (Rackayova et al., 2017; Braissant et al., 2019).

Metabolite kurtosis coefficients overall tended to decrease in the BDL group, suggesting that the intracellular space might be less heterogeneous with reduced structural disorder. Although previous numerical simulations have shown that the number of processes departing from the soma has almost no influence on the measured ADC at any diffusion time (Palombo et al., 2016), the former, observed here by histology, might have an influence on D_{intra}, which is higher in HE rats compared to control rats for most metabolites. Overall, we believe that increased diffusivities in type C HE rats versus control rats reflect (1) intracellular space alteration with reduced structural disorder, supported by decreased neuronal spines density, decreased length of astrocyte processes and number of ramifications shown by histology, and (2) a higher contribution of extracellular space diffusion in BDL rats compared to controls due to osmolytes leaving the cells counteracting intracellular Gln increase.

4.3 Limitations

dMRS is a challenging measurement, and different factors might affect the estimated diffusion metrics (Ligneul et al., 2024). In the present study, motion artifacts due to simple linear translational motion were compensated on individual shots by phase correction, while data affected by rotational and compressive motion were discarded in the outlier removal process. Consequently, we do not expect any significant effect of motion on the calculated metabolite diffusion metrics, i.e., an overall overestimation. Additionally, a change in metabolite concentration is unlikely to affect diffusivity through a change in cytosol viscosity given the small metabolite

concentrations (1–10 M) compared to water (45–50 M) (Kinsey et al., 2011).

For some metabolites (i.e., Tau, tCr, and tCho), the sticks model (Equation 1) showed some discrepancies with the measured data at high *b*-values. These discrepancies may result from a poorer LCModel spectral fit quality at higher *b*-values, exemplified by the high inter-animal variability of estimated concentrations for the highest *b*-values (Supplementary Figures S3,S4). Such variability might be partially alleviated by the use of simultaneous 2D fitting of the spectral and diffusion dimensions (Adalid et al., 2017).

The strict CRLB criterion for dMRS ensures a fair comparison between the groups. The use of each animal as its own control with a scan before the BDL surgery was beneficial as it ruled out possible inter-animal differences in brain microstructure or metabolism that could have biased the group comparison. A good concordance between individual and group-average fit for diffusion estimates was obtained in the current study. The possibility of fitting diffusion coefficients on individual animal signal decays provides an error estimation better representing the group dispersion than the one evaluated from the group-averaged signal decay. dMRS is also characterized by an overall low signal-to-noise ratio (SNR) compared to a simple MRS acquisition. In the present study, the LCModel SNR ranged from 15–20 to 45 depending on the *b*-value, guiding the choice of the randomly oriented sticks model (Equation 1) instead of the randomly oriented cylinder model (i.e., fitting, in addition, the radius of processes) (Vangelderen et al., 1994). This finding is highlighted in a recent dMRS consensus article showing that fitting the cylinder model would require a higher SNR and higher *b*-values than what was accessible in the present study (Ligneul et al., 2024). Finally, the increased brain Gln combined with the relatively short TE (15 ms) and high magnetic field allowed us to report brain Gln diffusivity for the first time.

Our study reports an overall increased diffusivity for all investigated metabolites, which was confirmed by histological measures. However, additional studies with an increased number of samples would be required to confirm this trend together with EM data on SHAM animals. dMRI could provide additional information with respect to dMRS, the former also informing on the extracellular space and on exchange between intracellular and extracellular spaces. An increased membrane permeability in BDL rats would also contribute to reduced compartmentalization (intracellular vs. extracellular) of metabolites (Ins, Gln, and Tau) and faster diffusion, which could be evaluated from joint dMRS and dMRI acquisitions in future studies. Future dMRS studies in this animal model should focus on targeting a specific brain region (the dMRS voxel here included several brain regions): brain regional differences in the neurometabolic profiles of BDL rats have been suggested, with the cerebellum exhibiting a stronger Gln increase than other brain regions (Simicic et al., 2019).

5 Conclusion

In conclusion, this study highlights the potential of dMRS as a unique tool to non-invasively monitor neuronal and astrocytic structural alterations in the rat model of type C HE via the measurement of cell-specific metabolite diffusion properties. The increased diffusivity and reduced kurtosis in BDL versus control rats, measured *in vivo* with dMRS, are consistent with an altered microstructure probed *ex vivo* by fluorescence, brightfield, and electron microscopy. Overall, dMRS evidenced that type C HE is characterized by complex and multicellular alterations beyond astrocyte swelling and holds enormous potential for future HE studies.

Data availability statement

The raw data supporting the conclusions of this article will be made available by the authors, without undue reservation.

Ethics statement

The animal study was approved by Committee on Animal Experimentation for the Canton de Vaud, Switzerland (VD 3022.1). The study was conducted in accordance with the local legislation and institutional requirements.

Author contributions

JM: Formal analysis, Methodology, Software, Visualization, Writing – review & editing. GB: Formal analysis, Methodology, Software, Visualization, Writing – review & editing. KP: Formal analysis, Methodology, Visualization, Writing – review & editing, Investigation, Writing – original draft. DS: Methodology, Writing – review & editing. AS: Methodology, Writing – review & editing, Formal analysis, Visualization. AA: Formal analysis, Methodology, Writing – review & editing, Visualization. IJ: Methodology, Software, Writing – review & editing. CC: Methodology, Software, Writing – review & editing, Conceptualization, Formal analysis, Funding acquisition, Investigation, Project administration, Resources, Supervision, Visualization, Writing – original draft.

Funding

The author(s) declare that financial support was received for the research, authorship, and/or publication of this article. CC, KP, and JM were supported by the CIBM Center for Biomedical Imaging of the UNIL, UNIGE, HUG, CHUV, EPFL, the Leenaards and Jeantet Foundations, and the SNSF project no. 310030_201218. IJ was supported by SNSF grant PCEFP2_194260. AS was supported by the Academy of Finland Research Project (#323385).

Acknowledgments

We would like to acknowledge the EPFL BioImaging & Optics Core Facility and, in particular, thank Knott Graham, Dubois Anaëlle Fabienne, and Rosset Stéphanie for their assistance in imaging and Julien Valette for his help with dMRS interpretation. The authors thank Stefanita Mitrea (CIBM) and Dario Sessa (HUG) for their help during BDL surgery, animal follow-up, sample collection, and for their assistance with histology.

Conflict of interest

The authors declare that the research was conducted in the absence of any commercial or financial relationships that could be construed as a potential conflict of interest.

Publisher's note

All claims expressed in this article are solely those of the authors and do not necessarily represent those of their affiliated organizations, or those of the publisher, the editors and the reviewers. Any product that may be evaluated in this article, or claim that may be made by its manufacturer, is not guaranteed or endorsed by the publisher.

Supplementary material

The Supplementary material for this article can be found online at: https://www.frontiersin.org/articles/10.3389/fnins.2024.1344076/full#supplementary-material

References

Abdollahzadeh, A., Belevich, I., Jokitalo, E., Sierra, A., and Tohka, J. (2021a). DeepACSON automated segmentation of white matter in 3D electron microscopy. *Commun. Biol.* 4, 179–114. doi: 10.1038/s42003-021-01699-w

Abdollahzadeh, A., Sierra, A., and Tohka, J. (2021b). Cylindrical shape decomposition for 3D segmentation of tubular objects. *IEEE Access* 9, 23979–23995. doi: 10.1109/ACCESS.2021.3056958

Adalid, V., Döring, A., Kyathanahally, S. P., Bolliger, C. S., Boesch, C., and Kreis, R. (2017). Fitting interrelated datasets: metabolite diffusion and general lineshapes. *MAGMA* 30, 429–448. doi: 10.1007/s10334-017-0618-z

Andersen, J. V., and Schousboe, A. (2023). Glial glutamine homeostasis in health and disease. *Neurochem. Res.* 48, 1100–1128. doi: 10.1007/s11064-022-03771-1

Behanova, A., Abdollahzadeh, A., Belevich, I., Jokitalo, E., Sierra, A., and Tohka, J. (2022). gACSON software for automated segmentation and morphology analyses of myelinated axons in 3D electron microscopy. *Comput. Methods Prog. Biomed.* 220:106802. doi: 10.1016/j.cmpb.2022.106802

Braissant, O., Rackayová, V., Pierzchala, K., Grosse, J., McLin, V. A., and Cudalbu, C. (2019). Longitudinal neurometabolic changes in the hippocampus of a rat model of chronic hepatic encephalopathy. *J. Hepatol.* 71, 505–515. doi: 10.1016/j.jhep.2019.05.022

Brand, A., Richter-Landsberg, C., and Leibfritz, D. (1993). Multinuclear NMR studies on the energy metabolism of glial and neuronal cells. *Dev. Neurosci.* 15, 289–298. doi: 10.1159/000111347

Callaghan, P. T., Jolley, K. W., and Lelievre, J. (1979). Diffusion of water in the endosperm tissue of wheat grains as studied by pulsed field gradient nuclear magnetic resonance. *Biophys. J.* 28, 133–141. doi: 10.1016/S0006-3495(79)85164-4

Cudalbu, C., Behar, K. L., Bhattacharyya, P. K., Bogner, W., Borbath, T., de Graaf, R. A., et al. (2021). Contribution of macromolecules to brain 1 H MR spectra: experts' consensus recommendations. *NMR Biomed.* 34:e4393. doi: 10.1002/nbm.4393

Cudalbu, C., and Taylor-Robinson, S. D. (2019). Brain Edema in chronic hepatic encephalopathy. *J. Clin. Exp. Hepatol.* 9, 362–382. doi: 10.1016/j.jceh.2019.02.003

de Marco, R., Ronen, I., Branzoli, F., Amato, M. L., Asllani, I., Colasanti, A., et al. (2022). Diffusion-weighted MR spectroscopy (DW-MRS) is sensitive to LPS-induced changes in human glial morphometry: a preliminary study. *Brain Behav. Immun.* 99, 256–265. doi: 10.1016/j.bbi.2021.10.005

DeMorrow, S., Cudalbu, C., Davies, N., Jayakumar, A. R., and Rose, C. F. (2021). 2021 ISHEN guidelines on animal models of hepatic encephalopathy. *Liver Int.* 41, 1474–1488. doi: 10.1111/liv.14911

Dharel, N., and Bajaj, J. S. (2015). Definition and nomenclature of hepatic encephalopathy. *J. Clin. Exp. Hepatol.* 5, S37–S41. doi: 10.1016/j.jceh.2014.10.001

Fendt, S.-M., and Verstreken, P. (2017). Neurons eat glutamate to stay alive. *J. Cell Biol.* 216, 863–865. doi: 10.1083/jcb.201702003

Flatt, E., Cudalbu, C., Braissant, O., Mitrea, S., Sessa, D., Gruetter, R., et al. (2017). 'Rifaximin in Chronic Liver Disease-induced Hepatic Encephalopathy: An *in vivo* longitudinal study of brain metabolism on BDL rats', *J. Clin. Exp. Hepatol.* 7, S55–S56. doi: 10.1016/j.jceh.2017.01.072

Gairing, S. J., Danneberg, S., Kaps, L., Nagel, M., Schleicher, E. M., Quack, C., et al. (2023). Elevated serum levels of glial fibrillary acidic protein are associated with covert hepatic encephalopathy in patients with cirrhosis. *JHEP Rep.* 5:100671. doi: 10.1016/j.jhepr.2023.100671

Genovese, G., Palombo, M., Santin, M. D., Valette, J., Ligneul, C., Aigrot, M. S., et al. (2021). Inflammation-driven glial alterations in the cuprizone mouse model probed with diffusion-weighted magnetic resonance spectroscopy at 11.7 T. *NMR Biomed.* 34:e4480. doi: 10.1002/nbm.4480

Govind, V., Young, K., and Maudsley, A. A. (2015). Corrigendum: proton NMR chemical shifts and coupling constants for brain metabolites. Govindaraju V, Young K, Maudsley AA, NMR biomed. 2000; 13: 129-153. *NMR Biomed.* 28, 923–924. doi: 10.1002/nbm.3336

Govindaraju, V., Young, K., and Maudsley, A. A. (2000). Proton NMR chemical shifts and coupling constants for brain metabolites. *NMR Biomed.* 13, 129–153. doi: 10.1002/1099-1492(200005)13:3<129::aid-nbm619>3.0.co;2-v

Gruetter, R. (1993). Automatic, localized in vivo adjustment of all first- and second-order shim coils. *Magn. Reson. Med.* 29, 804–811. doi: 10.1002/mrm.1910290613

Gruetter, R., and Tkác, I. (2000). Field mapping without reference scan using asymmetric echo-planar techniques. *Magn. Reson. Med.* 43, 319–323. doi: 10.1002/(sici)1522-2594(200002)43:2<319::aid-mrm22>3.0.co;2-1

Harris, J. L., Choi, I.-Y., and Brooks, W. M. (2015). Probing astrocyte metabolism in vivo: proton magnetic resonance spectroscopy in the injured and aging brain. *Front. Aging Neurosci.* 7:202. doi: 10.3389/fnagi.2015.00202

Häussinger, D., Dhiman, R. K., Felipo, V., Görg, B., Jalan, R., Kircheis, G., et al. (2022). Hepatic encephalopathy. *Nat. Rev. Dis. Primers* 8:43. doi: 10.1038/s41572-022-00366-6

Häussinger, D., Kircheis, G., Fischer, R., Schliess, F., and Dahl, S. (2000). Hepatic encephalopathy in chronic liver disease: a clinical manifestation of astrocyte swelling and low-grade cerebral edema? *J. Hepatol.* 32, 1035–1038. doi: 10.1016/s0168-8278(00)80110-5

Häussinger, D., Laubenberger, J., Vom Dahl, S., Ernst, T., Bayer, S., Langer, M., et al. (1994). Proton magnetic resonance spectroscopy studies on human brain myo-inositol in hypo-osmolarity and hepatic encephalopathy. *Gastroenterology* 107, 1475–1480. doi: 10.1016/0016-5085(94)90552-5

Heneka, M. T., Kummer, M. P., and Latz, E. (2014). Innate immune activation in neurodegenerative disease. *Nat. Rev. Immunol.* 14, 463–477. doi: 10.1038/nri3705

Hering, H., and Sheng, M. (2001). Dendritic spines: structure, dynamics and regulation. *Nat. Rev. Neurosci.* 2, 880–888. doi: 10.1038/35104061

Jelescu, I. O., and Budde, M. D. (2017). Design and validation of diffusion MRI models of white matter. *Front. Phys.* 5:61. doi: 10.3389/fphy.2017.00061

Jelescu, I. O., Palombo, M., Bagnato, F., and Schilling, K. G. (2020). Challenges for biophysical modeling of microstructure. *J. Neurosci. Methods* 344:108861. doi: 10.1016/j.jneumeth.2020.108861

Kale, R. A., Gupta, R. K., Saraswat, V. A., Hasan, K. M., Trivedi, R., Mishra, A. M., et al. (2006). Demonstration of interstitial cerebral edema with diffusion tensor MR imaging in type C hepatic encephalopathy. *Hepatology* 43, 698–706. doi: 10.1002/hep.21114

Kinsey, S. T., Locke, B. R., and Dillaman, R. M. (2011). Molecules in motion: influences of diffusion on metabolic structure and function in skeletal muscle. *J. Exp. Biol.* 214, 263–274. doi: 10.1242/jeb.047985

Kiselev, V. G., and Il'yasov, K. A. (2007). Is the "biexponential diffusion" biexponential? *Magn. Reson. Med.* 57, 464–469. doi: 10.1002/mrm.21164

Kreis, R. (2016). The trouble with quality filtering based on relative Cramér-Rao lower bounds. *Magn. Reson. Med.* 75, 15–18. doi: 10.1002/mrm.25568

Kunz, N., Cudalbu, C., Mlynarik, V., Hüppi, P. S., Sizonenko, S. V., and Gruetter, R. (2010). Diffusion-weighted spectroscopy: a novel approach to determine macromolecule resonances in short-echo time 1H-MRS. *Magn. Reson. Med.* 64, 939–946. doi: 10.1002/mrm.22490

Lanz, B., Rackayova, V., Braissant, O., and Cudalbu, C. (2017). MRS studies of neuroenergetics and glutamate/glutamine exchange in rats: extensions to hyperammonemic models. *Anal. Biochem.* 529, 245–269. doi: 10.1016/j.ab.2016.11.021

Laule, C., Vavasour, I. M., Kolind, S. H., Li, D. K. B., Traboulsee, T. L., Moore, G. R. W., et al. (2007). Magnetic resonance imaging of myelin. *Neurotherapeutics* 4, 460–484. doi: 10.1016/j.nurt.2007.05.004

Ligneul, C., Najac, C., Döring, A., Beaulieu, C., Branzoli, F., Clarke, W. T., et al. (2024). Diffusion-weighted MR spectroscopy: consensus, recommendations, and resources from acquisition to modeling. *Magn. Reson. Med.* 91, 860–885. doi: 10.1002/mrm.29877

Ligneul, C., Palombo, M., Hernández-Garzón, E., Carrillo-de Sauvage, M. A., Flament, J., Hantraye, P., et al. (2019). Diffusion-weighted magnetic resonance spectroscopy enables cell-specific monitoring of astrocyte reactivity in vivo. *NeuroImage* 191, 457–469. doi: 10.1016/j.neuroimage.2019.02.046

Lin, A., Andronesi, O., Bogner, W., Choi, I. Y., Coello, E., Cudalbu, C., et al. (2021). Minimum reporting standards for in vivo magnetic resonance spectroscopy (MRSinMRS): experts' consensus recommendations. *NMR Biomed.* 34:e4484. doi: 10.1002/nbm.4484

Martinez-Hernandez, A., Bell, K. P., and Norenberg, M. D. (1977). Glutamine synthetase: glial localization in brain. *Science (New York, N.Y.)* 195, 1356–1358. doi: 10.1126/science.14400

MOFFETT, J., ROSS, B., ARUN, P., MADHAVARAO, C., and NAMBOODIRI, A. (2007). N-Acetylaspartate in the CNS: from neurodiagnostics to neurobiology. *Prog. Neurobiol.* 81, 89–131. doi: 10.1016/j.pneurobio.2006.12.003

Monfort, P., Cauli, O., Montoliu, C., Rodrigo, R., Llansola, M., Piedrafita, B., et al. (2009). Mechanisms of cognitive alterations in hyperammonemia and hepatic encephalopathy: therapeutical implications. *Neurochem. Int.* 55, 106–112. doi: 10.1016/j.neuint.2009.01.021

Mosso, J., Simicic, D., Lanz, B., Gruetter, R., and Cudalbu, C. (2024). Diffusion-weighted SPECIAL improves the detection of J-coupled metabolites at ultrahigh magnetic field. *Magn. Reson. Med.* 91, 4–18. doi: 10.1002/mrm.29805

Mosso, J., Yin, T., Poitry-Yamate, C., Simicic, D., Lepore, M., McLin, V. A., et al. (2022). 'PET CMRglc mapping and 1H-MRS show altered glucose uptake and neurometabolic profiles in BDL rats', *Anal. Biochem.* 647:114606. doi: 10.1016/j.ab.2022.114606

Nahirney, P. C., and Tremblay, M.-E. (2021). Brain Ultrastructure: Putting the Pieces Together. *Front. Cell Dev. Biol.* 9:629503. doi: 10.3389/fcell.2021.629503

Najac, C., Branzoli, F., Ronen, I., and Valette, J. (2016). Brain intracellular metabolites are freely diffusing along cell fibers in grey and white matter, as measured by diffusion-weighted MR spectroscopy in the human brain at 7 T. *Brain Struct. Funct.* 221, 1245–1254. doi: 10.1007/s00429-014-0968-5

Najac, C., Marchadour, C., Guillermier, M., Houitte, D., Slavov, V., Brouillet, E., et al. (2014). Intracellular metabolites in the primate brain are primarily localized in long fibers rather than in cell bodies, as shown by diffusion-weighted magnetic resonance spectroscopy. *NeuroImage* 90, 374–380. doi: 10.1016/j.neuroimage.2013.12.045

Palombo, M., Ligneul, C., Najac, C., le Douce, J., Flament, J., Escartin, C., et al. (2016). New paradigm to assess brain cell morphology by diffusion-weighted MR spectroscopy in vivo. *Proc. Natl. Acad. Sci. USA* 113, 6671–6676. doi: 10.1073/pnas.1504327113

Palombo, M., Shemesh, N., Ronen, I., and Valette, J. (2018). Insights into brain microstructure from in vivo DW-MRS. *NeuroImage* 182, 97–116. doi: 10.1016/j.neuroimage.2017.11.028

Pierzchala, K., Hadjihambi, A., Mosso, J., Jalan, R., Rose, C. F., and Cudalbu, C. (2023). Lessons on brain edema in HE: from cellular to animal models and clinical studies. *Metab. Brain Dis.* doi: 10.1007/s11011-023-01269-5

Pierzchala, K., Simicic, D., Sienkiewicz, A., Sessa, D., Mitrea, S., Braissant, O., et al. (2022). Central nervous system and systemic oxidative stress interplay with inflammation in a bile duct ligation rat model of type C hepatic encephalopathy. *Free Radic. Biol. Med.* 178, 295–307. doi: 10.1016/j.freeradbiomed.2021.12.011

Rackayova, V., Braissant, O., McLin, V. A., Berset, C., Lanz, B., and Cudalbu, C. (2016). 1H and 31P magnetic resonance spectroscopy in a rat model of chronic hepatic encephalopathy: in vivo longitudinal measurements of brain energy metabolism. *Metab. Brain Dis.* 31, 1303–1314. doi: 10.1007/s11011-015-9715-8

Rackayova, V., Cudalbu, C., Pouwels, P. J. W., and Braissant, O. (2017). Creatine in the central nervous system: from magnetic resonance spectroscopy to creatine deficiencies. *Anal. Biochem.* 529, 144–157. doi: 10.1016/j.ab.2016.11.007

Rackayová, V., Flatt, E., Braissant, O., Grosse, J., Capobianco, D., Mastromarino, P., et al. (2021). Probiotics improve the neurometabolic profile of rats with chronic cholestatic liver disease. *Sci. Rep.* 11:2269. doi: 10.1038/s41598-021-81871-8

Rae, C. D. (2014). A guide to the metabolic pathways and function of metabolites observed in human brain 1H magnetic resonance spectra. *Neurochem. Res.* 39, 1–36. doi: 10.1007/s11064-013-1199-5

Santamaria, F., Wils, S., de Schutter, E., and Augustine, G. J. (2006). Anomalous diffusion in Purkinje cell dendrites caused by spines. *Neuron* 52, 635–648. doi: 10.1016/j.neuron.2006.10.025

Santamaria, F., Wils, S., de Schutter, E., and Augustine, G. J. (2011). The diffusional properties of dendrites depend on the density of dendritic spines. *Eur. J. Neurosci.* 34, 561–568. doi: 10.1111/j.1460-9568.2011.07785.x

Simicic, D., Cudalbu, C., and Pierzchala, K. (2022). Overview of oxidative stress findings in hepatic encephalopathy: from cellular and ammonium-based animal models to human data. *Anal. Biochem.* 654:114795. doi: 10.1016/j.ab.2022.114795

Simicic, D., Pierzchala, K., Rackayová, V., Braissant, O., Mitrea, S. O., Sessa, D., et al. (2019). P: 33 in vivo longitudinal 1H MRS study of hippocampal, Cereberal and striatal metabolic changes in the adult brain using an animal model of chronic hepatic encephalopathy. *Am. J. Gastroenterol.* 114:S17. doi: 10.14309/01.ajg.0000582108.29364.13

Simicic, D., Rackayova, V., Xin, L., Tkáč, I., Borbath, T., Starcuk, Z. Jr., et al. (2021). In vivo macromolecule signals in rat brain 1H-MR spectra at 9.4T: parametrization, spline baseline estimation, and T2 relaxation times. *Magn. Reson. Med.* 86, 2384–2401. doi: 10.1002/mrm.28910

Skripuletz, T., Manzel, A., Gropengießer, K., Schäfer, N., Gudi, V., Singh, V., et al. (2015). Pivotal role of choline metabolites in remyelination. *Brain J. Neurol.* 138, 398–413. doi: 10.1093/brain/awu358

Urenjak, J., Williams, S. R., Gadian, D. G., and Noble, M. (1993). Proton nuclear magnetic resonance spectroscopy unambiguously identifies different neural cell types. *J. Neurosci.* 13, 981–989. doi: 10.1523/JNEUROSCI.13-03-00981.1993

Vangelderen, P., Despres, D., Vanzijl, P. C. M., and Moonen, C. T. W. (1994). Evaluation of restricted diffusion in cylinders. Phosphocreatine in rabbit leg muscle. *J. Magn. Reson. B* 103, 255–260. doi: 10.1006/jmrb.1994.1038

Zaqout, S., and Kaindl, A. M. (2016). Golgi-Cox Staining Step by Step. *Front. Neuroanat.* 10:38. doi: 10.3389/fnana.2016.00038

Zeisel, S. H., Char, D., and Sheard, N. F. (1986). Choline, phosphatidylcholine and sphingomyelin in human and bovine milk and infant formulas. *J. Nutr.* 116, 50–58. doi: 10.1093/jn/116.1.50

frontiers | Frontiers in Oncology

TYPE Original Research
PUBLISHED 07 May 2024
DOI 10.3389/fonc.2024.1241776

OPEN ACCESS

EDITED BY
Maryam Afzali,
University of Leeds, United Kingdom

REVIEWED BY
Álvaro Planchuelo-Gómez,
University of Valladolid, Spain
Bilgin Kadri Aribas,
Bülent Ecevit University, Türkiye

*CORRESPONDENCE
Jiuquan Zhang
zhangjq_radiol@foxmail.com
Daihong Liu
liudaihong121@163.com

†These authors share first authorship

RECEIVED 10 July 2023
ACCEPTED 22 April 2024
PUBLISHED 07 May 2024

CITATION
Jiang L, Chen J, Tan Y, Wu J, Zhang J, Liu D and Zhang J (2024) Comparative analysis of the image quality and diagnostic performance of the zooming technique with diffusion-weighted imaging using different b-values for thyroid papillary carcinomas and benign nodules.
Front. Oncol. 14:1241776.
doi: 10.3389/fonc.2024.1241776

Comparative analysis of the image quality and diagnostic performance of the zooming technique with diffusion-weighted imaging using different b-values for thyroid papillary carcinomas and benign nodules

Liling Jiang[1†], Jiao Chen[2†], Yong Tan[2], Jian Wu[3], Junbin Zhang[3], Daihong Liu[2*] and Jiuquan Zhang[2*]

[1]Department of Radiology, Shapingba Hospital affiliated to Chongqing University (Shapingba District People's Hospital of Chongqing), Chongqing, China, [2]Department of Radiology, Chongqing University Cancer Hospital, Chongqing, China, [3]Head and Neck Cancer Center, Chongqing University Cancer Hospital, Chongqing, China

Objective: To compare image quality and diagnostic performance using different b-values for the zooming technique with diffusion-weighted imaging (ZOOMit-DWI) in thyroid nodules

Materials and methods: A total of 51 benign thyroid nodules and 50 thyroid papillary carcinomas were included. ZOOMit-DWI was performed with b-values of 0, 500, 1000, 1500 and 2000 s/mm^2. The sharpness was evaluated as subjective index. The signal intensity ratio (SIR), signal-to-noise ratio (SNR) and apparent diffusion coefficient (ADC) were measured as objective indices. Pairwise comparisons were performed among the different b-value groups using the *Friedman* test. A receiver operating characteristic curve of the ADC value was used to evaluate diagnostic performance. The DeLong test was used to compare diagnostic effectiveness among the different b-value groups

Results: In both the papillary carcinoma group (P = 0.670) and the benign nodule group (P = 0.185), the sharpness of nodules was similar between b-values of 1000 s/mm^{2}and 1500 s/mm^2. In the papillary carcinoma group, the SIR_{nodule} was statistically higher in DWI images with a b-value of 1500 s/mm^{2}than in DWI images with b-values of 500 s/mm^2(P = 0.004), 1000 s/mm^2(P = 0.002), and 2000 s/mm^2(P = 0.003). When the b-values were 1500 s/mm^2(P = 0.008) and 2000 s/mm^2(P = 0.009), the SIR_{nodule} significantly differed between the papillary carcinoma group and the benign nodule group. When b = 500 s/mm^2, the ADC had an AUC of 0.888. When b = 1000 s/mm^2, the ADC had an AUC of 0.881. When b = 1500 s/mm^2, the ADC had an AUC of 0.896. When b = 2000 s/mm^2, the ADC had an AUC of 0.871. The DeLong test showed comparable diagnostic effectiveness among the different b-value groups except for between b-values of 2000 s/mm^{2}and 1500 s/mm^2, with a b-value of 2000 s/mm^{2}showing lower effectiveness

Conclusion: This study suggests that 1500 s/mm^{2}may be a suitable b-value to differentiate benign and malignant thyroid nodules in ZOOMit-DWI images, which yielded better image quality

KEYWORDS

diffusion-weighted imaging, b-value, thyroid nodule, image quality, diagnostic performance

Introduction

Thyroid nodules are found in 19-67% of asymptomatic individuals using ultrasonography (1). Among these nodules, 10-15% of nodules are malignant (2). In patients with malignant nodules, early diagnosis and active follow-up treatment can elevate the 10-year survival rate to 90% (3). Therefore, it is essential to find a reliable non-invasive imaging tool to diagnose malignant thyroid nodules.

Ultrasound is a noninvasive technique for identifying thyroid nodules; however, the result can vary depending on the evaluator (4). Fine needle aspiration is an invasive examination, and one-third of the results are inconclusive (2). Computed tomography is limited in differentiating between malignant and benign thyroid nodules and has the disadvantage of radiation exposure. Many authors have investigated the important value of diffusion-weighted imaging (DWI) in differentiation between malignant and benign thyroid nodules (3, 5–8). With the development of magnetic resonance imaging (MRI), DWI has become a popular modality for identifying thyroid nodules in recent years and can assess the Brownian motion of water molecules at the cellular level (9).

In malignant nodules, water movement is restricted due to increased cellularity and reduced extracellular space. In most previous thyroid studies, the b-value of DWI was lower than 1000 s/mm^2 for differentiation between benign and malignant lesions (3, 5–8). With the advancement of high-field and DWI MRI techniques, high-b-value DWI of the thyroid has become much simpler. Past studies have shown that a high b-value of 2000 s/mm^2 is optimal for the diagnosis and differential diagnosis of thyroid nodules (10, 11). However, only a b-value of 800 s/mm^{2}was compared to 2000 s/mm^2 in the above study, and the diagnostic performance of b-values from 800 to 2000 s/mm^2 is unknown.

In MRI exams, the b-value is an index indicating the degree of sensitivity to diffusion in the images. The choice of b-value does, to some extent affect the distortion as the eddy currents may be weaker for smaller b-values, but susceptibility arguably is the main source of image distortion in DWI. Higher b values produce increased signal attenuation and usually requires increased signal averaging to compensate for the signal-to-noise ratio. Most malignant thyroid nodules were papillary carcinomas. The community still have not reached a consensus regarding the optimal b value for MRI exams to detect thyroid papillary carcinomas. Therefore, the optimal b-value to differentiate between thyroid papillary carcinomas and thyroid benign nodules in clinical applications must be explored.

In this study, we combined image quality and differential diagnostic performance to determine the optimal b-value for DWI detection of thyroid papillary carcinomas and thyroid benign nodules. Image quality included subjective and objective aspects. The zooming technique with diffusion-weighted imaging (ZOOMit-DWI) was used in this study, which entails a reduced field of view. We hypothesized that ZOOMit-DWI would show excellent performance in the thyroid. We aimed to identify the optimal b-value for differentiating thyroid papillary carcinomas and thyroid benign nodules.

Materials and methods

Patient enrollment and thyroid nodule selection

All procedures performed in this study involving human participants were in accordance with the ethical standards of the research committee and approved by the local research committee (IRB No. CZLS2021207-A). Informed consent was signed by all study participants. The study recruited 95 consecutive patients in Chongqing University Cancer Hospital from July 2021 to May 2022. All patients underwent thyroid MRI examinations in this study. Data collection was planned before surgical pathological results were performed.

The inclusion criteria were as follows: a) planned thyroid nodule surgical treatment; b) no needle biopsy or treatment before surgery; c) the pathologic finding was thyroid papillary carcinoma or thyroid benign nodule. The exclusion criteria were as follows: a) contraindications to MRI examination; b) obvious artifacts on DWI; c) incomplete DWI imaging data; d) the pathologic finding was borderline neoplasm.

Abbreviations: ADC, Apparent diffusion coefficient; DWI, Diffusion-weighted imaging; MRI, Magnetic resonance imaging; ROC, Receiver operating characteristic; ROI, Region of interest; SD, standard deviation; SI, Signal intensity; SIR, Signal intensity ratio; SNR, signal-to-noise ratio; ZOOMit-DWI, Zooming technique with diffusion-weighted imaging.

Sample size

There are no generally accepted approaches to estimate the sample size requirements for derivation studies, however, we ensured that the study met suggested requirements of having at least 10 events per candidate variable for the derivation of a model.

Examination method

In this study, Prisma 3.0 T MRI (Simens Healthcare, Germany Erlangen) was used for examination on MRI with a 16channel surface coil (Zhongzhi Medical, China Jiangsu). ZOOMit-DWI was performed with the following diffusion gradient b factors: 0, 500, 1000, 1500 and 2000 s/mm^2. ZOOMit-DWI uses the availability of fully independent parallel radiofrequency transmission coils, allowing excitation of selective "inner volumes" (12). When the field of view is reduced, the readout tends to be faster which decreases the susceptibility artifacts. The smaller field of view can also be used to enable higher spatial resolution without increasing the readout duration (13). The imaging parameters for DWI were TR: 4600 ms; TE: 72 ms; FOV (RL x AP): 160 × 58 mm; average: 1 (b=0 s/mm^2), 4 (b=500 s/mm^2), 6 (b=1000 s/mm^2), 9 (b=1500 s/mm^2), and 13(b=2000 s/mm^2); matrix size (RL x AP): 110 × 36 mm; slice thickness: 3 mm; intersection gap: 0.3 mm; diffusion gradient orientations: 3; flip angle:150; and examination time: 439 s. The imaging parameters for T2WI were TR: 3000 ms; TE: 88 ms; FOV: 200 × 200mm; average: 4; matrix size: 256×256; slice thickness: 3 mm; intersection gap: 0.3 mm; flip angle:150; and examination time: 158 s.

Image analysis

All morphological images and DWI images were evaluated in Siemens workstation (syngo.via). DWI images were evaluated by a radiologist (LLJ). To evaluate reproducibility, all nodules were evaluated one month later by the same radiologist (LLJ) and one other radiologist (JC). Image quality analysis included subjective and objective aspects. Diagnostic efficacy was evaluated according to differential diagnostic performance. Only the largest nodule was evaluated in one lobule.

Subjective image quality analysis

Subjective image quality of nodules and thyroids on DWI images with different b-values was evaluated respectively according to 4-point scale depending on sharpness: 4 = the boundary was clearly depicted; 3 = the boundary was unclearly depicted; 2 = the boundary was indistinctly visible; 1 = the nodule or thyroid cannot be displayed.

Objective image quality analysis

Signal intensity (SI) and standard deviation (SD) was measured in the nodule, thyroid and air in the same slice. The region of interest (ROI) of nodules was manually drawn along the nodule margin. The ROI of the thyroid was the largest and usually circularly drawn on normal regions of the thyroid gland. The ROI for air was circularly drawn around air in the trachea. First, an ROI was drawn on DWI image with b = 0 s/mm^2. Then, the ROI was copied to DWI images with b = 500, 1000, 1500, and 2000 s/mm^2.The cystic and hemorrhagic areas were avoided. Then, the signal intensity ratio (SIR) of nodules and signal-to-noise ratio (SNR) of thyroids were calculated according to the following formula: $SIR_{nodule}=(SI_{nodule}-SI_{thyroid})/SI_{thyroid}$; $SNR_{thyroid}=SI_{thyroid}/SD_{air}$ (14).

Differential diagnostic efficacy analysis

The mean apparent diffusion coefficient (ADC) was measured in different ADC maps (b = 500, 1000, 1500, 2000 s/mm^2). ADC calculated using the following formulas: ADC=In(S0/S1)/(b1-b0). The b0 mean 0. The b1 mean 500, 1000, 1500 0r 2000. S0 represented the signal intensity of ROI in the DWI images of b = 0 s/mm^2. S1 represented the signal intensity of ROI in the DWI images of b = 500, 1000, 1500 0r 2000 s/mm^2. The extraction of the ADC values was automatically performed by the Siemens workstation (syngo.via).

Four ADC values were recorded for each nodule. An ROI was manually drawn along the nodule margin. First, the ROI was drawn on a DWI image with b = 0 s/mm^2, and then the ROI was copied to different ADC maps. The above ROI was in the same slice, and cystic and hemorrhagic areas were avoided.

Pathology

According to long-time clinic experience, the histopathologic examination was used as the gold standards. All surgically resected nodules were subjected to an intra-operative frozen section for preliminary risk assessment. If the nodule was diagnosed as a benignancy by intra-operative frozen section, total thyroidectomy would not be applied and the specimen of lobectomy would be acquired for further paraffin section. If the nodule was suspicious malignant or atypical, total thyroidectomy would be further given and the specimen of total thyroidectomy would be acquired for further paraffin section and immunohistochemical staining. According to pathological examination results, the nodules were assigned to either the papillary carcinoma group or benign nodule group.

Statistical analysis

The statistical analyses were calculated on personal computers utilizing the Statistical Package for Social Sciences (SPSS–windows version 25.0). All variabilities of subjective and objective evaluation derived from MRI were exploratory. The interobserver and intraobserver variability were assessed by determining intraclass correlation coefficients, with the values of <0.50, 0.50–0.75, 0.75–0.90, >0.90 reflecting poor, moderate, good and excellent correlations (15). The interobserver agreement selected two-way

random model and intraobserver agreement selected two-way mixed model. Subjective and objective evaluation results were compared among the different b-value groups. The Kolmogorov–Smirnov test was performed to analyze normality. According to the results of the Kolmogorov–Smirnov test, Student's *t* test or Mann-Whitney *u* test was used to compare difference between papillary carcinomas and benign nodules. The data did not conform to a normal distribution. *Friedman* test was applied to assess whether significant differences existed among different b-value groups. Bonferroni correction was a useful technique for controlling the family-wise error rate in multiple comparisons. The area under the receiver operating characteristic (ROC) curve was also calculated. From ROC curve analysis on different b values, an optimal cut-off value of ADC to predict thyroid papillary carcinoma was determined by using Youden index. Youden's index = sensitivity + specificity−1. Based on this data-driven cut-off value, sensitivity, specificity and 95% confidence intervals were calculated. The DeLong test was used to assess the area under the curve values and compare diagnostic effectiveness among the different b-value groups.

Results

Clinical data

Of the 95 patients, 5 patients were excluded (3 with incomplete imaging data, 2 with severe artifacts on DWI, 4 were females, 1 was male, with ages ranging from 43 to 61 years old). Ultimately, the 104 nodules from 90 patients were included in this study. 68 were females, and 22 were males, and ages were 47.69 ± 12.09 ranging from 21 to 77 years old. Patients had surgical pathological results within a week after MRI. 53 nodules were malignant (50 papillary carcinomas, 1 follicular carcinoma, 1 medullary carcinoma, 1 metastatic tumor), and 51 nodules were benign (25 adenomas, 19 nodular goiters, 2 goiters with adenomatous hyperplasia, 2 cases of Hashimoto's thyroiditis, 2 cases of subacute thyroiditis, 1 case of granulomatous inflammation). There was not any adverse event in this study. The flow chart was showed in Figure 1.

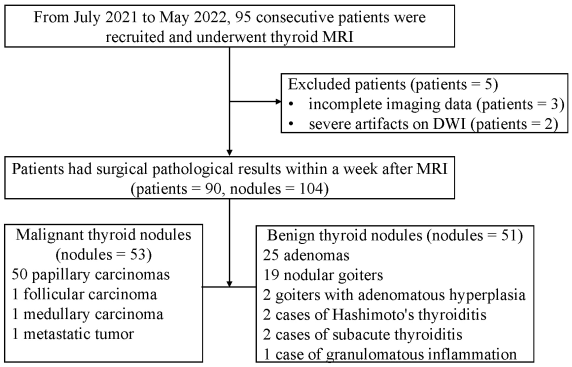

FIGURE 1
Flowchart of this study.

Interobserver and intraobserver agreement

Interobserver agreement was moderate and good (0.746-0.965) for subjective evaluations of thyroids and nodules, respectively (Table 1). Interobserver agreement was moderate and good (0.739-0.979) for objective evaluations of thyroids and nodules (Table 1). Intraobserver agreement was good and excellent (0.908-0.978) for subjective evaluations of thyroids and nodules, respectively (Table 1). Intraobserver agreement was good and excellent (0.811-0.995) for objective evaluations of thyroids and nodules (Table 1).

Evaluation of subjective image quality

The sharpness of thyroids decreased as the b value increased (Figure 2A). The multiple comparison results of sharpness are shown in Table 2. In both the papillary carcinoma group (P = 0.670) (Figure 2B) and benign nodule group (P = 0.185) (Figure 2C), the sharpness of nodules was similar between images with a b-value of 1000 s/mm^2 and those with a b-value of 1500 s/mm^2.

TABLE 1 The interobserver and intraobserver agreement of measurements of thyroid nodules.

		Inter-observer		Intrao-bserver	
		ICC value	95% CI	ICC value	95% CI
Signal intensity	Nodule (b=500)	0.929	0.846-0.985	0.995	0.992-0.997
	Thyroid (b=500)	0.834	0.706-0.921	0.991	0.987-0.994
	Air (b=500)	0.892	0.840-0.927	0.992	0.988-0.994
	Nodule (b=1000)	0.898	0.760-0.899	0.991	0.988-0.995
	Thyroid (b=1000)	0.889	0.839-0.890	0.992	0.988-0.995
	Air (b=1000)	0.862	0.796-0.907	0.992	0.989-0.995
	Nodule (b=1500)	0.953	0.792-0.991	0.993	0.990-0.996

(Continued)

10.3389/fonc.2024.1241776

TABLE 1 Continued

		Inter-observer		Intrao-bserver	
		ICC value	95% CI	ICC value	95% CI
	Thyroid (b=1500)	0.829	0.750-0.850	0.988	0.982-0.992
	Air (b=1500)	0.880	0.822-0.919	0.983	0.975-0.988
	Nodule (b=2000)	0.890	0.837-0.926	0.994	0.991-0.996
	Thyroid (b=2000)	0.839	0.816-0.889	0.811	0.772-0.887
	Air (b=2000)	0.922	0.884-0.947	0.995	0.992-0.996
Diagnostic performance	ADC (b=500)	0.837	0.806-0.857	0.892	0.808-0.894
	ADC (b=1000)	0.739	0.709-0.759	0.892	0.888-0.895
	ADC (b=1500)	0.941	0.913-0.906	0.889	0.883-0.892
	ADC (b=2000)	0.979	0.969-0.986	0.984	0.976-0.989
Sharpness	Nodule (b=500)	0.765	0.748-0.776	0.922	0.737-0.980
	Nodule (b=1000)	0.863	0.845-0.875	0.960	0.799-0.993
	Nodule (b=1500)	0.876	0.864-0.884	0.934	0.903-0.956
	Nodule (b=2000)	0.882	0.873-0.888	0.908	0.867-0.937
	Thyroid (b=500)	0.965	0.948-0.976	0.978	0.968-0.985
	Thyroid (b=1000)	0.746	0.720-0.764	0.915	0.874-0.943
	Thyroid (b=1500)	0.766	0.749-0.777	0.920	0.881-0.946
	Thyroid (b=2000)	0.846	0.750-0.877	0.919	0.880-0.946

ADC, apparent diffusion coefficient; CI, confidence interval; ICC, intraclass correlation coefficients.

Evaluation of objective image quality

The $SNR_{thyroid}$ decreased as the b value increased (Figure 3A). In the papillary carcinoma group (Figure 3B), the SIR_{nodule} was statistically higher in DWI images with a b-value of 1500 s/mm^2 than in DWI images with b-values of 500 s/mm^2 (P= 0.004), 1000 s/mm^2 (P = 0.002), and 2000 s/mm^2 (P = 0.003). In the benign nodule group (Figure 3C), the SIR_{nodule} was statistically lower in DWI images with a b-value of 1500 s/mm^2 than in DWI images with b-values of 1000 s/mm^2 (P = 0.017) and 2000 s/mm^2 (P = 0.006). The multiple comparison results of nodule sharpness are shown in Table 3. When the b-values were 1500 s/mm^2 (P = 0.008) and 2000 s/mm^2 (P = 0.009), the SIR_{nodule} significantly differed between the papillary carcinoma group and the benign nodule group (Table 4). In DWI images with a b-value of 1500 s/mm^2, the difference in SI between malignant and benign nodules was visible to the naked eye (Figures 4–7).

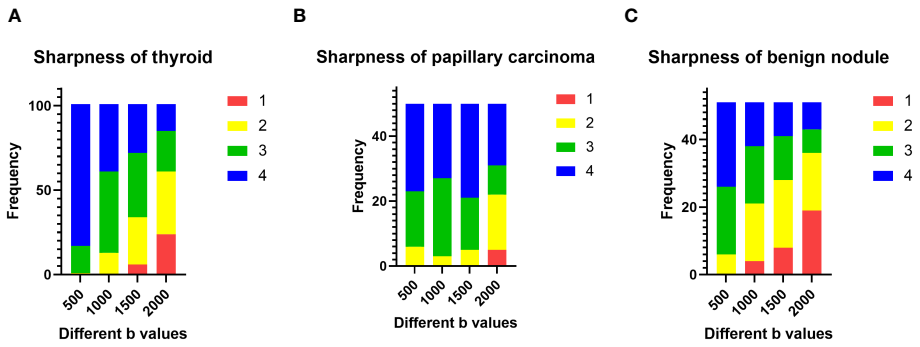

FIGURE 2
Evaluation of subjective image quality: **(A)** the sharpness of the thyroid decreased as the b value increased; **(B)** in the papillary carcinoma group, the sharpness of nodules was similar between b-values of 1000 s/mm^2 and 1500 s/mm^2; **(C)** in the benign nodule group, the sharpness of nodules was similar between b-values of 1000 s/mm^2 and 1500 s/mm^2.

TABLE 2 The pairwise comparison of sharpness of nodules and thyroids with different b-values (×10^{-3} s/mm^2) in DWI images.

	500-1000 (*P*)	500-1500 (*P*)	500-2000 (*P*)	1000-1500 (*P*)	1000-2000 (*P*)	1500-2000 (*P*)
Papillary carcinoma	0.877	0.786	0.002	0.670	0.004	< 0.001
Benign nodule	0.002	< 0.001	< 0.001	0.185	0.001	0.060
Thyroid	< 0.001	< 0.001	< 0.001	0.005	< 0.001	< 0.001

DWI, diffusion-weighted imaging.

Diagnostic performance evaluation

Quantitative ADC measurements under different b-values all differed significantly between malignant and benign thyroid nodules ($P < 0.05$). The mean ADCs of malignant and benign thyroid nodules are shown in Table 5. When b = 500 s/mm^2, the ADC had an AUC of 0.888, a sensitivity of 84.31%, and a specificity of 84.37%. When b = 1000 s/mm^2, the ADC had an AUC of 0.881, a sensitivity of 78.34%, and a specificity of 89.97%. When b = 1500 s/mm^2, the ADC had an AUC of 0.896, a sensitivity of 86.27%, and a specificity of 90.57%. When b = 2000 s/mm^2, the ADC had an AUC of 0.871, a sensitivity of 80.39%, and a specificity of 89.99% (Table 6, Figure 8). The DeLong test showed comparable diagnostic effectiveness among the different b-value groups except for between b-values of 2000 s/mm^2 and 1500 s/mm^2, with a b-value of 2000 s/mm^2 showing lower effectiveness (Table 7).

Discussion

DWI is an important method to differentiate malignant from benign lesions, but the most appropriate b-values for such differentiation are unknown because different tumors within different organs or tissues may have different sensitivities and specificities to different b-values. The purpose of this study was to explore the best b-value in ZOOMit-DWI to differential diagnosis. The results suggest that 1500 s/mm^2 was a suitable b value for differentiating thyroid papillary carcinomas and thyroid benign nodules, which yielded better diagnostic performance and image quality. Thyroid papillary carcinomas and thyroid benign nodules can be differentiated by comparing signals from thyroid nodules on DWI images.

About the evaluation of subjective image quality, the sharpness of the thyroid decreased as the b value increased. The b-value is an important factor in DWI. On low-b-value images, the diffusion characteristic of tissues has only a small impact. Higher-b-value images are noisier and much darker (a low signal-to-noise ratio) and have the disadvantage of requiring considerable time for acquisition (16). Images with high b-values are of great significance in detection of benign and malignant nodules (17). In this study, when the b-values were 1500 s/mm^2 and 2000 s/mm^2, the SIR_{nodule} significantly differed between the papillary carcinoma and benign nodule. Because at higher b-values, tissues with high water molecule path lengths tend to lose signal rapidly (18). In addition, the b value plays a crucial role in ADC measurements. The ADC values are derived by DWI data to a monoexponential model using

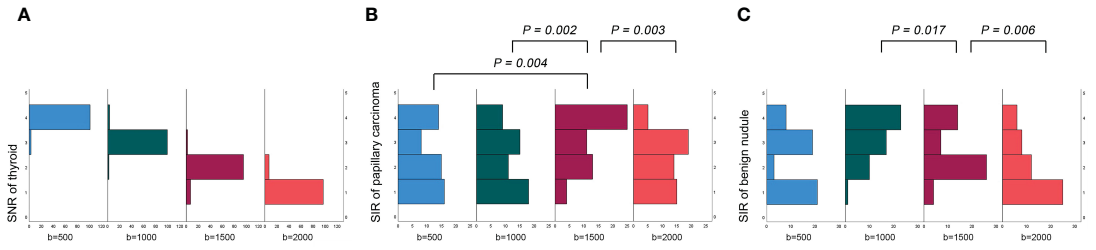

FIGURE 3
Evaluation of objective image quality: **(A)** the SNR of the thyroid decreased as the b value increased; **(B)** in the papillary carcinoma group, the SIR of nodules was statistically higher in DWI images with a b-value of 1500 s/mm^2 than in DWI images with b-values of 500 s/mm^2, 1000 s/mm^2 and 2000 s/mm^2; **(C)** in the benign nodule group, the SIR of nodules was statistically lower in DWI images with a b-value of 1500 s/mm^2 than in DWI images with b-values of 1000 s/mm^2 and 20000 s/mm^2.

TABLE 3 The pairwise comparison of SIR_{nodule} and $SNR_{thyroid}$ with different b-values (×10^{-3} s/mm^2) in DWI images.

	500-1000 (*P*)	500-1500 (*P*)	500-2000 (*P*)	1000-1500 (*P*)	1000-2000 (*P*)	1500-2000 (*P*)
$SIR_{papillary\ carcinoma}$	0.816	0.004	0.877	0.002	0.938	0.003
$SIR_{benign\ nodule}$	< 0.001	0.192	0.145	0.017	< 0.001	0.006
$SNR_{thyroid}$	< 0.001	< 0.001	< 0.001	< 0.001	< 0.001	< 0.001

DWI, diffusion-weighted imaging; SIR, signal intensity ratio; SNR, signal-to-noise ratio.

TABLE 4 Comparison of the SIR_{nodule} values of papillary carcinomas and benign nodules with different b-values ($\times10^{-3}$ s/mm^2) in DWI images.

	500	1000	1500	2000
Papillary carcinoma	0.61 ± 0.46	0.65 ± 0.80	1.05 ± 0.56	0.80 ± 0.65
Benign nodule	0.68 ± 0.58	0.65 ± 0.86	0.15 ± 0.43	0.10 ± 0.43
P	0.809	0.416	0.008	0.009

DWI, diffusion-weighted imaging; SIR, signal intensity ratio.

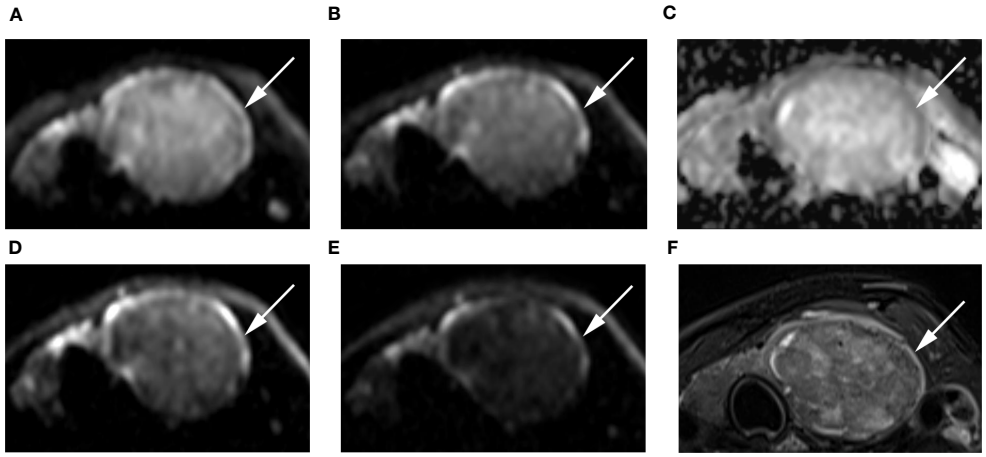

FIGURE 4
Images of a 55-year-old female with left lobe nodular goiters (arrow): DWI image with a b-value of 500 s/mm^2 **(A)**, 1000 s/mm^2 **(B)**, 1500 s/mm^2 **(D)**, 2000 s/mm^2 **(E)**; **(C)** ADC image with a b-value of 1500 s/mm^2; **(F)** T2-weighted image. The SNR of the thyroid decreased as the b value increased. In the DWI image with a b-value of 1500 s/mm^2, the SI of the nodule was significantly low relative to the other images.

2 b-values reflects tumor cellularity and thus the properties of diffusion restriction in tissue (19). ADC values are affected by both blood perfusion and extracellular space (20). Both in the papillary carcinoma and benign nodule, the ADC values decreased as the b value increased. The signal-to-noise ratio decreases as the b value increases (21).

In papillary carcinomas, the SIR_{nodule} was higher in DWI images with a b-value of 1500 s/mm^2 than in DWI images with b-values of 500, 1000, 2000 s/mm^2. In benign nodules, the SIR_{nodule} was lower in DWI images with a b-value of 1500 s/mm^2 than in DWI images with b-values of 1000 and 2000 s/mm^2. When the b-value was 1500 s/mm^2, the SIR_{nodule} significantly differed between

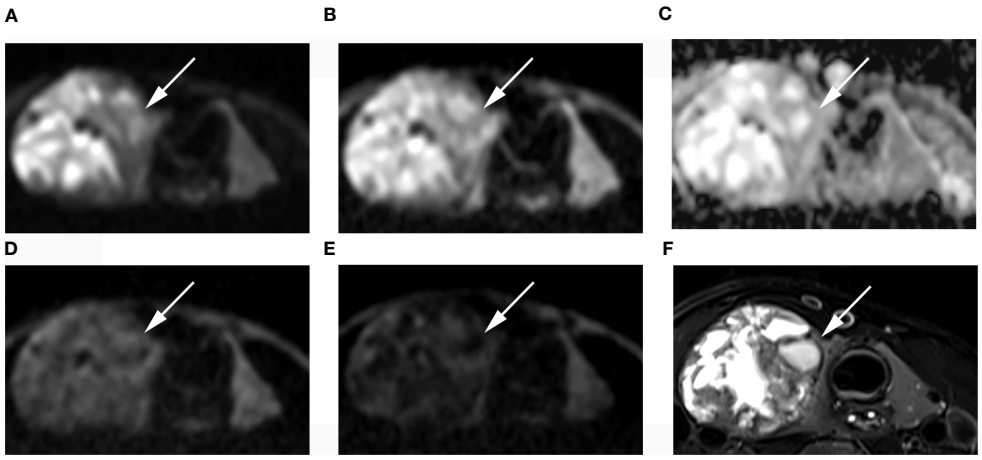

FIGURE 5
Images of a 49-year-old female with right lobe follicular adenoma (arrow): DWI image with a b-value of 500 s/mm^2 **(A)**, 1000 s/mm^2 **(B)**, 1500 s/mm^2 **(D)**, 2000 s/mm^2 **(E)**; **(C)** ADC image with a b-value of 1500 s/mm^2; **(F)** T2-weighted image. The SNR of thyroid decreased as the b value increased. In the DWI image with a b-value of 1500 s/mm^2, the SI of the nodule was significantly low relative to the other images.

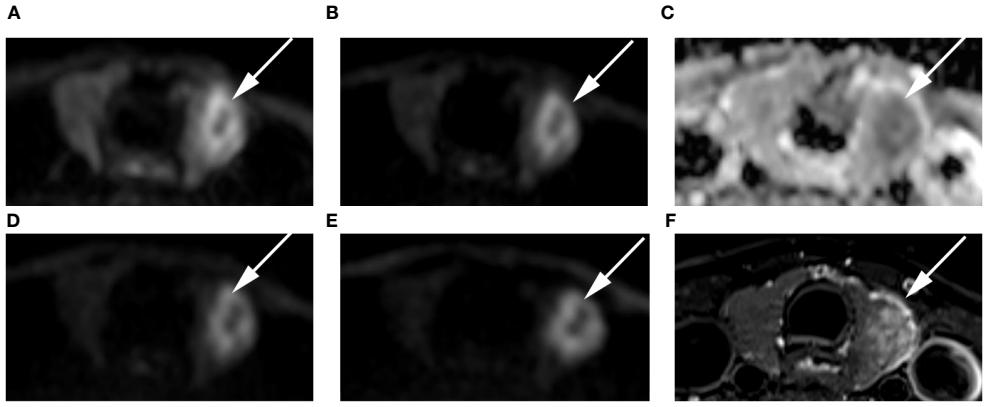

FIGURE 6
Images of a 54-year-old female with left lobe papillary carcinoma (arrow): DWI image with a b-value of 500 s/mm^2 **(A)**, 1000 s/mm^2 **(B)**, 1500 s/mm^2 **(D)**, 2000 s/mm^2 **(E)**; **(C)** ADC image with a b-value of 1500 s/mm^2; **(F)** T2-weighted image. The SNR of the thyroid decreased as the b value increased. In the DWI image with a b-value of 1500 s/mm^2, the SI of the nodule was significantly high relative to other out images.

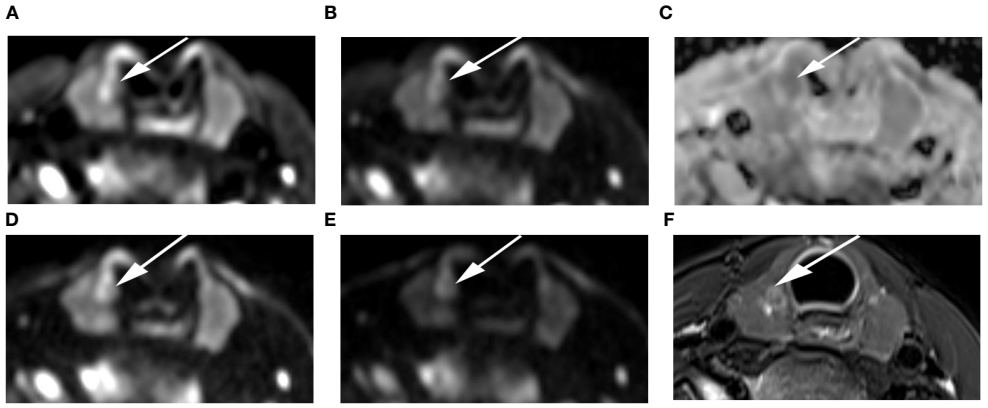

FIGURE 7
Images of a 24-year-old female with right lobe micropapillary carcinoma (arrow): DWI image with a b-value of 500 s/mm^2 **(A)**, 1000 s/mm^2 **(B)**, 1500 s/mm^2 **(D)**, 2000 s/mm^2 **(E)**; **(C)** ADC image with a b-value of 1500 s/mm^2; **(F)** T2-weighted image. The SNR of the thyroid decreased as the b value increased. In the DWI image with a b-value of 1500 s/mm^2, the SI of the nodule was significantly high relative to the other images.

thyroid papillary carcinomas and thyroid benign nodules, suggesting that the SI difference was visible to the naked eye when the b-value was 1500 s/mm^2. In addition, the ROC analysis with the ADC showed better classification results for b=1500 s/mm^2 compared to the remaining b-values. Therefore, 1500 s/mm^2 was the optimal b value for differentiating thyroid papillary carcinomas and thyroid benign nodules.

The sharpness of nodules and thyroids decreased as the b value increased. However, the sharpness of nodules was similar between images with a b-value of 1000 mm^2/s and those with a b-value of 1500 s/mm^2, suggesting that 1500 mm^2/s maintains good image quality, which is inconsistent with results from a past study, where b values ranged from 200 s/mm^2 to 800 s/mm^2 on 1.5 T MRI, and worse image quality was noted at high b values (8). This discrepancy

TABLE 5 Comparison of the mean ADC values of papillary carcinomas and benign nodules with different b-values (×10^{-3} s/mm^2) in ADC images.

	500	1000	1500	2000
Papillary carcinoma (×10^{-3} mm^2/s)	1.24 ± 0.30	1.03 ± 0.23	0.96 ± 0.24	0.79 ± 0.16
Benign nodule (×10^{-3} mm^2/s)	2.10 ± 0.55	1.75 ± 0.46	1.46 ± 0.40	1.15 ± 0.31
P	0.003	< 0.001	< 0.001	< 0.001

ADC, apparent diffusion coefficient.

TABLE 6 Diagnostic performance of the ADC in differentiating between thyroid papillary carcinoma and thyroid benign nodules with different b-values ($\times10^{-3}$ s/mm^2).

b value	500	1000	1500	2000
AUC (95% CI)	0.888 (0.819-0.957)	0.881 (0.810-0.952)	0.896 (0.828-0.964)	0.871 (0.794-0.947)
Sensitivity (95% CI)	84.31% (71.99%-91.83%)	78.43% (65.37%-87.51%)	86.27% (74.28%-93.19%)	80.39% (67.54%-88.98%)
Specificity (95% CI)	84.37% (71.49%-91.66%)	89.97% (78.64%-95.65%)	90.57% (76.20%-94.38%)	89.99% (78.64%-95.65%)
Cutoff ADC ($\times10^{-3}$ s/mm^2)	1.47	1.28	1.16	0.93

ADC, apparent diffusion coefficient; AUC, area under the curve; CI, confidence interval.

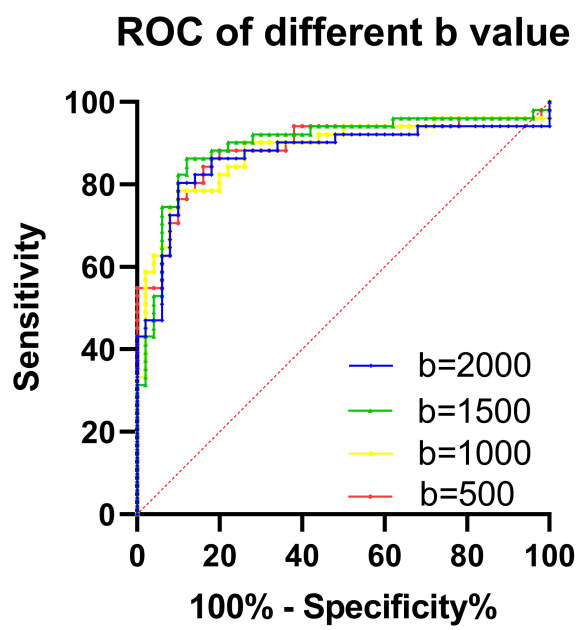

FIGURE 8
The ROC curve of the ADC with different b-values for predicting a papillary carcinoma.

may be due to the ZOOMit technique, which improves image quality compared to conventional single-shot echo planar imaging.

In this study, thyroid imaging was performed with a 3.0 T MR scanner. In past literature, authors highlight the advantages of DWI on strong magnetic fields machines, which can accurately measure the ADC values (22). A 16channel surface coil can provide better image signal-to-noise ratio performance and resolution for the thyroid, which ensures image quality. Past studies have shown that ZOOMit-DWI improves image quality compared with conventional DWI of the prostate, orbit and gallbladder (23–25), demonstrating that ZOOMit-DWI is a good tool to observe small organs. Due to the short scanning time, the relative homogeneity of signal excitation is increased, and image blurring and distortion are decreased (12). In this study, excellent image quality performance was achieved, which also benefited from ZOOMit-DWI. Good imaging quality is useful for manual ROI definition, which directly affects measurement results.

In this study, ADC maps were computed based on DWI images acquired with different b values and reflect the discrimination of thyroid papillary carcinoma from benign thyroid nodules. All past studies share one point of view: the diffusion of water molecules is restricted in malignant tumors, which lead to ADC values decrease, and the difference in the ADC values is valuable to make the differential diagnosis between benign and malignant tumors (26). This study also verified this view. Past studies demonstrated that the ADC values of malignant nodules was obviously lower than benign nodules in thyroid (6), which is similar to the results in this study, where the ADC value of thyroid papillary carcinomas was significantly lower than that of benign nodules regardless of whether the b-value was 500, 1000, 1500, or 2000 s/mm^2. Papillary carcinomas have some microscopic features, which include psammoma bodies, foci of squamous metaplasia, lymphoid infiltration of the tumor stroma, and a peculiar appearance of tumor cell nuclei. The microscopic features lead to increased cellularity and reduced extracellular space (27). In addition, fibrosis also hampers the diffusion of water molecules to varying degrees (28).

This study has a few limitations. First, different field strengths were not compared. Second, only four b-values were compared in this study. In the future, we will narrow the b-value interval for verification. Finally, the ADC was measured by Siemens Healthcare equipment. Further research is needed to determine whether the cutoff value is appropriate for other MRI machines and third-party postprocessing platforms.

In conclusion, 1500 s/mm^2 was a suitable b-value to differentiate benign and malignant thyroid nodules in ZOOMit-DWI images, which had better image quality, and a signal difference was visible to the naked eye.

TABLE 7 DeLong results for the ADC in predicting thyroid papillary carcinoma with different b-values ($\times10^{-3}$ s/mm^2).

	500-1000	500-1500	500-2000	1000-1500	1000-2000	1500-2000
P	0.891	0.546	0.399	0.337	0.486	0.006

ADC, apparent diffusion coefficient.

Data availability statement

The original contributions presented in the study are included in the article/supplementary material. Further inquiries can be directed to the corresponding author.

Ethics statement

The studies involving humans were approved by Chongqing University Cancer Hospital institutional review board. The studies were conducted in accordance with the local legislation and institutional requirements. The participants provided their written informed consent to participate in this study. Written informed consent was obtained from the individual(s) for the publication of any potentially identifiable images or data included in this article.

Author contributions

JW contributed to the conception and design of the study, data analysis and writing of the manuscript. LJ and DL contributed to performing the experiments and writing and revising the manuscript. JC, YT contributed to the data collection. JZ contributed to the data analysis and interpretation of the data. JZ is the guarantor of this study and approved the version to be submitted. All authors accept responsibility for the integrity of the data and the accuracy of the data analysis. All authors contributed to the article and approved the submitted version.

Funding

The author(s) declare financial support was received for the research, authorship, and/or publication of this article. This study has received funding by the National Natural Science Foundation of China (Grant No. 82071883).

Acknowledgments

We acknowledge the support of Zhitao Zhang from Siemens Healthcare, Ltd., Chengdu Branch.

Conflict of interest

The authors declare that the research was conducted in the absence of any commercial or financial relationships that could be construed as a potential conflict of interest.

Publisher's note

All claims expressed in this article are solely those of the authors and do not necessarily represent those of their affiliated organizations, or those of the publisher, the editors and the reviewers. Any product that may be evaluated in this article, or claim that may be made by its manufacturer, is not guaranteed or endorsed by the publisher.Abbreviation

References

1. Yoon JH, Lee HS, Kim EK, Moon HJ, Kwak JY. Malignancy risk stratification of thyroid nodules: comparison between the thyroid imaging reporting and data system and the 2014 american thyroid association management guidelines. *Radiology*. (2016) 278:917–24. doi: 10.1148/radiol.2015150056

2. Durante C, Grani G, Lamartina L, Filetti S, Mandel SJ, Cooper DS. The diagnosis and management of thyroid nodules: A review. *Jama*. (2018) 319:914–24. doi: 10.1001/jama.2018.0898

3. Khizer AT, Raza S, Slehria AU. Diffusion-weighted MR imaging and ADC mapping in differentiating benign from Malignant thyroid nodules. *J Coll Physicians Surg Pak*. (2015) 25:785–8.

4. Tappouni RR, Itri JN, McQueen TS, Lalwani N, Ou JJ. ACR TI-RADS: pitfalls, solutions, and future directions. *Radiographics: Rev Publ Radiological Soc North America Inc*. (2019) 39:2040–52. doi: 10.1148/rg.2019190026

5. Aghaghazvini L, Sharifian H, Yazdani N, Hosseiny M, Kooraki S, Pirouzi P, et al. Differentiation between benign and Malignant thyroid nodules using diffusion-weighted imaging, a 3-T MRI study. *Indian J Radiol Imaging*. (2018) 28:460–4. doi: 10.4103/ijri.IJRI_488_17

6. Chen L, Xu J, Bao J, Huang X, Hu X, Xia Y, et al. Diffusion-weighted MRI in differentiating Malignant from benign thyroid nodules: a meta-analysis. *BMJ Open*. (2016) 6:e008413. doi: 10.1136/bmjopen-2015-008413

7. Kong W, Yue X, Ren J, Tao X. A comparative analysis of diffusion-weighted imaging and ultrasound in thyroid nodules. *BMC Med Imaging*. (2019) 19:92. doi: 10.1186/s12880-019-0381-x

8. Linh LT, Cuong NN, Hung TV, Hieu NV, Lenh BV, Hue ND, et al. Value of diffusion weighted MRI with quantitative ADC map in diagnosis of Malignant thyroid disease. *Diagnostics (Basel Switzerland)*. (2019) 9:129. doi: 10.3390/diagnostics9040129

9. Le Bihan D. From Brownian motion to mind imaging: diffusion MRI. *Bull Acad Natl Med*. (2006) 190:1605–27.

10. Wang Q, Guo Y, Zhang J, Ning H, Zhang X, Lu Y, et al. Diagnostic value of high b-value (2000 s/mm2) DWI for thyroid micronodules. *Med (Baltimore)*. (2019) 98:e14298. doi: 10.1097/MD.0000000000014298

11. Wang Q, Guo Y, Zhang J, Shi L, Ning H, Zhang X, et al. Utility of high b-value (2000 sec/mm2) DWI with RESOLVE in differentiating papillary thyroid carcinomas and papillary thyroid microcarcinomas from benign thyroid nodules. *PloS One*. (2018) 13:e0200270. doi: 10.1371/journal.pone.0200270

12. Seeger A, Batra M, Süsskind D, Ernemann U, Hauser TK. Assessment of uveal melanomas using advanced diffusion-weighted imaging techniques: value of reduced field of view DWI ("zoomed DWI") and readout-segmented DWI (RESOLVE). *Acta Radiol*. (2019) 60:977–84. doi: 10.1177/0284185118806666

13. Sim KC, Park BJ, Han NY, Sung DJ, Kim MJ, Han YE. Efficacy of ZOOMit coronal diffusion-weighted imaging and MR texture analysis for differentiating between benign and Malignant distal bile duct strictures. *Abdom Radiol (NY)*. (2020) 45:2418–29. doi: 10.1007/s00261-020-02625-0

14. Schueller-Weidekamm C, Kaserer K, Schueller G, Scheuba C, Ringl H, Weber M, et al. Can quantitative diffusion-weighted MR imaging differentiate benign and Malignant cold thyroid nodules? Initial results in 25 patients. *AJNR Am J neuroradiology*. (2009) 30:417–22. doi: 10.3174/ajnr.A1338

15. Koo TK, Li MY. A guideline of selecting and reporting intraclass correlation coefficients for reliability research. *J Chiropr Med*. (2016) 15:155–63. doi: 10.1016/j.jcm.2016.02.012

16. Ablefoni M, Ullrich S, Surov A, Hoffmann KT, Meyer HJ. Diagnostic benefit of high b-value computed diffusion-weighted imaging in acute brainstem infarction. *J Neuroradiol*. (2022) 49:47–52. doi: 10.1016/j.neurad.2020.09.004

17. Sharafeldeen A, Elsharkawy M, Khaled R, Shaffie A, Khalifa F, Soliman A, et al. Texture and shape analysis of diffusion-weighted imaging for thyroid nodules classification using machine learning. *Med Phys*. (2022) 49:988–99. doi: 10.1002/mp.15399

18. Xia Y, Wang L, Wu Z, Tan J, Fu M, Fu C, et al. Comparison of computed and acquired DWI in the assessment of rectal cancer: image quality and preoperative staging. *Front Oncol*. (2022) 12:788731. doi: 10.3389/fonc.2022.788731

19. Baltzer P, Mann RM, Iima M, Sigmund EE, Clauser P, Gilbert FJ, et al. Diffusion-weighted imaging of the breast-a consensus and mission statement from the EUSOBI International Breast Diffusion-Weighted Imaging working group. *Eur Radiol*. (2020) 30:1436–50. doi: 10.1007/s00330-019-06510-3

20. Liu R, Li J, Jiang Y, Wu Z, Ji J, Li A, et al. The utility of diffusion-weighted imaging and ADC values in the characterization of mumps orchitis and seminoma. *Acta Radiol*. (2022) 63:416–23. doi: 10.1177/0284185121991980

21. Zhou X, Ma C, Wang Z, Liu JL, Rui YP, Li YH, et al. Effect of region of interest on ADC and interobserver variability in thyroid nodules. *BMC Med Imaging*. (2019) 19:55. doi: 10.1186/s12880-019-0357-x

22. Partridge SC, Nissan N, Rahbar H, Kitsch AE, Sigmund EE. Diffusion-weighted breast MRI: Clinical applications and emerging techniques. *J Magn Reson Imaging*. (2017) 45:337–55. doi: 10.1002/jmri.v45.2

23. Seeger A, Schulze M, Schuettauf F, Ernemann U, Hauser TK. Advanced diffusion-weighted imaging in patients with optic neuritis deficit - value of reduced field of view DWI and readout-segmented DWI. *Neuroradiol J*. (2018) 31:126–32. doi: 10.1177/1971400918757711

24. Attenberger UI, Rathmann N, Sertdemir M, Riffel P, Weidner A, Kannengiesser S, et al. Small Field-of-view single-shot EPI-DWI of the prostate: Evaluation of spatially-tailored two-dimensional radiofrequency excitation pulses. *Z Med Phys*. (2016) 26:168–76. doi: 10.1016/j.zemedi.2015.06.013

25. Wu S, Zou X, Wang Q, Hu D, Li Z, Xu C. Gallbladder carcinoma: an initial clinical experience of reduced field-of-view diffusion-weighted MRI. *Cancer imaging: Off Publ Int Cancer Imaging Soc*. (2020) 20:50. doi: 10.1186/s40644-020-00326-x

26. Henzler T, Schmid-Bindert G, Schoenberg SO, Fink C. Diffusion and perfusion MRI of the lung and mediastinum. *Eur J Radiol*. (2010) 76:329–36. doi: 10.1016/j.ejrad.2010.05.005

27. Schueller-Weidekamm C, Schueller G, Kaserer K, Scheuba C, Ringl H, Weber M, et al. Diagnostic value of sonography, ultrasound-guided fine-needle aspiration cytology, and diffusion-weighted MRI in the characterization of cold thyroid nodules. *Eur J Radiol*. (2010) 73:538–44. doi: 10.1016/j.ejrad.2008.12.013

28. Liu J, Zheng D, Li Q, Tang X, Luo Z, Yuan Z, et al. A predictive model of thyroid Malignancy using clinical, biochemical and sonographic parameters for patients in a multi-center setting. *BMC Endocr Disord*. (2018) 18:17. doi: 10.1186/s12902-018-0241-7

Frontiers in Neuroscience

Provides a holistic understanding of brain function from genes to behavior

Part of the most cited neuroscience journal series which explores the brain - from the new eras of causation and anatomical neurosciences to neuroeconomics and neuroenergetics.

Discover the latest Research Topics

See more →

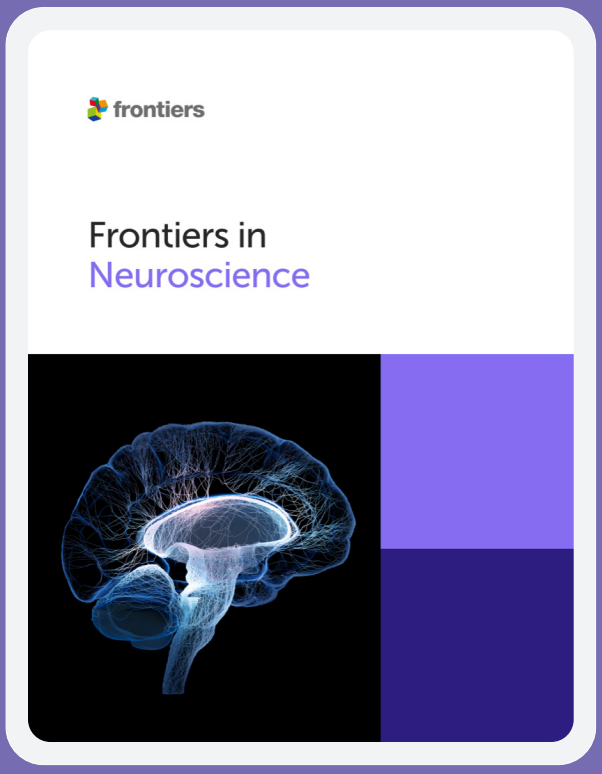

Frontiers

Avenue du Tribunal-Fédéral 34
1005 Lausanne, Switzerland
frontiersin.org

Contact us

+41 (0)21 510 17 00
frontiersin.org/about/contact